

Porous carbon fibers derived from PAN-based block copolymers

Ainhoa Álvarez Gómez

A dissertation submitted by in partial fulfillment of the
requirements for the degree of Doctor of Philosophy in

Materials Science and Engineering

Universidad Carlos III de Madrid

Advisor(s):

Berna Serrano Prieto

Verónica San Miguel Aranz

Tutor:

Berna Serrano Prieto

July, 2023

This thesis is distributed under license “Creative Commons **Attribution – Non Commercial – Non Derivatives**”.



A mis padres y hermana

ACKNOWLEDGMENTS

Todavía no me puedo creer que este escribiendo esta parte de la tesis, parecía imposible llegar a este momento hace unas semanas, pero cada vez está más cerca el final de esta etapa y llegado a este punto no sé por dónde empezar, tengo mucho que agradecer, pero intentaré ir al grano y no extenderme mucho.

Quería comenzar por agradecer a mis tutoras de tesis Berna Serrano y Verónica San Miguel. Gracias por darme esta oportunidad, me habéis enseñado y apoyado mucho durante estos años, la puerta de vuestros despachos siempre ha estado abierta y aunque ha sido un camino difícil en el que hemos ido aprendiendo las tres sobre la marcha, ahora se abren un montón de nuevas posibilidades. Tengo que agradecer también a Juan Pedro Fernández, que siempre ha estado dispuesto a echarme una mano y aconsejarme, ha sido un placer trabajar con los tres.

I also want to thank to professor Jiayin Yuan for giving me the opportunity to work in his group, you were very kind and supportive during my visiting research. I would also like to thank all the colleagues from the research group who welcome me from day one and taught me so many things. Finally, I would also like to thank the rest of the people with whom I shared those three months at Stockholm University and with whom I had the opportunity to travel and share moments that I will always remember.

Gracias a todas las personas del departamento de Ciencia e Ingeniería de Materiales con las que he coincidido estos años, a los técnicos, en especial a Cristina con la que he compartido muchas horas en la continua búsqueda de las porosidades imposibles. Quería agradecer también a las personas de IMDEA materiales que me han ayudado y aconsejado durante estos años.

Gracias sobre todo a todos mis compañeros, a los que ya no estáis, a los que acabáis de llegar y a los que seguís al pie del cañón. Gracias a las personas con las que he compartido horas de síntesis en el laboratorio, horas y horas de clases, con los que he compartido despacho, con los que he compartido descansos, desayunos, risas, con los que he tenido la oportunidad de viajar (me refiero a los congresos, pero si, también considero algunas comidas de campo como viajar), gracias a todos, me he encontrado con personas maravillosas que me han ayudado y apoyado muchísimo y que recordaré siempre.

Por supuesto, tengo que agradecer a mis amigas, toda la vida juntas, siempre apoyándome en todo, compartir la vida con vosotras ha sido y siempre será un placer, gracias chicas, sé que estáis deseando celebrar. Gracias también a mis amigos de la uni, hace ya diez años que empecé la carrera de química y ahí empezó todo... En esos años me encontré con gente increíble, con amigas que veo una vez al año y parece que el tiempo no ha pasado y al resto, gracias chicos, nos vemos en la revoltosa.

Gracias a toda mi familia, siempre pendiente y ayudándome, a mi abuelo que sé que está orgullísimo, y a mi abuela que me habría encantado que pudiera leer estas palabras, gracias por todas las cosas que me enseñaste que me ayudan hoy y que me ayudarán siempre. A mi madre, que te voy a decir mamá, me dijiste que tenía que estudiar... Gracias por estar siempre ahí incondicionalmente, esta tesis es tuya. Ricar, gracias por el apoyo, por escuchar presentaciones y por encima tener que hacer preguntas cuando acababa. Pao, gracias hermana, el coworking ha funcionado, siempre has sido y serás mi gran apoyo, se han cambiado las tornas y parece que ahora tú me cuidas a mí.

Adri, hace muchos años ya que caminamos juntos, hemos vivido de todo y es que lo bueno es más bueno contigo y lo malo es menos malo, gracias por acompañarme, esta etapa se termina y empiezan nuevas que comenzar. Kira, que absurdo escribirte palabras de agradecimiento, jamás lo leerás y jamás lo entenderás, eres un perro, pero llegaste a mi vida cuando empecé esta tesis y me has obligado a gestionar y priorizar mi tiempo, a caminar cuando no tenía ganas y a tener paciencia.

Papá, por siempre GRACIAS.

PUBLISHED AND SUBMITTED CONTENT

Publications:

- Álvarez-Gómez, A., Yuan, J., Fernández-Blázquez, J. P., San-Miguel, V., & Serrano, M. B. Polyacrylonitrile-*b*-Polystyrene Block Copolymer-Derived Hierarchical Porous Carbon Materials for Supercapacitor. *Polymers*, 2022, 14(23), 5109, doi.org/10.3390/polym14235109.

The information of this paper is reported in Chapter 3, 4 and 7. I participate in all the experimental part as well as the writing of the article itself.

- Álvarez-Gómez, A., Baselga, J., Cabanelas, J. C., San-Miguel, V., & Serrano, M. B. Porous carbon fibers based on block copolymers as multifunctional materials. **To be submitted**

The information of this review is reported in Chapter 1. I participate in the writing of the review article itself.

International conferences related to this thesis work:

- Author: A. Álvarez, B. Serrano, V. San Miguel.
Title: Porous Carbon Materials from Block Copolymer Template for Supercapacitors.
Communication type: Oral
Congress: ANM. Aveiro, Portugal (22–24 July 2021)
- Author: A. Álvarez, B. Serrano, V. San Miguel
Title: Porous carbon fibers from PAN-based block copolymer for energy applications.
Communication type: Oral
Congress: GEP–SLAP. San Sebastian, Spain (8–12 May 2022)

PREFACE

This PhD Thesis has been carried out at the Group of Polymers and Composites (GPC), belonging to the Department of Materials Science and Engineering and Chemical Engineering of the University Carlos III of Madrid (UC3M). This project has been financed through PIPF scholarship (2019) from the same University and the project PID2021-125302NB-I00 from the Spanish Ministry of Science and Innovation.

Thanks to the pre-doctoral research stay in the international center of recognized prestige Stockholm University (SU), Stockholm (Sweden), and the collaboration with the institution IMDEA Material, it has been possible to access to research resources facilitating this thesis work.

This Doctoral Thesis complies with the requirements for its mention as an International PhD that has been established in article 15 of the Real Decreto 99/2011 en la Ordenación de la Enseñanza Universitaria Oficial (B.O.E N° 35 of January 28, 2011, pp. 13909-13926) as is described in the Rules and Regulations for PhD studies at Universidad Carlos III de Madrid.

Resumen

Porous carbon fibers derived from PAN-based block copolymers

Durante años, los materiales porosos de carbono han suscitado un gran interés para su uso en innumerables aplicaciones tecnológicas, debido a sus excelentes propiedades fisicoquímicas y su elevada superficie específica. Estos materiales han demostrado tener un elevado potencial especialmente en aplicaciones relacionadas con el medioambiente y la energía debido a su alta capacidad para adsorber distintas especies, incluyendo gases, moléculas orgánicas y/o iones metálicos. En particular, las fibras de carbono porosas, PCFs por sus siglas en inglés (Porous Carbon Fibers), con una porosidad controlada y jerarquizada han captado una atención significativa en los últimos años, ya que combinan las ventajas de materiales macro-, meso- y microporosos, lo que las convierte en excelentes candidatas para aplicaciones de adsorción y energía, entre otras.

Las PCFs ofrecen una estructura de carbono continua que combina alta conductividad, altos valores de áreas superficiales y densidades muy bajas. Concretamente, en lo que respecta a su uso como materiales para electrodos de supercondensadores, las PCFs presentan algunas ventajas sobre los carbones activos, que son los materiales comúnmente utilizados como electrodos en este tipo de dispositivos. Estas fibras de carbono pueden emplearse idealmente como electrodos sin el uso de aglutinantes o aditivos conductores. Además, para esta aplicación específica, el desarrollo de PCFs con una estructura de poros jerarquizada es especialmente interesante, ya que los mesoporos facilitan la difusión de iones hacia los microporos confinados en las regiones internas del material. Por lo tanto, se consigue incrementar el área de superficie accesible a los iones de electrolito, que se traduce en una mayor capacidad de almacenamiento y con ello se incrementa el rendimiento electroquímico.

Destaca el uso de copolímeros en bloque, BCPs por sus siglas en inglés (Block copolymers), como materiales molde o plantilla para la obtención de PCFs, debido a su capacidad para autoensamblarse y separarse en microfases, lo que da lugar a múltiples morfologías. Mediante el empleo de un bloque de sacrificio compuesto por un polímero térmicamente degradable y otro bloque como fuente de carbono, es posible controlar las estructuras de carbono generadas, en términos de volumen, tamaño y forma de los poros. Ajustando la fracción volumétrica del bloque de sacrificio, la interacción entre los bloques

y/o el grado de polimerización del copolímero es posible modificar el número, tamaño y forma de los poros generados después de la carbonización del material plantilla.

Esta tesis analiza el uso de copolímeros en bloque como precursores para obtener fibras de carbono porosas. Se sintetizaron copolímeros con pesos moleculares definidos, a partir de una polimerización radical controlada (RAFT), basados en poliacrilonitrilo (PAN) y diferentes bloques de sacrificio, como poliestireno (PS) y poli(tert-butil acrilato) (PtBA), que dieron lugar a fibras con distintas propiedades fisicoquímicas. Se ha estudiado el comportamiento de autoensamblaje y separación de fases de los copolímeros durante el tratamiento térmico, así como el tamaño del poro y su distribución después de la pirólisis. La obtención de las fibras porosas se llevó a cabo mediante una técnica simple, versátil, y fácilmente escalable, el electrohilado. Mediante la pirólisis del bloque de sacrificio se obtuvieron fibras de carbono con estructuras de poro jerarquizadas, diámetros estrechos y varias formas y tamaños dependiendo de la naturaleza del bloque de sacrificio y el grado de polimerización.

Asimismo, se estudiaron diferentes parámetros que influyen en las propiedades capacitivas y el comportamiento electroquímico de las PCFs. Entre ellos se consideraron la incorporación de heteroátomos (nitrógeno y azufre) y nanopartículas con actividad redox (nanopartículas de magnetita). Las PCFs derivadas de un copolímero en bloque de poliestireno y poliacrilonitrilo (PS-*b*-PAN), se activaron/doparon con urea y tiourea como precursores de heteroátomos de N y N/S, respectivamente. Estos procesos permitieron obtener PCFs co-dopadas sin comprometer los valores de área superficial y mostrando un aumento de la capacitancia.

Por último, se presenta un estudio preliminar de la incorporación de nanopartículas de magnetita (MNPs) con actividad redox en la estructura de las fibras de carbono porosas (PCFs), y su influencia en la microestructura y la porosidad. Para ello, se introdujeron nanopartículas de magnetita en bajas concentraciones en la matriz del copolímero en bloque (PtBA-*b*-PAN), y posteriormente se utilizó esa dispersión como precursor de electrohilado en la fabricación de las fibras. Se obtuvieron PCFs con una porosidad y rendimiento electroquímico mejorados, en comparación con las fibras fabricadas sin la adición de nanopartículas.

En resumen, este trabajo de tesis tiene como objetivo investigar el comportamiento de los copolímeros de bloque basados en poliacrilonitrilo como precursores para la producción de fibras de carbono porosas. En particular, se pretende estudiar las variaciones en los parámetros que influyen en la separación de fases, lo que a su vez permitirá explorar nuevas vías para modular el tamaño y la forma de los poros. Además, a través de la caracterización electroquímica de los materiales generados se analiza el impacto en el rendimiento electroquímico de las variaciones en el área de superficie específica, la distribución del tamaño de los poros y las funcionalidades de la superficie.

Abstract

Porous carbon fibers derived from PAN-based block copolymers

For years, porous carbon materials have attracted wide interest for their use in countless technological applications, due to their excellent physicochemical properties and their high specific surface area. These materials have shown a high potential, especially for environmental and energy-related applications, due to their ability to adsorb different species, including gases, organic molecules and/or metal ions. In particular, porous carbon fibers (PCFs) with a well-controlled and hierarchical porosity have attracted significant attention recently, since they combine the advantages of macro-, meso- and microporous materials, making them excellent candidates for adsorption and energy applications, among others.

PCFs offer a continuous carbon structure that combines high conductivity, high surface area values, and very low densities. Specifically, concerning their use as electrode materials for supercapacitor, PCFs present some advantages over active carbons, which are commonly used as electrodes in these devices. These carbon fibers can ideally be used as self-standing electrodes without using binders or conductive additives. Furthermore, for this specific application, the development of PCFs with a hierarchical pore structure is especially interesting, since the mesopores facilitate the ion-diffusion towards the micropores confined in the internal regions of the material. Therefore, the surface area accessible to electrolyte ions is increased, which translates into a higher storage capacity and thus increases the electrochemical performance.

The use of block copolymers (BCPs) as template materials for obtaining PCFs stands out due to the ability of block copolymers to self-assemble and separate into microphases, producing miscellaneous morphologies. By using a sacrificial block composed of a thermally degradable polymer and another block as a carbon source, it is possible to control the carbon structures produced in terms of pore volume, size, and shape. Adjusting the volume fraction of the sacrificial block, the interaction between the blocks and/or the overall degree of polymerization of the copolymer allows to modify the number, size and shape of the pores generated after carbonization of the template.

This thesis analyzes the use of block copolymers as precursors to obtain porous carbon fibers. Copolymers with defined molecular weights were synthesized using controlled radical polymerization (RAFT), based on polyacrylonitrile (PAN) and different sacrificial blocks, such as polystyrene (PS) and poly(*tert*-butyl acrylate) (PtBA), resulting in fibers with different physicochemical properties. The self-assembly and phase separation behavior of block copolymers during thermal treatments, as well as the pore size and distribution after pyrolysis, have been studied. PCFs were obtained using a simple, versatile, and easily scalable technique, electrospinning. By pyrolysis of the sacrificial block, carbon fibers with hierarchical pore structures, narrow diameters, and various shapes and sizes were obtained, depending on the nature of the sacrificial block and the degree of polymerization.

Different parameters influencing the capacitive properties and electrochemical behavior of the obtained PCFs were also studied. Among them, the introduction of heteroatoms (nitrogen and sulfur) and redox active nanoparticles (magnetite nanoparticles) were considered. PCFs derived from a polystyrene and polyacrylonitrile block copolymer (PS-*b*-PAN) were activated/doped with urea and thiourea as N and N/S heteroatom precursors, respectively. These processes allowed to obtain co-doped PCFs without compromising surface area values and showing an increase in capacitance.

Finally, a preliminary study is presented based on the addition of magnetite nanoparticles (MNPs) with redox activity in the structure of porous carbon fibers (PCFs), and its influence on the microstructure and porosity. For this purpose, magnetite nanoparticles were introduced in low concentrations into the block copolymer matrix (PtBA-*b*-PAN), and this dispersion was subsequently used as an electrospinning precursor to produce fibers. PCFs with improved porosity and electrochemical performance were obtained, compared to fibers produced without the addition of nanoparticles.

In summary, this thesis aims to investigate the behavior of polyacrylonitrile-based block copolymers as precursors to produce PCFs. In particular, it is intended to study the variations in the parameters that influence phase separation, allowing to explore new ways of modulating the size and shape of the pores. In addition, through the electrochemical characterization of the generated materials, the impact on electrochemical performance

of variations in the specific surface area, pore size distribution, and surface functionalities is analyzed.

Table of contents

Chapter 1: Introduction and objectives

1.1. Introduction.....	1
1.1.1. Advanced carbon materials for supercapacitors.....	4
1.1.2. Advanced carbon materials for CO ₂ capture and dye removal .	6
1.1.3. Production of porous carbon fibers and precursors.....	7
1.1.4. Porous carbon fibers: pseudocapacitance contribution	14
1.2. Motivation and Objectives.....	16

Chapter 2: Materials and methods

2.1. Materials	20
2.1.1. BCP polymerization reagents	20
2.1.2. Heteroatom precursors	22
2.2. Methods and characterization	22
2.2.1. BCPs characterization techniques	22
2.2.2. Electrospinning.....	25
2.2.3. Fiber characterization techniques.....	27
2.2.4. Electrochemical characterization	33

Chapter 3: Synthesis and characterization of block copolymer precursors

3.1. RAFT Polymerization.....	41
3.2. Synthesis and characterization of PS- <i>b</i> -PAN	43
3.2.1. Synthetic route.....	43
3.2.2. Polymer characterization.....	45
3.2.3. Thermal characterization.....	48
3.2.4. High molecular weight PS- <i>b</i> -PAN	50
3.3. Synthesis and characterization of PtBA- <i>b</i> -PAN.....	54
3.3.1. Synthetic route.....	54
3.3.2. Polymer characterization.....	55
3.3.3. Thermal characterization.....	58

Chapter 4: Porous carbon fibers derived from block copolymers

4.1. Phase-separation and morphology of PS- <i>b</i> -PAN.....	62
4.2. PCFs derived from PS- <i>b</i> -PAN	68
4.2.1. Electrospinning optimization	70
4.2.2. PS-PCFs: Morphological and structural characterization	74

4.2.3.HN_PS-PCFs: Morphological and structural characterization	83
4.3. PCFs derived from PtBA- <i>b</i> -PAN	92
4.3.1. PtBA-PCFs: Morphological and structural characterization..	95

Chapter 5: N and N/S co-doped porous carbon fibers

5.1. Experimental procedure	105
5.2. NPCFs and SPCFs: Morphological and structural characterization	106

Chapter 6: Porous carbon fibers with magnetite nanoparticles

6.1. Experimental procedure	119
6.1.1. Synthesis of magnetic nanoparticles	119
6.2. MNPs-PCFs: Morphological and structural characterization	120

Chapter 7: Porous carbon fiber material: electrochemical performance

7.1. PCFs derived from PS- <i>b</i> -PAN copolymer	130
7.2. Sacrificial block and degree of polymerization influence	136
7.3. N and N/S co-doped PCFs	140
7.4. PCFs containing magnetite nanoparticles	145

Chapter 8: Conclusions and future prospects

8.1. Conclusions	148
8.2. Future prospects	151

Bibliography

List of abbreviations and symbols

SCs	Supercapacitors
EDCLs	Electric double layer capacitors
Cs	Specific capacitance
PCFs	Porous carbon fibers
BCPs	Block copolymers
NPs	Nanoparticles
MNPs	Magnetite nanoparticles
PAN	Polyacrylonitrile
PS	Polystyrene
PtBA	Poly(tert-butyl acrylate)
DMF	Dimethylformamide
THF	Tetrahydrofuran
<i>f</i>	Volume fraction
M_w	Molecular weight
<i>N</i>	Degree of polymerization
χ	Polymer–polymer interaction parameter
CV	Cyclic voltammetry
GCD	Galvanostatic charge–discharge
EIS	Electrochemical impedance spectroscopy
DSC	Differential scanning calorimetry
TGA	Thermogravimetric analysis
SEM	Scanning electron microscopy
TEM	Transmission electron microscopy
XRD	X–ray diffraction
XPS	X–ray photoelectron spectroscopy
SSA	Specific surface area

Chapter 1

Introduction and objectives

1.1. Introduction

In today's society, energy demand increases exponentially driven by socioeconomic and population growth, as well as by the improvement and expansion of new electrical technologies, among other reasons. In fact, this energy dependence is predicted to double by 2050. Considering that sustainable development implies meeting the needs of the present without compromising resources of future generations [1], the use and development of more sustainable energy resources has become a major concern. Specifically in Spain, according to the 2021 energy balance report, the main source of energy is derived from the use of fossil fuels. This directly contributes to increasing CO₂ emissions, damaging the environment, and actively participating in climate change. To prevent that situation, EU set the target of using 40 % renewable energy sources to meet energy demand by 2030. Although Spain currently cannot reach that figure, within renewable energies the use of wind and solar energy stands out. These sources produce energy intermittently, which does not provide a flexible supply between the energy demanded and that generated. Therefore, it is essential to store and conserve the energy produced.

Electrochemical energy storage devices play an important role in advancing high-efficiency renewable energies [2,3]. Among these devices, batteries and supercapacitors stand out for offering advanced and modular features, long life cycle, high efficiency, and adequate power/energy density. Specifically, supercapacitors (SCs) are distinguished from other electrochemical storage devices by exhibiting rapid charge-discharge, high power densities ($> 1 \text{ kW kg}^{-1}$), and ultra-long cycle life ($> 500,000$ cycles) due to the storage mechanism, which does not involve irreversible reactions [4]. Based on their features, SCs complement the deficiencies of other electrochemical storage devices, such as batteries, fuel cells or conventional capacitors (**Figure 1.1**).

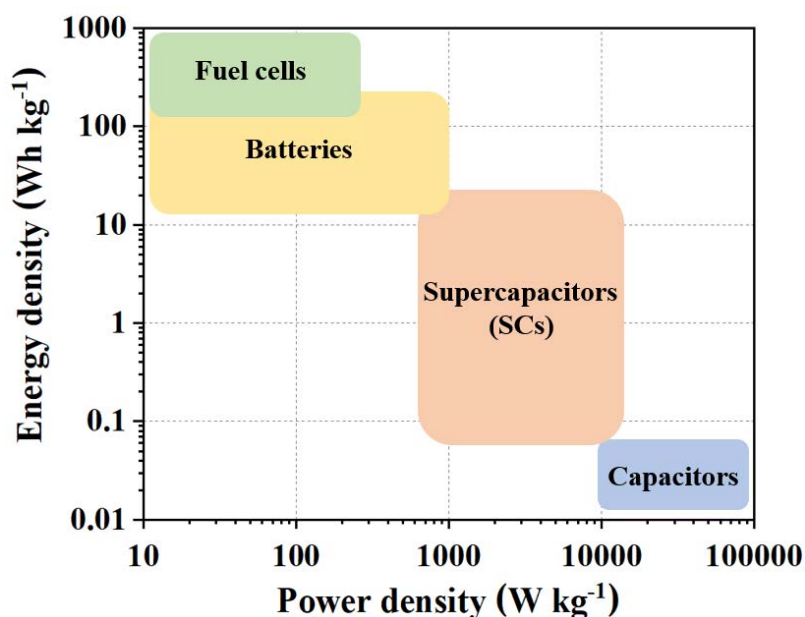


Figure 1.1. Ragone plot showing energy and power densities of conventional capacitors, supercapacitors, batteries, and fuel cells.

Supercapacitors can be divided into two main types based on their storage mechanism: (a) electrochemical double layer capacitors (EDLCs) and (b) pseudocapacitors. EDLCs store energy by intercalating charges at the electrode–electrolyte interface forming a double layer of charges [5]. On the other hand, pseudocapacitors store electrochemical energy, generally through Faradaic redox reactions between electrolyte ions and active functional groups on the electrode surface or by pseudocapacitive ion intercalation mechanism [6].

EDLCs electrodes are generally porous carbon materials with high specific surfaces areas [7]. The use of carbon–based electrodes presents some advantages, including high stability and long life cycle, due to the absence of irreversible reactions between the electrode and the electrolyte. On the other hand, pseudocapacitor electrode materials are usually transition metal oxides [8], which improve energy storage capability due to fast redox reactions, but sometimes compromise electrode stability. With this premise, the design of highly porous carbon materials with heteroatom–containing surface functionalities [9] or metal oxides [10] combines the advantages of both storage mechanism, increased capacitance values while maintaining long–cycle stability.

A typical SC cell is formed by two identical (symmetrical cell) or different (asymmetrical) electrodes, isolated by a separator material soaked in the aqueous electrolyte (**Figure 1.2**). As mentioned above, carbon-based electrodes without additional surface functionalities follow an electrical double layer storage mechanism. Charge storage occurs through electrostatic adsorption of cations on the negative electrode and anions on the positive electrode under an applied cell voltage, forming an electrical double layer at the electrode–electrolyte interface.

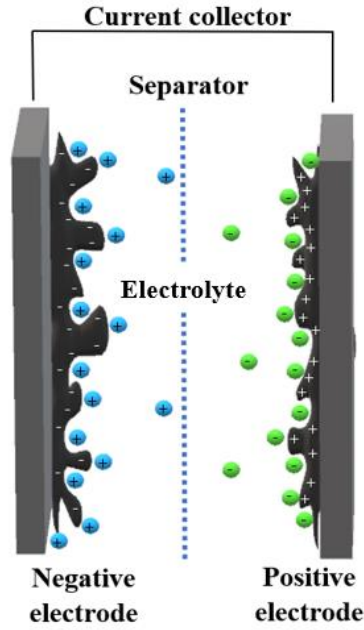


Figure 1.2. Symmetric supercapacitor cell schematic showing electric double layer (charged).

For EDLCs, capacitance (C), mainly depends on the dielectric constant of the electrolyte (ϵ_r), the effective thickness of the double layer (d), and electrode surface area (A), as follows:

$$C = \frac{\epsilon_r \epsilon_0 A}{d} \quad (1.1)$$

Therefore, the ion-accessible surface area of the electrode material is directly related to the SC electrochemical performance. In this regard, many studies have been carried out to develop new advanced porous carbon electrodes that allow higher capacitance values, which are discussed below.

1.1.1. Advanced carbon materials for supercapacitors

Most of the electrode materials used in commercially available SCs are active carbons [11]. These materials present high specific surface areas ($> 1000 \text{ m}^2 \text{ g}^{-1}$), high conductivity, relatively low cost, and good corrosion resistance. However, although active carbons reach high specific surface areas, they do not always achieve high capacitance values and power densities, since not all the pores are accessible to electrolyte ions. In fact, high power densities can only be obtained if the electrolyte ions have fast access to the entire surface area of the material, including pores at the interior regions. Therefore, given the challenges posed by fast ion adsorption–desorption requirements at high current densities, it becomes essential to ensure maximum pore accessibility. Consequently, the pore size, geometry, and distribution of the carbon electrode material greatly influence the electrochemical performance [12].

According to the IUPAC classification [13], pore sizes can be divided into three main ones: (a) micropores ($< 2 \text{ nm}$), (b) mesopores ($2\text{--}50 \text{ nm}$), and macropores ($> 50 \text{ nm}$). Most activated carbons are predominantly microporous materials [14]. However, in this type of materials, certain micropores may be enclosed or encapsulated in interior regions, making them inaccessible to electrolyte ions and increasing ion–diffusion resistances.

In this context, SCs electrode materials present several sources that participate into the internal resistance and limit their performance. The sum of all resistances is named as equivalent series resistance, or ESR [15]. Different contributions to the ESR includes the following ones: (a) electronic resistance; (b) interfacial resistance between electrode–current collector; (c) ionic diffusive resistance; (d) electrolyte resistance.

Thus, by focusing on minimizing resistances, the emergence of carbon materials with a hierarchical porous structure has provided a new avenue to improve accessible surface area and maximize capacitance values in high–performance supercapacitors [16,17]. Hierarchical porous materials combine macropores, which serve as ion supply and reduce ion diffusion distance to the inner surface, mesopores that provide low–resistance channels for ion diffusion, and micropores that facilitate the formation of the electric double layer (**Figure 1.3**).

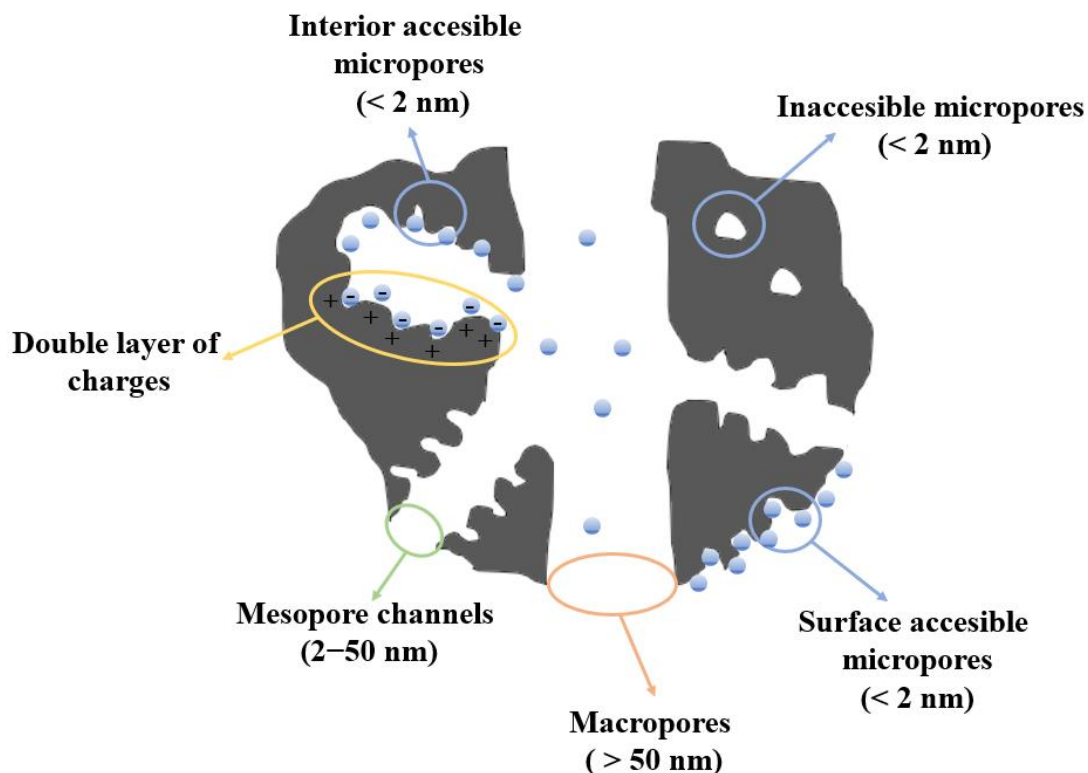


Figure 1.3. Schematic of hierarchical porous material connecting macro– and mesopores with interior micropores.

The pore induction process for active carbons is most of the times performed by thermal activation with a pore-forming agent, such as KOH [18] or ZnCl₂ [19]; although, some tedious acid washing steps are required to recover the added metal cation. Furthermore, optimizing activation methods to modulate porosity and generate hierarchical porous materials remains a considerable challenge and is a key parameter to improve electrochemical performance.

In addition, active carbons present some limitations that must be overcome to achieve higher performance and reduce resistance. Electrode preparation involves mixing the active material with additives such as carbon black or graphite to improve electrical conductivity, and binders, often polytetrafluoroethylene (PTFE) or polyvinylidene fluoride (PVDF) in proportions ranging from 5–10 wt% to form a ‘slurry’ that coats the current collector [20]. Binders are used to improve the integrity of the electrode but decrease the active surface area by blocking part of the pores; contributing to increase electrical resistance.

Considering the current limitations of commercially available active carbon electrode materials, many studies have been conducted to develop new materials with hierarchical pore size distributions and ion-accessible surfaces, which are key parameters to influence and increase the capacitance values. Among various carbon configurations and forms, carbon fibers stand out for offering continuous fast electron conduction which is essential for ultra-fast charging and discharging. Specifically, porous carbon fibers (PCFs) have been positioned as promising active electrode materials [21,22] due to their excellent mechanical properties (high strength and flexibility in contrast to low density), exceptional specific surface areas, high electrical conductivity and thermal stability, and chemical inertness. Furthermore, compared to traditional active materials, PCFs allow their direct use as self-standing electrode material without the addition of binders or conductive additives that introduce additional interfacial resistance [23].

1.1.2. Advanced carbon materials for CO₂ capture and dye removal

Controlling greenhouse carbon dioxide emissions is a great challenge for today's society, as CO₂ contributes to global climate warming and has risen to dangerous levels up to ~ 418.9 ppm [24]. In order to decrease high CO₂ atmosphere concentrations, not only the development of renewable energy sources has been considered, but also CO₂ adsorption or capture has been studied as a direct approach. Porous carbons with hierarchical porosity facilitate the access of CO₂ molecules to internal adsorption active sites (micropores) increasing adsorption yield.

However, carbon powder materials may exhibit some drawbacks, such as low bulk density. This feature presents the risk of potential escape or filtration with the airflow as it passes through the packed column. The use of porous carbon fibers (PCFs) can prevent this issue and allow for easier handling [25]. In addition, heteroatom-rich materials have been demonstrated to enhance CO₂ interaction and adsorption, since the nitrogen- and oxygen-containing functionalities present a high affinity for CO₂ [26].

On the other hand, as stated by the World Health Organization, by 2025, half of the world's population will live in water-stressed areas. Therefore, it is essential to guide research to solve issues related to clean and freshwater production. In particular, the purification of wastewater from different industries, specifically textiles and cosmetics, which very often disposed of water that contains high levels of industrial dyes, is

presented as a fundamental environmental concern [27]. Extensive research has been conducted on the potential harmful effects of low concentrations of organic industrial dyes on the physiological systems of humans and animals [28]. Faced with these challenges, PCFs stand out as highly porous materials, presenting high removal yields of methylene blue [29] and methyl orange [30], among others. Furthermore, PCFs with hierarchical porous structure has been studied to improve the electroadsorption of organic dye molecules [31].

Considering all of these factors, it becomes evident that PCFs exhibiting a hierarchical porous structure stand out as promising and necessary materials for a wide range of energy and environmental applications. Their multifunctional nature further enhances their potential to address various challenges in these fields (**Figure 1.4**).

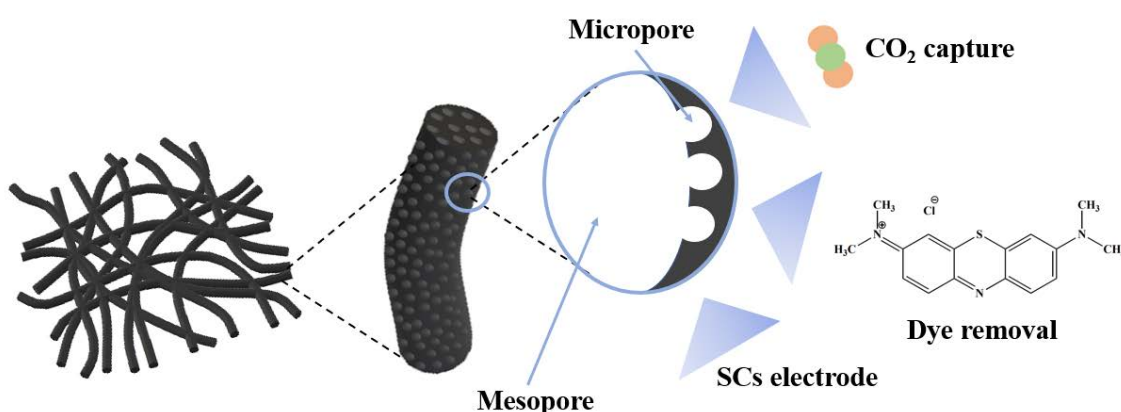


Figure 1.4. Hierarchical PCFs as multifunctional materials.

1.1.3. Production of porous carbon fibers and precursors

In the last few decades, PCFs have been produced by different methods [32]; however, electrospinning is emerging as one of the most used, efficient, and versatile technique that uses the force of a voltage supply to produce fibers with nanometer diameters [33], from both natural and synthetic polymer precursors [34]. The electrospun nanofibers exhibit low density, high specific surface area, and outstanding mechanical properties. In addition, this technique allows the adjustment of different parameters during the procedure, such as solution parameters (concentration, conductivity...), process parameters (voltage, flow rate), and environmental parameters (temperature,

humidity, and airflow rate), which allows to control the characteristics of the fibers, leading to various morphologies.

Porous carbon fibers have been produced by direct pyrolysis of suitable polymer precursors including natural polymers such as lignin [35], and synthetics as polyvinylidene fluoride (PVDF) [36], and polyacrylonitrile (PAN) [37]. Among these polymers, PAN is one of the main precursor materials for carbon fiber manufacturing ($\approx 96\%$ of commercial fibers) due to its excellent spinnability and high carbon yield. Carbon fibers made from PAN often present low specific surface areas and pore sizes in the micropore range (< 2 nm). As previously explained, microporous materials increase ion resistance and obstruct access to internal pores, negatively affecting capacity. Therefore, different methods have been used to induce pores in the PAN matrix to improve and increase the specific surface area and mesopore content in electrospun fibers, which is essential for applications that require high adsorption capacity and efficient mass transport. These methods include the activation process using KOH [38] and the incorporation of various porogens, such as inorganic particles [39]. The aforementioned procedures achieve high specific surface areas, although, similarly to the production of active carbons, they require tedious washing steps and involve challenges in controlling the pore size and pore size distribution. These factors can make the process more complex and time consuming and limit the ability to tailor pore size to specific application requirements.

One of the most extensively used strategies to produce carbon porous materials with well-defined pore structures are templating methods, which can be divided into hard- and soft-templating (**Figure 1.5**) [40]. Hard-templating involves the use of inorganic materials, such as SiO_2 [41] or Al_2O_3 [42], that can be easily synthesized and form highly porous structures efficiently. This method follows a specific sequence of steps: (i) synthesis of the hard template material, (ii) coating the hard template with carbon sources, (iii) pyrolysis of the carbon sources, and (iv) etching the templates with acid or alkali solutions. While this procedure can be used for producing PCFs [43], it has limitations in terms of achieving precise control over porosity, as in order to obtain micropores, an additional activation step is required, making the overall approach extremely complicated.

On the other hand, soft-templating is based on the self-assembly of a multiphase system and generally uses polymers as carbon precursors. Polymers are ideal precursors to produce different structures for a wide range of applications, especially when nanostructure features and controlled morphology are required. This is mainly due to their versatility in terms of tunable molecular weight, chemical composition, and diverse processing techniques [44]. These inherent characteristics of polymers allow obtaining materials with precise control over their nanostructure and morphology. In addition, various polymerization methods, including reversible addition-fragmentation chain-transfer polymerization (RAFT) [45] and atom transfer radical polymerization (ATRP) [46], facilitate the design of multiple polymer structures.

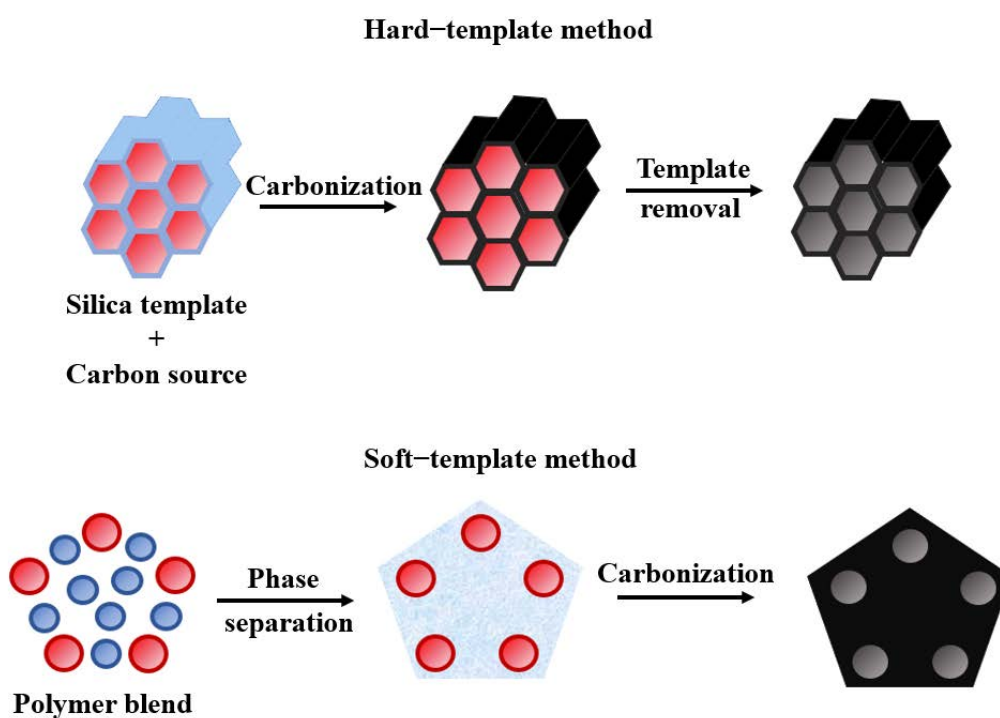


Figure 1.5. Schematic representation of hard- and soft-templating methods.

- Polymer blends as PCFs precursors

The use of polymer blends as a template to produce microstructured carbons has been extensively studied [47,48], since it allows obtaining porous carbons with large surface areas without additional activation processes. This approach requires the proper selection of two polymers that form the binary blend, normally immiscible with each other. This immiscibility is crucial to induce a certain phase separation morphology,

where isolated polymeric domains are formed within a continuous matrix. Generally, a sacrificial polymer with a low decomposition temperature is needed. That polymer is used to create pores within the carbon matrix of a carbon precursor polymer through pyrolysis (**Figure 1.5**). The sacrificial polymer completely decomposes without leaving any carbon residue, resulting in the formation of a porous carbon structure. By selecting polymers with different compatibility, it is possible to control the size and distribution of the resulting pores in the carbon material.

As previously mentioned, polyacrylonitrile (PAN) has been one of the most widely used polymers as a carbon matrix [49], since among other important characteristics, it allows obtaining fiber materials with high carbon yield and high mechanical properties. Jo *et al.* [50] studied the phase separation and immiscibility of polymer blends formed by PAN as a carbon matrix precursor and different sacrificial polymers, including poly (acrylic acid) (PAA), polyethylene glycol (PEG), poly (methyl methacrylate) (PMMA), and polystyrene (PS). The obtained carbon nanofibers exhibited significant variations in terms of specific surface area and pore size distribution, attributed to solubility differences between the two immiscible blocks. These variations also led to differences in capacitance values, highlighting how the immiscibility between the carbon precursor (PAN) and the sacrificial polymer significantly influenced the pore size distribution of the resulting PCFs. Other sacrificial polymers have also been studied as part of PAN-based blends to obtain PCFs, including poly (m-aminophenol), polystyrene foam from packaging waste [51], and polyvinylpyrrolidone [52].

Although it is possible to adjust the pore volume by varying the ratio of the sacrificial polymer, achieving precise control over the pore size distribution can be a reasonable challenge. This difficulty arises because phase separation in polymer blends generally leads to large phase domains, making it difficult to obtain small-sized mesopores and well-controlled morphologies. This macrophase-separated morphologies, after carbonization, often produce large meso- and macropores. Consequently, additional strategies are needed to achieve a more precise and uniform pore structure in the resulting materials.

- **Block copolymer templating**

Over the past few decades, a promising new approach has focused on the use of block copolymers (BCPs) as template materials to obtain miscellaneous porous carbon structures [44,53]. By taking advantage of the self-assembling properties of BCPs, it addresses the crucial requirements of high specific surface areas and controlled porosity with hierarchical pore structures in the resulting carbon materials. This approach opens up new possibilities to improve performance of supercapacitors by optimizing the pore characteristics of carbon electrodes.

Driven by phase separation due to chemical incompatibility between constituents or building blocks, BCPs provide a high degree of control over self-assembled nanostructures in terms of morphology, and domains size by varying their characteristic parameters (i.e., molecular weight and composition) [54]. Thermodynamic self-assembly induces different stable morphologies, such as cubic, hexagonal, gyroid, or lamellar (**Figure 1.6a**). These nanostructures are highly influenced by the volume fraction (f) of the different blocks, the degree of polymerization (N), and the polymer-polymer interaction parameter (χ) that measures the compatibility within different polymers [55,56]. Therefore, by modifying and adjusting these parameters, supramolecular structures can be designed to meet a specific requirement [57,58]. The ability and great flexibility provided by the self-assembly of BCPs offer the opportunity to use them as a nanopatterning tool to design and produce a wide range of porous materials.

The presence of a covalent bond connecting the two blocks in BCPs prevents the macrophase separation typically observed in polymer blends. Instead, it promotes the formation of nanostructured organizations within the material. This particular feature of block copolymers allows the unique frameworks to be preserved even after pyrolysis, resulting in a wide variety of carbon nanostructured materials (**Figure 1.6b**). Producing nanoscale morphologies is essential to obtain micropores and small-sized mesopores.

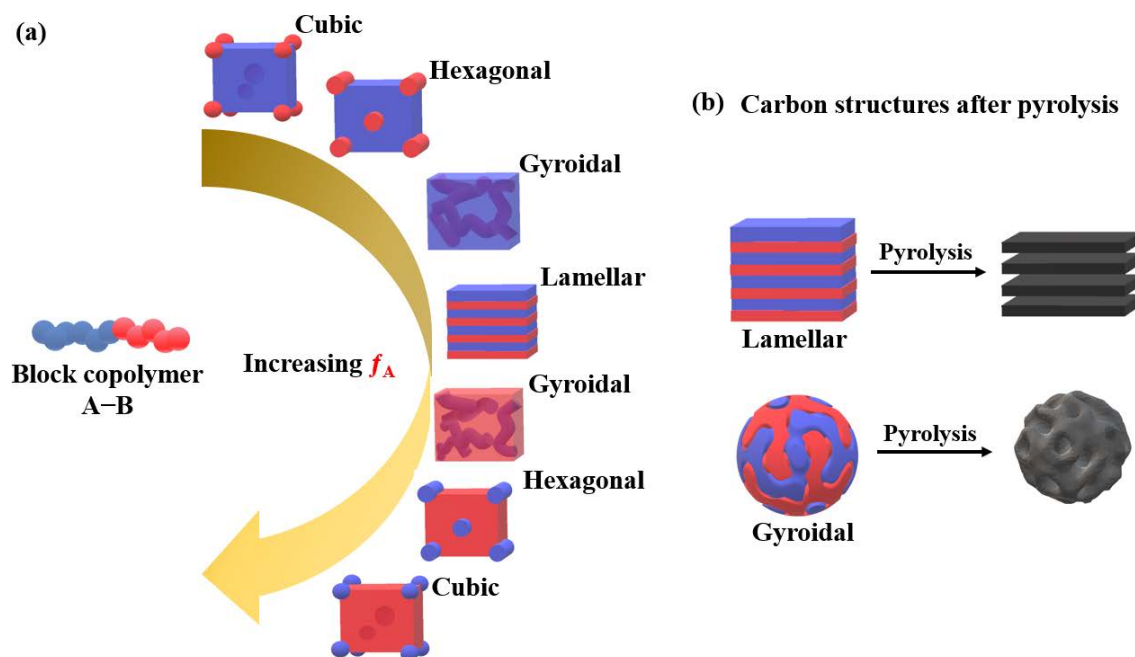


Figure 1.6. (a) Typical morphologies obtained by increasing volume fraction (f) of A block in a diblock copolymer, (b) preparation of nanostructured carbon materials by direct pyrolysis of a block copolymer, where red domains represent the sacrificial block and blue domains the carbon precursor block.

In this approach, one of the blocks serves as a carbon precursor, while the other block acts as a sacrificial block. During the carbonization process, the sacrificial block undergoes degradation, leaving the space occupied as pores within the carbonaceous matrix. Therefore, careful selection of both blocks is vital to achieve the desired pore structure and properties. Block copolymers capable of self-assembly generally consist of hydrophobic blocks such as polystyrene (PS), polyacrylonitrile (PAN), or polyisoprene (PI), and hydrophilic blocks including poly(methyl methacrylate) (PMMA), poly(ethylene oxide) (PEO), poly(2-vinylpyridine), among others. They are usually synthesized via controlled living polymerization methodologies, such as atom transfer polymerization (ATRP) [46] and reversible addition-fragmentation chain transfer polymerization (RAFT) [59]. In this context, it is worth highlighting the use of polyacrylonitrile (PAN) as a carbon precursor. As previously mentioned, PAN exhibits a high carbon yield between 50–60% and possesses a unique thermal chemistry. Between 200–300 °C under air atmosphere, cross-linking of the side chains occurs, which causes the cyclization of the structure. Nitrile functional groups ($-\text{C}\equiv\text{N}-$) convert to $-\text{C}=\text{N}-$ bonds forming thermally stable networks, along with some dehydrogenation and

oxidation reactions that introduce oxygen functional groups into the carbon framework (**Figure 1.7**). This stabilization step leads to structural changes that increase the rigidity and is critical to preserving the generated morphology and maintaining a high carbon yield. Dehydrogenation between 300–400 °C and subsequent denitrogenation from 600 °C, under nitrogen atmosphere, leads to partially graphitized structures.

Thanks to the stabilization process, the improved stability helps to retain the generated morphologies even after carbonization, preserving the desired pore structures and resulting in well-defined carbon nanostructures.

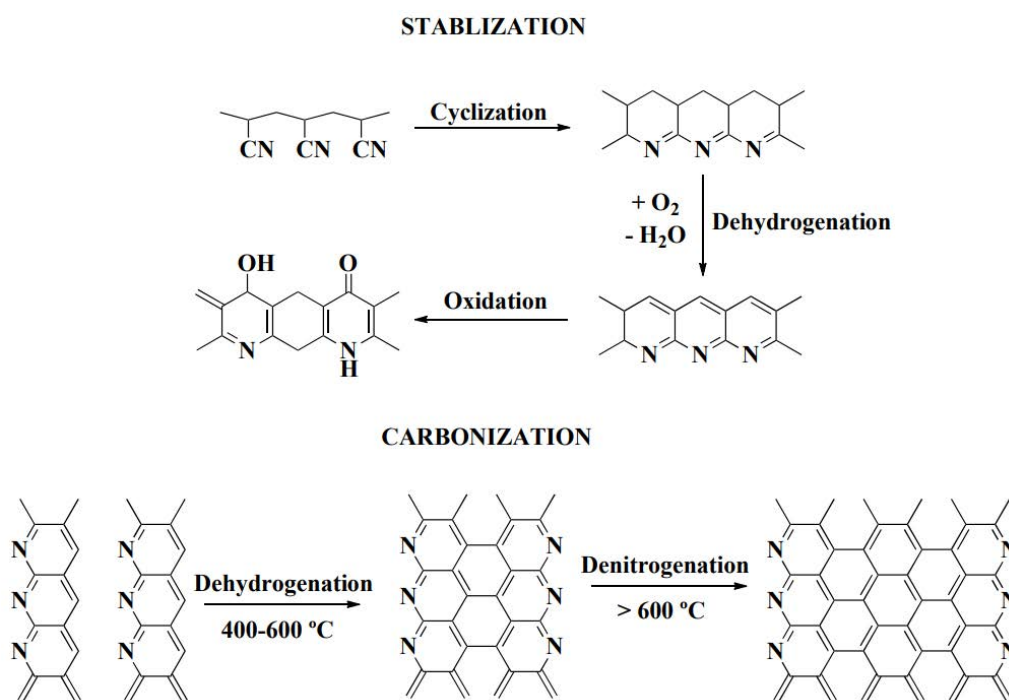


Figure 1.7. Thermal chemistry of polyacrylonitrile (PAN) throughout the two-step thermal treatments, stabilization, and carbonization.

Multiple PAN-based block copolymers can be prepared with precise control over molecular weight and polydispersity (PDI), which is a key parameter to improve pore size control and tunability. Furthermore, a wide variety of sacrificial blocks have been studied, including poly(butyl acrylate) (PBA) [57], polystyrene (PS) [60], poly(ethylene oxide) [61], poly(acrylic acid) (PAA) [62], and poly(methyl methacrylate) (PMMA) [63]. By exploring different combinations of PAN-based block copolymers with various

sacrificial blocks, researchers aim to tailor the morphology and porosity of the resulting carbon materials for specific applications and performance requirements.

In recent years, the use of BCPs has been expanded beyond the manufacture of bulk or powder porous carbons to include the production of porous carbon fibers (PCFs). Zhou *et al.* [64] used for the first time a PAN-based BCP containing PMMA as sacrificial block to produce fibers by electrospinning. After carbonization, the resulting PCFs exhibited higher specific surface areas and superior electrochemical performance than those obtained from PAN/PMMA blends. These results demonstrated the remarkable potential of PAN-based BCPs as precursors to produce PCFs with well-defined pore structures, including a suitable ratio of micro- and mesopores. This characteristic contributes to high capacitance values and low internal resistance, which improves their overall electrochemical performance.

Moreover, a series of PMMA-*b*-PAN block copolymers with different total degrees of polymerization and sacrificial block content were also investigated [58]. The resulting PCFs exhibited various specific surface areas and pore size distributions, highlighting the ability of this approach to modulate and control pore size. This demonstrates the versatility and tunability of the BCP-based method to obtain PCFs with tailored porosity. In addition, PAN/PAN-based BCPs blends have also been examined for the manufacture of PCFs [65]. This method allows obtaining mesoporous PCFs with controlled mesoporous structures by adjusting the BCP content. These studies emphasize the versatility and potential of using block copolymers in the production of PCFs with controlled porosity.

1.1.4. Porous carbon fibers: pseudocapacitance contribution

Numerous approaches have been developed to increase the electrochemical performance of PCFs and other carbon materials, including the introduction of heteroatoms such as N, S, O, and P [66,67]. This proposal enhances the overall capacitance by creating additional electrochemical active sites. The presence of heteroatoms into the carbon lattice can improve electronic and ionic conductivity, wettability with the electrolyte, and introduce pseudocapacitance. This strategy combines the use of carbon porous materials with high specific surfaces areas suitable pore size distributions to enable efficient energy storage. It involves the formation of an electric

double layer of charges at the electrode–electrolyte interface, facilitated by the large surface area, which promotes reversible ion adsorption. Additionally, the incorporation of heteroatom–containing surface functionalities enables redox reactions with the electrolyte ions, leading to increased capacitance.

Different heteroatom doping methods have been studied, such as chemical vapor deposition (CVD) [68]. In addition, PCFs have been doped with N, P and S atoms using thiourea and melamine phosphate, showing a high heteroatom content of 3.78 at%, 0.32 at%, and 3.36 at%, respectively [69]. In the same way, carbon fibers were carbonized with a mixture of urea and thiourea, achieving a N, S co–doping content of 14% and 0.9%, respectively [70]. Considering this, the activation process that introduces heteroatom through the use of natural and non–toxic precursors such as urea, thiourea and melamine has demonstrated to be an efficient, easy, and affordable method.

Likewise, to improve the PCFs electrochemical performance, the incorporation of transition metal oxides or redox active nanoparticles (NPs) into the porous carbon matrix has been extensively studied. Many different transition metal oxide nanoparticles (NPs) have been embedded in a carbon matrix to form PCFs composite material, exhibiting a certain degree of pseudocapacitance. Examples of these transition metal oxide nanoparticles include MnO₂ [71], Fe₃O₄ [72], and NiO [73].

The introduction of NPs into porous carbon fibers has been developed using different approaches. One strategy involves the direct growth of NPs confined in the PCFs framework by impregnation with NPs precursors followed by thermal treatment [74] and/or the use of atomic layer deposition of the NPs on the PCFs substrate [75]. Finally, the dispersion of NPs within the polymer electrospinning precursors has also been studied to produce PCFs with NPs encapsulated in the internal region [76]. This method offers simplicity and efficiency in controlling the distribution of NPs within PCFs.

The integration of nanoparticles (NPs) in carbon porous fibers has opened new pathways for the development of advanced materials with enhanced functionalities. The choice of the method depends on factors such as the NPs loading and distribution desired. This strategy offers new avenues to tailor the properties of PCFs and expand their applications in various fields, including energy storage, catalysis, and environmental remediation [77–80].

1.2. Motivation and objectives

Porous carbon fibers derived from block copolymers have attracted significant attention in recent years as promising electrode materials for supercapacitors. These materials combine the advantages of block copolymers (BCPs), which produce well-defined microstructures through self-assembly, with the appropriate properties of carbon fibers, such as large surface areas. BCPs self-assembly offers a versatile and precise modelling tool, enabling the design of a wide range of porous carbon materials. In particular, the use of polyacrylonitrile-based block copolymers as precursors has emerged as a powerful method for producing highly uniform micro- and mesoporous carbon structures. This approach opens up new pathways for obtaining advanced carbon materials with controlled and tunable porosity for energy storage applications.

Based on previous work and the aforementioned premise, **the main objective of this thesis is the development of porous carbon fibers (PCFs) derived from PAN-based block copolymers with well-defined pore structures.** The research methodology involves the synthesis of PAN-based block copolymers with different molecular weights and compositions. These copolymers will be then used as electrospinning precursors to produce a fiber mat, which after carbonization will produce well-defined porous carbon fibers. The resulting PCFs will be morphologically and structurally characterized. Additionally, an evaluation of the electrochemical performance will be carried out testing electrodes prepared from the PCFs produced.

With this main aim, the following specific objectives have been proposed:

Objective 1: Synthesis and characterization of block copolymers. The first step of this project is the synthesis using controlled polymerization techniques, such as RAFT polymerization, and characterization of various block copolymers (BCPs) as suitable precursors for obtaining porous carbon fibers. This involves designing and optimizing the synthesis procedures while controlling the block ratios and molecular weight to form well-defined domains of various sizes that can be selectively removed during carbonization. Various strategies will be investigated, such as adjusting the block copolymer composition and total molecular weight and exploring different sacrificial blocks (styrene and tert-butyl acrylate). Additionally, the study will focus on

investigating the self-assembly behavior of the PAN-based BCPs and exploring their potential to produce well-defined carbon structures. The goal is to achieve precise control over porosity by modulating the phase separation of the BCP precursor.

Objective 2: Production of porous carbon fibers. The next objective is to use the already synthesized BCPs to produce fibers by electrospinning. Then, the electrospun fiber mat is subjected to oxidative thermal treatment, which stabilize the PAN block structure through some cyclization reactions. The stabilized fiber mat is further carbonized under nitrogen atmosphere to partially graphitize the PAN structure. This objective focuses on achieving homogenous fiber mats, which after carbonization present highly porous structures with controlled pore size distribution.

Objective 3: Structural and morphological characterization. This objective involves the detailed characterization of the porous carbon fibers produced. Through the use of different techniques such as scanning electron microscopy (SEM), transmission electron microscopy (TEM), X-ray photoelectron spectroscopy (XPS), and nitrogen physisorption, fiber morphology and structure, surface area and surface chemical composition will be assessed.

Objective 4: Electrochemical performance evaluation. The project aims to evaluate the electrochemical performance of the produced PCFs as electrode material for supercapacitors. Specific parameters will be determined to assess their performance, including capacitance, cycling stability, rate capability and charge-transfer resistance, among others. The objective is to relate the differences in the structural and physicochemical characteristics with the capacitive behavior and electrochemical performance, in order to find the most suitable characteristics.

Objective 5: Optimization of properties through material modifications. Based on the results of the characterization and electrochemical performance, this objective focuses on modulating and optimizing the PCFs properties. Including the incorporation of heteroatoms (N and S), and the introduction of magnetite nanoparticles, with the aim to improve the electrochemical performance. The goal of this purpose is to minimize ion-diffusion resistance by designing a mesopore structure and electrochemically active surface that allow for fast and efficient ion transport.

By achieving these objectives, the project aims to contribute to the development of efficient and scalable block copolymer-based porous carbon fibers for use as high-performance electrodes in energy storage devices.

Through this doctoral thesis the proposed objectives will be carried out. The manuscript is organized into the following chapters:

Introduction: It includes a literature review of the synthesis and production of porous carbon materials, with particular emphasis on block copolymer self-assembly techniques. A background of relevant previous studies on block copolymer-based porous carbon fibers is also provided. Furthermore, the need to develop porous carbon fibers with controlled porosity for use as electrode materials for supercapacitors and other promising applications, such as CO₂ capture and dye removal, is exposed. Different approaches to introduce heteroatoms and nanoparticles are also detailed.

Materials and methods: It presents the chemical and physical characteristics of the starting materials, as well as the methodology, techniques, and equipment used to characterize the block copolymer precursors and PCFs.

Precursor characterization: It includes the experimental procedure followed to obtain the PAN-based block copolymer precursors, as well as their structural and thermal characteristics.

Porous carbon fibers derived from block copolymers: It details the process and optimization of the production of PCFs derived from the different PAN-based block copolymer precursors, as well as their morphological and structural characterization.

N and S/N co-doped porous carbon fibers: It describes the approach to obtain N and N/S co-doped PCFs derived from PS-*b*-PAN through thermal activation with urea and thiourea precursors. Also, the morphological and structural characterization of the resulting PCFs after activation is described.

Porous carbon fibers with magnetite nanoparticles: It introduces the process of obtaining PCFs derived from PtBA-*b*-PAN containing magnetite nanoparticles. Moreover, the morphological and structural characterization of the resulting composite material is reported.

Porous carbon fiber material: electrochemical characterization: It details the electrochemical characterization of the different PCFs produced in this thesis work.

Conclusions and perspectives: This chapter describes the summary of the key findings, the main conclusions of this thesis work, limitations and challenges encountered and future directions to improve the electrochemical performance of PCFs under study. Future perspectives for developing advanced porous carbon fibers for different applications are also presented.

Chapter 2

Materials and methods

This chapter describes the physical and chemical properties of the required reagents for the synthesis of block copolymers (BCPs) used as precursors or template materials to produce porous carbon fibers (PCFs). In addition, the necessary reagents used as heteroatom precursors to obtain N-doped and N/S co-doped PCFs are also addressed. The most relevant aspects of the different techniques and methods used for the characterization of BCPs, electrospun nanofibers, and resulting PCFs are also described. The experimental conditions with which measurements and experiments have been carried out are also included.

2.1. Materials

2.1.1. BCP polymerization reagents

The following reagents compiled in **Table 2.1**, including physical properties, were used for the synthesis and purification of BCPs via reversible addition–fragmentation chain–transfer polymerization (RAFT).

Table 2.1. Summary of reagents required for RAFT polymerization, description, and physical properties.

Reagent	Purity	Density (g mL ⁻¹)	Molecular weight (g mol ⁻¹)	Description
2-Cyano-2-propyl dodecyl trithiocarbonate (CPDT)	97.0	0.991	345.63	RAFT agent.
2,2'-Azobis (2-methylpropionitrile) (AIBN)	≥98.0	1.1	164.21	RAFT initiator
Acrylonitrile (AN) Stabilized with hydroquinone monomethyl ether	≥99.0	0.806	53.06	Monomer
Styrene (St) Stabilized with 4-tert- Butylpyrocatechol	≥99.0	0.906	104.15	Monomer
Tert-butyl acrylate (tBA) Stabilized with hydroquinone monomethyl ether	≥98.0	0.875	128.17	Monomer
Basic alumina	Standard grade	—	101.96 (63–200 μm particle size)	Inhibitor/ Stabilizer remover
<i>N,N</i> -Dimethyl formamide (DMF) anhydrous	≥99.9	0.944	73.09	Solvent
Methanol (MeOH)	≥99.6	0.792	32.04	Solvent
Tetrahydrofuran (THF) anhydrous	≥99.9	0.889	72.11	Solvent

Acrylonitrile, styrene, and tert-butyl acrylate were purified prior to use by passing through basic alumina column to remove inhibitor. Other reagents and solvents were used

as received without further purification. All reagents and solvents were supplied by Sigma–Aldrich.

2.1.2. Heteroatom precursors

Table 2.2 shows the reagents, including their description and physical properties, used as heteroatom (N and S) precursors in PCFs doping–activation to produce N–doped and N/S co–doped PCFs.

Table 2.2. Description and physical properties of heteroatom precursor reagents.

Reagent	Purity	Density (g mL ⁻¹)	Molecular weight (g mol ⁻¹)	Description
Urea	≥99.0	1.335	60.06	N–heteroatom precursor
Thiourea	≥99.0	1.400	76.12	N/S–heteroatom precursor
Water deionized	MQ100	0.997	18.02	Solvent

2.2. Methods and characterization

2.2.1. BCPs characterization techniques

The following characterization techniques were used to characterize macro–chain–transfer agents and BCPs used as precursors in this thesis work, structurally and thermally.

- ***Nuclear magnetic resonance (NMR)***

Nuclear magnetic resonance (NMR) is an advanced structural characterization technique in which an external magnetic field causes nuclei to align in one of two possible states, depending on the field direction. The external magnetic field excites the nuclei from a lower to a higher energy state. After returning to the original state, they emit a detectable signal characteristic of the nucleus type (¹H–NMR, ¹³C–NMR). By analyzing the frequency and intensity of these signals, various properties of the material under study,

such as chemical composition, structure, and dynamics, can be determined. Functional groups and chemical environment influence the peaks shape and number.

NMR has been used to analyze BCPs structure and composition, as it can provide information about the number average molecular weight (M_n) and degree of polymerization (N). M_n is the total weight of polymer divided by the total number of molecules. In other words, it is the polymer chains statistical average molecular weight. N is the sum of number of monomers or repeating units in the two different blocks ($n + m$). Determination of n and m values for a block copolymer can be easily calculated by NMR measurements, according to J. Izunobi et al. [53]. ^1H -NMR spectra were acquired using a Bruker DPX 300 MHz equipment. Samples were prepared by solving ~5 mg in $\text{DMF}-d_7$ containing 0.03% (v/v) tetramethyl silane (TMS; $\delta = 0$ ppm).

- *Size exclusion chromatography (SEC)*

Size exclusion chromatography (SEC), also known as gel permeation chromatography (GPC), is a type of liquid chromatography used to separate molecules based on their size by filtration through a gel column to determine the molecular weight of the sample. In SEC, a sample is passed through one or various columns packed with a stationary phase, typically a porous gel, that contains a range of different pore sizes. As the sample molecules flow through the column, smaller molecules diffuse into the pores and are temporarily trapped, while larger molecules do not enter the pores and pass through the column more quickly. Consequently, this results in separation of the sample into different fractions based on their size and eluting in decreasing order of molecular weight.

SEC is used to determine number average molecular weight (M_n) and polydispersity index (PDI, M_w/M_n), to measure the width of the particle size distribution, of macro-chain-transfer agents and block copolymers. The equipment used is composed of a Waters 515 HPLC pump instrument equipped with a Waters 24214 Refractive Index Detector and Agilent PLgel columns (500, 100, and mixed C). DMF was used as eluent at a flow rate of 0.5 mL min^{-1} with 10 mM LiBr and 45°C of working temperature. All the sample solutions were injected at a concentration of 0.1 wt% in DMF. Solutions were previously filtered through PTFE filter membrane ($0.25 \mu\text{m}$ pore size). Polystyrene

standards from PolyScience were used for calibration with molecular weights ranging from 4,490 g mol⁻¹ to 7,500,000 g mol⁻¹.

- *Differential scanning calorimetry (DSC)*

Differential scanning calorimetry (DSC) is a thermal analysis technique used to study the thermal behavior of materials. DSC allows to determine and quantify first order thermodynamic processes, such as heats of fusion and crystallization, specific heats, and reaction enthalpies. In addition, second-order transitions, such as glass transitions of polymeric materials can be analyzed. The glass transition temperature (T_g) corresponds to temperature at which a solid material, such as a polymer, transitions from a rigid, glassy state to a more flexible, rubbery state; that is, as the temperature increases and reaches the T_g , the polymer chains start to gain mobility [81]. In DSC, a sample with a known mass is subjected to a controlled temperature program (heating or cooling), and the resulting changes in its heat flow are monitored as a function of temperature.

Calorimetry technique was used to measure glass transition temperatures of macro-chain-transfer agents and block copolymers; and to detect the specific exothermic peak of PAN block related to cyclization reactions [82]. The thermal transitions and exothermic reactions were measured using a Mettler Toledo DSC SC822 equipment. Around 8 mg of sample were placed in a sealed aluminum pan, using a heating and cooling rate of 10 °C min⁻¹ from 25 to 350 °C for the block copolymer and a ramp from 25 to 200 °C for the macro-chain-transfer agents. All measurements were carried out under N₂ flow. As reference, an empty and sealed aluminum pan was used. Glass transition temperature (T_g) of the macroinitiator was determined from inflection point in the second heating cycle.

- *Thermogravimetric analysis (TGA)*

Thermogravimetric analysis (TGA) is a type of thermal analysis technique that measures the change in weight of a material as a function of temperature or time, while the material is subjected to a controlled temperature program in a specified environment (e.g., air, nitrogen, or other gases). To quantitatively analyze the mass loss (%) associated with each degradation process, it is necessary to carefully select the dynamic temperature program, the working atmosphere, and an adequate sample weight, typically less than 10

mg. TGA is widely used in material science, chemistry, and engineering to study the thermal stability, composition, and behavior of various materials, including polymers, composites, minerals, and biomaterials.

Thermogravimetry is used to determine BCPs carbon yield after carbonizing under N₂ at 800 °C. In addition, PAN stabilization temperature and sacrificial block degradation temperature are analyzed to ensure their potential application as template material for PCFs obtention. In a typical TGA experiment, around 8 mg of the sample were placed in a small aluminum container. The samples were heated under N₂ flow in a temperature range between 25–900 °C at a heat rate of 10 °C min⁻¹. TGA experiments were carried out using TA instruments Q50 equipment.

2.2.2. Electrospinning

All the fibers presented in this thesis work have been produced by electrospinning. Electrospinning is a versatile and efficient method that uses the force of a voltage supply to produce fibers with nanosized diameters. A typical electrospinning set up consist of the following main components as shown in **Figure 2.1**. A high voltage supply connected to both, needle, and collector plate and a syringe pump to push the polymer solution from the syringe through the needle. This pump allows to control the feed rate. The surface tension of the polymer droplet at the needle tip is overcome by the force of the electric field. The droplet is then distorted to form the Taylor cone, resulting in the formation of an electrically charged polymer fiber, that is produced in the direction of the collector. Two main types of collectors can be used, cylindrical, used primarily to prepare aligned polymeric fibers, and flat platforms, used to produce randomly disordered fibers. Moreover, collectors can be stationary or mobile and arranged horizontally or perpendicular to the polymer jet. Along this thesis work, electrospinning process were performed in a NANON 01 instrument supplied by MECC nanofiber. This instrument was operated with a horizontal plate collector arrangement.

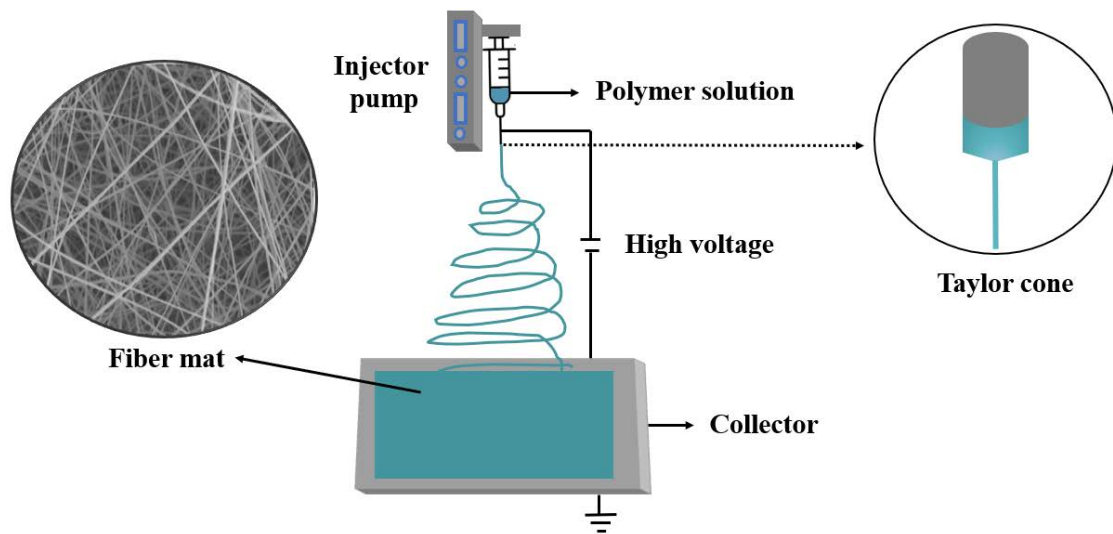


Figure 2.1. Scheme of a typical electrospinning setup with a horizontal collector plate.

There are different parameters that affects fiber stability and morphology, and can be classified into two main groups:

Polymer solution parameters:

- Polymer solution concentration: Fiber diameter and morphology are directly related to the polymer concentration [83,84], which influences solution viscosity. Generally, if the polymer solution is too diluted, an electrospray will be produced, generating beads instead of fibers. On the other hand, if polymer concentration is too high, the flow of the viscous solution over the needle is hindered, which prevents fiber production, and also causes solidification of the polymer at the needle tip.
- Polymer solution conductivity: Adding salts to the electrospinning solution leads to a decrease in fiber diameter and reduces bead formation. Since the addition of ionic salts increases the jet charge density, and as the charges carried by the jet increase, the elongational forces also increase [85].

Processing parameters:

- Voltage: The applied voltage represents one of the main parameters since it needs to overcome the surface tension of the polymer drop to generate a stable Taylor cone. High voltage generally provides higher fiber stretching, promoting a decrease in fiber diameter, and a decrease in bead formation [86].

- Feed rate: The feed rate must be slow enough to maintain a stable Taylor cone, as well as allow sufficient time for the solvent to evaporate before the fibers contact the collector.
- Distance between needle and collector: This distance can affect fiber morphology, fiber diameter, and bead formation. If the distance is too short, fibers will not have enough time to elongate and stretch, and solvent may not have enough time to evaporate.

It should be noted that each polymer will require different parameters. Therefore, controlling and optimizing electrospinning conditions provides unique characteristics to the produced fibers and is an extremely important step on the way to generate a homogenous fiber mat.

The electrospinning parameters used for producing a homogenous fiber mat derived from PS-*b*-PAN have been selected after an optimization process, that will be detailed in **Chapter 4. Table 2.3** shows the final selected electrospinning parameters. Fiber mats derived from other BCPs were also produced with the parameters shown in **Table 2.3**, without additional parameter optimization, although feed rate was varied in some cases to avoid dripping.

Table 2.3. Selected electrospinning parameters to produce fibers derived from BCPs

Solvent	Concent (wt %)	Voltage (kV)	Feed rate (mL h ⁻¹)	T (°C)	Working distance (cm)	RH
DMF	20	18	1.5	20–25	15	~40 %

Note that ambient parameters were not evaluated as a part of the optimization process, remaining constant with operating temperatures; between 20–25 °C under ~40 % RH humidity.

2.2.3. Fiber characterization techniques

The following characterization techniques were used to morphologically, and structurally characterize the electrospun fiber mat obtained by block copolymer templating method, as well as the resulting PCFs after carbonization.

- *Scanning electron microscopy (SEM)*

Scanning electron microscopy (SEM) is based on the emission of an electron beam which interacts with a sample surface, producing different types of signals captured by various detectors. The information from detectors is transformed to produce a high-definition image of the sample surface topography with a resolution between 0.7–50 nanometers [87]. The electron beam penetration through the sample surface will depend on the operation voltage. A standard penetration often allows between 1–5 microns.

Using different detectors allows to obtain miscellaneous information from the sample surface. Fiber images generated in this work have been obtained using T1 detector, which is mostly dedicated to capture backscattered electrons (BSE) images [88]. Fiber samples before carbonization required tapping a small piece of fiber mat into a double-sided carbon tape, and consequent coating with a thin layer of gold. FESEM (Field emission SEM) was operated with ~ 3 mm between the sample surface and the beam and a potential of 2 kV. On the other hand, a small piece of the carbonized fiber mat was also tapped into a double-sided carbon tape. Images were collected using 1.5 kV and ~ 2 mm between the sample and the beam. Porous carbon fibers present low graphitization degrees, resulting in insufficient conductivity to allow for the detection of the pores (generally ~ 10 nm) by SEM. Coating with a thin layer of gold, covered the pores.

To qualitatively assess the N and N/S co-doping efficiency of the starting PCFs material, EDS was performed. This detector captures the energy from the X-rays generated on the surface, typical of specific elements present in the sample, providing information on the elemental composition. Additionally, EDS can be applied to a specific point on the sample surface. When the analysis is applied to an area, it is possible to obtain a map with the different elements present in the selected area. Each element is displayed with a different color. Unlike the BSE, these electrons do not provide information about larger volume samples. This type of SEM has a field emission gun as an electron source to provide high and low energy electron beams. As these beams are closely aligned, they allow for better resolution, focusing on a single fiber surface. Fiber samples for FE-SEM measurements were prepared by dispersing a dilute concentration of PCFs in ethanol and

depositing a few drops of the dispersion on holey carbon copper grids. All SEM and EDS mapping images were obtained using a FEI TENEO LoVac microscope.

- *Transmission electron microscopy (TEM)*

Transmission electron microscopy (TEM) takes advantage of the same concept as SEM. This technique uses the interaction between an electron beam and the sample to generate a high-resolution image. The operating voltage is higher than that used for SEM; therefore, the penetration of the electron beam is deeper. Once the electron beam passes through the sample, it generates photons and secondary electrons that are captured by the detectors, allowing to produce an image at the atomic level. Fiber TEM images were collected using a Philips Tecnai 20 FEG microscope operated at 200 kV, which allows differentiating pore sizes at ~ 4 nm. Samples were prepared by dispersing a dilute concentration of PCFs in ethanol and depositing a few drops of the dispersion on holey carbon copper grids.

- *Raman spectroscopy*

Raman spectroscopy is a high-resolution photonic technique that provides in a few seconds chemical and structural information of organic and/or inorganic materials. Raman spectroscopy analysis is based on the characterization of scattered light produced by the sample surface when a monochromatic light beam is incident on it. A small portion of the light is scattered inelastically by the sample surface, experiencing slight frequency changes, which are characteristic of the sample. The Raman spectrum is normally obtained for wave numbers from 100 to 2000 cm^{-1} . In this range, two distinctive bands appeared for carbon materials; disordered induced D-band from 1300 to 1450 cm^{-1} and graphitic induced G-band from 1450 to 1600 cm^{-1} . The G-band is related to the Raman active E_{2g} in-plane vibration mode, which involves a combination of stretching and bending of C-C bonds. The D-band is a second order Raman band, referred to the A_{1g} mode similar to an in-plane breathing vibration type, resulting from relaxation of the symmetry rule for Raman scattering due to the presence of disorder parts [89,90]. It is well known how the intensity ratio between D and G bands (I_D/I_G) provides information about graphitic order or disorder features of the carbon material, which allows to elucidate the carbon structure. Raman spectrums were collected using a Renishaw PLC spectrometer with a 532 nm Nd:YAG laser excitation (50 mW).

- *X-ray diffraction (XRD)*

X-ray diffraction is one of the physical phenomena that occurs when an X-ray beam of a certain wavelength interacts with a crystalline or partially crystalline sample. X-rays wavelengths are on the order of angstroms, as are the interatomic distances of crystalline lattices components. When the sample to be analyzed is irradiated, X-rays are diffracted with different angles that depend on the interatomic distances. When irradiating X-rays on a sample composed of multitude crystals placed randomly in all possible directions, Bragg's Law (equation 1), is applicable and predicts the direction in which constructive interference occurs between coherently scattered X-ray beams from a crystal.

$$n \cdot \lambda = 2d \cdot \sin \theta \quad (2.1)$$

Where θ is the angle between the incident rays and the scattering planes, λ is the wavelength of the X-rays, and d is the distance between the interatomic planes that produce the diffraction. X-ray patterns of amorphous or disordered carbon materials often presents two broad peaks [91–93] at $\sim 24^\circ$ and $\sim 43^\circ$, assigned to the crystallographic planes of carbon (002) and (10 l), respectively. The (10 l) referred to the overlapping diffraction peaks (100) and (101). Shifts and changes of those peaks can provide information about the orientation and order of the graphitic planes, that can be related to the pore structure. X-ray diffraction (XRD) patterns were collected from 10 to 70° using a Philips X'PERT equipment with conventional X ray tube of Cu anode.

- *Nitrogen physisorption*

Physical adsorption of nitrogen is a widely used technique for the characterization of textural properties such as pore size distribution, specific surface area, and pore volume of porous solids. Adsorption isotherms provide information to determine the solid (*adsorbent*) specific surface area, as well as information about porosity, regarding to volume and pore size accessible to gas molecules being adsorbed (*adsorbate*). Physical adsorption takes place when nitrogen molecules encounter the solid degassed surface at a specific temperature (77 K). The adsorbate molecules formed a multilayer in the solid surface because of attractive forces (Van der Waals). In a typical adsorption experiment, the pressure in the system gradually increases, until reaching the saturation pressure of

the adsorbate. The adsorption isotherm represents the relationship between the amount of gas adsorbed per unit mass of solid and the equilibrium relative pressure. According to IUPAC published report isotherms can be classified into six different types [13]:

- Type I isotherm is characteristic of microporous solids (< 2 nm). This isotherm presents a rapid initial rise, in the low-pressure range, due to the filling of micropores, and a long pseudo-horizontal platform (plateau), which reflects the absence of multilayer adsorption on the solid surface.
- Type II isotherm is characteristic of macroporous (> 50 nm) or non-porous solids. The continuous slope, without the presence of plateau is due to the monolayer-multilayer adsorption on the external surface of the solid, without the presence of micropores or mesopores (2–50 nm).
- Type III isotherm occurs when adsorbate-adsorbent interaction is low, in non-porous solids, not very common type.
- Type IV isotherm is characteristic of mesoporous solids in which capillary condensation occurs. These isotherms present the characteristic hysteresis loop, different types of hysteresis loops are related to various pore shapes.
- Type V isotherm, similar to type III isotherm, is characteristic of weak adsorbate-adsorbent interactions, differing from the previous one that in this case the solid is mesoporous.
- Type VI isotherm is rare. This type of stepwise adsorption occurs only for solids with a highly uniform non-porous surface.

The textural characterization of the different porous carbon fibers was carried out using a Micromeritics Gemini IV instrument. Before analysis, samples were degassed for at least 5 h at 250 °C under N₂ to remove adsorbed water and other gases.

From the adsorption isotherm, material textural parameters such as specific surface area (SSA), micropores volume (V_{micro}), pore size distribution (PSD) and total pore volume (V_T) can be determined. In this work, SSA was calculated using the linearization of Brunauer–Emmett–Teller (BET) equation method (equation 2).

$$\frac{1}{W[P_0/P - 1]} = \frac{1}{W_m C} + \frac{C - 1}{W_m C} \left(\frac{P}{P_0} \right) \quad (2.2)$$

Where P/P_0 represents the relative pressure, W is the amount of gas adsorbed at the determined pressure P , W_m is the amount of gas required to form a monolayer in the surface of the adsorbent at pressure P , P_0 is the saturation pressure of the adsorbate at the adsorption temperature, and C is a parameter related to adsorption energy in the monolayer. Linearity range of the BET equation is usually fulfilled for P/P_0 values between 0.05 and 0.35, although this range changes at lower relative pressures for microporous materials.

BJH (Barrett–Joyner–Halenda) method [94] is a procedure to calculate pore size distribution and pore volumes of mesoporous adsorbents from the experimental isotherms. BJH method uses Kelvin equation (equation 3) to relate the amount of adsorbate removed from the pores of the material, as the relative pressure (P/P_0) increases, to the size of the pores.

$$\ln\left(\frac{P}{P_0}\right) = -\frac{2\gamma\bar{V}}{rRT} \quad (2.3)$$

Where P/P_0 represents the relative pressure, γ is the surface tension, \bar{V} is the molar volume of liquid, and r is the pore radius. In a pore, condensation will occur at a lower pressure. Thus, as the relative pressure is increased, condensation will first take place in the smaller radius pores and progress towards the larger pores. Although, BJH presents some limitations since it estimates pore radius of a cylindrical shape [95]. Therefore, contrasting with TEM imaging is essential.

- *X-ray photoelectron spectroscopy*

X-ray photoelectron spectroscopy (XPS) is a surface analytical technique for compositional analysis, both qualitative and quantitative. It is suitable for the study of surfaces and interfaces of various materials. This spectroscopy method involves the acquisition of photoelectron spectra induced by X-ray photons. The technique consists of excitation through a beam of X-ray photons of the internal energy levels of atoms, producing the emission of photoelectrons. It provides information of energy level, and therefore, information on the nature of the emitting atom. Atom binding energy (E_{binding}), characteristic of specific elements, is determined by equation 4; where $h\nu$ corresponds with the X-ray photon beam energy, E_K is the kinetic energy of the photoelectron emitted

by the sample surface, and ϕ is the spectrometer work function. In summary, this technique is based on measurements of photoelectron rate emitted from the sample surface, for this reason, ultra-high vacuum is required.

$$E_{binding} = hv - (E_K + \phi) \quad (2.4)$$

XPS was used to determine C, N, and O content of the different produced PCFs, as well as other heteroatoms, such as S, in PCFs co-doped with N/S and Fe content due to magnetic nanoparticles present in the PCFs. Moreover, deconvolution of the high-resolution C 1s, N 1s, O 1s, S 2p and Fe 2p peaks allows quantifying information about the type of bonds and functional groups present on the sample surface. All the XPS spectra analyzed in this thesis work have been collected using a SPECS GmbH with UHV system and energy analyzer PHOIBOS 150 9MCD; employing a non-monochromatic Al Mg X-ray source operated at 200 W.

2.2.4. Electrochemical characterization

- *Electrode preparation*

Most of the PCFs produced in this work presented a lack of flexibility and relative fragility since, among other reasons, PCFs presented narrow diameters (~ 100 nm), which caused fiber breakage after carbonization. Therefore they cannot be used as self-standing electrodes. In those cases, electrodes were prepared by pressing into a clean nickel foam a mixture of active material (~ 1 mg), carbon black, and PTFE 60 wt% dispersion in water with a ratio of 80:10:10, respectively. PTFE was used as binder to maintain the electrode mechanical stability. Carbon black was used as conductive additive and Ni foam was selected as current collector, since it is electrochemically stable to basic electrolytes, such as the chosen electrolyte (KOH). Ni foam was cut into a circular shape with a diameter of 0.50 and was cleaned before use by sonicating in ethanol for 30 minutes.

- *Electrochemical cells*

The electrochemical characterization of PCFs as electrode materials for supercapacitors was performed in a three-electrode configuration cell (**Figure 2.2**). The cell is composed of a working electrode (WE), which is the active material electrode under study, a counter electrode (CE), and a reference electrode (RE). This type of cell is

normally used for preliminary characterization stages, allowing to determine the electrochemical behavior of a single electrode. The cell used was a glass beaker with platinum wire as counter electrode and Ag/AgCl as reference electrode.

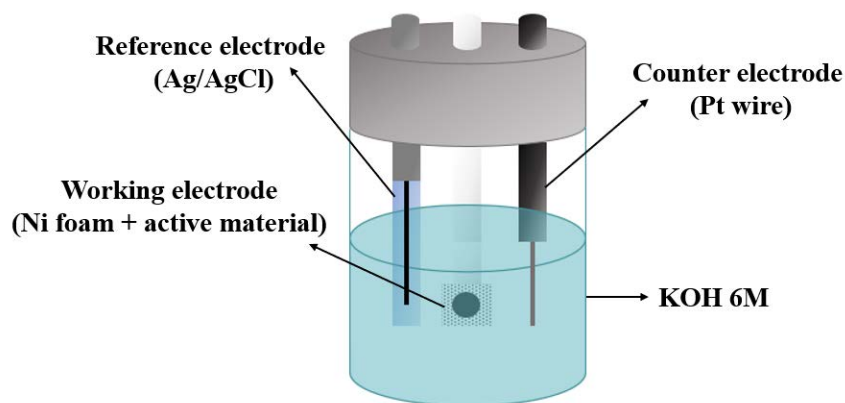


Figure 2.2. Representative scheme of a three-electrode configuration cell.

Additionally, some measurements were performed in a Swagelok[®] type symmetrical cell (**Figure 2.3**). In this cell, the identical electrodes are isolated by a separator material (cellulose paper) soaked in the electrolyte. The current collector is the intrinsic cell parts of stainless steel that keeps both electrodes in close contact. They do not require reference electrode; therefore, measurements are closer to those of a supercapacitor assembly, since it allows to evaluate the behavior of the two identical working electrodes.

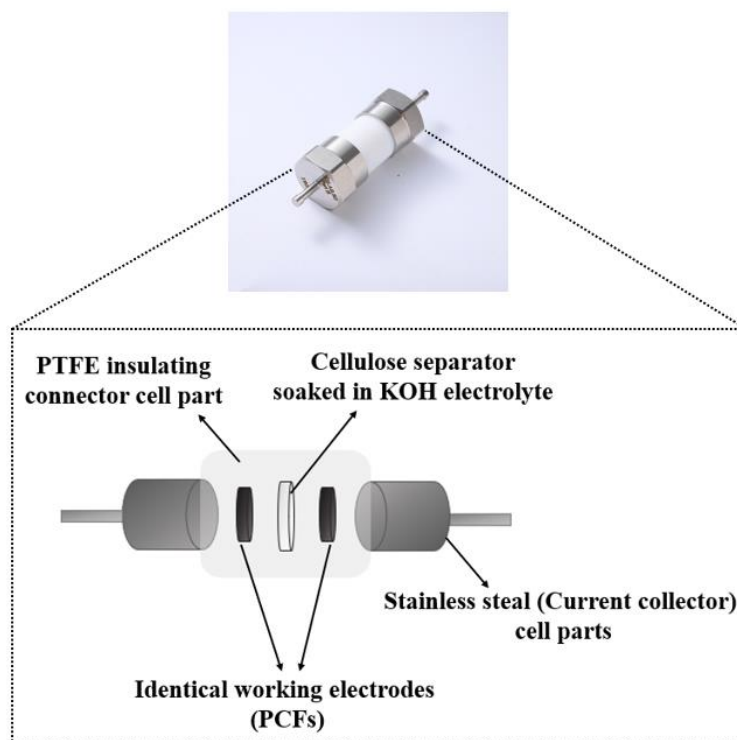


Figure 2.3. Representative scheme of a symmetrical configuration cell.

- ***Electrochemical measurements***

Electrochemical characterization techniques used in this research have been Cyclic voltammetry (CV), Galvanostatic charge–discharge (GCD) and Electrochemical impedance spectroscopy (EIS). The individual techniques are described below:

Cyclic voltammetry (CV)

Cyclic voltammetry (CV) is especially used in electrochemistry for studies of redox reactions between the electrode material and the electrolyte. This technique is based on applying a linear variation of potential as a function of time and the consequent recording of the current response. The potential range or potential window applied is established between two limits to avoid undesired reactions, such as electrolyte degradation. Measurements were also carried out in KOH (6 M) electrolyte, and the selected potential window was 0–(–0.8 V) for the three–electrode cell measurements and 0–0.8 V for the symmetrical cell. In addition to the potential window, it is also possible to modify other parameters such as sweep rate, which is the voltage variation per unit of time (dV/dt). To study how the behavior of PCFs varied respect to sweep rate, several

measurements were performed at different sweep rates in the range 5–500 mV s⁻¹. The higher the scan rate, the higher current responses can be recorded. The working electrode current response as a function of the applied potential is called voltammogram. **Figure 2.4** shows the typical CV voltammogram for a pure capacitive material (ideal behavior) and normal capacitive carbon material deviation, and CV non-idealities.

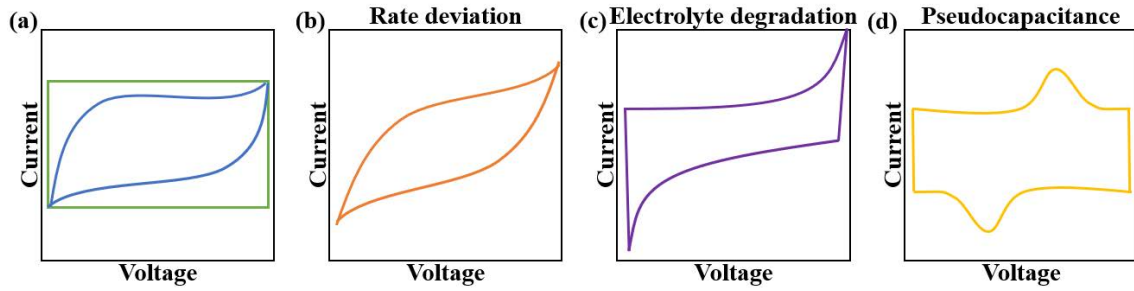


Figure 2.4. Example of a typical CV voltammogram of (a) ideal capacitive material (green line) and normal capacitive carbon material curve (blue line), (b) rate deviations curve, (c) electrolyte degradation curve, and (d) pseudocapacitance showing redox peaks curves.

The voltammogram shape provides an idea of the charge storage mechanism. A perfect rectangular shaped voltammogram is associated with an ideal capacitive material, due to the formation of the electrical double layer. Nevertheless, deviation from the ideal shape is usually caused by the intrinsic resistance of the carbon material. As shown in **Figure 2.4**, other typical deviations can occur, such as the presence of redox peaks that show a pseudocapacitive storage mechanism, and deviations due to higher sweep rates, which restrict electrolyte coupling to form the electrical double layer. On the other hand, the presence of exaggerated elongation at the potential limits can be attributed to the electrolyte decomposition [96].

From the CV curves, the specific or gravimetric capacitance of the active material can be determined by integrating the area under the curve ($I(V) \cdot dV$), according to Equation 2.5 for three-electrode measurements:

$$C_s(\text{F g}^{-1}) = \frac{1}{2 \cdot m \cdot v \cdot \Delta V} \int_{V_0}^{V_t} |I(V) \cdot dV| \quad (2.5)$$

Where ΔV is the voltage window, m is the active material electrode mass, I is the current used in the measure, and v is the sweep rate.

Galvanostatic charge–discharge (GCD)

Galvanostatic charge–discharge (GCD) test is an electrochemical technique based on the collection or measurement of the time required to subject the sample to a specific voltage application (voltage window). While a constant positive current is applied for charging and during discharge a constant negative current is applied. Potential curves are obtained by recording the applied voltage versus the time required to charge and discharge the electrode material (**Figure 2.5**).

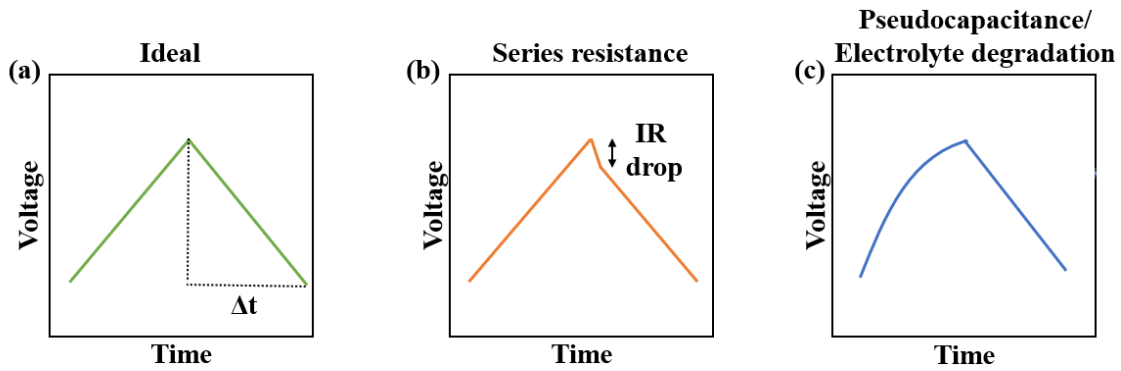


Figure 2.5. Example of a typical GCD curve showing (a) ideal behavior, (b) IR drop and (c) pseudocapacitance or electrolyte degradation deviations.

As for the cyclic voltammetry, GCD curves show some deviations, due to electrolyte degradation or pseudocapacitance storage mechanism, and the series resistance is reported as an IR (ohmic potential drop) or voltage drop, which is usually related to the setup configuration on three–electrodes cells, since it is the amount of potential that is lost on the way from the reference electrode to the working electrodes [96]. Specific or gravimetric capacitance of one electrode can be calculated from the discharge curve according to Equation 2.6 for the three–electrode cell configuration and according to Equation 2.7 for the symmetrical cell.

$$C_s(\text{F g}^{-1}) = \frac{I \cdot \Delta t}{m \cdot \Delta V} \quad (2.6)$$

$$C_s(\text{F g}^{-1}) = \frac{4 \cdot I \cdot \Delta t}{m \cdot \Delta V} \quad (2.7)$$

Where ΔV (V) is the voltage window, m (g) is the active material electrode mass, I (A) is the current used in the measure, and Δt (s) is the time to take place in the discharge curve.

Cycling 10,000 times GCD curves at a current density of 100 A g⁻¹ was carried out in order to determine the electrode stability. Moreover, capacitance values calculated from symmetrical cell measurements allow to obtain energy density (E) and power density (P), according to Equations 2.8 and 2.9, respectively.

$$E \text{ (Wh Kg}^{-1}\text{)} = \frac{\frac{1}{2} C_s V^2}{3.6} \quad (2.8)$$

$$P \text{ (W Kg}^{-1}\text{)} = \frac{E \cdot 3600}{\Delta t} \quad (2.9)$$

Where Δt (s) is the discharge time, V (V) is the discharge voltage range, and C_s (F g⁻¹) is the specific capacitance.

All the CV and GCD measurements carried out through this thesis work have been performed using a Metrohm autolab PGSTAT302N potentiostat.

Electrochemical impedance spectroscopy (EIS)

Electrochemical impedance spectroscopy is a powerful electrochemical technique used for the analysis of interfacial properties [97]. It is based on the possibility of separating different contributions of the overall impedance response of the electrode material corresponding to different regions, electrode surface, electrode–electrolyte interface, and bulk electrode. Impedance technique involves the application of a synodal perturbation on the voltage (over a wide range of frequencies) by monitoring the current response of the system. Impedance, $Z(f)$, is defined as the ratio between the applied potential signal and the current response of the electrochemical system. Generally, impedance (Z) is expressed in terms of complex numbers, being the real part Z' and the imaginary part Z'' . The most common impedance data representation is the Nyquist diagram. An example of a carbon electrode material Nyquist diagram is represented in **Figure 2.6a**.

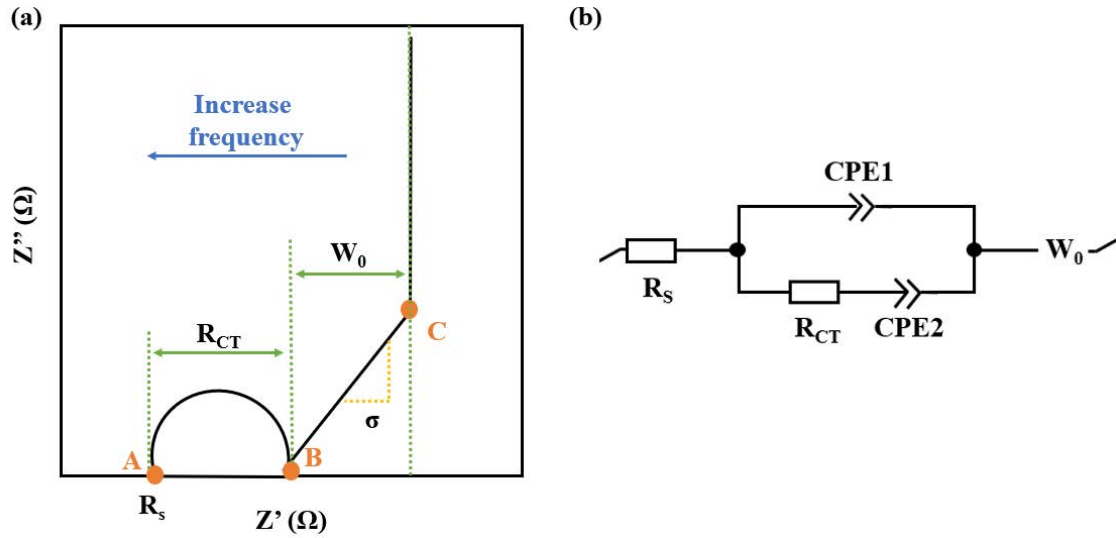


Figure 2.6. (a) Nyquist diagram for a carbon material with capacitive and pseudocapacitive behavior, and (b) equivalent circuit.

The diagram can be divided into four different parts [98]. At high frequencies a semicircle shape can be distinguished. The intersection of the semicircle with Z' axis (part A) provides the series resistance (R_s) values. This resistance can be related to the electrode internal resistance and is mainly associated with the conductivity of the electrode material. Moreover, at high frequencies (part A–B), the semicircle diameter provides the charge–transfer resistance (R_{CT}) values. It is related to the resistance associated with the porous structure of carbon electrodes and is mainly governed by the faradaic process that involves faradaic reactions with heteroatoms of surface functional groups. At low frequencies, the typical behavior of most capacitive and pseudocapacitive materials includes a region with a 45° inclination line, (part B–C). From this part, it is possible to obtain the Warburg diffusion coefficient (W_0) and ion–diffusion resistances (σ). This inclined line is followed by a region with a vertical line, related to purely capacitive behavior.

Considering the main resistance contributions, the Nyquist plots were fitted to the equivalent circuit show in **Figure 2.6b**, which displayed a set of resistors and capacitors in series or parallel. This model represents the series resistance (R_s), the charge–transfer resistance (R_{CT}) and the Warburg diffusion coefficient (W_0). W_0 was in series with both CPE1 and CPE2, indicating that ion diffusion is influenced by both, the electrical double layer capacitive (CPE1) and, pseudocapacitive (CPE2) storage mechanism [91].

All the EIS measurements were performed using a Biologic VSP-300 potentiostat in the range of frequencies between 0.1 and 100 KHz with a 5 mV perturbation.

Chapter 3

*Synthesis and characterization of block
copolymer precursors*

This chapter focus on the synthesis and characterization of the different block copolymers that have been used as precursors or template materials to produce porous carbon fibers (PCFs). A detailed analysis of the polymerization synthetic routes is also described. Additionally, a structural and compositional characterization will be carried out using nuclear magnetic resonance (NMR) and size exclusion chromatography (SEC). From these techniques molecular weight, block composition and degree of polymerization will be determined. The thermal transitions and processes will be further determined using differential scanning calorimetry (DSC) and thermogravimetric analysis (TGA) to evaluate the viability of these block copolymers as suitable precursors to obtain carbon porous structures.

The block copolymers used in this thesis work have been synthesized by Reversible Addition–Fragmentation chain–Transfer polymerization (RAFT). Along this thesis work, 2,2′-azobis(2-methylpropionitrile) (AIBN) has been used as initiator, and 2-cyano-2-propyl dodecyl trithiocarbonate (CPDT) has been selected as RAFT agent for all the polymerizations, since it has been demonstrated to be an effective chain transfer agent for polymerization of styrene [99] and tert-butyl acrylate [100] (sacrificial blocks). In addition, it allows to keep growing the chains with other monomers, including acrylonitrile, to formed well defined block copolymers [101].

3.1. RAFT Polymerization

Reversible addition–fragmentation chain–transfer polymerization (RAFT) has proven to be an effective method to obtain block copolymers with controlled molecular weights as building blocks of a wide variety of nanostructures [45]. RAFT exhibits the advantage of obtaining high molecular weights relatively easily, compared to other types of controlled polymerization, such as atom transfer radical polymerization (ATRP) [46]. Although ATRP offers high control over the generated structures (hyperbrach, star-, or brush-type), achieving high molecular weights remains a challenge, which is an essential parameter for obtaining fibers by electrospinning. RAFT polymerization can be classified as a controlled polymerization, or reversible–deactivation radical polymerization according to IUPAC [102], and the mechanism involves the following two main steps [103]:

Pre-equilibrium set of reactions: The pre-equilibrium reactions take place at the beginning of the polymerization. Scheme of the RAFT polymerization mechanism is shown in **Figure 3.1** with 2,2'-azobis(2-methylpropionitrile) (AIBN) as initiator, styrene as monomer and a generic dithio compound as CTA agent. A radical initiator such as AIBN is thermally activated producing the rupture of the molecule through the azo bond, generating radicals. These radicals react with a single monomer molecule (1), giving place to a polymeric radical of a determined length (n), mostly oligomeric at these early stages. These propagating oligomeric radical chains (2) react with the sulfur-carbon double bond of the chain transfer agent (CTA agent), giving place to an intermediate radical (3). This intermediate radical, which corresponds with the dormant specie, is in equilibrium either towards the formation of a polymeric dithioester compound (4) or to the reagents.

Main equilibrium reactions: In this stage of the polymerization, the mechanism is similar to the pre-equilibrium step. The polymeric radicals (2) react with the polymeric dithioester compound (4). These reactions are in equilibrium with dormant species (5) or living chains.

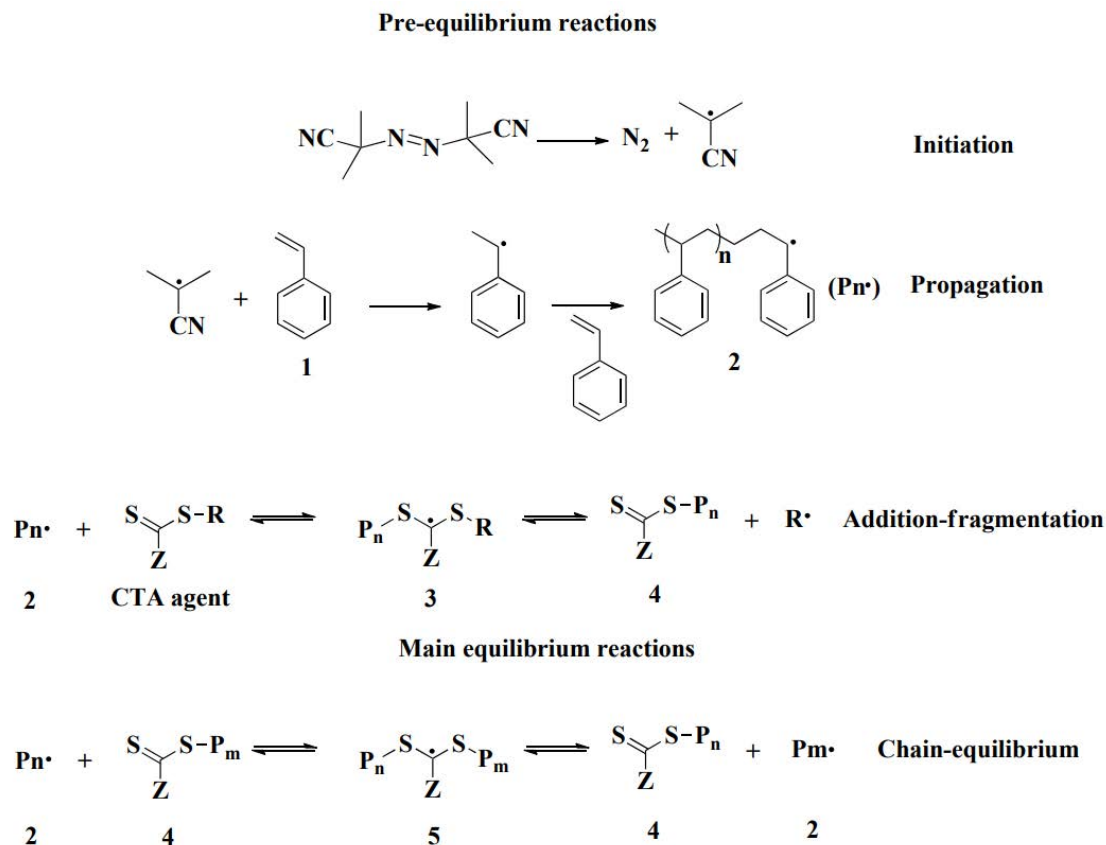


Figure 3.1. RAFT polymerization mechanism.

As it can be seen from the polymerization mechanism, the chain-transfer agent is a key reagent, as it participates in the pre-equilibrium reactions. Most of the RAFT agents are thio-derived compounds, but many studies have been conducted by changing the R and Z functional groups, since the type of monomer dictates the use of a suited CTA agent [104].

3.2. Synthesis and characterization of PS-*b*-PAN

3.2.1. Synthetic route

PS-*b*-PAN copolymer was synthesized by RAFT polymerization in two steps, as shown in **Figure 3.2**. First, the sacrificial block of PS was polymerized using 2-cyano-2-propyl dodecyl trithiocarbonate (CPDT) as CTA agent, resulting in the macro-CTA (PS-CPDT). PS macro-CTA was then used to chain extend with

acrylonitrile, leading to the formation of the block copolymer, according to our published work [105].

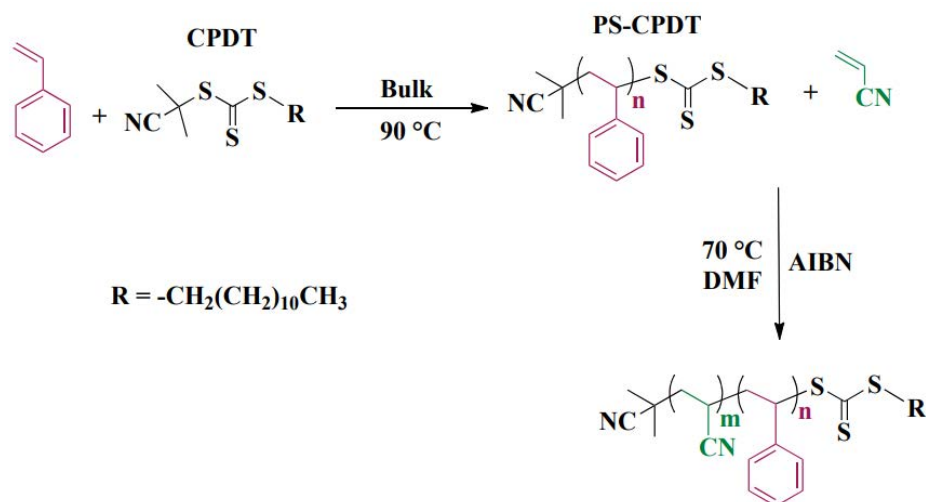


Figure 3.2. RAFT polymerization synthetic route to obtain PS-*b*-PAN copolymer.

Macro-CTA (PS-CPDT) synthetic procedure was carried out as follows:

In a Schlenk flask with a magnetic stirrer were placed 2 mL of styrene (17 mmol) and 14.8 μL of CPDT (0.043 mmol), and the system was sealed with a rubber septum. The mixture was deoxygenated through three freeze-pump-thaw cycles. Afterwards, the Schlenk flask under an inert atmosphere of nitrogen was placed into a thermostatic oil bath at 140 $^\circ\text{C}$ for 30 min, and maintained at 90 $^\circ\text{C}$ for 48 h. Then, the reaction mixture was cooled down and diluted with a small amount of THF. The product was purified by precipitation in a large amount of MeOH twice and filtered. The yellow solid polymer was dried under vacuum for 24 h at 30 $^\circ\text{C}$.

This synthetic procedure presented some advantages: firstly, it allows RAFT agent (CPDT) to be used as initiator simultaneously, without the requirement of AIBN, and the reaction is carried out in bulk, which avoids the use of solvents.

In a second step, the *PS-b-PAN* polymerization procedure is described as follows:

PS-CPDT macro-CTA (0.1 g, 0.0056 mmol), AIBN (0.6 mg, 0.0038 mmol), and AN (2.9 mL, 44 mmol) were added to a Schlenk flask equipped with a magnetic bar, and the mixture was dissolved in anhydrous DMF (6 mL). The flask was sealed with a rubber

septum stopper and the reaction system was frozen in liquid nitrogen and subjected to three freeze–pump–thaw cycles to remove oxygen. Then, the flask under nitrogen was placed into a thermostatic bath at 70 °C for 24 h. After that time, the reaction mixture was cooled down, precipitated in a large volume of MeOH, and filtered, repeated twice. Finally, the block copolymer was dried at 30°C for 24 h to obtain a white powder.

3.2.2. Polymer characterization

Throughout the PS–CPDT polymerization, aliquots of the reaction mixture were taken at different reaction times to monitor the reaction. The aliquots were precipitated in MeOH and dissolved again in DMF to measure the molecular weight by SEC. **Figure 3.3** shows the progress of the molecular weight as a function of the reaction time until adequate molecular weight was reached.

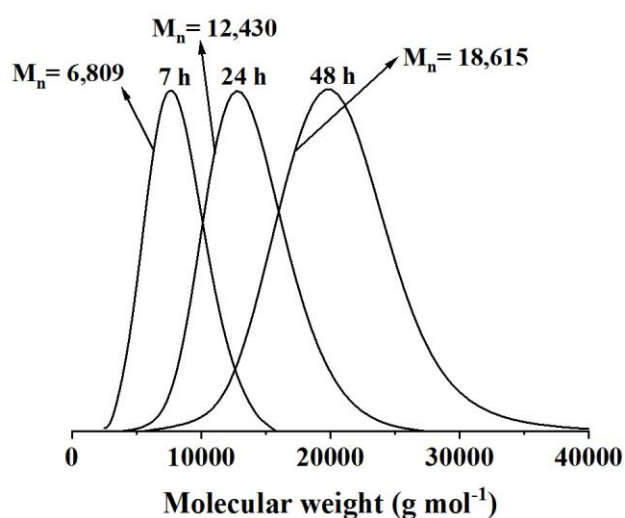


Figure 3.3. SEC chromatographs of aliquots of the PS–CPDT reaction mixture at different reaction times.

One of the challenges in this work was to synthesize a block copolymer with a high carbon precursor block content and low sacrificial block content, to produce carbon materials with a high carbon yield. Therefore, the synthesis was stopped after 48 h of reaction, considering the molecular weight obtained as optimal without compromising the control of polydispersity due to high reaction time.

Figure 3.4 shows the SEC chromatographs of PS–CPDT and PS-*b*-PAN. Both presented unimodal narrow peaks, although the block copolymer exhibited a slightly

visible tail at larger retention times. Those SEC traces indicated the presence of some lower molecular weight chains or ‘dead chains’ derived from the large reaction times [106]. The production of lower molecular weight dead chains can be affected by the target degree of polymerization (N). Since at higher N , growing chains spend longer cumulative time as propagating radicals, and consequently a higher probability of termination or other side reactions arises, stopping the chain growth [107]. To that effect, the high concentration of acrylonitrile used in the synthesis plays a fundamental role, since it increases the viscosity of the reaction medium, limiting the terminations [108]. Polar solvents, as DMF, has also been demonstrated to stabilize the transition state of propagating radicals [109].

Despite the slightly visible tail, low polydispersity indexes were obtained with 1.06 and 1.26 values and number average molecular weights (M_n) of 18,615 and 118,710 g mol^{-1} for PS-CPDT and PS-*b*-PAN, respectively, indicating a successful control of the radical polymerization. Additionally, the high molecular weight obtained ensures easier fiber fabrication by electrospinning.

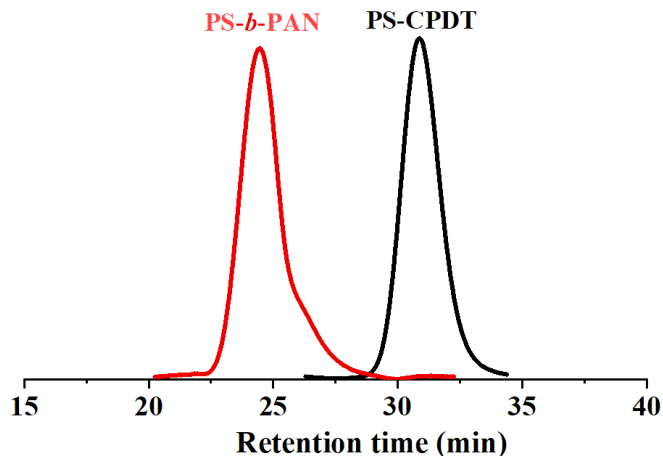


Figure 3.4. SEC chromatographs of PS-CPDT and PS-*b*-PAN.

Number average molecular weights (M_n) and degree of polymerization were determined by NMR spectroscopy. **Figure 3.5** shows the ^1H -NMR spectra of polystyrene macro-CTA and block copolymer measured in d_7 -DMF. Signals related to both polymers were fully identified in the spectra.

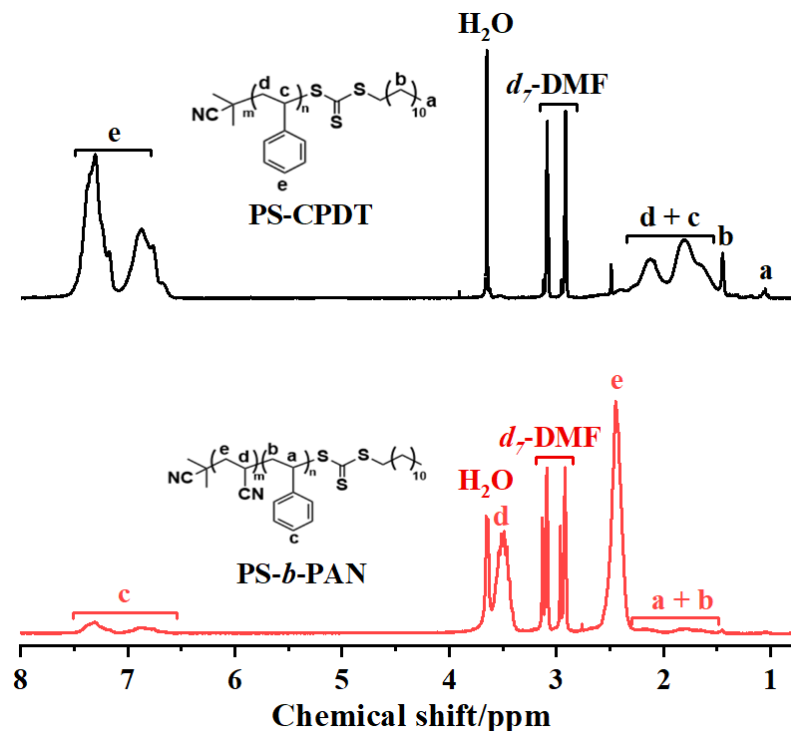


Figure 3.5. ^1H -NMR spectra of macro-CTA (PS-CPDT) and block copolymer (PS-*b*-PAN).

PS-CPDT molecular weight and degree of polymerization (n) were determined by comparison of the relative integration of the signals at 1.44 ppm (b) assigned to the protons of methylene groups $-(\text{CH}_2)_{10}-$ of the RAFT agent and those at the range 6.7–7.4 ppm (e) ascribed to the phenyl protons of PS as follows:

$$n(N_{PS}) = \frac{I_e \cdot a_e}{I_b \cdot a_b} \quad (3.1)$$

Where I is the integral of the signal assigned to e protons, and a is the number of protons of that moiety. PAN block molecular weight and degree of polymerization (m) were determined as well, by comparison of the relative integration of the signals at 2.45 ppm (e) assigned to the protons $-\text{CH}_2-\text{CH}(\text{CN})-$ of PAN and those at the range 6.7–7.4 ppm (c) ascribed to the phenyl protons of PS as follows:

$$m(N_{PAN}) = \frac{I_c \cdot a_c \cdot n}{I_e \cdot a_e} \quad (3.2)$$

where I is the integral of the signal assigned to e protons, a is the number of protons of that moiety, and n is the PS–CPDT degree of polymerization. Calculations revealed the following composition: Polystyrene exhibited a degree of polymerization and molecular weight of $n \approx 162$ and $M_{n, \text{NMR}} = 16,403 \text{ g mol}^{-1}$, respectively. On the other hand, polyacrylonitrile presented a degree of polymerization of $m \approx 1908$ and $M_{n, \text{NMR}} = 101,230 \text{ g mol}^{-1}$, respectively. Considering each polymer densities ($\rho_{\text{PS}} = 1.02 \text{ g cm}^{-3}$ and $\rho_{\text{PAN}} = 1.18 \text{ g cm}^{-3}$) [110], their molar concentrations in percent (c) obtained by NMR, and the solvent density ($\rho_{\text{DMF}} = 0.994 \text{ g cm}^{-3}$), volume fraction of each block was calculated as follows:

$$f_{\text{block}} = \frac{\frac{c_{\text{block}}}{\rho_{\text{block}}}}{\frac{c_{\text{block}}}{\rho_{\text{block}}} + \frac{(100 - c_{\text{block}})}{\rho_{\text{Solvent}}}} \quad (3.3)$$

Calculations revealed a composition of 0.16 volume fraction of polystyrene and 0.84 of polyacrylonitrile.

3.2.3. Thermal characterization

As previously explained in **Chapter 1**, the unique and exceptional thermal properties of polyacrylonitrile allow it to produce well-defined carbon materials [15]. Around 280 °C under air atmosphere, the cross-linking of the side chains occurs through some cyclization reactions. In addition, dehydrogenation and oxidation reactions take place introducing oxygen functionalities (see **Figure 1.7** in **Chapter 1**). This oxidative stabilization step leads to structural changes, stabilizing the structure and allowing the generated morphologies to be preserve. Dehydrogenation between 300–400 °C and further denitrogenation from 600 °C, under nitrogen atmosphere, leads to partially graphitic structures.

PAN stabilization process was revealed in the block copolymer DSC curve as a sharp exotherm peak at 260 °C (**Figure 3.6**). Due to the low heating rates ($<30 \text{ °C min}^{-1}$), oxidation/cyclization reactions occurred prior to melting, and as a result, no melting peak of the PAN block was detected [111]. The DSC trace of PS–CPDT, inset graph in **Figure 3.6**, showed a T_g at around 100 °C, corresponding to the amorphous region of PS, which was slightly visible in the PS-*b*-PAN thermogram at $\sim 105 \text{ °C}$. According to DSC data,

no endothermic peak corresponding to the decomposition of PS appeared up to 350 °C, therefore, stabilization of PAN and decomposition of PS are well separated processes. This is strongly important since PS is the sacrificial block and should not interfere with the stabilization of PAN domains. To ensure effective stabilization before PS decomposition and prevent low efficiency of cyclization reactions, the upper limit temperature of the exothermic peak was fixed during the stabilization process (280 °C for 2 h), as indicated by DSC data.

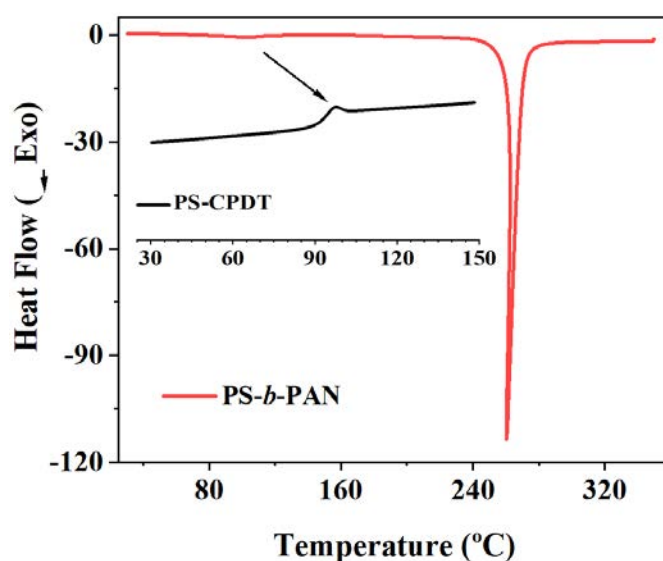


Figure 3.6. DSC thermogram of PS-*b*-PAN and inset graph of PS-CPDT showing T_g .

Thermogravimetric analysis was used to evaluate the weight loss of PS-*b*-PAN resulting from pyrolysis. The TGA profile of PS-CPDT, showed in **Figure 3.7**, exhibited a single weight loss stage at 400 °C; while PAN homopolymer (commercial; $M_w = 150,000 \text{ g mol}^{-1}$) displayed three main loss stages, related to its thermal chemical reactions [49]. The first weight loss stage ($\sim 260\text{--}290 \text{ °C}$) is characteristic of cyclization, partially dehydrogenation and crosslinking reactions. The second loss stage ($\sim 295\text{--}465 \text{ °C}$) is due to dehydrogenation of the cyclized PAN structure. The third stage exhibited a slight weight loss between 460 and 870 °C that corresponds with the carbonization of the pre-stabilized PAN, through some denitrogenation reactions.

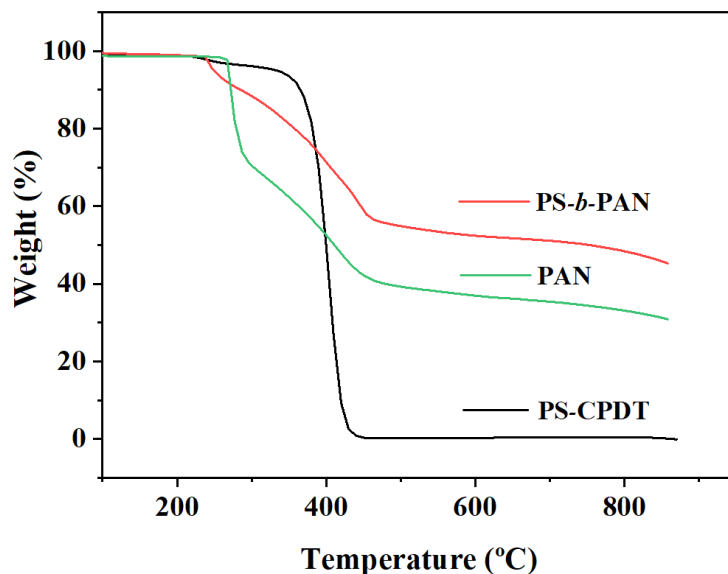


Figure 3.7. TGA curves of PS-CPDT, PS-*b*-PAN, and PAN homopolymer.

PS-*b*-PAN profiles also showed three main loss stages. The first one in the range between 220 and 290 °C corresponded to mainly cyclization reactions of PAN block. The second loss stage (~310–460 °C) was attributed to the thermal decomposition of PS block. The third stage exhibited a slight weight loss (~460–870 °C) corresponding to the carbonization of the pre-stabilized PAN. The block copolymer showed a 5% weight loss at 290 °C in N₂ atmosphere and a final carbon yield close to 50% after 800 °C. This is highly beneficial to be used as carbon precursor, since it increases the yield of the processes by reducing the amount of fiber precursor required. It is worth mentioning that in the literature, most of the synthesized block copolymers for similar purposes exhibited lower carbon yields (20–40%) due to a higher sacrificial block content [57,60].

3.2.4. High molecular weight PS-*b*-PAN

- *Synthetic route*

To study the influence of the total degree of polymerization (N) on the fiber morphology and overall porosity, a new PS-*b*-PAN copolymer with a higher molecular weight (St₂₉₁-*b*-AN₄₅₀₇) than the previously obtained (St₁₆₂-*b*-AN₁₉₀₈) was synthesized, where $N_{\text{tot}} = N_{\text{PAN}} + N_{\text{PS}}$. Since the first synthesized St₁₆₂-*b*-AN₁₉₀₈ copolymer presented a remarkably high carbon yield (~ 50 %) due to the low sacrificial block content, the main idea of synthesizing this new copolymer (St₂₉₁-*b*-AN₄₅₀₇) was maintaining the low PS

volume fraction that allows to preserve a high carbon yield, and at the same time increasing the total degree of polymerization or total molecular weight.

For this purpose, the PS macro-CTA synthetic route was modified by increasing styrene equivalents, as follows:

Styrene (2 mL, 17 mmol) and CPDT (5.93 μ L, 0.017 mmol) were added to a Schlenk flask equipped with a magnetic stirrer and sealed with a rubber septum. The mixture was subjected to three freeze-pump-thaw cycles to remove oxygen. Afterwards, the Schlenk flask under N₂ was placed into a thermostatic bath at 140 °C for 30 min, followed by 24 h at 90 °C. Then, the reaction mixture was cooled down and diluted with a small amount of THF. The product was isolated by precipitation in a large amount of MeOH twice, filtered, and dried under vacuum for 24 h at 30 °C to give a yellowish solid.

- **Polymer characterization**

The obtained PS-CPDT was then used as macro-CTA for acrylonitrile chain extension to obtain a St₂₉₁-*b*-AN₄₅₀₇ copolymer with higher total molecular weight; by using the same synthetic procedure and equivalents as mentioned in **Section 3.2**. According to SEC chromatographs showed in **Figure 3.8** and ¹H-NMR spectrum in **Figure 3.9**, polydispersity index (PDI), degree of polymerization of both blocks, total degree of polymerization, molecular weight and composition, can be determined (**Table 3.1**).

SEC chromatographs (**Figure 3.8**) showed the comparative molecular weight peaks of PS macro-CTA and PS-*b*-PAN copolymer presenting different degree of polymerization. Both, St₂₉₁ and St₂₉₁-*b*-AN₄₅₀₇, exhibited unimodal peaks with the expected shoulder or tail of the block copolymer peak at larger retention times; indicating the presence of some premature polymerization endings, which generates dead chains with lower molecular weight. Nevertheless, it can be clearly observed how both polymers reached higher number weight average molecular weights (lower retention times), achieving an increment of the total molecular weight or degree of polymerization (*N*). Polydispersity indices increased moderately for both, St₂₉₁ and St₂₉₁-*b*-AN₄₅₀₇, indicating a slightly lower control over the polymerization.

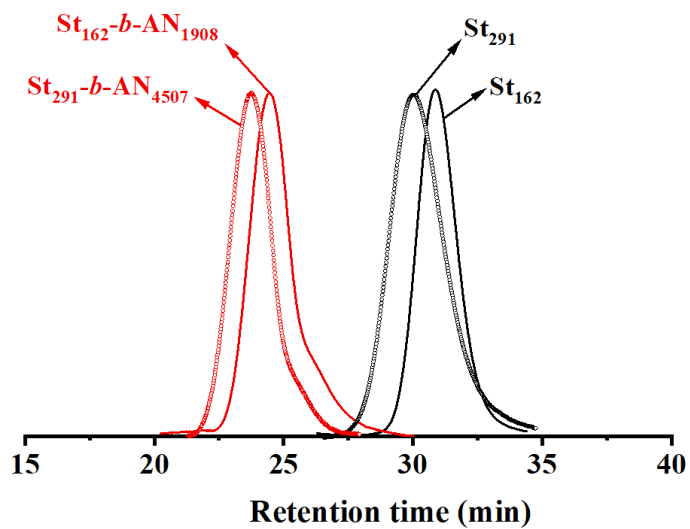


Figure 3.8. SEC chromatographs of St_{291} , St_{162} , $St_{291}-b-AN_{4507}$, and $St_{162}-b-AN_{1908}$.

Figure 3.9 showed the 1H -NMR spectra of high molecular weight polystyrene macro-CTA (St_{291}) and resulting block copolymer ($St_{291}-b-AN_{4507}$) measured in d_7 -DMF. Signals related to macro-CTA and copolymer were fully identified in the spectra.

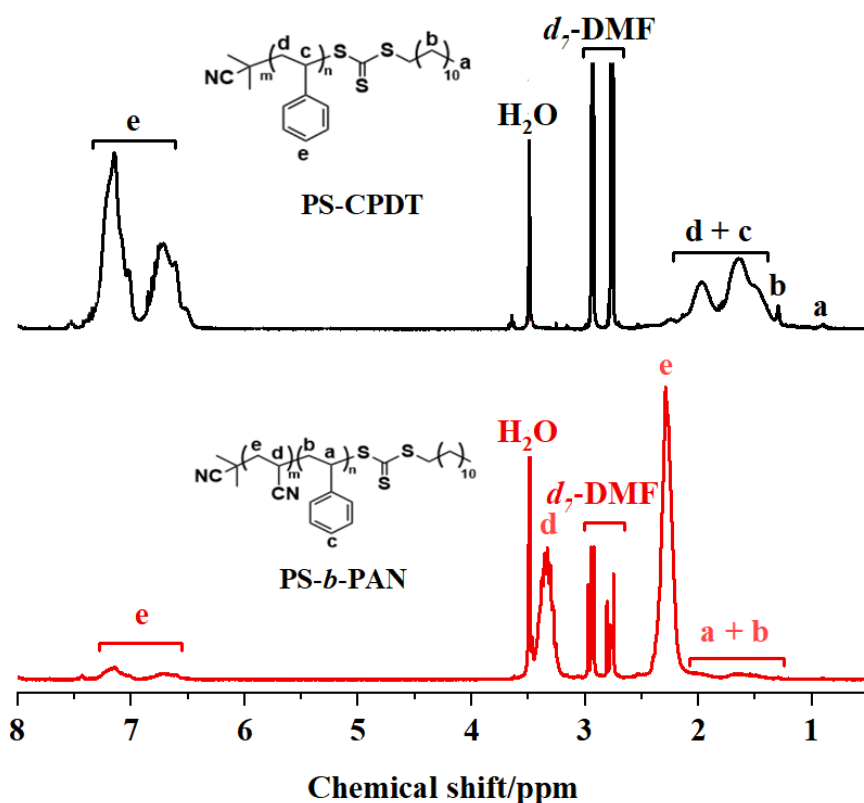


Figure 3.9. ^1H -NMR spectra of high molecular weight macro-CTA (PS-CPDT) and block copolymer (PS-*b*-PAN).

The PS volume fraction was $f_{\text{PS}} = 0.11$, calculated according to (3) formula, slightly lower than the already obtained (St₁₆₂-*b*-AN₁₉₀₈; $f_{\text{PS}} = 0.16$), but close enough to disregards its contribution to the fiber morphology, since the difference in total degree of polymerization (N) is much higher than the difference in sacrificial block volume fraction.

Table 3.1. Summary of PS macro-CTAs and PS-*b*-PAN copolymers composition.

PS- <i>b</i> -PAN					
DP _{PS} , PDI	[PS]:[CTA]	Composition	M _{n,NMR}	M _{n,GPC}	PDI
162, 1.06	400:1	St ₁₆₂ - <i>b</i> -AN ₁₉₀₈	30,297	32,395	1.26
291, 1.20	1000:1	St ₂₉₁ - <i>b</i> -AN ₄₅₀₇	239,141	271,654	1.35

3.3. Synthesis and characterization of PtBA-*b*-PAN

3.3.1. Synthetic route

To study the influence of the sacrificial block on fiber morphology and porosity, tert-butyl acrylate (tBA) was selected. Poly tert-butyl acrylate and polyacrylonitrile block copolymer was synthesized, by using the same approach as for PS-*b*-PAN copolymer; through RAFT polymerization in two steps (**Figure 3.10**). In the first step, polymerization of PtBA sacrificial block took place, using CPDT and AIBN as RAFT agent and initiator, respectively, resulting in macro-CTA (PtBA-CPDT). In a second step, PtBA macro-CTA was then used to chain extend with acrylonitrile, leading to the formation of the block copolymer.

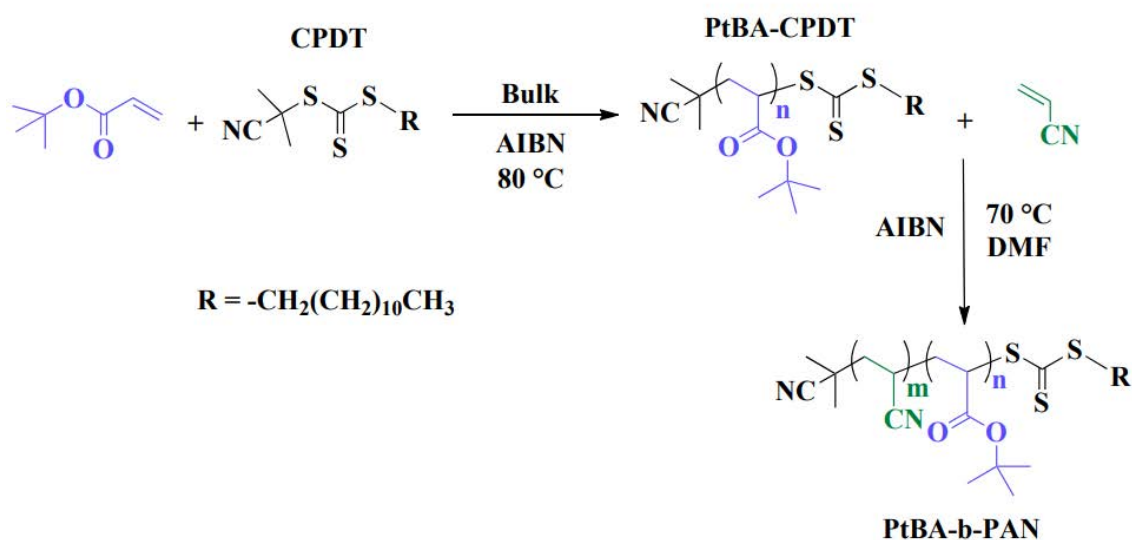


Figure 3.10. RAFT polymerization synthetic route to obtain PtBA-*b*-PAN copolymer.

Macro-CTA (PtBA-CPDT) synthetic procedure was carried out as follows, based on previously reported synthesis [100]:

Tert-butyl acrylate (2 mL, 13.65 mmol), CPDT (47.6 μL , 0.14 mmol), and AIBN (1.12 mg, 0.0068 mmol) were added to a Schlenk flask equipped with a magnetic stirrer and sealed with a rubber septum. The mixture was subjected to three freeze-pump-thaw cycles to remove oxygen. Afterwards, the Schlenk flask under N_2 was placed into a thermostatic bath at 80 $^\circ\text{C}$ for 24 h. Then, the reaction mixture was cooled down and

diluted with a small amount of dichloromethane. The product was isolated by precipitation in a large amount of cold H₂O/MeOH (50/50; v/v) twice. The sticky viscous yellow solid was separated by decantation and dried under vacuum at 40 °C up to constant weight, to give a yellow solid.

In a second step, the *PtBA-b-PAN* polymerization procedure was performed as follows:

PtBA-CPDT macro-CTA (0.1 g, 0.0056 mmol), AIBN (0.6 mg, 0.0038 mmol), and AN (2.9 mL, 44 mmol) were placed in a Schlenk flask equipped with a magnetic bar and dissolved in anhydrous DMF (6 mL). The tube was sealed with a rubber septum and the mixture was deoxygenated through three freeze-pump-thaw cycles. Then, the flask was placed into a thermostatic bath at 70 °C for 24 h under a N₂ atmosphere. Thereafter, the reaction mixture was cooled down, precipitated in a large amount of MeOH, and filtered, repeated twice. At last, the resulting block copolymer was dried under vacuum for 24 h at 30 °C as a white powder.

3.3.2. Polymer characterization

With the aim of focusing the study exclusively on the sacrificial block influence, an attempt was made to keep constant the rest of parameters that could affect the fiber morphology, such as sacrificial block volume fraction and block copolymer total molecular weight. Therefore, a PtBA-CPDT molecular weight comparable to PS-CPDT one (~18,000 g mol⁻¹) was required.

SEC chromatographs of PtBA-CPDT and PtBA-*b*-PAN are shown in **Figure 3.11**. Both presented unimodal narrow peaks. Although, as expected, the block copolymer SEC traces exhibited a shoulder at higher retention times. As mentioned in **Section 3.2.2**, this type of peak tails or shoulders are indicative of low molecular weight polymer chains that have undergone some premature termination, which is common in radical polymerizations. Nevertheless, low polydispersity indexes were obtained with 1.1 and 1.3 values and number weight average molecular weights (M_n) of 17,635, and 147,352 g mol⁻¹ for PtBA-CPDT and PtBA-*b*-PAN, respectively; indicating good control of polymerization. Both molecular weights were very close to those obtained for PS-CPDT and PS-*b*-PAN.

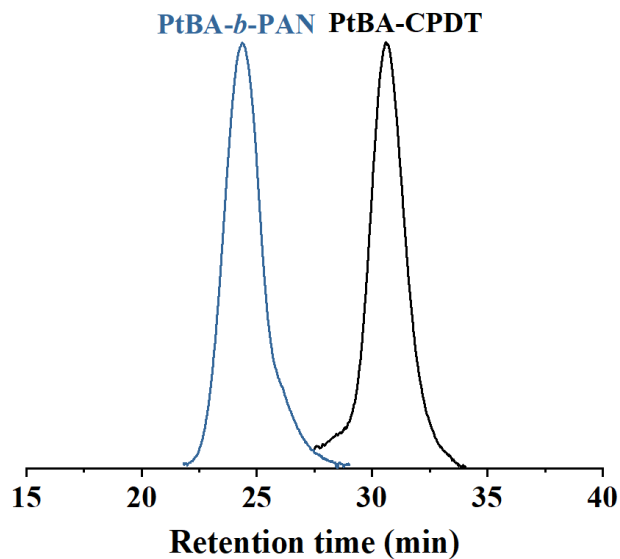


Figure 3.11. SEC chromatographs of PtBA-CPDT and PtBA-*b*-PAN copolymer.

Figure 3.12 showed the ^1H -NMR spectra of PtBA-CPDT and PtBA-*b*-PAN copolymer measured in d_7 -DMF and focused on chemical shifts between 1 to 4.5 ppm, where all signals were concentrated. Signals related to macro-CTA and block copolymer were fully identified in the spectra.

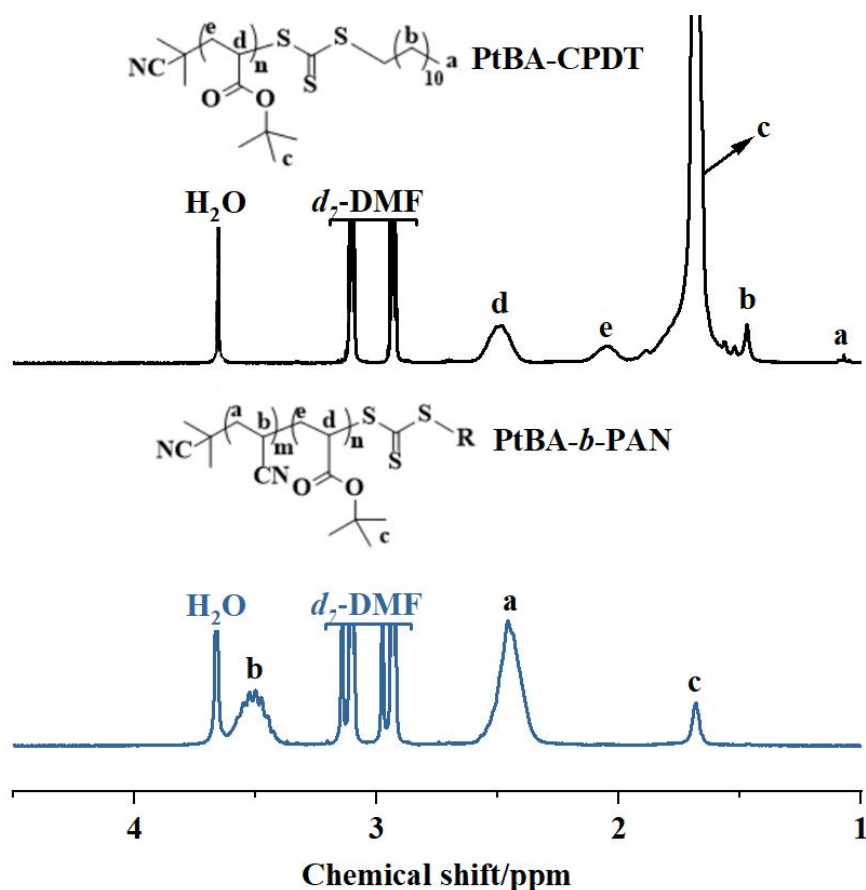


Figure 3.12. ^1H -NMR spectra of macro-CTA (PtBA-CPDT) and block copolymer (PtBA-*b*-PAN).

PtBA-CPDT molecular weight and degree of polymerization (n) were determined by comparison of the relative integration of the signals at 1.47 ppm (b) assigned to the protons of methylene groups ($-(\text{CH}_2)_{10}-$) of the RAFT agent termination and those at 1.68 ppm (e) ascribed to the tert-butyl functional group protons of PtBA, using formula (1) described in **Section 3.2.2**. On the other hand, molecular weight, and DP (m) of the PAN block were determined by comparison of the relative integration of the signals at 2.45 ppm assigned to the protons $-\text{CH}_2-\text{CH}(\text{CN})-$ of PAN and those at 1.68 ppm ascribed to the tert-butyl functional group protons of PtBA, using formula 3.2.

Calculations revealed the following composition: Poly tert-butyl acrylate exhibited a degree of polymerization and molecular weight of $n \approx 121$ and $M_{n, \text{NMR}} = 15,567 \text{ g mol}^{-1}$, respectively. Polyacrylonitrile presented a DP $m \approx 2689$ and $M_{n, \text{NMR}} = 142,678 \text{ g mol}^{-1}$. Considering each polymer densities and taking into consideration that the density of PtBA was not found in the literature, instead poly tert-butyl methacrylate

density was used ($\rho_{\text{PtBMA}} = 1.03 \text{ g cm}^3$ and $\rho_{\text{PAN}} = 1.18 \text{ g cm}^3$). PtBA volume fraction was 0.10, calculated using formula 3.3.

According to these results, even though similar molecular weight was obtained for PtBA-CPDT compared to PS-CPDT, PAN block was larger than the one found for PS-*b*-PAN. Therefore, PtBA-*b*-PAN exhibited a slightly lower sacrificial block volume, and this difference will be taken into consideration for an honest comparison of both block copolymers as precursors for PCFs.

3.3.3. Thermal characterization

As previously exhibited in the PS-*b*-PAN DSC trace, PAN stabilization process in the PtBA-*b*-PAN was revealed in the DSC curve as a sharp exotherm peak at 270 °C (**Figure 3.13**). This peak was shifted compared to the observed in PS-*b*-PAN (260 °C). It is expected that this behavior occurs due to the distinct blocks present in the copolymers. Previous studies have shown that the sacrificial block's nature may influence the exothermic peak observed in copolymers based on PAN

As previously exhibited in the PS-*b*-PAN DSC trace, PAN stabilization process was revealed in the PtBA-*b*-PAN DSC curve as a sharp exotherm peak at 270 °C (**Figure 13**). This peak was shifted compared to the observed PS-*b*-PAN (260 °C). This behaviour is expected due to the presence of different sacrificial block as it was previously observed for PAN-based copolymers [112]. Prior to this characteristic PAN peak, it could be detected a slight exotherm peak around 240 °C, due to degradation of the tert-butyl functional group [113].

The DSC trace of PtBA-CPDT, inserted graph in **Figure 3.13**, showed a T_g at ~45 °C, corresponding to the amorphous region of PtBA. However, in the PtBA-*b*-PAN thermogram, the T_g was slightly visible at around 60 °C. According to DSC data, any endothermic peak corresponding to the decomposition of PtBA appeared up to 350 °C, therefore, it seems that stabilization of PAN and decomposition of PtBA are well separated processes.

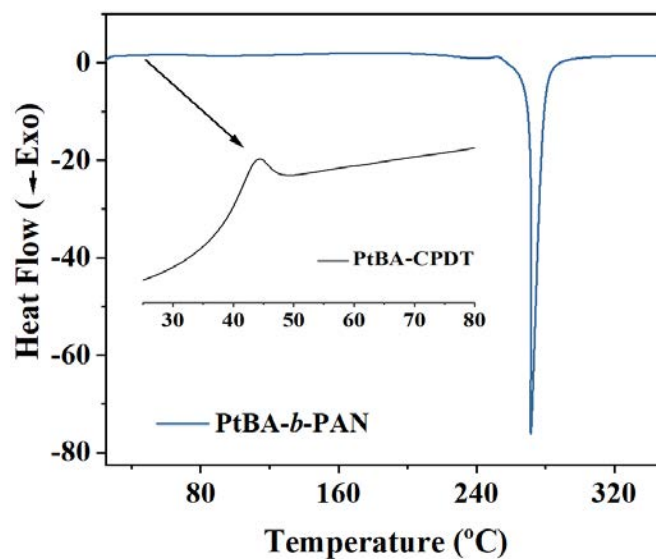


Figure 3.13. DSC thermogram of PtBA-*b*-PAN and insert graph of PtBA-CPDT showing T_g .

The TGA curve of PtBA-CPDT (**Figure 3.14**) clearly showed two different stages. The first one between 210 and 240 °C was due to degradation of the tert-butyl functional group. The formed carboxylic acid functional groups dehydrated to form a cyclic anhydride-type structure [20], as shown the degradation sequence outlined in **Figure 3.15**. The second stage started around 300 °C and ending around 470 °C, corresponded with the full degradation of the polymer. This suggested that PAN cyclization process occurs together with the PtBA degradation, which may interfere with the PAN stabilization and affect the pore structure of the resulting porous carbon fibers.

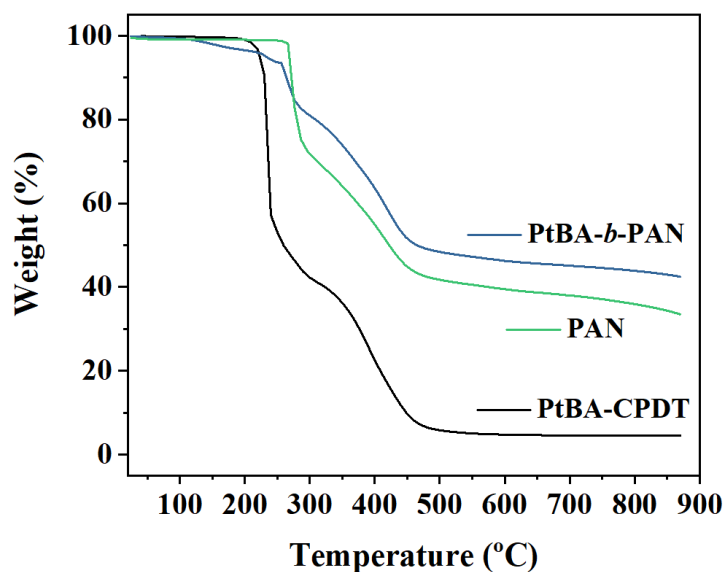


Figure 3.14. TGA curves of PtBA-CPDT, PtBA-*b*-PAN and PAN homopolymer.

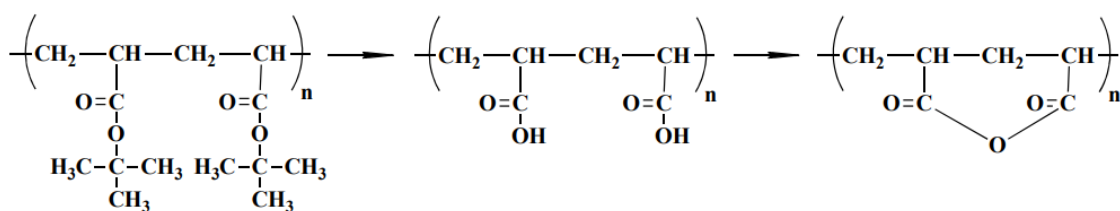


Figure 3.15. Mechanism of tert-butyl acrylate decomposition.

PAN homopolymer (commercial; $M_w = 150,000 \text{ g mol}^{-1}$) profile showed the three main loss stages already explained in **Section 3.2.3**.

PtBA-*b*-PAN exhibited four main loss stages. In the range 25–150 °C, some weight loss could be observed due to evaporation of solvent traces. The first brief weight loss stage, between 225 and 260 °C, was due to degradation of tert-butyl functional group. A second loss stage, between 260 and 280 °C, was attributed to PAN cyclization process. The third stage and most significant one in the range 285–465 °C, was due PAN dehydrogenation together with PtBA full degradation. Finally, a slight weight loss (~460–870 °C) corresponded with the fourth stage was due to carbonization of the pre-stabilized PAN, through some denitrogenation reactions. The block copolymer showed a final carbon yield close of 45 % after 800 °C.

According to the presented results PtBA-*b*-PAN can be considered a potential suitable precursor for PCFs.

Chapter 4

*Porous carbon fibers derived from
block copolymers*

Throughout this chapter, the process for obtaining fibers derived from PAN-based block copolymers (BCPs) will be detailed as follows:

Firstly, the potential use of PS-*b*-PAN as precursor will be evaluated, by studying the morphology and porous structure generated after carbonization of a film derived from PS-*b*-PAN, and direct carbonization of the BCP powder right after precipitation (bulk) without any additional processing. Besides, a description of the obtention of PS-*b*-PAN fibers will be presented, including the optimization of electrospinning to obtain the most suitable parameters to produce a homogenous fiber mat. After establishing the thermal conditions, the resulting porous carbon fibers were structurally and physiochemically characterized.

Moreover, a comparative structural study has been carried out, based on the influence of total degree of polymerization of PS-*b*-PAN precursor on the fiber structure and overall porosity. This will be performed analyzing the morphology and physicochemical characteristics of PCFs obtained using BCPs with lower and higher total molecular weight, maintaining in both cases similar PS volume fraction.

Finally, the influence of the sacrificial block on morphology, carbon structure and porosity of the fiber has also been evaluated. A BCP containing poly (tert-butyl acrylate) (PtBA) as sacrificial block has been used to study the morphological and physicochemical characteristics of PCFs, comparing both carbon fibers obtained from PS-*b*-PAN (PS-PCFs) and PtBA-*b*-PAN (PtBA-PCFs).

4.1. Phase-separation and morphology of PS-*b*-PAN

The obtention of porous carbon materials based on carbonization of PAN-based block copolymers containing a sacrificial block has attracted significant interest. This method, called soft-templating, allows to obtain well defined carbon structures presenting meso- and micropores simultaneously, through self-assembly between the two immiscible blocks [114]. After thermal treatments that stabilize the generated morphologies, carbon materials with controlled porosity can be obtained, preserving the original morphology. In addition, the use of block copolymer templating presents a huge versatility since it allows to obtain a wide range of morphologies by varying the

parameters that define the phase domains, such as sacrificial block, molecular weight, and composition, among others [115].

A preliminary study was carried out to confirm the PS-*b*-PAN suitability as precursor of well-controlled porous carbon materials, and therefore to be able to produce fibers by electrospinning, presenting high and controlled porosity after carbonization. Moreover, this study was used to determine the optimal thermal treatments that allow to preserve the generated morphologies.

A PS-*b*-PAN film was prepared by spin-coating and subjected to a two-step thermal treatment, schematically illustrated in **Figure 4.1**. Spin-coating allows to produce polymer thin films (60–100 nm) on a flat substrate. A solution of PS-*b*-PAN at 1.5 wt% in DMF was coated onto a clean silicon wafer at 3000 rpm. The porous carbon film was obtained by subjecting the polymer film to post-thermal treatment. The film was thermally annealed at 280 °C for 1 h under air flow, leading to PAN stabilization into a ladder-like structure [49], followed by degradation of PS sacrificial block. In a second thermal treatment at 800 °C for 1 h under N₂ atmosphere, carbonization of the already stabilized PAN block was carried out, obtaining a partially graphitized structure, as previously explained in **Section 1.1.3 of Chapter 1 (Figure 1.7)**.

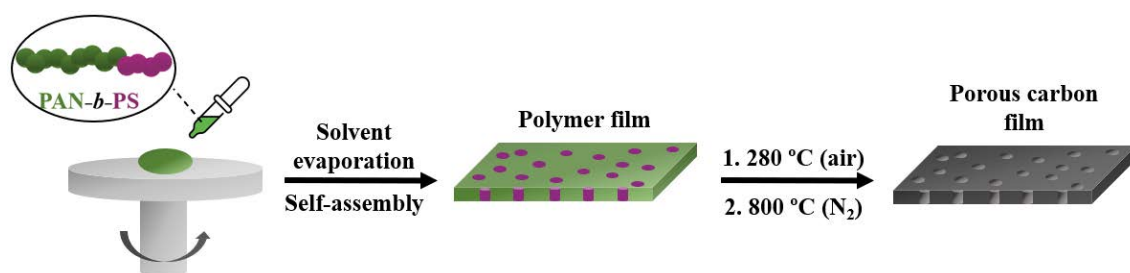


Figure 4.1. Preparation of porous carbon film derived from PS-*b*-PAN.

Therefore, to be a suitable carbon precursor, BCPs must contain a thermally degradable and immiscible sacrificial block, which will produce uniform domains in the PAN matrix. Furthermore, the decomposition temperature should not interfere with PAN thermal stabilization, to maintain the original microphase-separated morphology. According to PS-*b*-PAN thermal characterization showed in **Section 3.2.3 of Chapter 3**, PAN stabilization/cyclization and PS degradation are well separated process.

As shows **Figure 4.2a**, the block copolymer exhibited a microphase separation right after spin-coating, presenting a well-defined morphology consisting of nanoribbons with lengths between 50–80 nm and laterally separated by a few tens of nanometers. This nano-wired type of morphology has been detected in PS-containing block copolymers [115]. Due to the similar electron density of PS and PAN blocks, SEM was unable to detect the sacrificial block domains since there is no contrast between phases.

However, after subsequent thermal treatments, PAN block was stabilized and PS domains were thermally degraded, providing sufficient electron density contrast to clearly detect the morphology. After carbonization, a topography forming discrete pores on the PAN matrix was observed (**Figure 4.2b**). This image was captured using a T1 detector, to observe the surface details with a contrast in z ($A+B$), which allows to visualize the pores with higher quality. Due to the absence of phase contrast since PS and PAN blocks present similar electron density, the right after spin-coating film images were captured with a T2 detector in a topography mode. This detector allows to focus on the surface topography and morphology.

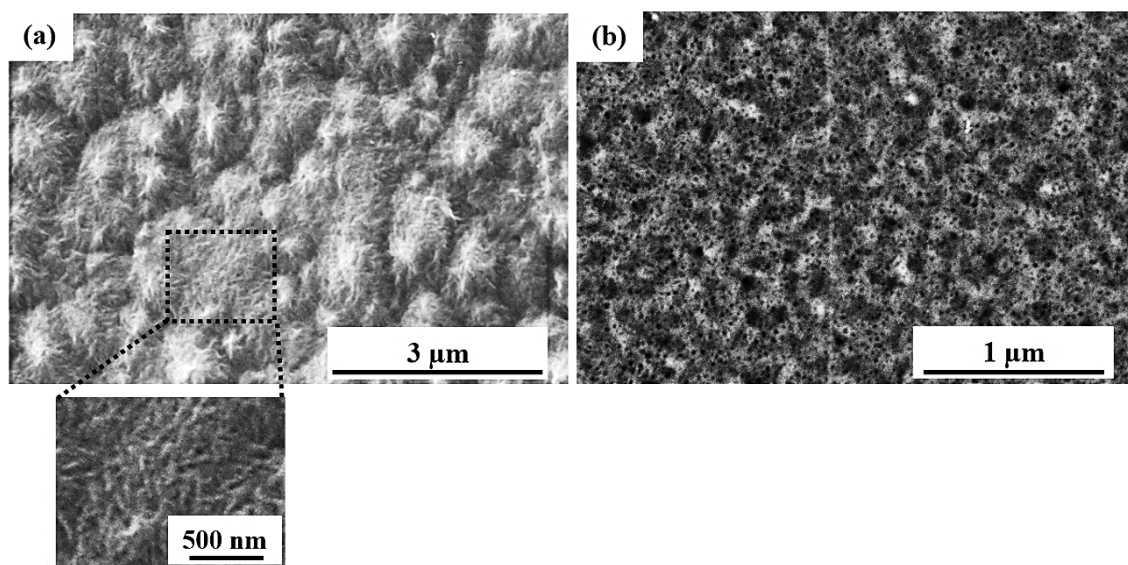


Figure 4.2. (a) PS-*b*-PAN film after spin coating and (b) carbon film after stabilization and subsequent carbonization.

Self-assembly of diblock copolymers into microphase-separated morphologies takes place during spin-coating process due to the high solubility parameter differences

between PS and PAN ($\Delta\delta = 11.56 \text{ cal cm}^{-3}$) in DMF [50], as well as the highly unfavorable Flory Huggins interaction parameter between AN and St monomers ($\chi = 0.829$) [116].

It should be noted that this block copolymer did not show an ordered domain morphology, typical of thermodynamic phase separation with similar compositions. Instead, disordered PS domains were observed. This behavior was expected since, from a kinetic point of view and due to the fast solvent evaporation, rapid phase separation occurred during spin-coating process (similar to electrospinning). Furthermore, Kowalewski et al. [117] observed that the phase diagram can be significantly modified for PAN-based copolymers. This is attributed to the influence of intramolecular dipole repulsion between neighboring pendant nitrile groups ($-\text{C}\equiv\text{N}-$), which forms irregular helical nanostructures. This tendency prevents the block copolymer from rearranging into ‘classical’ thermodynamic structures.

However, considering the phase-separation diagram of a diblock copolymer, and according to the low volume fraction of PS ($f = 0.16$), the film phase separation morphology should correspond with PS spherical domains in a PAN matrix. Although, it is closer to a transition into PS cylinders domains [118]. Therefore, both PS spherical/cylindrical phase domains could be present, outlines in **Figure 4.3**.

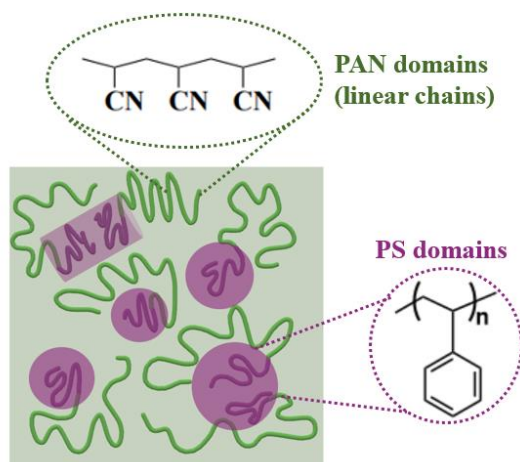


Figure 4.3. Scheme of the expected PAN and PS film phase-separation morphology.

On the other hand, and as previously mentioned, at around 280 °C under air atmosphere PAN block stabilizes through cyclization reactions of nitrile groups. This first

step is significantly important since it allows to “freeze” the microstructure before the carbonization.

Further heating until 800 °C under N₂ atmosphere, revealed a highly porous carbon film presenting mesopores with sizes ranging from 15–20 nm. Throughout the carbonization process, although the structure already generated during stabilization is retained, some increase in pore sizes may occur due to the large difference in the thermal expansion coefficient of PAN and PS; $1.4 \cdot 10^{-5} \text{ K}^{-1}$ and $4.1 \cdot 10^{-4} \text{ K}^{-1}$, respectively. These pore size variations may also be found due to the completion of PAN cyclization process and total PS degradation.

To study in depth the pore formation mechanism and pore structure generated through the thermal treatment of PS-*b*-PAN precursor, the morphology and structure of porous carbon powder (bulk) derived from the carbonization of PS-*b*-PAN was studied. With this aim, the polymer powder obtained right after the synthesis, without any additional processing, was thermally annealed at 280 °C under air atmosphere for 1 h and carbonized at 800 °C under N₂ atmosphere for 1 h, following the scheme represented in **Figure 4.4**. The resulting carbon powder was named as bulk.

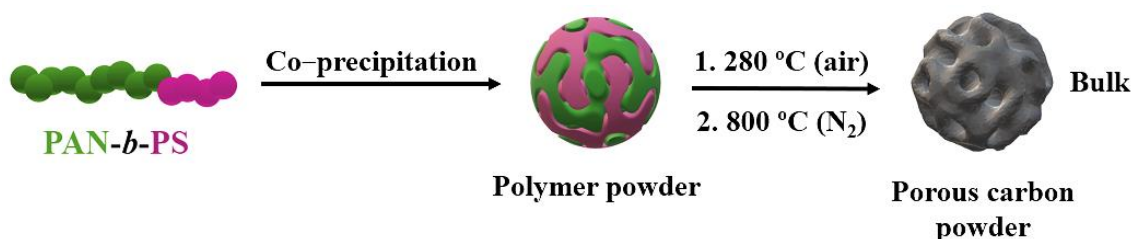


Figure 4.4. bulk material preparation scheme.

Figure 4.5. shows SEM and TEM images of bulk material after carbonization. Similar to the morphology found in the film, bulk carbon material does not self-assembled into any conventional block copolymer morphology. Instead, during the co-precipitation process with a non-solvent (methanol), as described in the synthetic procedure in **Section 3.2.1** of **Chapter 3**, disorder domains are formed.

The bulk material exhibited a continuous porous surface morphology, which can be detected not only in the surface but also along the internal material, suggesting certain

degree of pore interconnectivity. This type of disordered carbon structure presenting percolated pores has been seen in other PS-derived block copolymers [119].

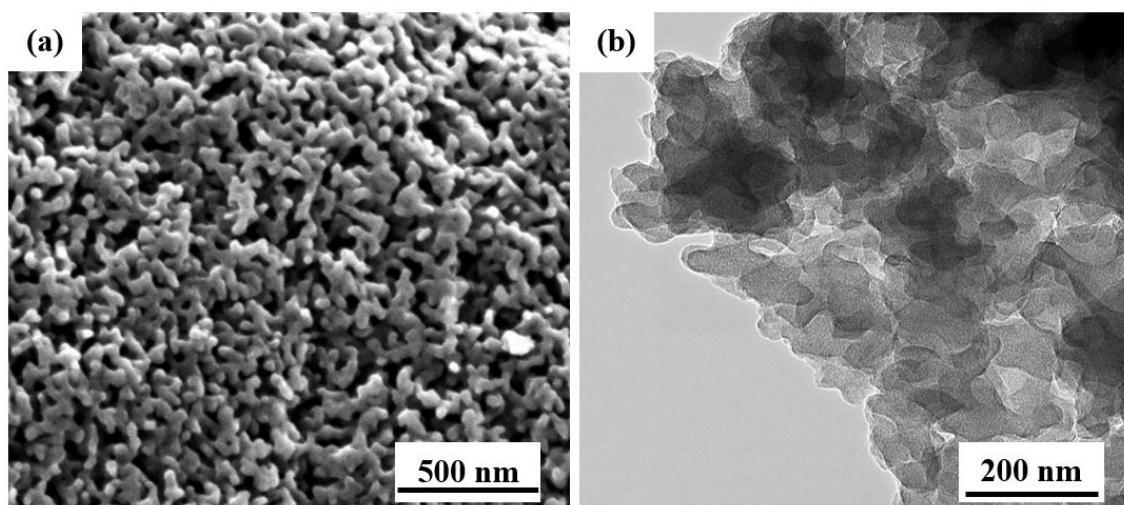


Figure 4.5. (a) SEM and (b) TEM images of bulk material after carbonization.

Additionally, N_2 physisorption was carried out to determine SSA_{BET} value and pore size distribution. Bulk material exhibited, according to IUPAC report [13], a type II isotherm (**Figure 4.6a**) characteristic of macroporous or non-porous materials, suggesting a low pore density material. The SSA_{BET} value measured was $242 \text{ m}^2 \text{ g}^{-1}$, with a micropore SSA value obtained with t-plot method of $93.9 \text{ m}^2 \text{ g}^{-1}$. Even though a low pore density is achieved, pore size distribution, shown in **Figure 4.6b**, exhibited several pore adsorption peaks in the meso- and micropore range, revealing a hierarchical pore structure. That structure has been reported to favor ion diffusion and thus, results in high capacitance electrode materials [120]. The morphology retention capacity after carbonization, together with the generated pore structure including micro- and mesopores (hierarchical porosity) exhibited in carbon film and bulk carbon material, justifies the use of PS-*b*-PAN as a suitable precursor to produce PCFs.

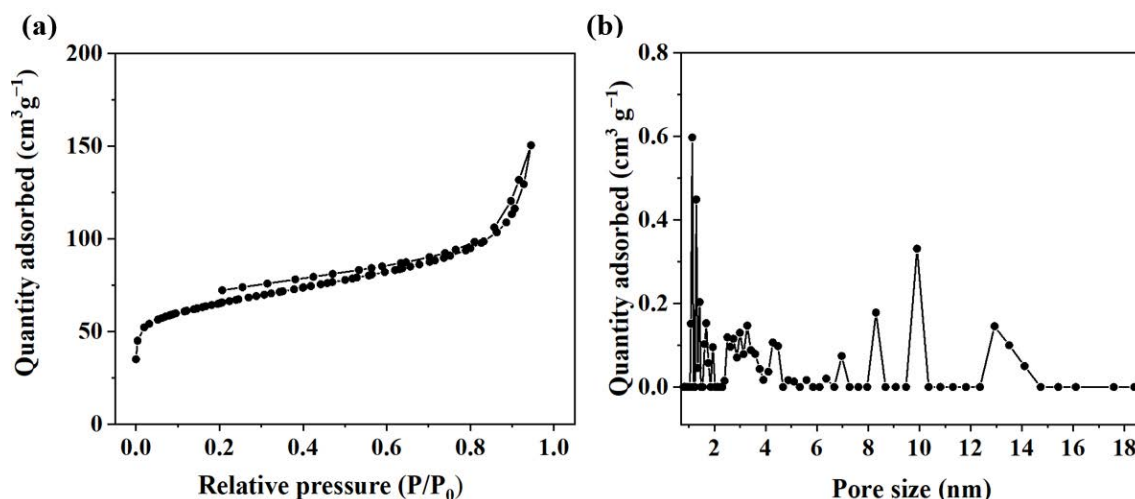


Figure 4.6. (a) N₂ adsorption/desorption isotherm and (b) pore size distribution of bulk carbon material.

4.2. PCFs derived from PS-*b*-PAN

Electrospinning is an efficient technique that uses the force of a voltage supply to produce fibers with nanosized diameters, large surface area to volume ratio, and high number of intra/inter fibrous pores, among others. Fibers obtained by electrospinning had been used for a wide range of applications, from biological and chemical sensors to part of flexible electronic devices [121,122]. Moreover, electrospinning allows to obtain nanofibers from very different precursors, such as polyacrylonitrile or lignin [123–126].

Particularly, the use of electrospinning has become in the last few years a powerful and versatile technique for obtaining nanofibers from block copolymer (BCP) solutions as fiber precursor [64]. After carbonization of the polymer mat, carbon porous fibers (PCFs) can be obtained. The use of BCPs as precursors allows the generation of microdomain rearranged fiber structures derived from the BCP self-assembly. The obtained self-assembled microstructure can be retained after carbonization producing uniform meso- and micropores throughout the fiber.

Multiple morphologies of the resulting phase separation can be generated during thermodynamic BCP self-assembly, including spheres, cylinders, or lamellas, among others [127]. However, due to fast solvent vaporization during electrospinning, less thermodynamic control is expected. Instead, disordered, and interconnected

morphologies via kinetic pathways are predictable. The use of BCPs as precursor to obtained PCFs offers numerous advantages, including low cost, relatively simple process, and high control over porosity.

Furthermore, PCFs represent an advanced and multifunctional material. PCFs possess a combination of properties such as high conductivity, high surface areas, and, very low densities, that make them ideal for their use in high efficiency electrochemical energy storage devices. In addition, using BCP as precursors allows to obtain hierarchical porous structures, improving access of electrolyte ion through the mesopores to the micropore active sites.

Pore size distribution represents a critical factor to obtain ion-accessible surfaces and fast ion diffusion kinetics, which strongly influence the electrochemical performance. In this work, a soft template method has been used for obtaining porous carbon fibers (PCFs) based on PAN-derived BCPs phase separation, using PS as a thermally degradable sacrificial block.

Polymeric fibers were prepared by electrospinning of PS-*b*-PAN as precursor dissolved in DMF, according to **Figure 4.7**.

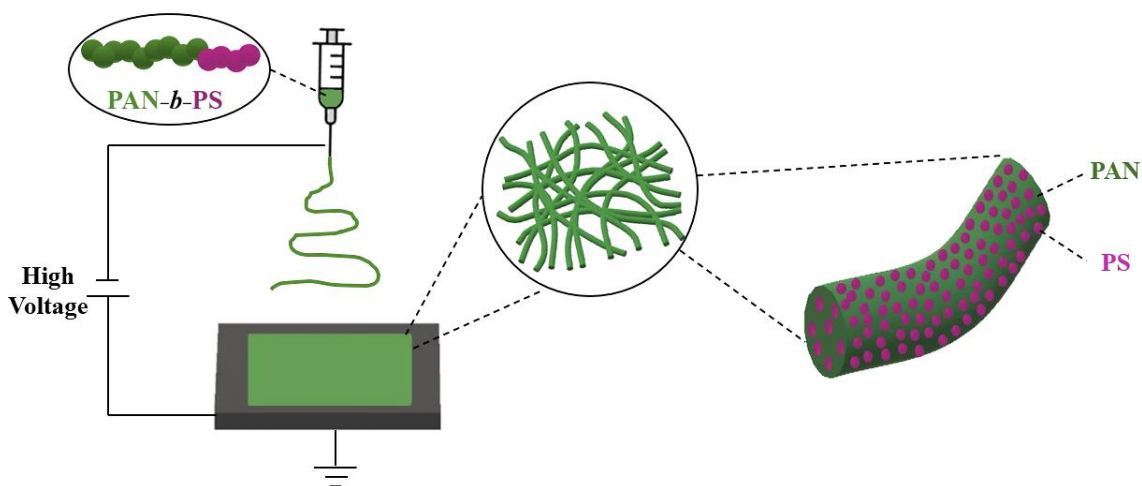


Figure 4.7. Scheme of the electrospinning process for obtaining nanofibers derived from PS-*b*-PAN.

4.2.1. Electrospinning optimization

As mentioned above, the use of BCPs as precursors to produce PCFs is a promising and remarkably new method. In 2019, Zhou et al. [64] published the first report on fibers produced from a PMMA-*b*-PAN block copolymer by electrospinning. The study focused on the design of a high electrical conductivity and fast-charging PCFs electrode. The reported PCFs present internal uniform mesopores, defined by block copolymer microphase separation, with a high surface area. It is worth noting that our work ‘Polyacrylonitrile-*b*-Polystyrene Block Copolymer-Derived Hierarchical Porous Carbon Materials for Supercapacitor’ reported for the first time the use of PS-*b*-PAN to produce fibers by electrospinning [105]. Therefore, electrospinning optimization was notably important.

As mentioned in **Section 2.2.2 of Chapter 2**, the main parameters affecting electrospinning are divided into three types, and variations of them can cause substantial fiber shape changes [128]:

- Parameters affecting the **solution**: viscosity, polymer molecular weight, solution concentration, surface tension, and conductivity.
- Parameters affecting the **process**: working voltage, feed rate, and distance between the tip and collector.
- **Ambient** parameters: temperature, pressure, and humidity.

For the selection of the starting work parameters, the reported parameters found in the bibliography based on electrospinning of PS/PAN blends were taken as a starting point (**Table 4.1**).

Table 4.1. Summarized parameter conditions for electrospinning of fibers obtained from PS/PAN blends compiled from literature.

Molecular weight (10³ g mol⁻¹)	wt% PS/PAN in DMF	Voltage (kV)	Feed rate (mL h⁻¹)	Working distance (cm)	Ref
PS; 150 PAN; 80	18	25	0.6–1.8	10	[129]
PS; 250 PAN; 150	15	14	1.0	17	[130]
PS; 350 PAN; 150	9–15	18–20	0.6	15	[131]
PS; 280 PAN; 150	10	15	0.5	15	[132]
PS; 35 PAN; 130	10	15	1.0	15	[133]

Considering a midpoint of the parameters collected in **Table 4.1**, the following parameters were initially selected: 0.5 mL h⁻¹ feed rate, 18 kV of working voltage, and 15 cm of distance between tip and collector.

Solution viscoelasticity, charge density carried by the jet, and solution surface tension are the main factors influencing the formation of beads in electrospinning. Beaded electrospun fibers usually appear when the solution concentration or polymer molecular weight are too low, among other influencing parameters. Those fibers can reduce specific surface area and affect fiber diameters and mechanical strength; therefore, electrospinning parameters are often optimized to remove beads from the fiber mat. These parameters were first evaluated and fitted to select our working conditions.

- Effect of solution concentration

Polymer concentration is the key and more critical electrospinning parameter to obtain homogenous fibers, since polymer solutions with a low concentration affect the surface tension, which leads to the formation of beads through the fiber. It was previously reported for PVP [134] and PMMA [135] electrospun fibers how an increase in polymer concentration leads to increased fiber formation against beading, considering a single molecular weight. In the same way, it was shown how low molecular weights (< 60,000 g mol⁻¹) only achieved the formation of bead–fiber morphology even if concentration

increased. To evaluate solution viscosity, concentration was varied between 10–25 wt% in DMF, while PS-*b*-PAN molecular weight was maintained ($\sim 118,710 \text{ g mol}^{-1}$).

It was confirmed that for low concentration, 10 wt% of PS-*b*-PAN in DMF, electrospun beads were mainly obtained (show in **Figure 4.8a**) since low viscosity affects the jet stability during electrospinning. Keeping the rest of the parameters constant, an increase in concentration between 10 and 18 wt%, led to the formation of beaded fibers with a progressive decrease in the bead number (**Figure 4.8b, c**). Polymer solution concentration between 20–25 wt% produces too viscous formula, causing dripping and solidification at the needle tip during the electrospinning process. Therefore, an increase up to 20 wt% was finally the most suited concentration, obtaining a more uniform fiber shape, even though some isolated beads still remain (not shown in **Figure 4.8**). **Figure 4.9** summarized the electrospinning optimization in terms of shape and beaded electrospun fibers for different concentrations of PS-*b*-PAN in DMF.

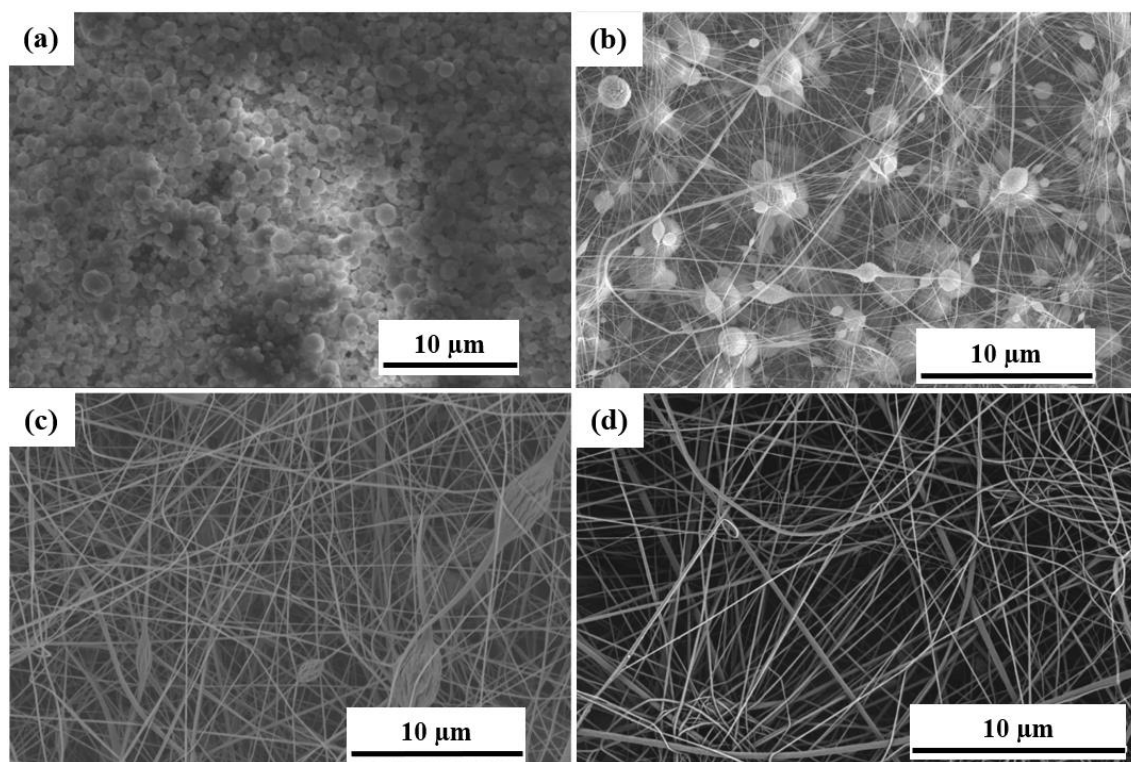


Figure 4.8. (a) Electrospray beads obtained from PS-*b*-PAN solution at 10 wt%, (b) beaded-fiber morphologies obtained from solution at 14 wt% and (c) 18 wt% and (d) Electrospun fibers obtained from solution at 20 wt%.

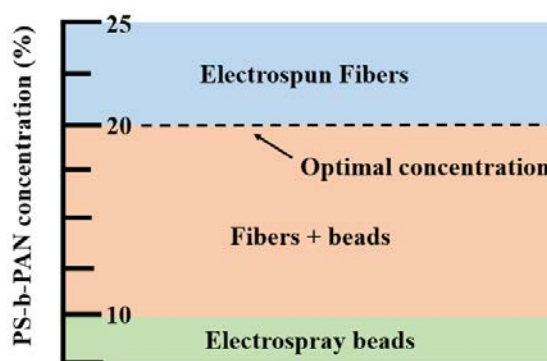


Figure 4.9. Scheme representing the three morphologies obtained through varying solution concentration.

- Effect of working potential

Electrospun fiber formation occurs only when the applied voltage surpasses the threshold voltage (about $\sim 1 \text{ kV cm}^{-1}$). An increase in the applied electric voltage involves an increase of the polymer solution electrostatic force and stretching of the jet. It was observed for PVA fibers that an increase in applied voltage leads to changes in fiber shape and to obtain larger fiber diameters [136]. Throughout the optimization process, some tests were carried out to verify the influence of voltage on the fiber shape, since it was intended to obtain larger fiber diameters in addition to the bead removal. Electrospinning was carried out varying the working voltage from 18 to 22 kV. As shown in **Figure 4.10**, unnoticeable shape changes were detected with an increase in applied voltage. In all cases the same diameter distribution was maintained. As a result, for practical reasons the applied voltage was fixed at 18 kV.

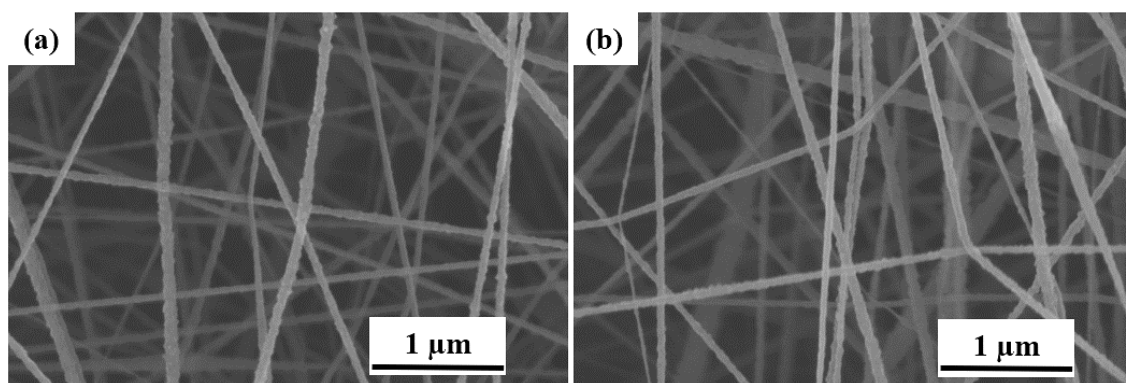


Figure 4.10. SEM images of the electrospun fibers with applied voltage of (a) 18 kV and (b) 22 kV.

- Effect of feed rate

Feed rate variations were tested to accelerate fiber production. The feeding rate increased from 0.5 to 2.0 mL h⁻¹. As observed, no substantial changes were detected on fiber morphology by increasing feed rate, showing similar diameters in all tested samples (**Figure 4.11**). For higher feed rates (2 mL h⁻¹) solution dripping was observed along the electrospinning process, so the optimal feed rate was fixed at 1.5 mL h⁻¹.

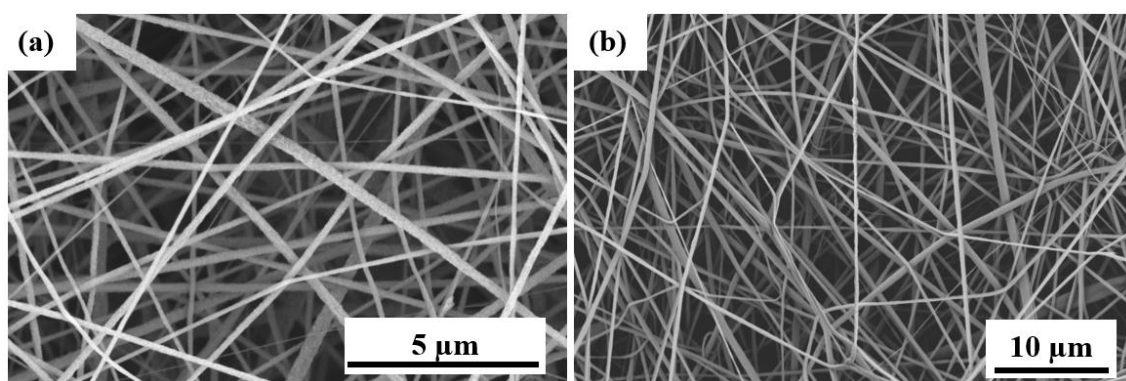


Figure 4.11. SEM images of the electrospun fibers obtained with a feed rate of (a) 0.5 mL h⁻¹ and (b) 1.5 mL h⁻¹.

After optimization, the most suited electrospinning parameters and conditions were the following ones (**Table 4.2**):

Table 4.2. Summary of the electrospinning parameters.

Solvent	Concentration (wt%)	Voltage (kV)	Feed rate (mL h ⁻¹)	T (°C)	Working distance (cm)	RH (%)
DMF	20	18	1.5	20–25	15	~ 40

Note that ambient parameters were not considered as a part of the optimization process, maintaining constant with operating temperatures between 20–25 °C under ~ 40 % RH humidity.

4.2.2. PS–PCFs: Morphological and structural characterization

The electrospun fiber microstructure was characterized by scanning electron microscopy (SEM). Fibers were sputtered applying an ultra-thin coating of Au layer. SEM images (**Figure 4.12a**) show an entangled fiber mat with relatively homogenous

diameters, presenting an average value of 107 ± 4 nm. Size distribution is represented in **Figure 4.12c** (distributions were calculated using a logarithmic function). Nanofibers showed rough surfaces (see **Figure 4.12b**) due to fast evaporation and deformation during electrospinning process. As it was predicted, this rapid evaporation prevents the block copolymer from self-assembling into any classical thermodynamic morphologies [56], forming disorder microphase-separated structures instead.

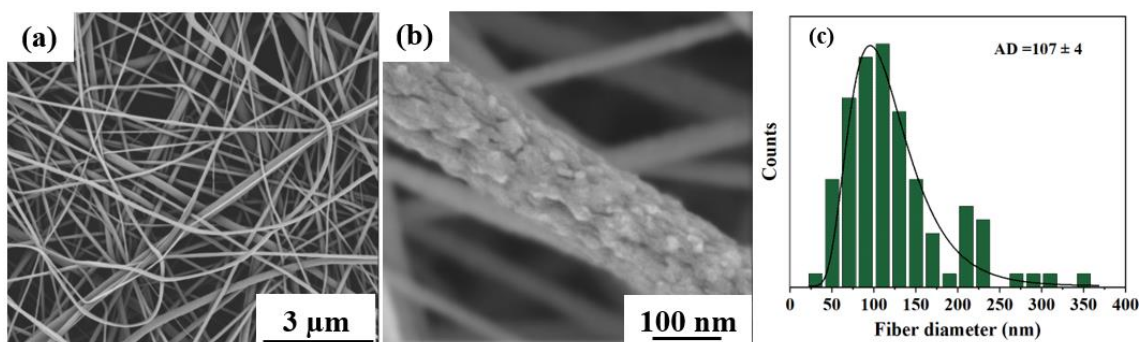


Figure 4.12. (a) PS-*b*-PAN fiber mat, (b) fiber surface and (c) fiber diameter distribution.

The electrospun PS-*b*-PAN fiber mat was sequentially carbonized in a two-step thermal treatment: First stage at 280 °C stabilizes the structure through oxidation and cyclization of PAN block. A second stage at 800 °C leads to complete carbonization, where first PS thermal decomposition takes place. The following scheme represents the process (**Figure 4.13**). Porous carbon fibers derived from PS-*b*-PAN were named as PS-PCFs.

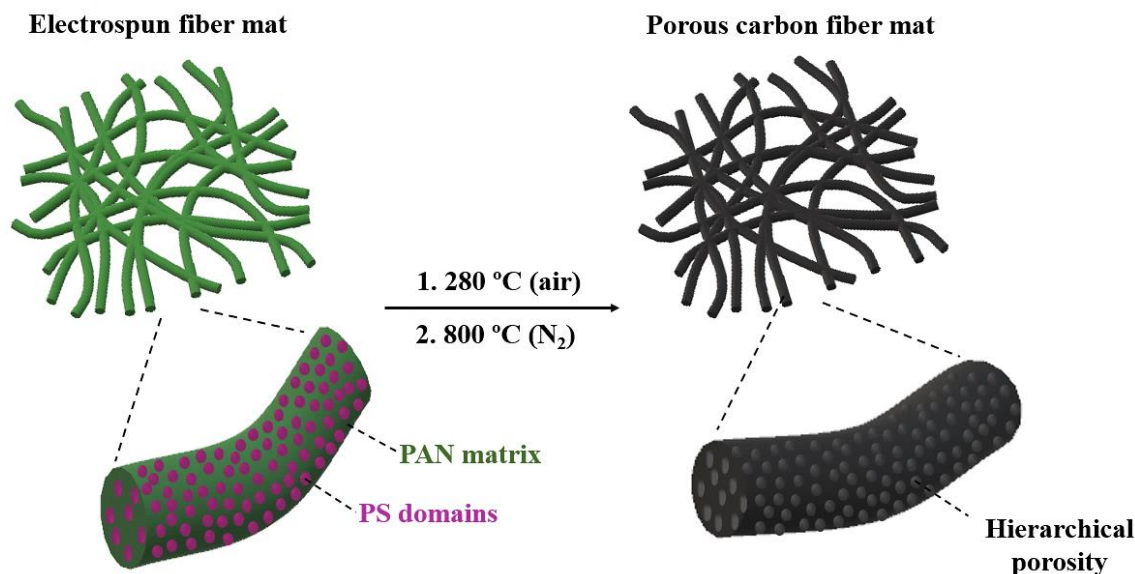


Figure 4.13. Scheme of the obtention of PCFs from PS-*b*-PAN-derived fibers (PS-PCFs).

PS-PCFs microstructure was characterized by scanning electron microscopy (SEM) and transmission electron microscopy (TEM) as shown in **Figure 4.14** and **4.15**, respectively. After carbonization, fibers maintain their shape, presenting an average diameter of 105 ± 5 nm (**Figure 4.14b**). The diameters showed a slight decrease in reference to the 107 ± 4 nm average diameter of as-spun nanofibers. Fibers exhibit abundant mesopores along the surface and cross section, with an average pore size of 9.5 ± 2 nm (**Figure 4.15d**). Although, it should be noted that due to the low-resolution of high-magnification SEM images, it is not possible to confirm if surface and interior mesopores are interconnected. Covering with a thin layer of iridium has demonstrated to increase conductivity of the PS-PCFs samples, detecting around 10 nm pore sizes with high resolution [58]. Anyway, regarding the morphology obtained in bulk material (see **Section 4.1**), it may be possible to assume that interior pores are not closed and present a certain degree of interconnectivity.

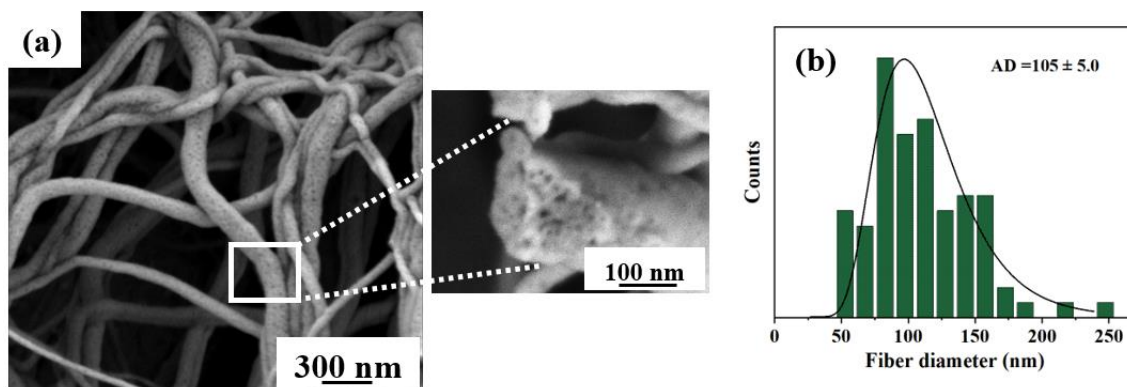


Figure 4.14. (a) SEM image of fiber mat after carbonization with cross section of a single carbon fiber and (b) PCFs diameter distribution.

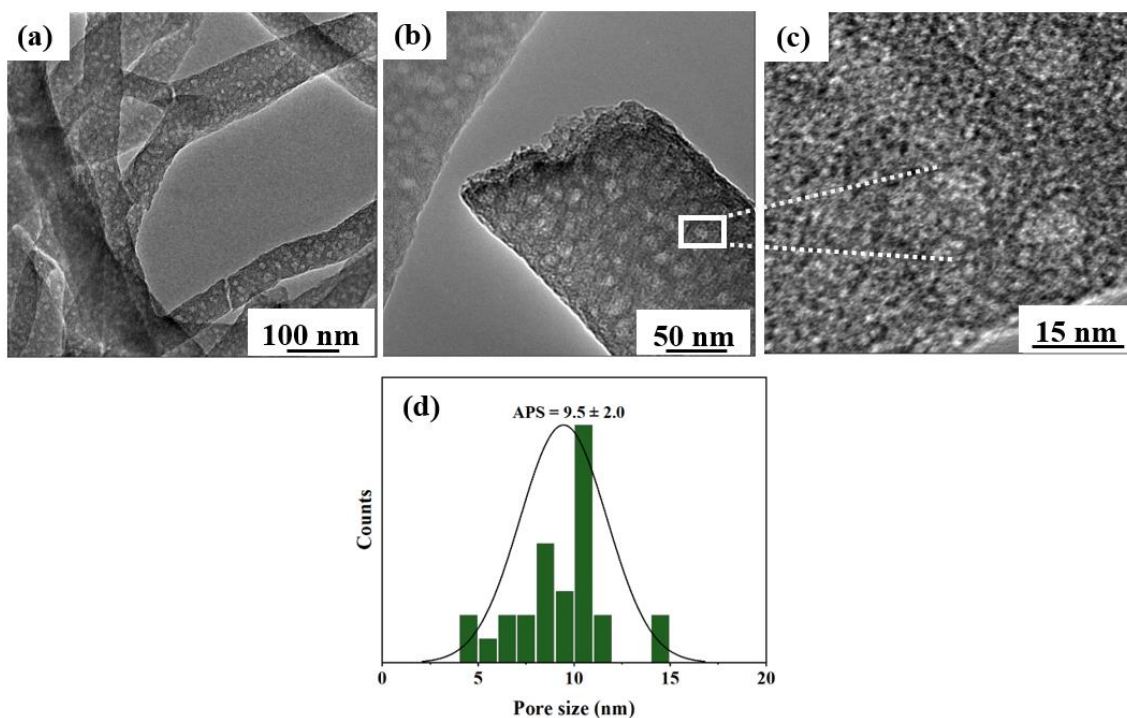


Figure 4.15. (a), (b) and (c) PS-PCFs TEM images, and (d) pore size distribution.

Raman spectroscopy provides information about ordered and disordered carbon structures. In **Figure 4.16a**, mesoporous fiber Raman spectra shows the characteristic bands of graphitic features (“G band”) at 1334.9 cm^{-1} and disordered structures (“D band”) at 1583.6 cm^{-1} . G band corresponds to phonons propagating along the graphene sheets and is related to nanocrystalline graphite. The D band is consistent to disorder features in the graphite. Therefore, the intensity ratio of D and G bands (I_D/I_G) is indicative of the amorphous or graphitic character of the carbon material [90,137]. PS-PCFs

presented a value of 1.11, showing a preferentially disorder carbon structure with moderate degree of graphitization. This is confirmed with the XRD pattern (**Figure 4.16b**), which showed a broad peak around 25° assigned to (002), typically related to pyrolytic or graphitic carbon structures [138]. The low intensity suggests a predominantly amorphous carbon structure, presenting a low concentration of ordered graphitic planes, which can be a beneficial feature since higher graphitization degrees are related to lower micropore and heteroatom content [139]. This is due to the decrease in the number of defects in the carbon structures and consequent collapse of the micropores.

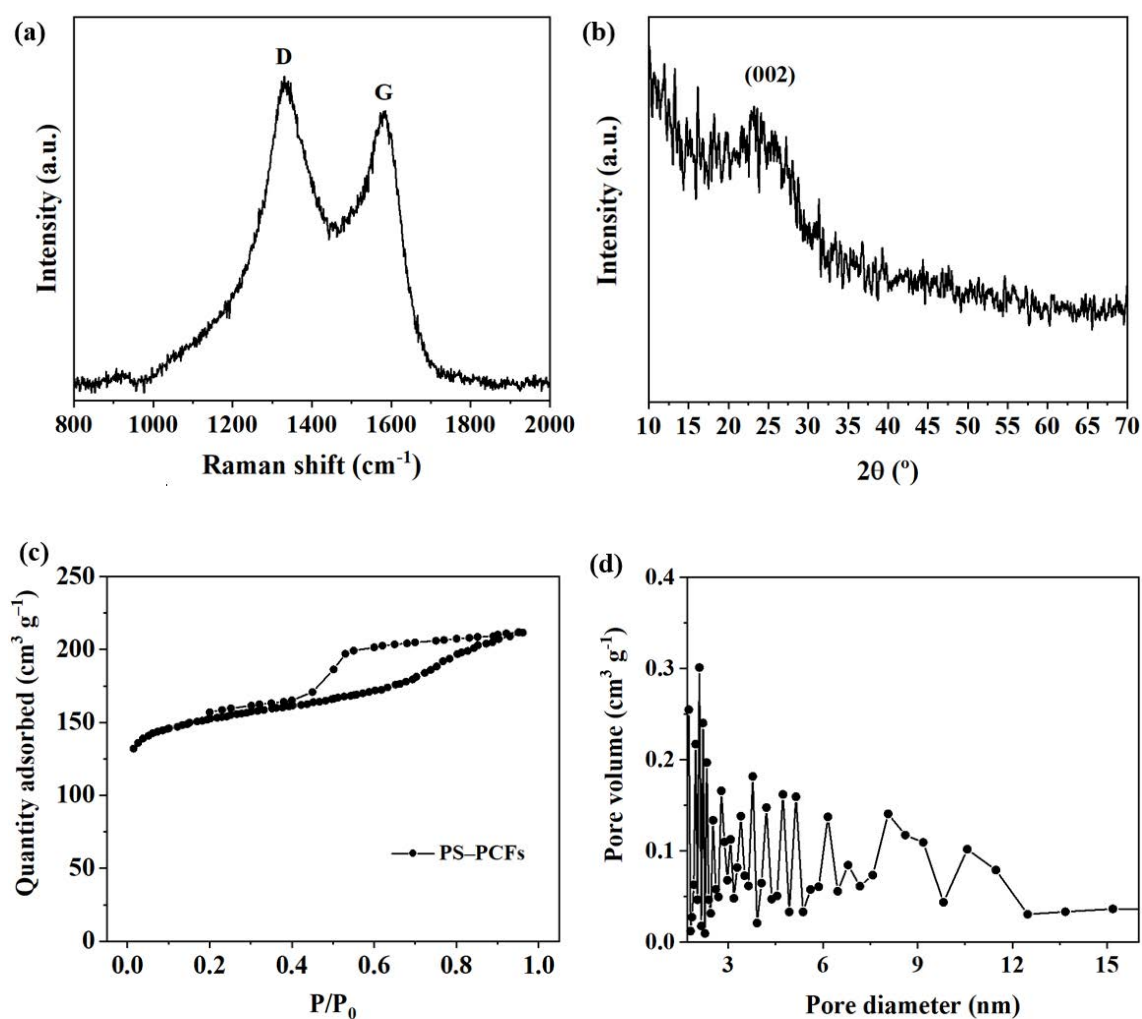


Figure 4.16. (a) Raman spectra, (b) XRD pattern, (c) N_2 adsorption/desorption isotherm, and (d) BJH pore size distribution of PS-PCFs.

To further examined the overall mesopore structure observed by TEM (**Figure 4.15**) and determined specific surface area and pore size distribution, N_2 adsorption/desorption analysis was conducted. PS-PCFs exhibited an isotherm with a

large hysteresis loop, which according to IUPAC [13] indicates the presence of mesopores (2–50 nm) (**Figure 4.16c**). The hysteresis loop can be classified as a combination of type H1 and type H2 (see scheme in **Figure 4.17**). In the first type, cylindrical type pores can be found. In the second one, the pore presented in the carbon network is ink–bottle type preferentially. In the last case, desorption depends on the neck size and pore interconnectivity and its beginning is associated with the percolation threshold and the formation of a continuous group of pores opened to the surface. Since gas physisorption is only able to determine the volume adsorbed in open pores, closed pores cannot be accessible by this technique [140]. Moreover, this type of H2 hysteresis loop starting at a relative pressure of 0.45 is associated with a cavitation type of desorption mechanism [141]. **Figure 4.17** shows the pore structure expected for PS–PCFs according to isotherm information. The BET specific surface area reached a moderately high value of $495.7 \text{ m}^2 \text{ g}^{-1}$, with a high surface area of micropores ($366.1 \text{ m}^2 \text{ g}^{-1}$) as revealed by the t–plot analysis. The BJH pore size distribution of the adsorption branch (**Figure 4.16d**) showed multiple peaks, predominantly micro–/mesopores in the range between 1.7–15 nm. Therefore, PCFs shown hierarchical pore structure, comprising micro–/meso– and inter–fiber macropores. This type of porosity has been demonstrated to improve ion pathways that reduce distances from the electrolyte to the micropores active sites [30].

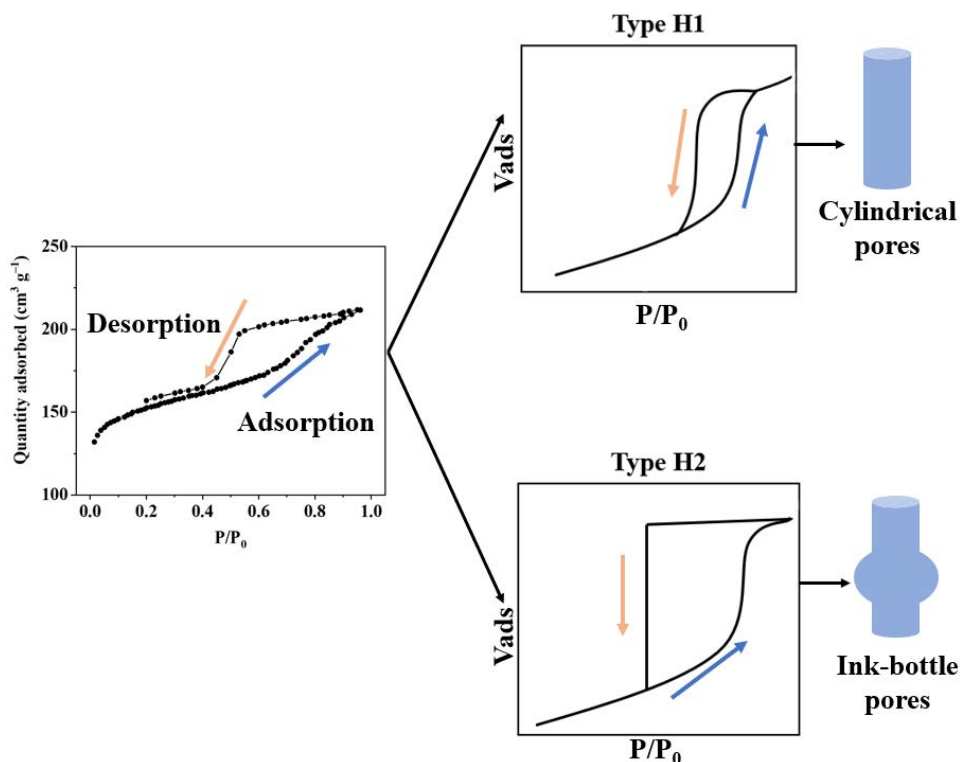


Figure 4.17. Scheme of the pore structure-type expected for PS-PCFs.

The surface element composition was determined using X-ray photoelectron spectroscopy (XPS). The PS-PCFs XPS survey spectrum shown in **Figure 4.18a** displays peaks corresponding with C 1s, N 1s, and O 1s. The N 1s spectrum (**Figure 4.18b**) was deconvoluted into four peaks corresponded to pyridinic nitrogen (N-6) at 398.2 eV, pyrrolic and amide nitrogen at 399.9 eV (N-5 and O=C-N), graphitic or quaternary nitrogen (N-Q) at 400.9 eV, and oxidized pyridinic nitrogen (N-O) at 403.3 eV according to literature [142,143]. The O 1s spectrum (**Figure 4.18c**) can be deconvoluted as well into four different peaks corresponding to quinone type groups (C=O; O-I) at 530.6 eV, phenol and/or ether groups (C-OH and/or C-O-C; O-II) at 532.5 eV, ester and/or carboxylic groups (O-C=O and/or COOH; O-III) at 534 eV, and chemisorbed water or amide groups (O=C-N; O-IV) at 535.5 eV [144,145].

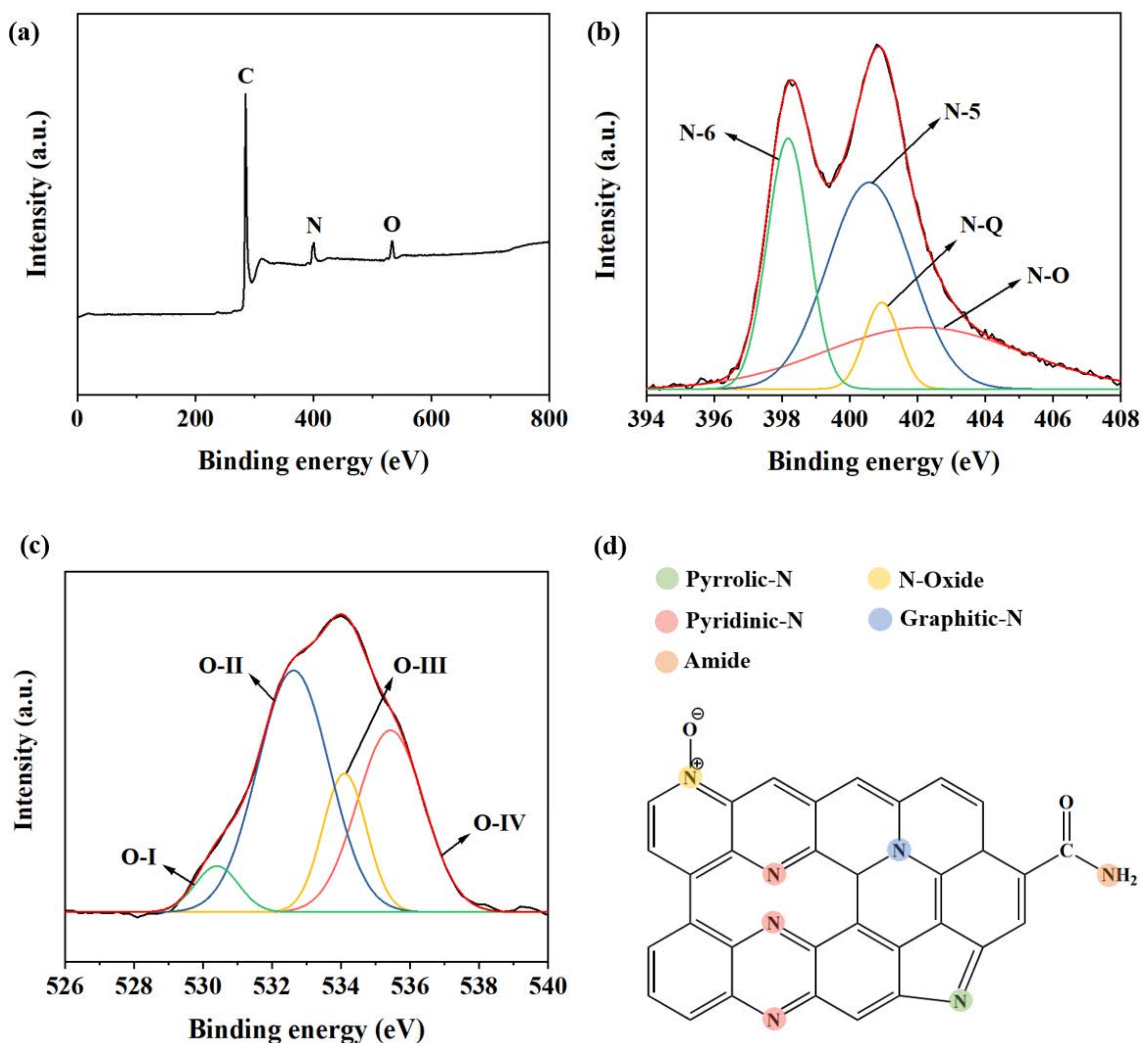


Figure 4.18. (a) XPS survey spectrum of PS-PCFs, (b) and (c) display the deconvoluted high-resolution spectra of N 1s and O 1s, respectively, and (d) shows the different types of N-containing functionalities.

PS-PCFs nitrogen atoms are intrinsically present in the PAN block, while oxygen atoms were introduced along the stabilization thermal treatment under air atmosphere. The relative surface concentrations of N and O heteroatoms, as well as the different functional groups concentrations were collected in **Table 4.3**, showing a reasonably N/O-rich carbon material. N peak deconvolution centered at 398.2 and 399.9 eV revealed a high relative content of pyridinic and pyrrolic nitrogen atoms (24.3 and 40.4 %, respectively). It has been reported that these N-derived functional groups actively participate in electrochemical activity [146], increasing surface redox reactions, and thus introducing pseudocapacitance, which contributes to obtain higher energy densities.

Table 4.3. Relative atomic composition, and nitrogen and oxygen species content obtained by fitting N 1s and O 1s high-resolution XPS spectra of PS-PCFs.

Heteroatom functional group	Content (%); (binding energy (eV))	N/O (%)
N-6	24.3; (398.2)	7.8
N-5	40.4; (400.6)	
N-Q	7.0; (400.9)	
N-O	28.3; (398.2)	
O-I	5.3; (530.4)	4.5
O-II	46.2; (532.6)	
O-III	16.2; (534.1)	
O-IV	32.3; (535.4)	

Furthermore, it is well known that the presence of basic heteroatoms in the carbon network enhances ion diffusion and electrolyte wettability [147]. The wettability of the fiber mat was studied by contact angle measurement, before and after carbonization. A KOH (6M) solution was used, since it is the electrolyte selected for the electrochemical measurements. **Figure 4.19** shows the images of the droplet on the fiber mat surface. Clearly, a large contact angle was observed on the fiber mat prior to carbonization, while the droplet rapidly spread on carbonized fiber surface, resulting in an increase of the wetting capability, and therefore increasing hydrophilic behavior. This high KOH solution wettability may result in an improvement of available surface for ion diffusion.

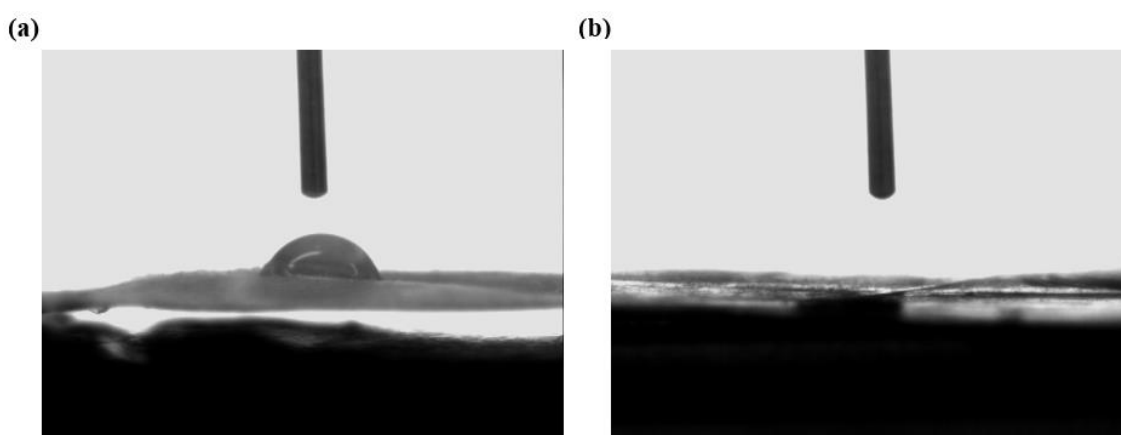


Figure 4.19. Image of KOH solution drops on the fiber mat surface (a) before and (b) after carbonization.

4.2.3. HN_PS-PCFs: Morphological and structural characterization

The produced PS-PCFs from PS-*b*-PAN as precursor showed a highly porous structure with a considerably high carbon yield (~ 50 %) due to the low volume fraction of PS sacrificial block ($f_{PS} = 0.16$). The idea of increasing the degree of polymerization ($N_{tot} = N_{PS} + N_{PAN}$) of the PS-*b*-PAN copolymer precursor while maintaining a low volume fraction of PS sacrificial block, has been proposed. This approach aims to achieve larger fiber diameters, while preserving high porosity and carbon yield. As it was previously mentioned, increasing molecular weight leads to larger fiber diameters [148]. It has been observed that increasing the molecular weight of the copolymer precursor results in larger fiber diameters, as mentioned earlier. Moreover, varying N values in PAN-based block copolymers while maintaining similar block compositions, has revealed to be an effective method for modulating the pore volume and specific surface area of the resulting porous carbon materials [57].

It is well established that the phase diagram of an A-B diblock copolymer is mainly affected by intrinsic parameters, such as interaction parameter (χ), number of statistical segments per chain or total degree of polymerization (N) and volume fraction (f) [55,149,150]. At a given temperature, these parameters determine the type of morphologies generated during self-assembly, and therefore directly influence the porous microstructure. A study comparing two PS-*b*-PAN block copolymers with different molecular weights has been carried out, focused on the effect of molecular weight on the microphase separation, and consequent carbon fiber structure and morphology. A schematic illustration is presented in **Figure 4.20**. Fiber precursor with lower N and higher N corresponded with St₁₆₂-*b*-AN₁₉₀₈ and St₂₉₁-*b*-AN₄₅₀₇, respectively. Carbon fibers obtained from PS-*b*-PAN with higher degree of polymerization (N) were named as HN_PS-PCFs.

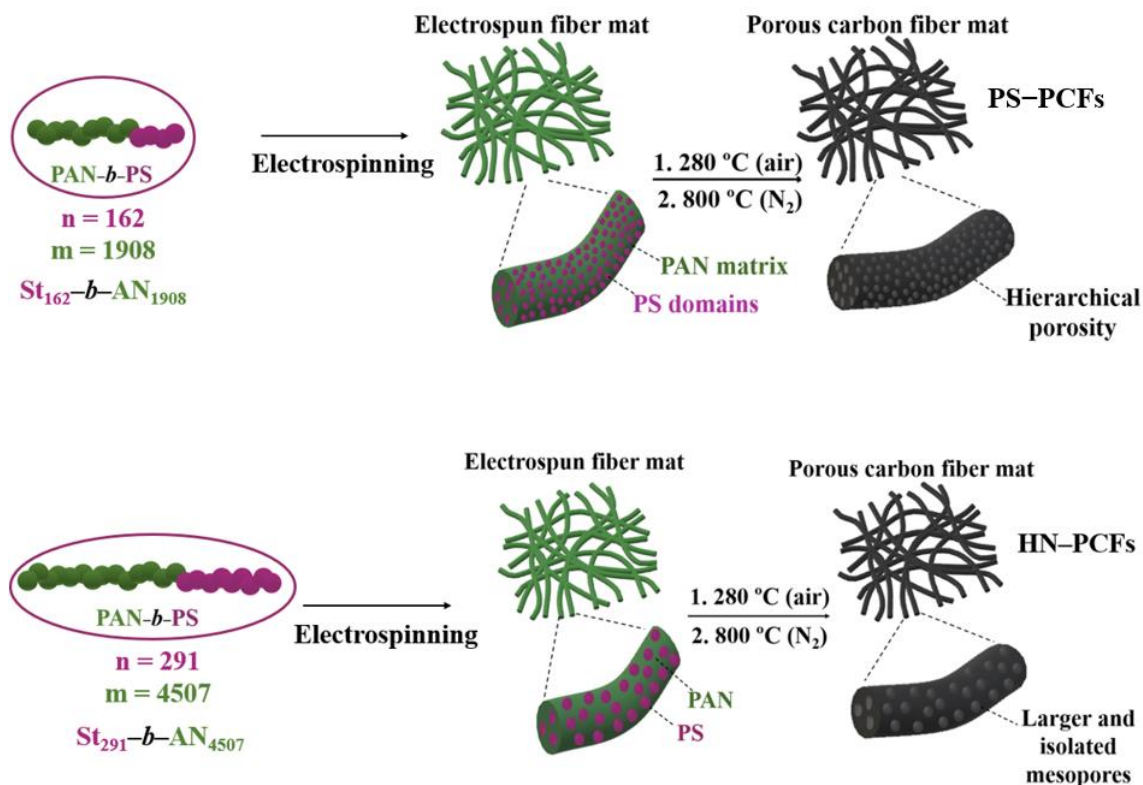


Figure 4.20 Schematic illustration of the representative morphology of lowest N (above) and highest N (below): PS-PCFs and HN-PCFs, respectively.

As explained above, PS- b -PAN does not self-assemble into any classical morphology, due to the fast solvent evaporation during electrospinning, as well as the influence of intramolecular dipole repulsion between neighboring pendant nitrile groups ($-\text{C}\equiv\text{N}-$) of PAN block, resulting in the formation of irregular helical nanostructures that avoid rearrangement into thermodynamic structures. However, size of the disorder domains, as mentioned earlier, is mainly affected by the volume fraction of the sacrificial PS block (f_{PS}) and the product of the Flory-Huggins interaction parameter and the degree of polymerization of the PAN block (χN).

The copolymer $\text{St}_{291}\text{-}b\text{-AN}_{4507}$ was synthesized and characterized as described in **Section 3.2.4 of Chapter 3**. This BCP exhibited a slightly lower PS volume fraction ($f_{\text{PS}} = 0.11$) than that obtained in $\text{St}_{162}\text{-}b\text{-AN}_{1908}$ ($f_{\text{PS}} = 0.16$) but closed enough to minimize or reduce its contribution to the phase separation morphology, since the difference between N values is substantially great. Total N can be easily calculated by adding the respective degree of polymerization of both blocks ($N = N_{\text{PS}} + N_{\text{PAN}}$). $\text{St}_{291}\text{-}b\text{-AN}_{4507}$ and $\text{St}_{162}\text{-}b\text{-AN}_{1908}$ showed N values of 4798 and 2070, respectively.

Moreover, without considering the contribution of the molecular weight in the interaction parameter, we can assume that both copolymers ($\text{St}_{291}\text{-}b\text{-AN}_{4507}$ and $\text{St}_{162}\text{-}b\text{-AN}_{1908}$) have the same polymer–polymer interaction parameter ($\chi_{\text{PS-PAN}} = 0.3$). Considering that polymers with very large N values show hindered chain mobility after T_g , it is expected to find less disperse PS domains in the highest N value BCP ($\text{St}_{291}\text{-}b\text{-AN}_{4507}$), and thus fewer or more isolated pores in the resulting PCFs (**Figure 4.21**).

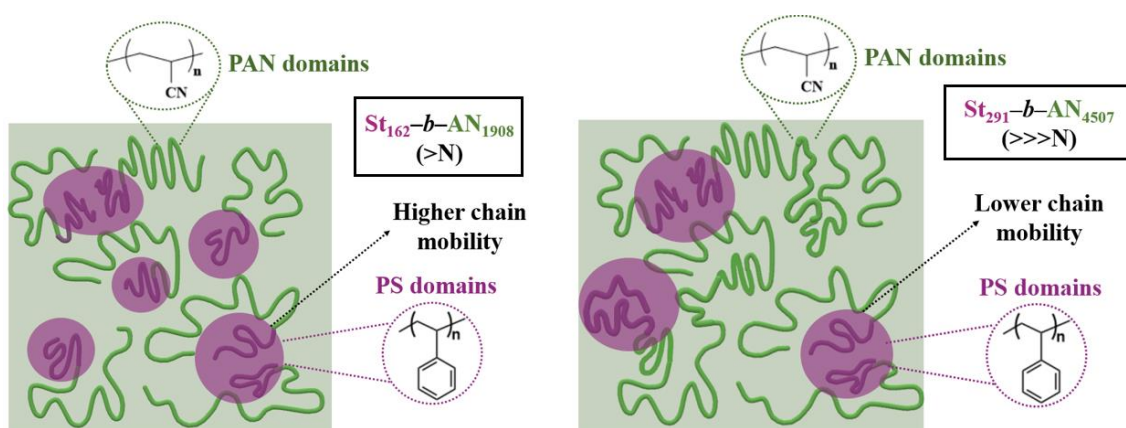


Figure 4.21. Expected phase-separation behavior of $\text{St}_{291}\text{-}b\text{-AN}_{4507}$ and $\text{St}_{162}\text{-}b\text{-AN}_{1908}$ showing PAN and PS domains according to the predicted chain mobility.

The electrospinning parameters used to obtain BCP-derived fibers with the highest N value ($\text{St}_{291}\text{-}b\text{-AN}_{4507}$) were the same as those used for the BCP-derived fibers with the lowest N value, see **Table 4.2** in **Section 4.2**. Prior to electrospinning, block copolymer solutions were stirred at 50 °C for 24 h to ensure complete dissolution.

Right after electrospinning, the fiber mat was examined by SEM, showing fibers along with the presence of some isolated beads as showed in **Figure 4.22a**. However, diameters appeared moderately homogenous. Diameter distribution is centered at 118 ± 5 nm, which is substantially larger than those fibers obtained from a BCP with lower N (107 ± 5 nm). This agrees with previous homopolymer studies, in which increasing molecular weight leads to an increment in fiber diameters [151]. Regarding the identification of phases in the fiber morphology, SEM images do not show the rough surface seen for $\text{St}_{162}\text{-}b\text{-AN}_{1908}$ copolymer (see **Figure 4.12**) which may be due to the acquisition mode. However, after oxidation and carbonization, TEM images clearly revealed a microstructure with abundant mesopores along the fiber length.

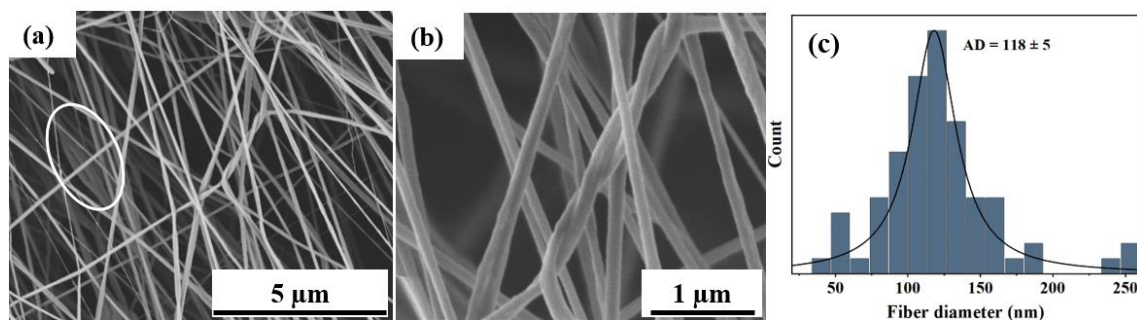


Figure 4.22. (a) $\text{St}_{291}\text{-}b\text{-AN}_{4507}$ -derived fiber mat, (b) fiber surface, and (c) fiber diameter distribution.

$\text{St}_{291}\text{-}b\text{-AN}_{4507}$ -derived fiber mat was thermally annealed at 280 °C for 1 h under oxidizing atmosphere and carbonized at 800 °C for 1 h under N_2 flow. The resulting HN_PS-PCFs were analyzed by TEM. TEM images shown in **Figure 4.23**, exhibited mesopore size significantly larger and more isolated pores, centered at around 14.0 ± 3 nm, than those in PS-PCFs (mesopore size ~ 9.5 nm). This corroborates that higher degree of polymerization produces fewer and isolated PS domains in the PAN arrays.

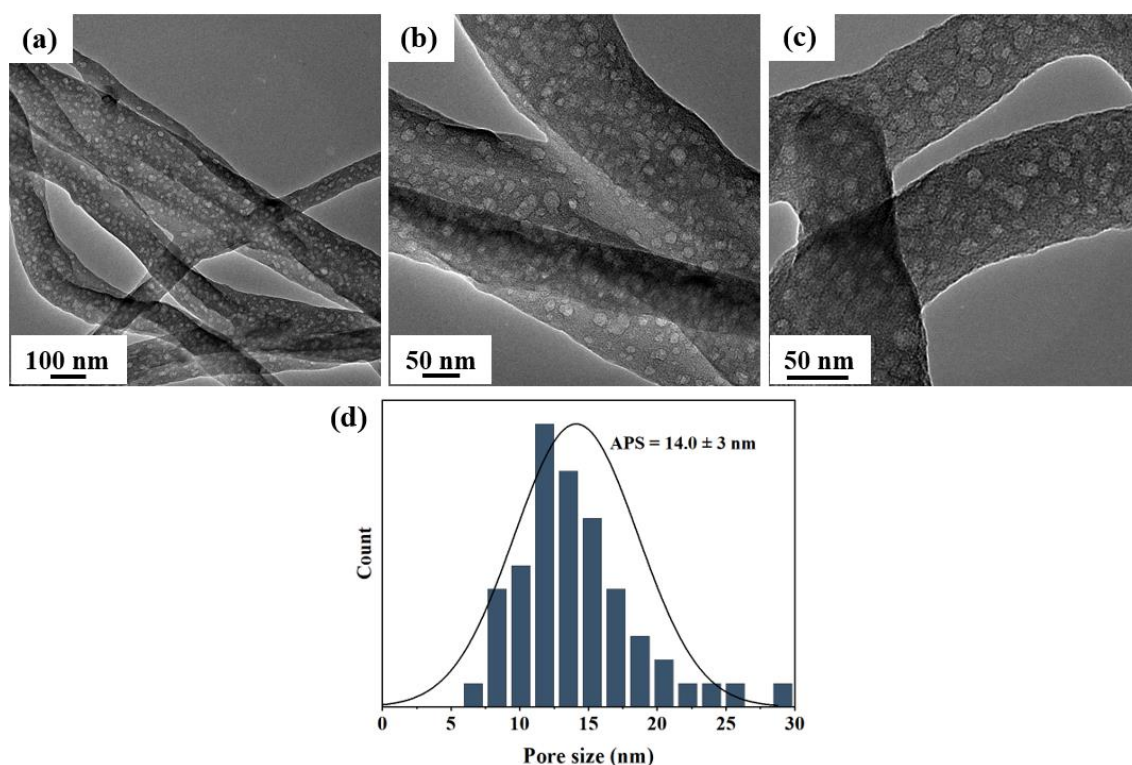


Figure 4.23. (a), (b) and (c) TEM images of mesoporous HN_PS-PCFs and (d) pore size distribution.

Raman spectroscopy (**Figure 4.24a**) was analyzed to further elucidate the carbon structure and compare the influence of using BCPs with higher and lower N as precursor. Both materials, HN_PS-PCFs and PS-PCFs, displayed the distinctive bands related to graphitic (“G band”) between $\sim 1560\text{--}1600\text{ cm}^{-1}$ and disordered features (“D band”) between $\sim 1320\text{--}1350\text{ cm}^{-1}$. As it was determined in previous section, intensity ratio between D and G bands (I_D/I_G) presented a value of 1.11 for PS-PCFs, demonstrating a preferentially disorder carbon structure. This ratio is significantly reduced for HN_PS-PCFs, exhibiting a value of 0.86. Therefore, HN_PS-PCFs fibers apparently showed a higher degree of graphitization. This outcome may be attributed to the formation of more isolated PS domains, which results in larger PAN domains size. Upon carbonization, the increased size of PAN domains contributes to a greater number of graphitic layers in the final material.

The XRD pattern (**Figure 4.24b**) of both carbon fiber materials showed the characteristic broad peak around 25° assigned to (002), commonly observed in pyrolytic or graphitic carbon structures [93]. The XRD pattern of HN_PS-PCFs does not show any significant shift in the (002) peak compared to PS-PCFs, indicating that there are no important changes in the order of the graphitic planes.

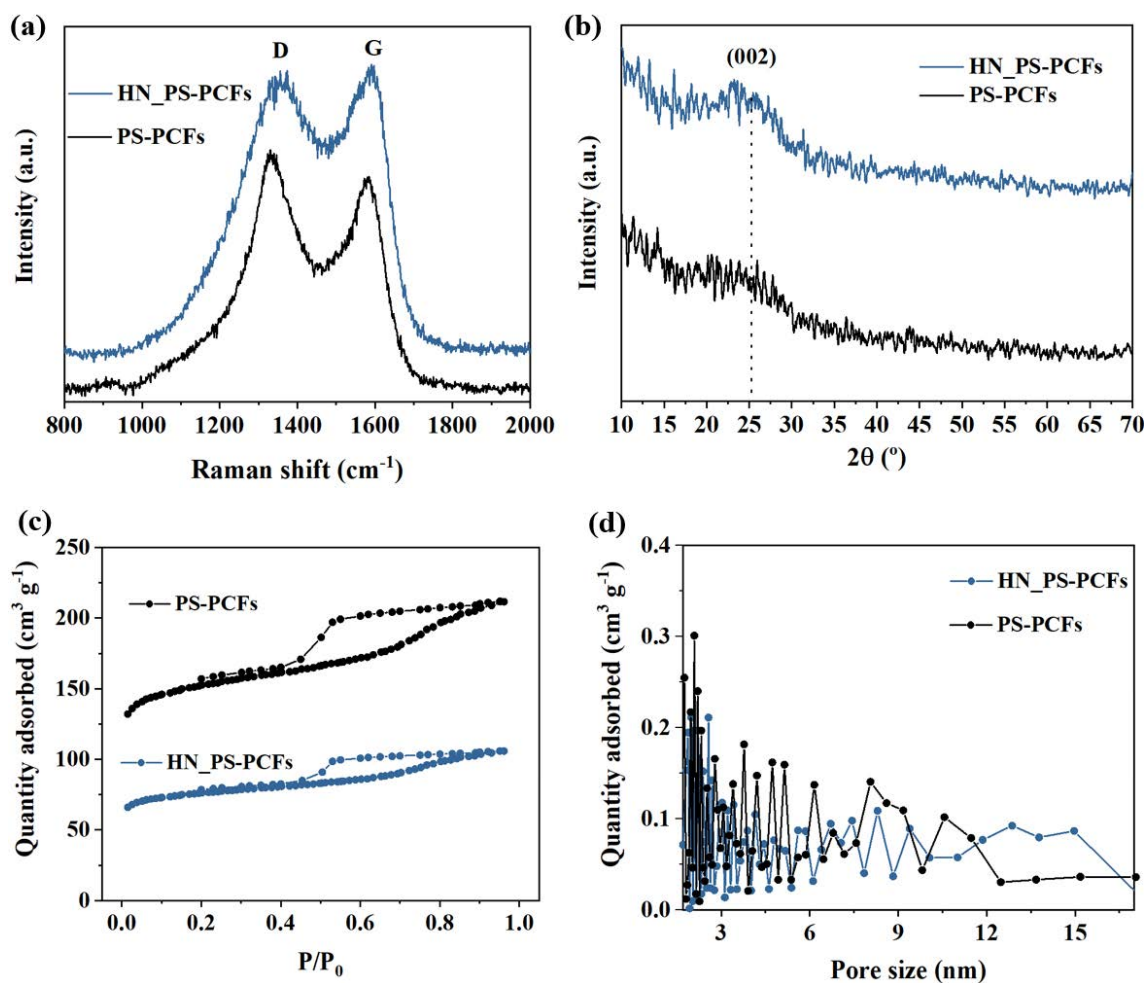


Figure 4.24. (a) Raman spectra, (b) XRD pattern, (c) N₂ adsorption/desorption isotherms, and (d) BJH pore size distribution of HN_PS-PCFs and PS-PCFs.

Pore size distribution and specific surface areas were determined by N₂ physisorption. HN_PS-PCFs presented a similar isotherm (showed in **Figure 4.24c**) to that found for PS-PCFs, exhibiting the characteristic hysteresis loop related to capillary condensation within the material mesopore [13]. As shown in **Table 4.4**, the SSA_{BET} value reached for HN_PS-PCFs is considerably reduced respect to PS-PCFs, in fact, a decrease in the micropore content was also observed. This behavior is in agreement with other results obtained for PAN-based BCP-derived PCFs [58]. The decrease SSA_{BET} is caused by the increase in *N* value, which reduces or hinders the chain mobility, causing larger and isolated sacrificial block domains, and thus leading to an increase in the average mesopore size and a decrease in SSA_{BET} value. Confirming the pore size distribution measured from TEM images, HN_PS-PCFs presented a few adsorption peaks related to pore sizes between 11–17 nm that cannot be detected for PS-PCFs

(Figure 4.24d). These results verify that mesopore size is strongly affected by the overall molecular weight of the BCP precursor.

Table 4.4. HN_PS-PCFs and PS-PCFs textural characteristics.

Material	SSA _{BET} ^a (m ² g ⁻¹)	SSA _{micro} ^b (m ² g ⁻¹)	V _{tot} ^c (cm ³ g ⁻¹)	V _{micro} ^d (cm ³ g ⁻¹)	SSA _{meso} / SSA _{micro} ^e
HN_PS-PCFs	220.5	115.8	0.18	0.11	0.90
PS-PCFs	495.7	366.1	0.33	0.18	0.35

^a BET surface area calculated from the linear part of the BET plot ($P/P_0 = 0.05-0.25$); ^b t-plot micropore area; ^c total pore volume, taken from the N₂ volume adsorbed at $P/P_0 = 0.90$; ^d total pore volume, taken from the N₂ volume adsorbed at $P/P_0 = 0.015$; and ^e mesopore/micropore ratio, where $SSA_{meso} = SSA_{BET} - SSA_{micro}$.

XPS was carried out in order to study changes in the fiber surface chemical composition as the total molecular weight of the PS-*b*-PAN copolymer precursor increased. Full spectra shown in **Figure 4.25** exhibited peaks corresponding to C 1s, N 1s, and O 1s, for both fiber materials (HN_PS-PCFs and PS-PCFs). Nitrogen content and N-containing functional groups concentrations are summarized in **Table 4.5**. The nitrogen relative content reached for HN_PS-PCFs (16.1%) doubles that of PS-PCFs (7.8%). This can be attributed, as previously explained, to the highest number of isolated PS domains that causes larger PAN domain sizes, which after carbonization lead to larger graphene-type layers, together with a slightly decrease in PS volume fraction ($f = 0.11$). Moreover, the content of N-graphitic notably increased, since larger PAN-derived carbon graphite layers may contribute to reaching a higher degree of graphitization, as demonstrated by Raman spectroscopy.

On the other hand, high-resolution O 1s spectra in **Figure 4.26** showed similar oxygen functional groups concentration for both fibers. The total content of oxygen and nitrogen increased for HN_PS-PCFs (**Table 4.5**), due to the different PAN rearrangement along the fiber. These findings highlight how variations in the molecular weight of the block copolymer precursor can cause remarkable structural modifications, in terms of carbon fiber diameter, degree of graphitization, pore structure, and surface heteroatom content.

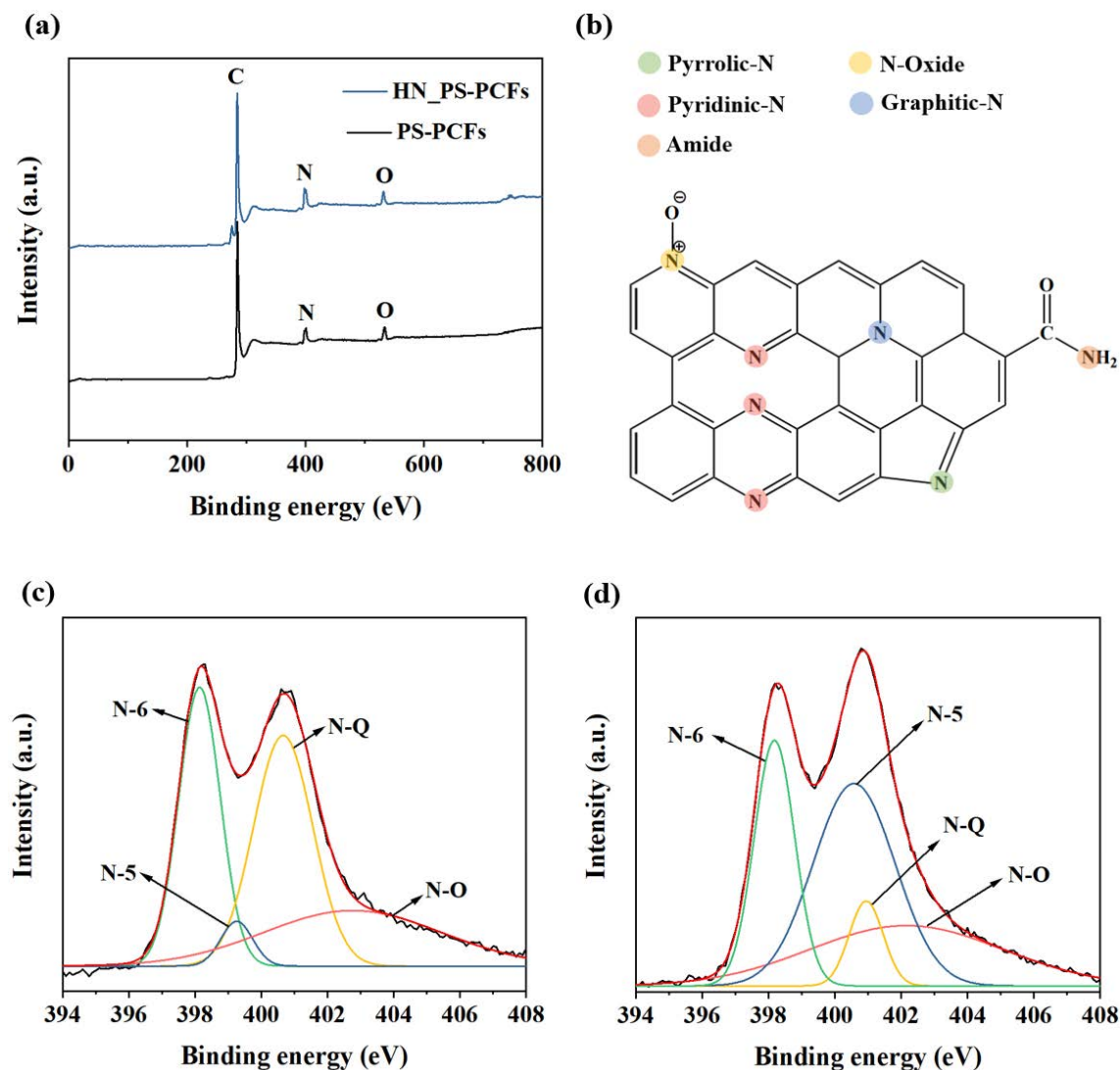


Figure 4.25. (a) Comparative XPS full spectra of HN_PS-PCFs and PS-PCFs, (b) scheme representing N-containing functional groups presented in the PCFs, and high-resolution N 1s spectra of (c) HN_PS-PCFs and (d) PS-PCFs.

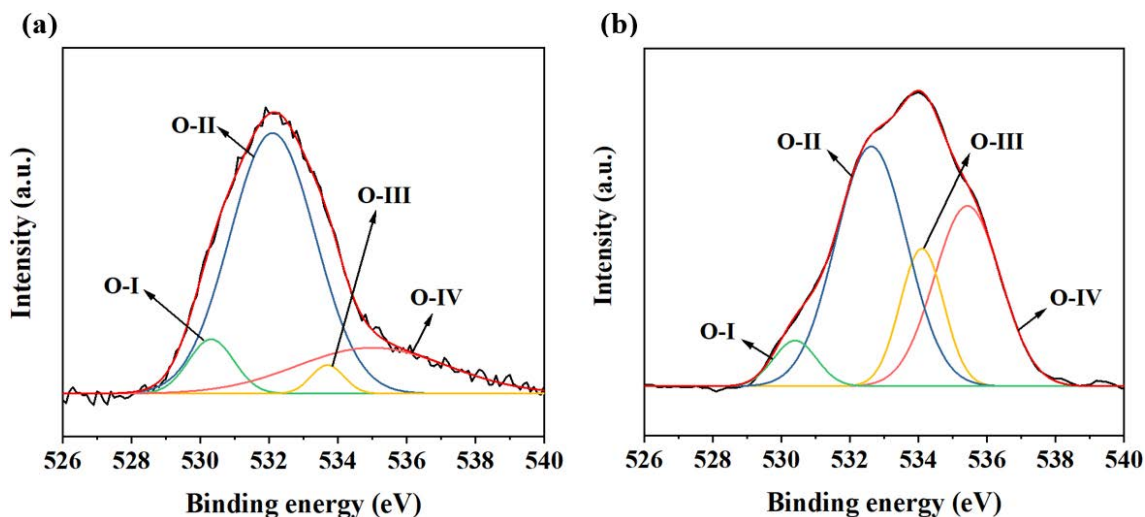


Figure 4.26. High-resolution O 1s spectra of (a) HN_PS-PCFs and (b) PS-PCFs.

Table 4.5. Relative atomic composition and nitrogen and oxygen species content of PS-PCFs and HN_PS-PCFs obtained by fitting N 1s and O 1s high-resolution peaks.

Material	Heteroatom functional group	Content (%); (binding energy (eV))	N/O (%)
PS-PCFs	N-6	24.3; (398.2)	7.8
	N-5	40.4; (400.6)	
	N-Q	7.0; (400.9)	
	N-O	28.3; (402.5)	
	O-I	5.3; (530.4)	4.5
	O-II	46.2; (532.6)	
	O-III	16.2; (534.1)	
	O-IV	32.3; (535.4)	
HN_PS-PCFs	N-6	31.7; (398.1)	16.1
	N-5	3.9; (399.3)	
	N-Q	37.4; (400.7)	
	N-O	27.0; (402.8)	
	O-I	7.6; (530.3)	5.5
	O-II	68.4; (532.1)	
	O-III	2.9; (533.7)	
	O-IV	21.2; (535.0)	

4.3. PCFs derived from PtBA-*b*-PAN

Fiber morphology and pore structure can be also modified by varying the nature of the sacrificial block in the PAN-based BCP fiber precursor. Producing PCFs presenting various fiber diameters, pore sizes, and chemical surface composition is essential to expand their field of potential applications. Therefore, to study the influence of sacrificial block on the pore structure and fiber morphology, a comparative study between fibers produced from PS-*b*-PAN and PtBA-*b*-PAN copolymers has been carried out. A scheme illustrating this study is represented in **Figure 4.27**. Fibers produced from PS-*b*-PAN and PtBA-*b*-PAN were named as PS-PCFs and PtBA-PCFs, respectively.

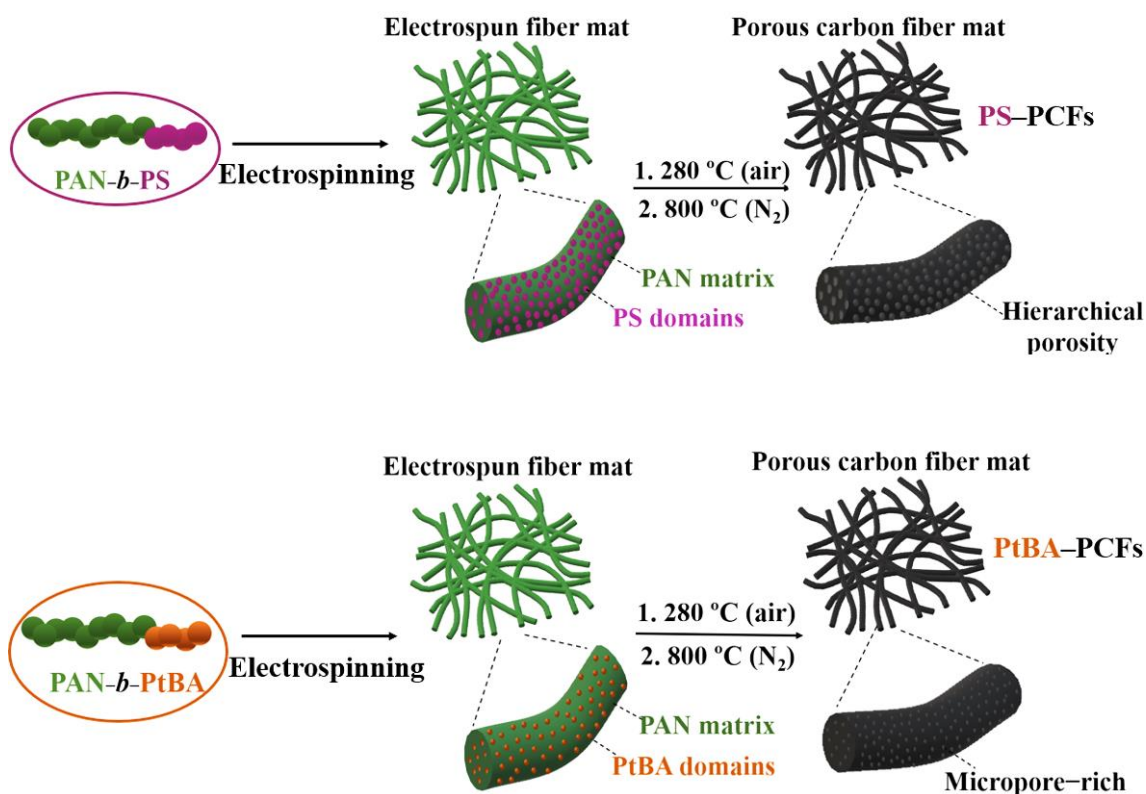


Figure 4.27. Comparison of PCFs obtained from electrospinning of PS-*b*-PAN and PtBA-*b*-PAN copolymers as precursors.

The influence on the pore structure of the thermally unstable sacrificial block in PAN-containing polymer blends has been widely studied using different sacrificial polymers, including PS and PMMA [132,152,153]. Compatibility between sacrificial and carbonizing polymer (PAN) is a key parameter to obtain well-controlled and tunable pore

size structures [50]. Phase separation occurs in the absence of favorable intermolecular interactions between the two polymers. The morphology generated by the phase-separated domains due to polymer immiscibility will determine the shape and pore size of carbon microstructures upon pyrolysis. Therefore, pore formation and microstructure are highly dependent on the compatibility between PAN and sacrificial polymer. Herein, a study focusing on morphological changes was performed by introducing a different sacrificial block, Poly (t-butyl acrylate) (PtBA), in PAN-based BCP fiber precursor.

Despite the fact that the use of PS-*b*-PAN, presenting a low PS volume fraction ($f = 0.16$), leads to a disordered morphology due to rapid evaporation the solvent (kinetic control) during electrospinning, the size of the generated disorder domains will be affected by two main parameters:

- χN : Degree of segregation, in which χ corresponds with interaction parameter between the two immiscible block polymers and N represents total degree of polymerization.
- f_{SB} : Volume fraction of the sacrificial block polymer.

Increasing both χN , and f_{SB} has been demonstrated to produce larger sacrificial block domains sizes [57,58].

The choice of PtBA as sacrificial block (SB) to evaluate the influence of SB nature on the pore structure is based on three main characteristics. First, PtBA is incompatible with PAN block, second, it can be thermally degraded at a relative low temperature (~ 465 °C) and third, it exhibits quite different thermal behavior compared to PS ($T_{g(PS)} = 90$ °C; $T_{g(PtBA)} = 40$ °C), which can also affect the final morphology.

PtBA-*b*-PAN synthesis and characterization is described in **Section 3.3** of **Chapter 3**. This BCP exhibited slightly higher molecular weight and slightly lower SB volume fraction ($f_{SB} = 0.11$) than that found in PS-*b*-PAN ($f_{SB} = 0.16$), but close enough to ignore its contribution to the phase separation morphology. Therefore, SB volume fraction should not be the determining parameter in the expected morphological and structural changes of the fibers. An analysis of the interaction parameter χ between PAN and both SB (PS and PtBA) revealed a significant difference in the predicted SB-PAN

miscibility. χ_{SB-PAN} interaction parameter can be easily calculated using an approximation with the following equation [154]:

$$\chi_{AB} = \frac{V_{ref}(\delta_A - \delta_B)^2}{RT} \quad (4.1)$$

where V_{ref} is the reference volume of the binary polymer mixture, often used as $100 \text{ cm}^3 \text{ mol}^{-1}$. δ_A and δ_B are solubility parameters of the constituent blocks, R is gas constant ($8.31 \text{ J K}^{-1} \text{ mol}^{-1}$), and T is room temperature (293 K).

Hildebrand solubility parameter (δ) provides a number estimating the degree of interaction between polymers and can be a reliable indicator of polymer solubility. Solubility parameters of PAN, PS, and PtBA found in the bibliography were compiled in **Table 4.6**, as well as the calculated polymer–polymer interaction parameters.

Table 4.6. Solubility parameters (δ) of PAN and sacrificial blocks (PS and PtBA), solubility parameters differences, and polymer–polymer interaction (χ).

Polymer	$\delta \text{ (MPa}^{1/2}\text{)}$	$(\delta_{PAN}-\delta_{SB})^{1/2*}$	Polymer–Polymer interaction (χ)*	Ref
PAN	25.6	–	–	[50]
PS	18.6	2.95	0.3	[50]
PtBA	24.7	0.95	0.08	[155]

* Considering the interaction between PAN and sacrificial block.

As can be detected from the polymer–polymer interaction parameter, the immiscibility between PAN and PS is much higher than that with PtBA. Increasing the difference in solubility or immiscibility leads to larger domain sizes of disperse phase (sacrificial block). Therefore, PtBA-*b*-PAN is expected to form smaller PtBA domains, and as a result, a predominance of micropores *versus* mesopores will be also predicted after carbonization. **Figure 4.28** provides a schematic and comparative illustration of phase domains for both sacrificial blocks.

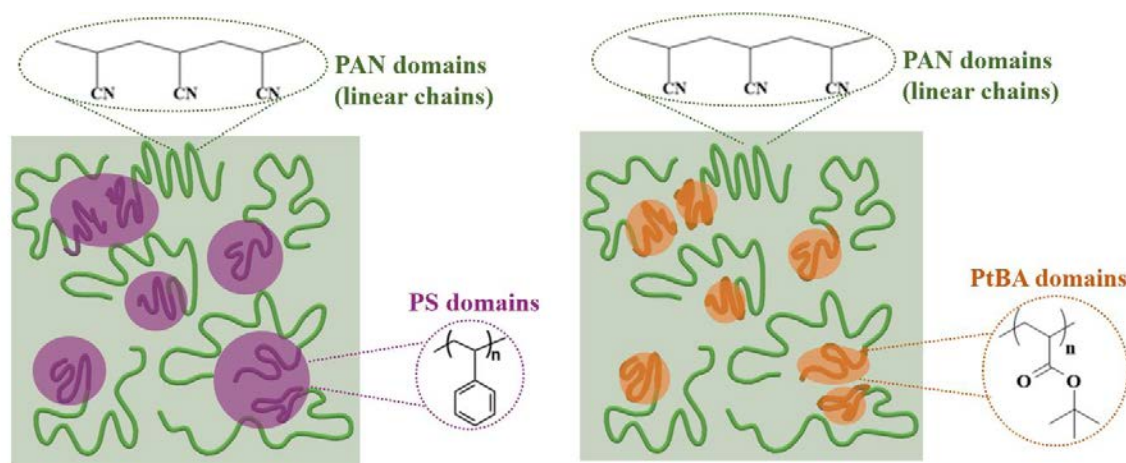


Figure 4.28. Expected phase domains resulting from the phase separation of PS-*b*-PAN and PtBA-*b*-PAN.

Reducing size domains may be particularly interesting since increasing compactness with minimal ‘dead volume’ is crucial for efficient supercapacitors in electric devices. Large mesopore sizes between > 20 nm had been demonstrated not to contribute to electrochemical performance [156,157]. Although electric double layer formation requires micropores, mesopores are necessary to serve as ion-buffer reservoirs and ion transportation pathways that reduces distances from the bulk electrolyte to micropore active sites. Thus, it is essential to be able to create a strategy to packing the carbonaceous structure by reducing mesopore sizes without compromising the charge storage capacity. This can be achieved modifying pore size of carbonaceous materials by using different sacrificial blocks.

4.3.1. PtBA-PCFs: Morphological and structural characterization

The following section describes the microstructural differences found in PtBA-*b*-PAN-derived fibers, compared to PS-*b*-PAN-derived fibers described above (section 4.2). To study the influence of the sacrificial block on fiber morphology, the same electrospinning parameters and conditions were used as for obtaining PS-*b*-PAN-derived fibers (see Table 4.2 in Section 4.2). Prior to electrospinning, the block copolymer solutions were stirred at 35 °C for 24 h to ensure complete dissolution.

Fiber morphology was evaluated by SEM (images shown in Figure 4.29a). The PtBA-*b*-PAN fiber mat showed a bead-fiber type of morphology, with the presence of several beads of different sizes (see Figure 4.22a). It has already been explained in

Section 4.2, that the formation of beads is associated, among others, with low viscosity. This parameter has a huge impact on the shape of the fiber. The observed changes in fiber morphology, using the same electrospinning parameters, demonstrate how the sacrificial block, even at lower volume fractions ($f_{SB} = 0.11\text{--}0.16$), not only affects the size of the disperse phase domains, but also influences the intrinsic properties of the solution, like viscosity. Since the idea of this project was to modify the sacrificial block keeping the other parameters constant, fiber optimization was not performed. It is worth noting that to obtain a homogenous fiber mat, varying the polymer concentration (to increase viscosity) or ionic strength of the solution, by introducing a small amount of ionic salts, would probably reduce the bead formation.

Fiber diameters were decreased compared to PS-*b*-PAN-derived fiber mat (105 ± 5 nm), showing widely disperse diameters centered in 61.8 ± 3.0 nm. Furthermore, the PtBA-*b*-PAN-derived fibers showed smother surfaces, presumably due to the weaker phase segregation between PtBA and PAN compared to PS.

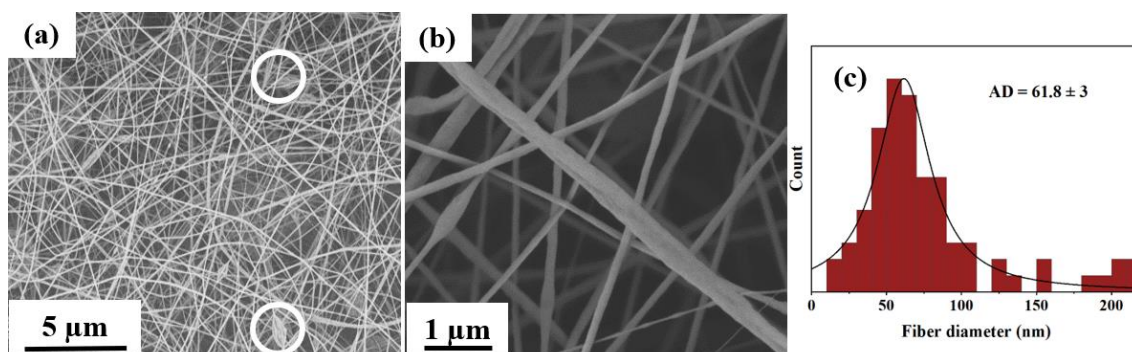


Figure 4.29. (a) SEM image of PtBA-*b*-PAN-derived fiber mat showing bead formation, (b) fiber surface, and (c) fiber diameter distribution.

PtBA-*b*-PAN-derived fiber mat was thermally annealed at 280 °C for 1 h under oxidizing atmosphere and carbonized at 800 °C for 1 h under N₂ flow. TEM images of PtBA-PCFs (**Figure 4.30**) showed significantly lower pore concentration along the fiber length than PS-PCFs. At high magnification it is possible to distinguish small mesopores centered at ~ 6.6 nm, which are clearly smaller compared to the average mesopore size (~ 9.5 nm) found for PS-PCFs.

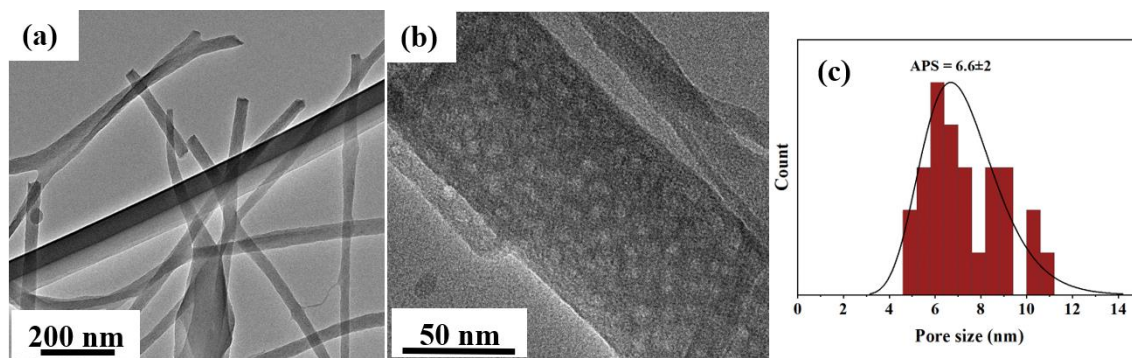


Figure 4.30. (a) TEM image of PtBA-PCFs, (b) magnified TEM image showing mesopores around 6.6 nm, and (c) pore size distribution.

Raman spectroscopy was evaluated to examine and compare the two different carbon fiber structures derived from PAN-based BCPs (**Figure 4.31a**). Both fiber materials (PS-PCFs and PtBA-PCFs) displayed the distinctive bands related to graphitic (“G band”) between $\sim 1560\text{--}1600\text{ cm}^{-1}$ and disordered features (“D band”) between $\sim 1320\text{--}1350\text{ cm}^{-1}$. While intensity ratio between D and G bands (I_D/I_G) presented a value of 1.11 for PS-PCFs, demonstrating a preferentially disorder carbon structure, this ratio is considerably reduced for PtBA-PCFs, with a value of 0.85. PtBA-PCFs seem to exhibit a higher degree of graphitization. This increase may be related to the slightly higher PAN content, which after carbonization introduces more graphitic layers.

XRD patterns (**Figure 4.31b**) of both carbon nanofibers, showed a broad peak around 25° that can be assigned to (002), typically related to pyrolytic or graphitic carbon structures [153]. The low intensity together with the poor definition of the peak suggest a predominantly amorphous carbon structure. Moreover, this peak is shifted to higher angles for PtBA-PCF ($\sim 26.5^\circ$) compared to PS-PCFs ($\sim 25.2^\circ$), which according to Bragg’s law, shows a decrease in the interlayer spacing $d_{(002)}$. This decrease indicates that the graphite crystallites change from a turbostratic structure towards a more slightly ordered alignment. Regardless of this slight change in crystallinity and graphitization degree, both fiber materials present a highly disorder and amorphous structure. The obtaining of preferentially disordered structures can be attributed to the porous channels produced by the sacrificial block, which may structurally obstruct the orientation of PAN crystals along the fiber axis [138].

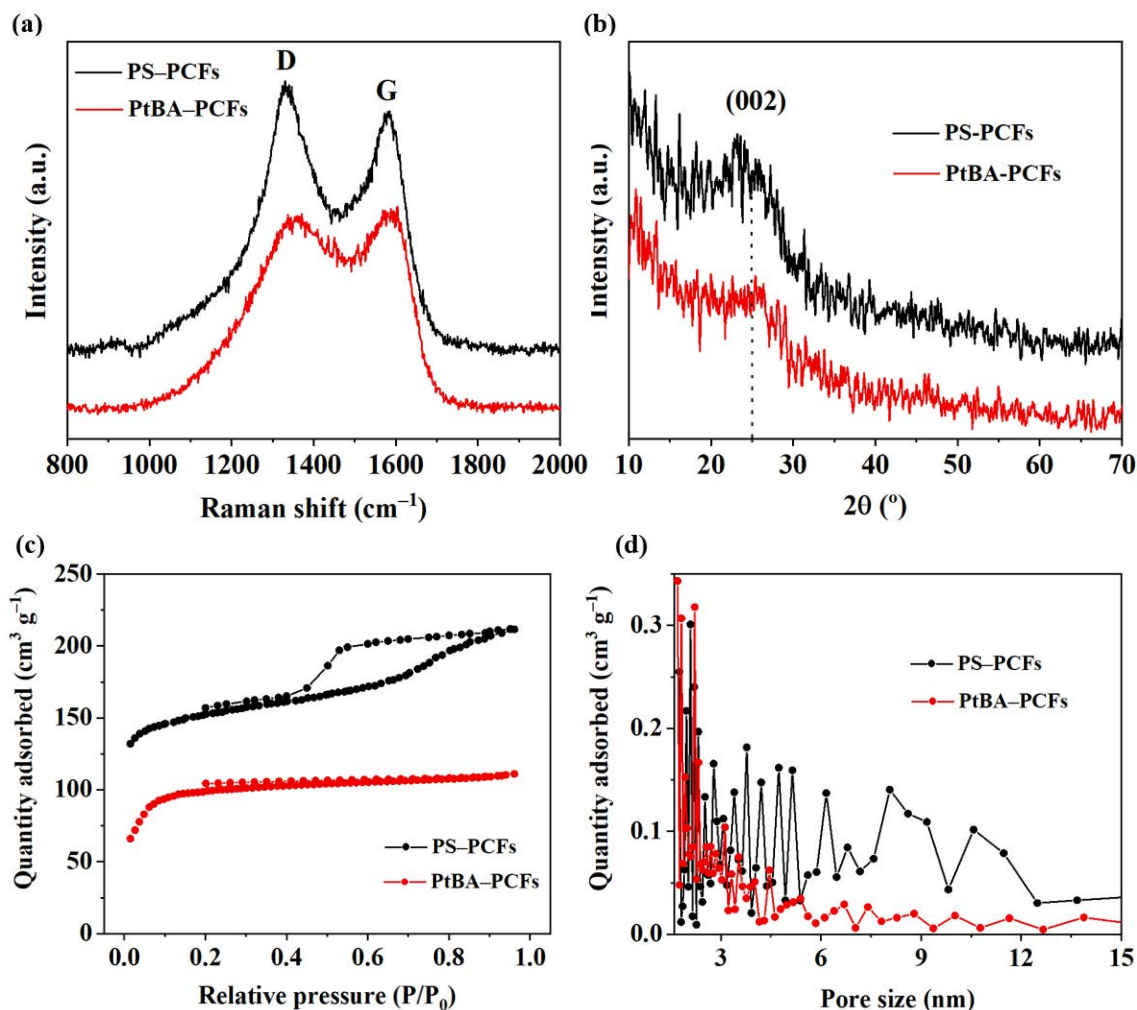


Figure 4.31. (a) Raman spectra, (b) XRD patterns, (c) N_2 adsorption/desorption isotherms, and (d) BJH pore size distribution of PS-PCFs and PtBA-PCFs.

N_2 adsorption/desorption analysis was performed to further study and confirm the expected changes in the overall pore structure. PtBA-PCF showed an isotherm with rapid N_2 uptake at lower relative pressures ($P/P_0 < 0.1$), followed by a plateau without the presence of a hysteresis loop (**Figure 4.31c**). This type of isotherm according to IUPAC report [13] can be classified as Type Ib, related to microporous solids with narrow mesopores (< 2.5 nm). These pore structure changes found in PtBA-PCF are related to the low immiscibility between PtBA and PAN block, that produces smaller sacrificial block size domains. After PtBA decomposition and PAN carbonization, the sacrificial block domains turn into small-size pores, mainly in the micropore range (< 2 nm), compared to the mesopore-rich structure of PS-PCF. In addition, the BET_{SSA} value for PtBA-PCF is $304.0 \text{ m}^2 \text{g}^{-1}$, which is considerably lower than that obtained for PS-PCF (**Table 4.7**). This may be assigned to the slight decrease in the PtBA volume fraction

($f_{\text{PtBA}} = 0.11$) compared to PS volume fraction in PS-PCF ($f_{\text{PS}} = 0.16$). This decrease induces fewer PtBA domains, which after pyrolysis, leads to a lower pore concentration in the carbon matrix structure. BJH pore size distribution of the adsorption branch (**Figure 4.31d**) confirms the information related to the isotherm. PtBA-PCF predominantly exhibited micropores, as well as some mesopores, most of them concentrated in the 2–4 nm range.

Table 4.7. PS-PCFs and PtBA-PCFs textural properties

Material	SSA _{BET} ^a (m ² g ⁻¹)	SSA _{micro} ^b (m ² g ⁻¹)	V _{tot} ^c (cm ³ g ⁻¹)	V _{micro} ^d (cm ³ g ⁻¹)	SSA _{meso} / SSA _{micro} ^e
PS-PCFs	495.7	366.1	0.33	0.18	0.35
PtBA-PCFs	304.0	236.75	0.17	0.13	0.28

^a BET surface area calculated from the linear part of the BET plot ($P/P_0 = 0.05$ – 0.25); ^b t-plot micropore area; ^c total pore volume, taken from the N₂ volume adsorbed at $P/P_0 = 0.90$; ^d total pore volume, taken from the N₂ volume adsorbed at $P/P_0 = 0.015$; and ^e mesopore/micropore ratio, where $\text{SSA}_{\text{meso}} = \text{SSA}_{\text{BET}} - \text{SSA}_{\text{micro}}$.

Surface element composition was determined using X-ray photoelectron spectroscopy (XPS). Full spectra for both fiber materials shown in **Figure 4.32a**, displayed peaks corresponding with C 1s, N 1s, and O 1s. The high-resolution nitrogen spectrum of PtBA-PCFs (**Figure 4.32d**) was deconvoluted into the same four peaks previously detailed for PS-PCFs in **Section 4.2**. As shown in **Table 4.8**, PtBA-PCFs exhibited a higher total nitrogen content than PS-PCFs. This can be explained by the slightly higher PAN volume fraction exhibited by PtBA-PCFs, which corresponds to the nitrogen-precursor block. However, higher nitrogen exposure to the surface may also be attributed to the spatial arrangement and conformation of the graphitic layers along the fiber, as it is explained below. Furthermore, concentration of electrochemical active species pyridinic (N-6) and pyrrolic nitrogen (N-5) (**Figure 4.32b**) is increased as well, reaching 70.9% compared to 64.7% obtained for PS-PCFs.

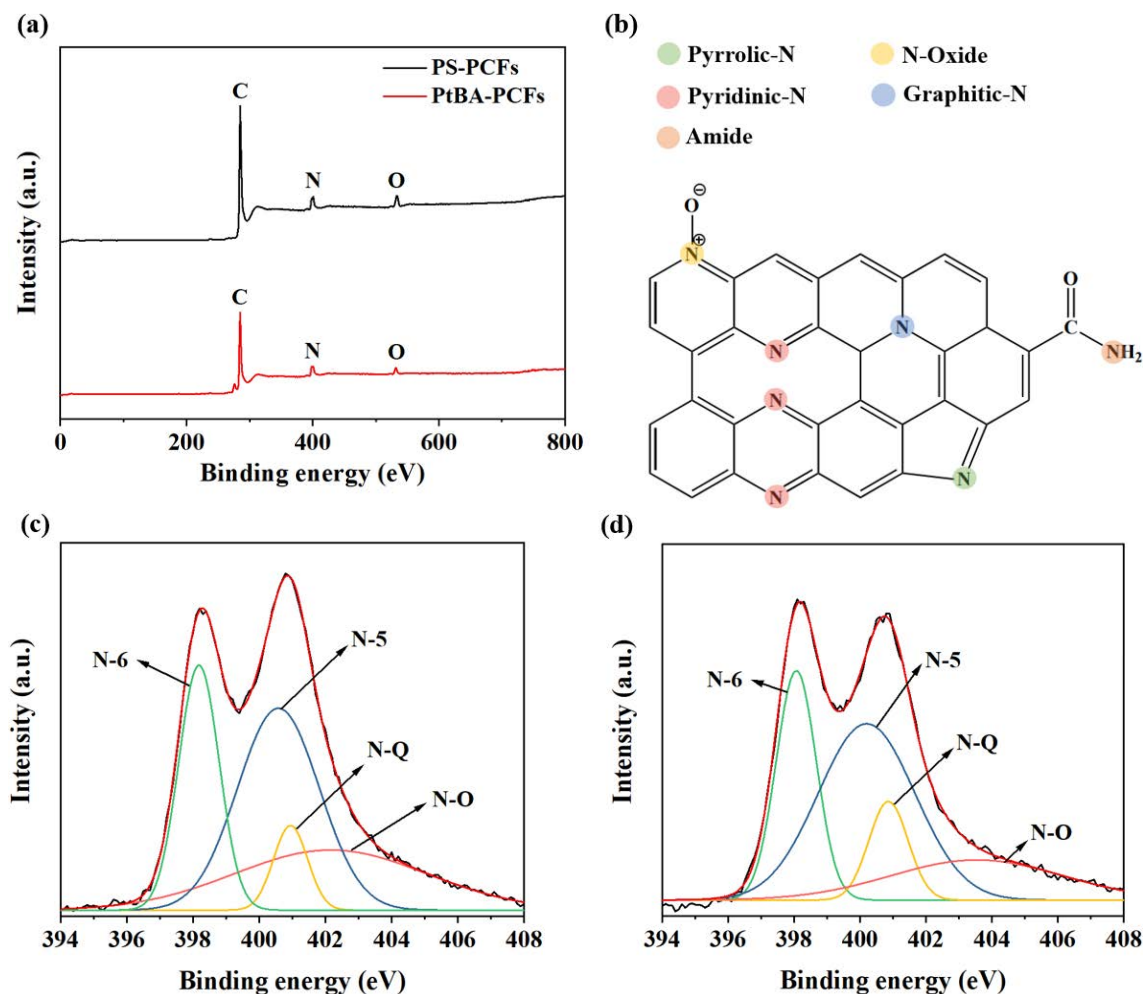


Figure 4.32. (a) Comparative XPS full spectra of PS-PCFs and PtBA-PCFs, (b) scheme representing N-containing surface functionalities presented in PCFs, and high-resolution N 1s spectra of (c) PS-PCFs and (d) PtBA-PCFs.

On the other hand, high-resolution O 1s spectra can be deconvoluted into the same three peaks already detected for PS-PCFs, except for the chemisorbed water (O-IV) which cannot be detected (**Figure 4.33**). Oxygen surface content decreased in PtBA-PCFs compared to PS-PCFs. This can be explained by the thermal decomposition of tBA, which was previously described in **Chapter 3**. Around 240 °C tBA suffered some cyclization reactions followed to complete degradation, which take place parallel to stabilization and oxidation of PAN. These parallel thermal reactions can interfere and decrease the oxidation yield of the PAN block.

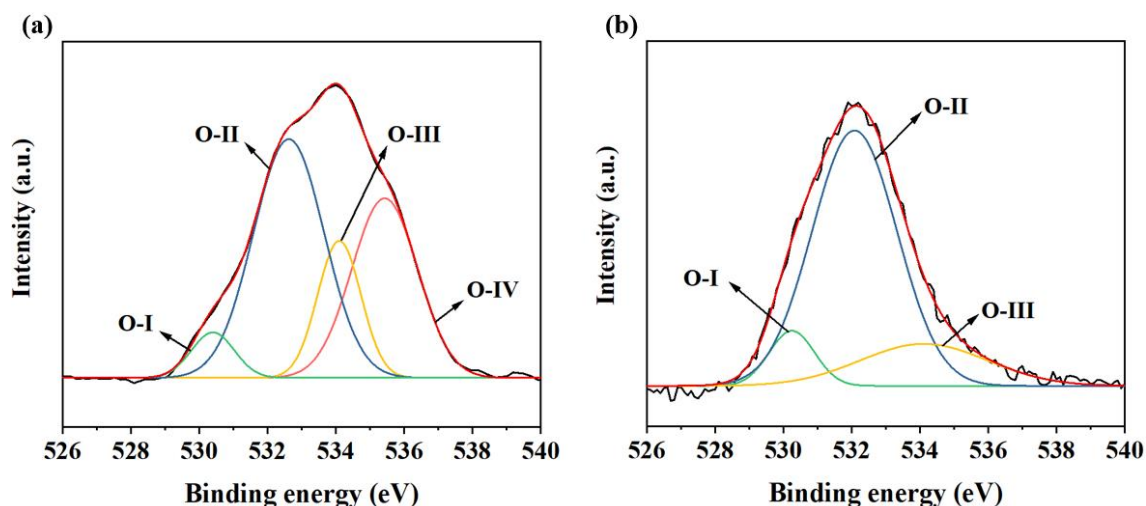


Figure 4.33. High-resolution O 1s spectra of (a) PS-PCFs and (b) PtBA-PCFs.

Table 4.8. Relative atomic composition and nitrogen and oxygen species content obtained by fitting N 1s and O 1s XPS spectra of PS-PCFs and PtBA-PCFs.

Material	Heteroatom functional group	Content (%); (binding energy (eV))	N/O(%)
PS-PCFs	N-6	24.3; (398.2)	7.8
	N-5	40.4; (400.6)	
	N-Q	7.0; (400.9)	
	N-O	28.3; (402.5)	
	O-I	5.3; (530.4)	4.5
	O-II	46.2; (532.6)	
	O-III	16.2; (534.1)	
	O-IV	32.3; (535.4)	
PtBA-PCFs	N-6	26.9; (398.1)	12.6
	N-5	44.0; (400.2)	
	N-Q	10.5; (400.9)	
	N-O	18.6; (403.5)	
	O-I	8.4; (530.2)	4.0
	O-II	73.4; (532.1)	
	O-III	18.1; (534.1)	

Based on the XRD analysis, the spatial arrangement of the graphitic sheets is found to have a more oriented conformation. This behavior can be explained by the smaller sacrificial block domain sizes formed in PtBA-PCFs, compared to PS-PCFs, which generated fewer and smaller pore channels, allowing PAN graphitic sheets to be

more orientated through the fiber axis. The graphitic orientation of PAN has been detected in PAN-derived carbon fibers [158], and although both fibers, PtBA-PCFs and PS-PCFs, showed preferentially carbon amorphous structures, PtBA-PCFs exhibited a slightly more ordered graphitic plane. This type of turbostratic or more ordered orientation may result in some exposure of nanographene edges at the fiber surface. Nanographene edges derived from PAN stabilization and carbonization are rich in pyridinic and pyrrolic species, that together with the narrow fiber diameter, allows to expose more nanographene edges than in a broader fiber, which can remain buried within the bulk material [159]. **Figure 4.34** displays a scheme illustration of PAN graphitic planes orientation in PtBA-PCFs.

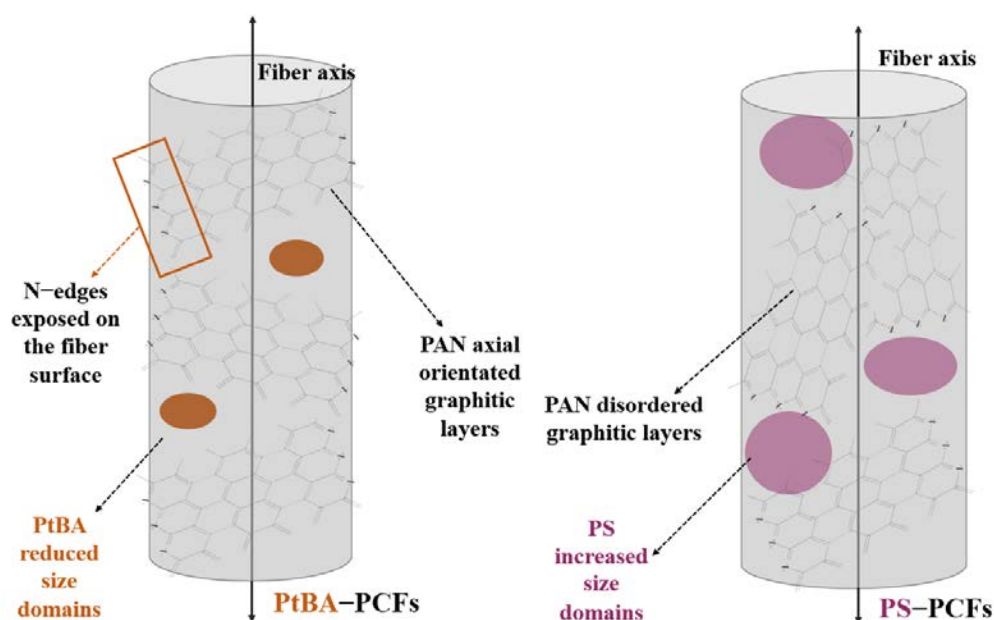


Figure 4.34. Scheme illustrating the different expected PAN graphitic layers orientation of PtBA-PCFs and PS-PCFs according to XPS, Raman and XRD data.

A comparison of structural and physicochemical parameters of the three different PCFs materials produced and discussed throughout this chapter can be found in **Table 4.9**.

Table 4.9. Summary of PCFs structural and physicochemical characteristics.

	PS-PCFs	HN_PS-PCFs	PtBA-PCFs
Microscopy			
Fiber diameter	105±5	118±5	62±3
Raman			
I _D /I _G	1.11	0.86	0.85
N₂ adsorption/desorption analysis			
SSA _{BET} (m ² g ⁻¹)	495.7	220.5	304.0
SSA _{micro} (m ² g ⁻¹)	366.1	115.8	236.8
Meso-/micropore ratio	0.35	0.90	0.28
V _{tot} (cm ³ g ⁻¹)	0.33	0.18	0.17
V _{micro} (cm ³ g ⁻¹)	0.18	0.11	0.13
Total heteroatom content			
N (%)	7.8	16.1	12.6
O (%)	4.5	5.5	4.0
C (%)	87.0	78.4	83.4

Chapter 5

N and N/S co-doped porous carbon fibers

Throughout this chapter, the doping–activation process carried out on porous carbon fibers (PCFs) derived from PS–*b*–PAN will be detailed. PCFs activation process was developed to introduce N and S heteroatoms in the carbon structure by soaking the PCFs mat into urea and thiourea aqueous solutions, followed by carbonization, as shown in **Figure 5.1**. PCFs doped with urea as N precursor and thiourea as N/S precursor were named NPCFs and SPCFs, respectively.

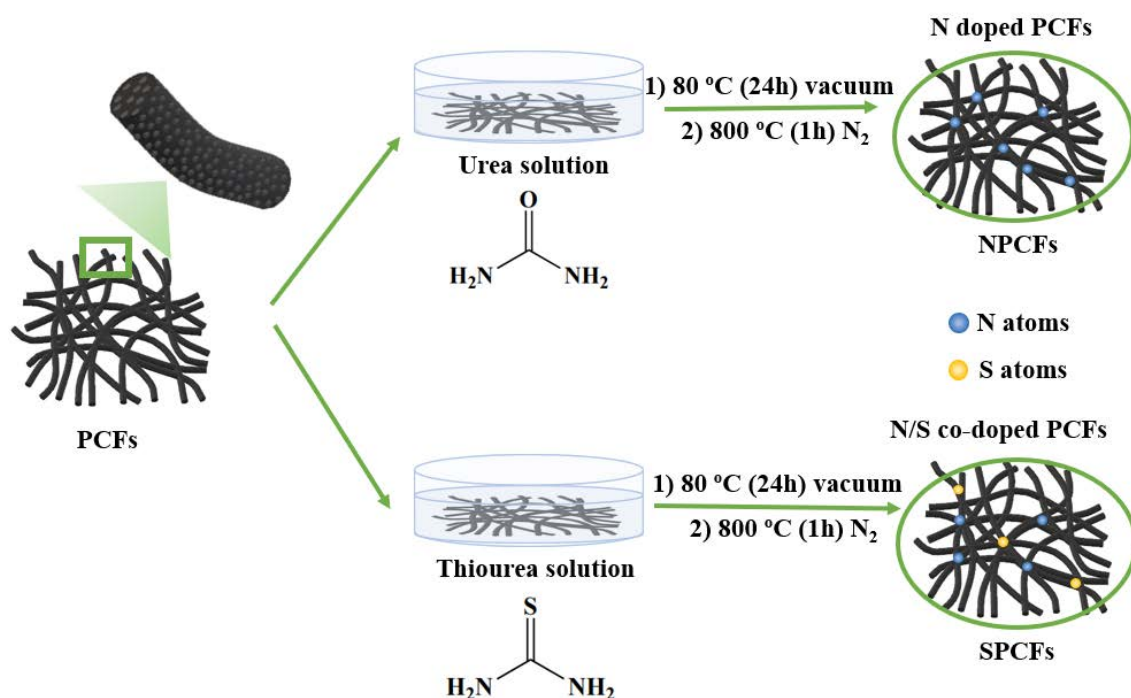


Figure 5.1. Scheme representing the preparation of N-doped (NPCFs) and N/S co-doped (SPCFs) porous carbon fibers.

The introduction of N and S heteroatoms into the carbon structure produced several changes in terms of microstructure, porosity, and chemical surface composition. Therefore, a study based on morphological and physicochemical changes observed after the activation process is described.

Based on the storage mechanism, supercapacitors can be divided into EDLCs (Electrical Double Layer Capacitors) and pseudocapacitors. EDLCs store energy by intercalating charges at the electrode–electrolyte interface. Therefore, electrode materials with high specific surface areas are required, as explained in previous chapters. However, it has been studied how pore size of the active electrode material directly influences the

electrochemical performance because not all the pores are accessible to the electrolyte ions [160,161]. As previously discussed, of particular interest are hierarchical porous materials comprising macro-, meso-, and micropores [16,17]; since it is well known that macropores, and particularly mesopores, enhance ion diffusion to the micropore active sites [54].

On the other hand, pseudocapacitors store electrochemical energy generally through a combination of faradaic redox reactions between electrolyte ions and active functional groups on the electrode surface, and the formation of the electrical double layer [6]. The effectiveness of heteroatom doping into the carbon network has been demonstrated through the introduction of pseudocapacitance. Furthermore, dopant activation with heteroatoms can enhance electronic and ion conductivity [162] as well as wettability with the electrolyte, which benefits capacitive performance [9]. For this reason, porous materials with a high content of heteroatoms, such as N, S, O, and P [66,67], or redox active nanoparticles [163], are demanded.

Different methods of doping with heteroatoms have been studied; among others, activation process with natural and non-toxic precursors such as urea, thiourea, and melamine have demonstrated to be an efficient, easy, and affordable strategy [164]. Dual-heteroatoms doping approach [69,70] enhances the capacitance even further, since not only increases the concentration of heteroatoms but also combines the benefits of diverse heteroatoms within the conjugated carbon backbone, creating additional non-electron-neutral active sites [165].

5.1. Experimental procedure

Porous carbon fibers (PCFs) were soaked into urea and thiourea saturated aqueous solutions (1.85 M) for 24 h. After that, PCFs mats were dried at 80 °C under vacuum overnight. Then, fiber activation was done at 800 °C for 1 h under N₂ atmosphere. This temperature, the same as the one used for carbonizing the PCFs starting material, was selected to fully decompose the urea and thiourea heteroatoms precursors without decreasing the heteroatom content. The resulting urea (NPCFs) and thiourea (SPCFs) activated fibers were washed with distilled water and dried at 80 °C.

5.2. NPCFs and SPCFs: Morphological and structural characterization

Fiber morphology was analyzed by SEM and TEM (**Figure 5.2**). After the doping–activation process using urea and thiourea at 800 °C, a slight decrease in diameter size was observed, from 105 ± 5 nm determined for undoped nanofibers (PCFs) to 92 ± 3 and 94 ± 4 nm for the N-doped (NPCFs) and N/S co-doped (SPCFs) fibers, respectively. The heteroatom-doped procedure involves two thermal treatments at 800 °C, the carbonization of the fiber mat to obtain PCFs and subsequent activation process. Consequently, volatilization of non-carbon-based elements in the form of carbon monoxide, carbon dioxide, methane, water, or hydrogen cyanide, among other gases, is produced, causing a repacking of the carbon structure, which, together with a slight increase in graphitization, leads to a decrease in diameter [166–168]. In both activated fibers, no more additional visible cracks were observed along the fiber surface; however, it was detected some fragility in doped nanofiber mats.

As shown in the TEM images, morphology remained unaltered for both NPCFs and SPCFs fibers, exhibiting a similar pore structure than undoped PCFs (**Figure 5.2g–i**). This is especially relevant since it allows us to verify that a second thermal treatment up to 800 °C did not modify the internal microstructure.

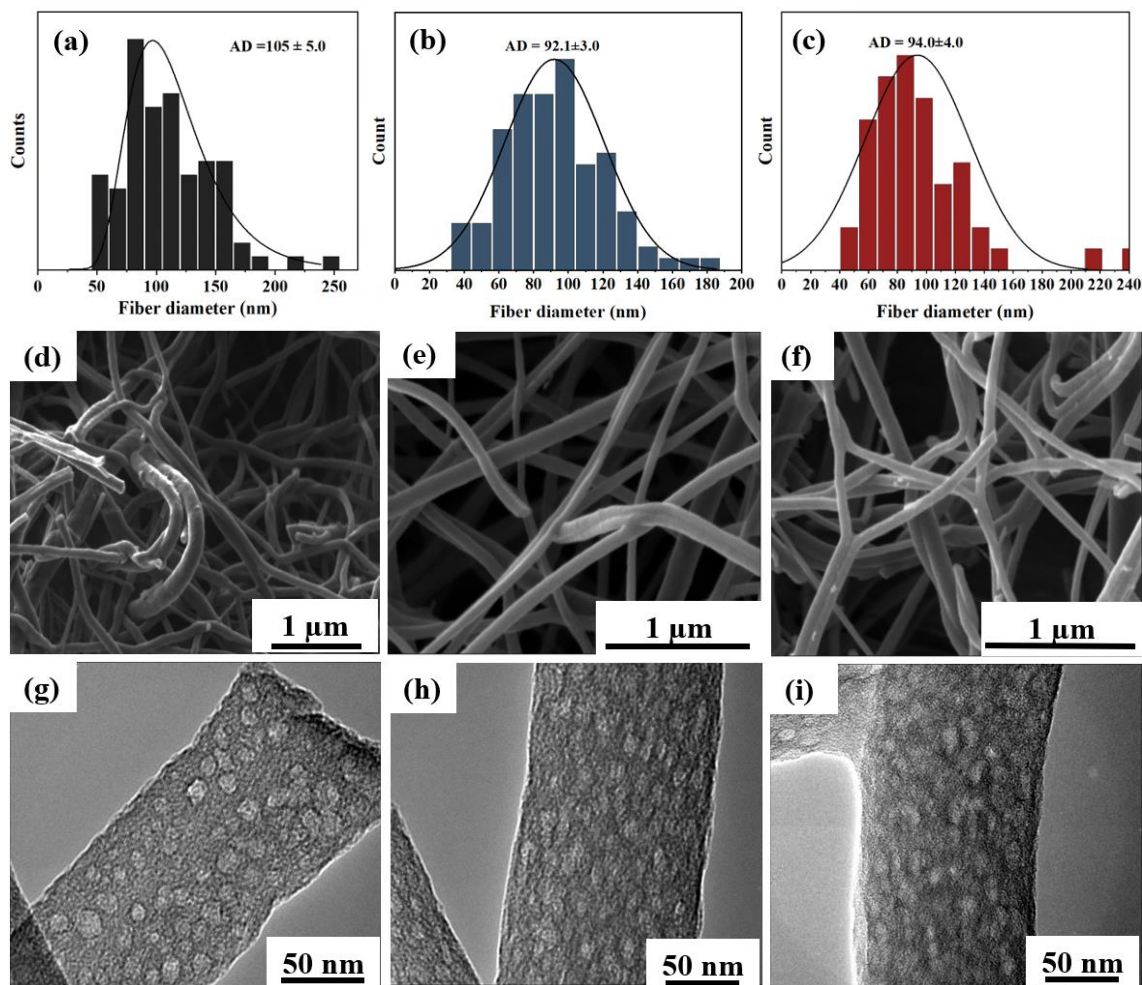


Figure 5.2. Fiber diameter distribution of (a) PCFs, (b) NPCFs, and (c) SPCFs. SEM images of (d) PCFs, (e) NPCFs, and (f) SPCFs. TEM images of (g) PCFs, (h) NPCFs and (i) SPCFs.

Energy dispersive spectrometry (EDS) was performed to assess qualitatively the efficiency in the nitrogen doping process of the PCFs (**Figure 5.3**). Elemental analysis concluded that all samples contained C, N, and O. Detailed elemental chemical bonding information of the N and S doped PCFs using XPS is described below. Nitrogen mapping shows N atoms homogeneously distributed throughout the entire fiber surface for all three nanofibers. Nevertheless, NPCFs and SPCFs exhibited brighter yellow color, that is, higher N content than the non-activated fibers (PCFs). The mapping of S was inconclusive since the S peak appears at an X-ray energy of around 2.5 keV, which was slightly superior to the accelerating voltage (2 keV) applied to collect the images.

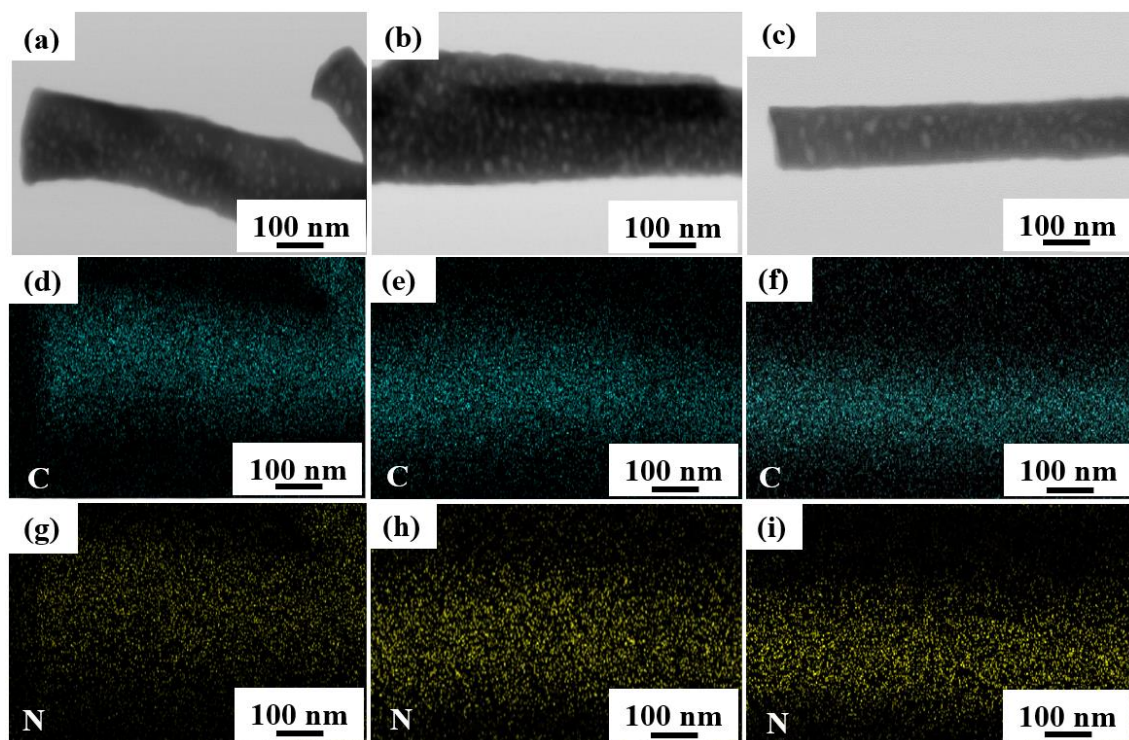


Figure 5.3. FESEM image of a single carbon fiber (a) PCFs, (b) NPCFs, (c) SPCFs. EDS mapping of C and N of PCFs (d and g), NPCFs (e and h), and SPCFs (f and i).

The fiber carbon structure was evaluated by Raman spectroscopy. The Raman spectra in **Figure 5.4a** revealed a significant structural change in the fibers after the urea and thiourea activation process. All three nanofibers presented the characteristic Raman bands located at around 1330 and 1580 cm^{-1} , corresponding to disordered domains (“D band”) and highly graphitic structures (“G band”), respectively. The degree of graphitization or defect concentration can be associated with the I_D/I_G ratio. This ratio gradually decreased with the activation process from 1.11 for PCFs to 0.86 for NPCFs and 0.85 for SPCFs, indicating an increase in the graphitic character, associated with higher electrical conductivity, after heteroatom doping.

XRD pattern (**Figure 5.4b**) of the three samples showed a broad peak around 25° , revealing a predominantly amorphous carbon structure. The peak assigned to (002) typically related to pyrolytic or graphitic carbon structures [138], is slightly more intense for doped fibers, especially for SPCFs, confirming an increase in the graphitization degree after both activation processes.

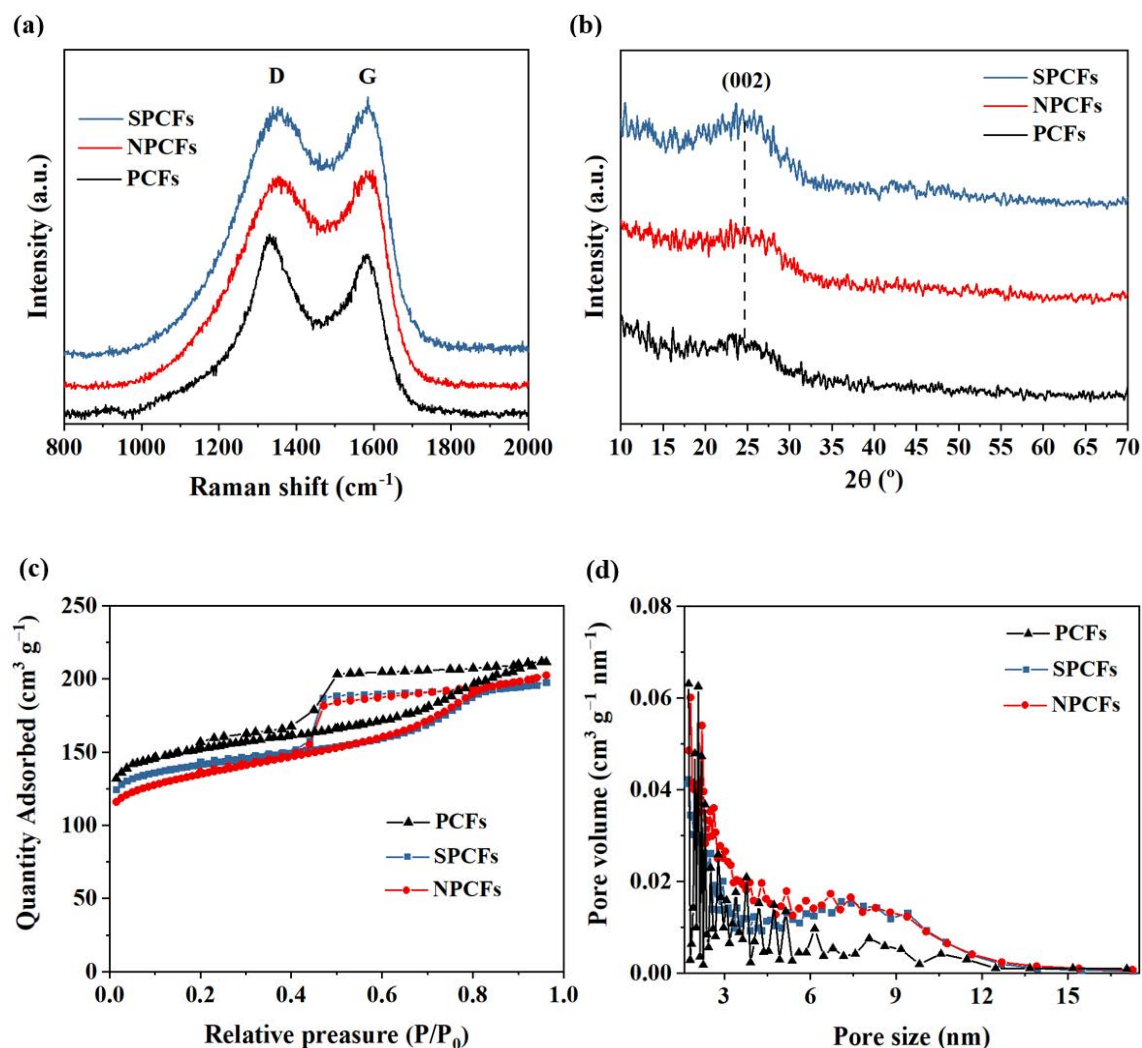


Figure 5.4. (a) Raman spectra, (b) XRD patterns, (c) N_2 adsorption/desorption isotherms, and (d) pore size distributions, calculated using BJH method of the adsorption branch, of PCFs, NPCFs, and SPCFs.

To further study the influence of heteroatom-doped activation on the specific surface area and pore size distribution, N_2 adsorption/desorption measurements of the fibers were performed. PCFs starting material and fibers after activation with urea (NPCFs) and thiourea (SPCFs) showed comparable BET specific surface areas of 495.7, 427.9 and 440.8 $\text{m}^2 \text{g}^{-1}$, respectively. Nanofiber materials exhibited very similar isotherms (**Figure 5.4c**), displaying a large and characteristic hysteresis loop that, according to a published IUPAC report [13], is related to the presence of mesopores.

Pore size distributions were studied using BJH method of the adsorption branch. For the three fiber materials, pore sizes were concentrated in the range 1.7–15 nm (**Figure**

5.4d). However, NPCFs and SPCFs exhibited a higher pore volume adsorption of mesopores with a wide distribution center around 8 nm

Furthermore, mesopore/micropore ratios varied from one sample to another; see **Table 5.1**. After both activation processes, micropore surface area slightly decreased from $366.1 \text{ m}^2 \text{ g}^{-1}$ of the starting material (PCFs) to $271.2 \text{ m}^2 \text{ g}^{-1}$ for NPCFs and $305.6 \text{ m}^2 \text{ g}^{-1}$ for SPCFs. This change in micropore content may be attributed to the different heteroatom environment or carbon structure since an increase in the graphitization degree can lead to micropore blocking [139]. Nevertheless, the doping-activation process seems to increase the mesopore content throughout the fiber promoting the formation of the electric-double layer, since the presence of mesopores enhances ion-diffusion, and maximize effective surface area accessible to electrolyte ions [58].

Table 5.1. Textural properties of the carbon porous fibers.

Material	SSA _{BET} ^a ($\text{m}^2 \text{ g}^{-1}$)	SSA _{micro} ^b ($\text{m}^2 \text{ g}^{-1}$)	V _{tot} ^c ($\text{cm}^3 \text{ g}^{-1}$)	V _{micro} ^d ($\text{cm}^3 \text{ g}^{-1}$)	SSA _{meso} /SSA _{micro} ^e
PCFs	495.7	366.1	0.33	0.18	0.35
NPCFs	427.9	271.1	0.31	0.14	0.6
SPCFs	440.8	305.6	0.30	0.17	0.44

^a BET surface area calculated from the linear part of the BET plot ($P/P_0 = 0.05\text{--}0.25$); ^b t-plot micropore area; ^c total pore volume, taken from the N_2 volume adsorbed at $P/P_0 = 0.90$; ^d total pore volume, taken from the N_2 volume adsorbed at $P/P_0 = 0.015$; and ^e mesopore/micropore ratio, where $\text{SSA}_{\text{meso}} = \text{SSA}_{\text{BET}} - \text{SSA}_{\text{micro}}$.

According to these results, after fiber activation with urea and thiourea, the pore structure has been slightly modified, which leads to a higher mesopore concentration without compromising surface area values. Likewise, a relatively high micropore content was preserved, which resulted in materials with hierarchical porosity.

The fiber materials surface element content and composition were further analyzed using X-ray photoelectron spectroscopy (XPS). XPS measurement confirmed the chemical identities of the heteroatoms in doped fibers. The different functional groups were identified by fitting the high-resolution XPS spectra into several peaks (**Figure 5.5**). The N 1s spectra were deconvoluted into four peaks corresponding with pyridinic nitrogen (N-6) at 398.2 eV, pyrrolic and amide nitrogen at 399.9 eV (N-5 and O=C-N),

graphitic or quaternary nitrogen (N-Q) at 400.9 eV, and oxidized pyridinic nitrogen (N-O) at 403.3 eV [142,143]. Porous carbon fibers O 1s spectra (**Figure 5.6**) were deconvoluted in three different peaks, corresponding to quinone type groups (C=O; O-I) at 530.6 eV, phenol and/or ether groups (C-OH and/or C-O-C; O-II) at 532.5 eV, and ester and/or carboxylic groups (O-C=O and/or COOH; O-III) at 534 eV [144]. Additionally, a strong peak can be detected for PCFs, corresponding to chemisorbed water and/or amide groups (O=C-N; O-IV) at 535.5 eV [145]. Likewise, the S 2p peak observed for SPCFs can be also deconvoluted in two peaks derived from a thiophene-type structure (C-S-C; S-I and S-II) at 163.8 eV and 164.9 eV, respectively, and a peak corresponding to CSO_x oxygenated groups (S-III) at 167.7 eV [169]. These results verified the successful doping of N and N/S into the carbon matrix in NPCFs and SPCFs, respectively.

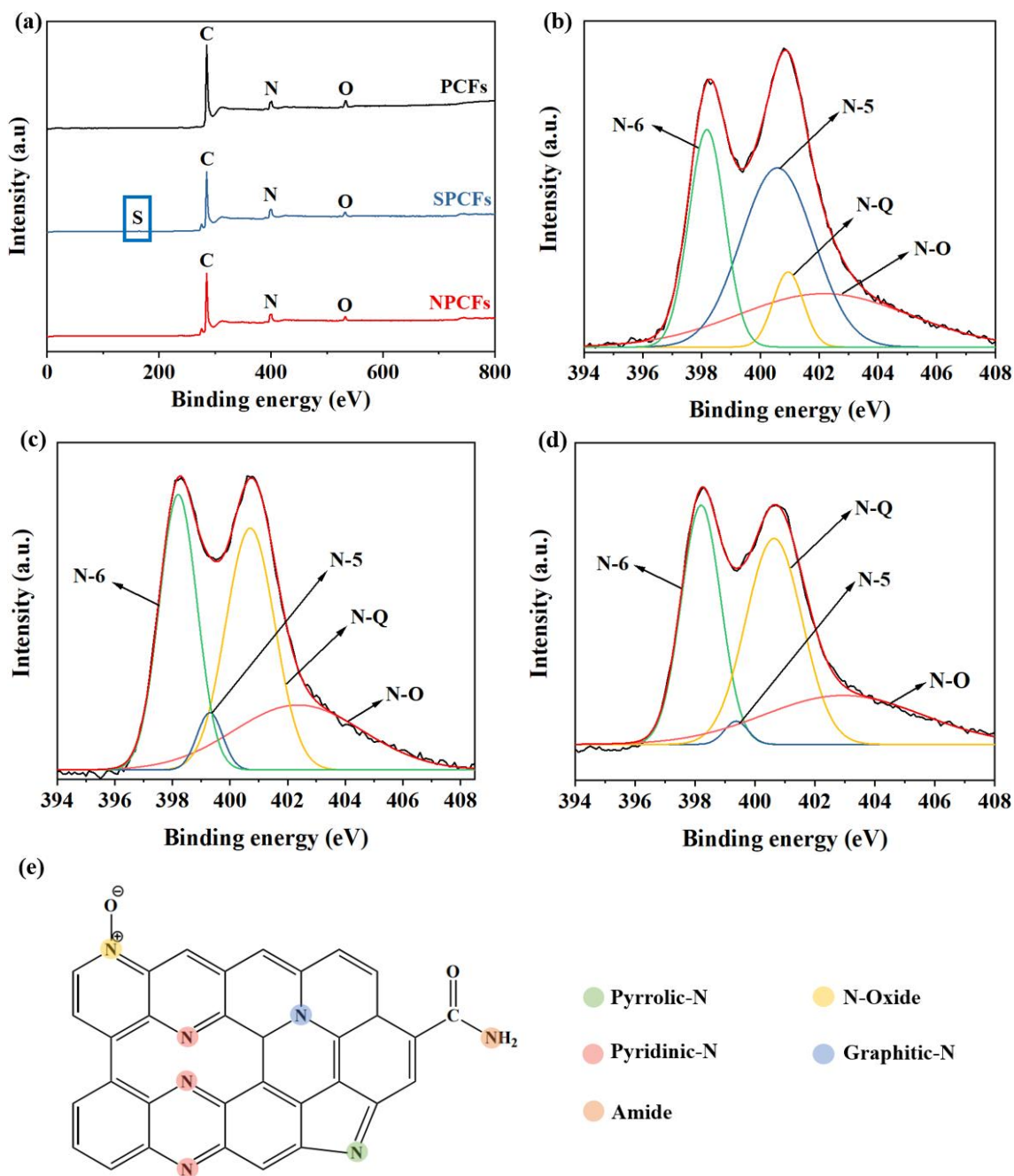


Figure 5.5. (a) XPS survey spectra of the three fibers, (b) N1s high-resolution spectrum of (c) PCFs, (d) NPCFs, (e) SPCFs, and (e) schematic model of N-containing surface functional groups on carbon fibers.

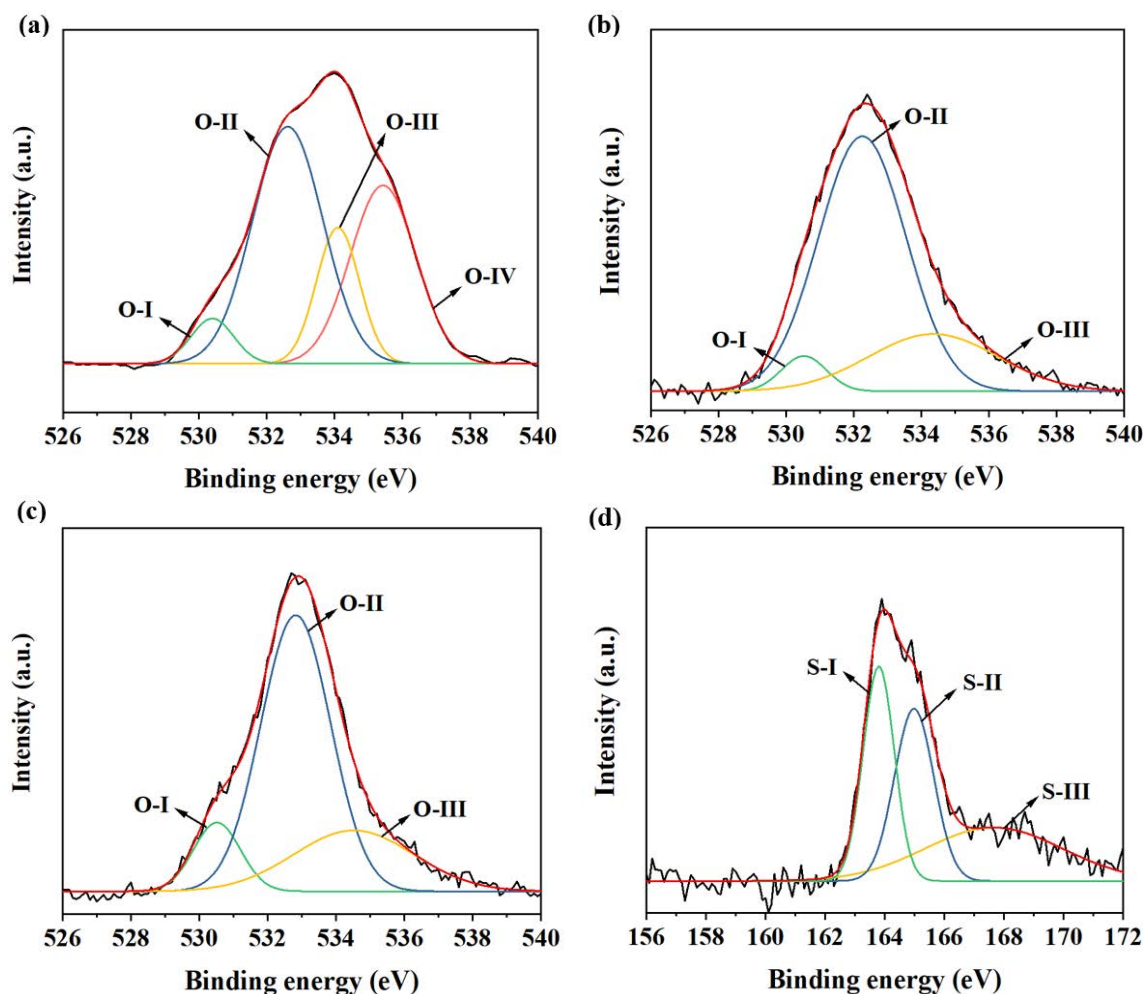


Figure 5.6. XPS high-resolution spectrum of O1s of (a) PCFs, (b) NPCFs, and (c) SPCFs; (d) S1p high-resolution spectrum of SPCFs fibers.

Relative atomic nitrogen, oxygen, and sulfur species concentrations in the porous fibers surface are detailed in **Table 5.2**. PCFs after urea (NPCFs) and thiourea activation (SPCFs) presented an increased total nitrogen content with values of 12.2 and 14.2%, respectively, compared to the starting material (PCFs) that shows a 7.8%, which confirms a high nitrogen doping yield.

In accordance with higher graphitization degree shown in Raman spectra after the heteroatom-doped process, pyridinic (N-6) and quaternary nitrogen (N-Q) peaks increased significantly in SPCFs and NPCFs. In contrast, pyrrolic nitrogen and/or amide groups (N-5) decreased in both fibers. This may be caused by the relatively low thermal stability of pyrrole and amide nitrogen groups, which at high activation temperatures, up to 800 °C, are mainly converted to more thermally stable species, such as N-Q and N-6

[170]. This result agrees with different previously reported studies using similar activation temperatures [171–173].

At the edges or defect sites of the carbon framework, pyridinic nitrogen provides a lone electron pair to the π system, which enhance ion diffusion and generate electrochemically active sites, leading to an increase in faradaic capacitance [174]. On the other hand, pyrrole nitrogen and oxidized pyridinic nitrogen exhibit exceptional charge mobility and advanced electron donor characteristics. In addition, quaternary nitrogen, which is incorporated in the graphitic layered structure, effectively improves electrical conductivity and charge transfer at high current density [175,176]. Several studies have explored the influence of nitrogen content on the capacitive behavior [53,93], concluding that the presence of nitrogen significantly influences and enhances capacitance values and rate capability. Therefore, it is expected that N-doped carbon fibers, NPCFs and SPCFs, improve the electrochemical performance of the PCFs starting material.

Relative surface concentrations of oxygen species decrease in both doping activation process. The presence of oxygen heteroatoms in the carbon structure might provide a pseudocapacitance storage mechanism through faradaic charge-transfer reactions [177]. In particular, the peak corresponding with chemisorbed water and/or amide groups was unnoticeable in doped fibers, since activation process involve applying high temperatures, and amide groups are thermally unstable species. Less oxygen-rich materials were obtained, and this suggests that N- and N/S-doping processes influence in the oxygen surface functionalities content. Although, the relative content of quinone-type oxygen, designated as O-I (C=O), increase for NPCFs, which has been shown to contribute actively to the pseudocapacitance, since is preferably located in defects sites or pores walls[144]. Furthermore, SPCFs fibers reached 0.4% of sulfur surface content. These results are consistent with previously reported ones using thiourea as heteroatom precursor[178,179].

Table 5.2. Relative atomic composition and surface content of nitrogen, oxygen, and sulfur species obtained by fitting N 1s, O 1s, and S 2p XPS spectra of PCFs, NPCFs, and SPCFs.

Material	Heteroatom functional group	Content (%); (binding energy (eV))	N/O/S (%)
PCFs	N-6	24.3; (398.2)	7.8
	N-5	40.4; (400.6)	
	N-Q	7.0; (400.9)	
	N-O	28.3; (402.5)	
	O-I	5.3; (530.4)	4.5
	O-II	46.2; (532.6)	
	O-III	16.2; (534.1)	
	O-IV	32.3; (535.4)	
NPCFs	N-6	36.5; (398.2)	12.2
	N-5	4.6; (399.3)	
	N-Q	34.9; (400.7)	
	N-O	24.0; (402.4)	
	O-I	10.8; (530.5)	3.3
	O-II	64.7; (532.3)	
	O-III	24.5; (534.4)	
SPCFs	N-6	30.1; (398.2)	14.2
	N-5	2.9; (399.4)	
	N-Q	42.6; (400.6)	
	N-O	24.4; (402.9)	
	O-I	5.0; (530.5)	3.5
	O-II	71.4; (532.8)	
	O-III	23.6; (534.5)	
	S-I/S-II	67.9 (163.8/165.0)	0.4
	S-III	32.1 (167.7)	

The presence of oxygen-containing functional groups in PCFs starting material and amino groups in urea and thiourea are believed to play a crucial role in the formation of C-N bonds. Doping-activation process involves a gradual transformation of nitrogen bonding configurations, starting from amide form nitrogen, progressing through pyrrolic and pyridinic species, and finally leading to the incorporation of "graphitic" nitrogen in the carbon framework as the temperature increases [180]. The differences found in N content for NPCFs and SPCFs are in accordance with previous work that followed a

similar experimental procedure for the doping-activation process [181]. Carbon fibers exhibited higher adsorption of thiourea from the aqueous solution than urea, due to differences in the basic character of both precursors.

A comparison of the structural and physicochemical parameters obtained for PCFs, NPCFs, and SPCFs can be found in **Table 5.3**.

Table 5.3. Summary of PCFs structural and physicochemical characteristics.

Material	PCFs	NPCFs	SPCFs
<i>Microscopy</i>			
Fiber diameter	100±4	94±2	90±2
<i>Raman</i>			
I _D /I _G	1.11	0.86	0.85
<i>N₂ adsorption/desorption analysis</i>			
SSA _{BET} (m ² g ⁻¹)	495.7	427.9	440.8
SSA _{micro} (m ² g ⁻¹)	366.1	271.1	305.6
Meso/micropore ratio	0.35	0.58	0.44
V _{tot} (cm ³ g ⁻¹)	0.33	0.31	0.30
V _{micro} (cm ³ g ⁻¹)	0.18	0.14	0.17
<i>Total heteroatom content</i>			
N (%)	7.8	12.2	14.2
O (%)	4.5	3.3	3.5
C (%)	87.0	84.5	81.9
S (%)	-	-	0.4

Chapter 6

*Porous carbon fibers with magnetite
nanoparticles*

This chapter describes a preliminary study of the incorporation of magnetite nanoparticles (MNPs) in the structure of porous carbon fibers (PCFs), and their influence on microstructure and overall porosity. PCFs derived from the nanocomposite formed by PtBA-*b*-PAN and Fe₃O₄ nanoparticles were produced by electrospinning and subsequent carbonization. **Figure 6.1** shows a scheme representing the preparation of PCFs derived from nanocomposite (PtBA-*b*-PAN/MNPs) and block copolymer (PtBA-*b*-PAN) precursors, designated as MNPs-PCFs and PtBA-PCFs, respectively.

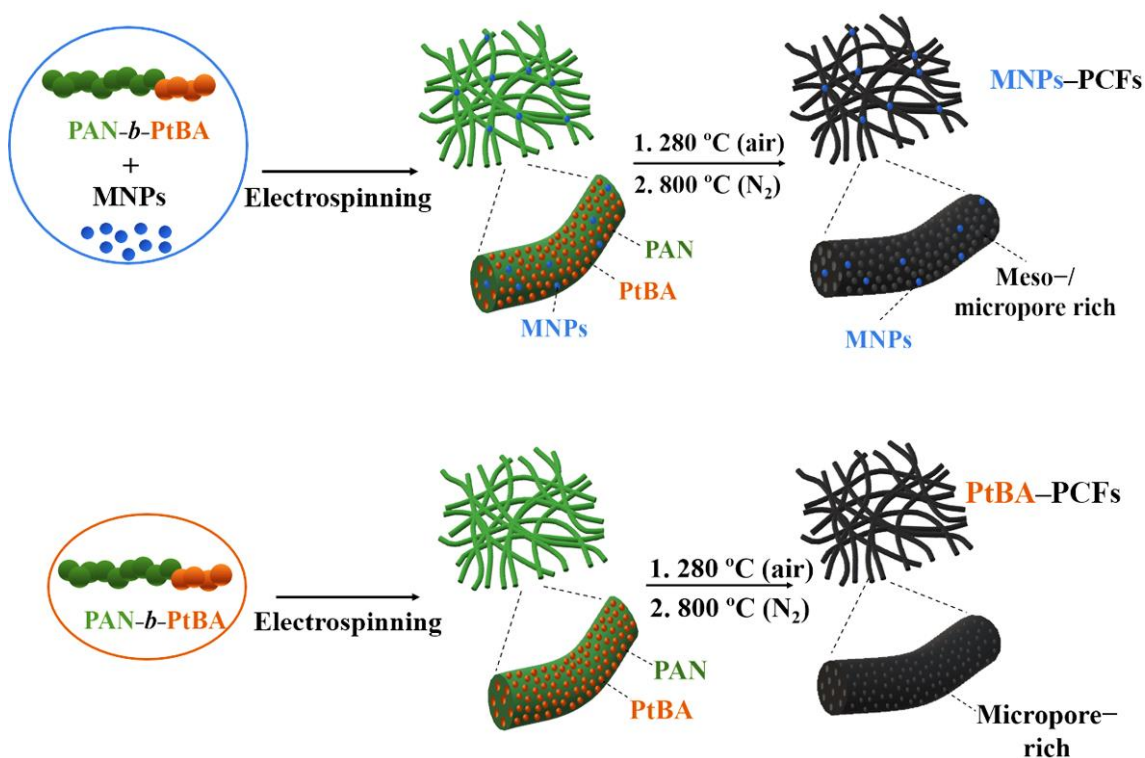


Figure 6.1. Scheme representing the preparation of MNPs-PCFs (above) and PtBA-PCFs (below).

As it was previously mentioned in **Chapter 5**, supercapacitors can be classified, according to the storage mechanism, as electric double-layer capacitors (EDLCs) or pseudocapacitors. EDLCs store energy by intercalating charges and forming a double layer of charges at the electrode-electrolyte interface [4]. On the other hand, pseudocapacitors store electrochemical energy, generally through a combination of faradaic redox reactions between electrolyte ions and active functional groups on the electrode surface, and the formation of the electrical double layer. This type of storage mechanism combines the advantage of redox reactions, which improves capacitance

values and energy density, and highly porous carbon materials, which improve electrode stability [6]. For this reason, carbon porous electrode materials containing redox active nanoparticles have been widely explored [182,183]. Many attempts have been developed to introduce transition metal oxide nanoparticles into a carbon matrix, such as MnO_2 [184] or Fe_3O_4 [72], to produce composite materials [185] that show some degree of pseudocapacitance. Among various metal oxide electrode materials, Fe_3O_4 with a theoretical capacity of $346.5 \text{ mA h g}^{-1}$ in alkaline solution based on possible variations in valence states ($\text{Fe}^{3+} \rightleftharpoons \text{Fe}^0$) and low cost has received wide attention [186]. However, Fe_3O_4 presents some limitations, including low surface area due to self-aggregation and low conductivity. These deficiencies can be overcome by producing composites with other carbon materials, such as graphene [187] or PAN-derived carbon fibers [188].

Therefore, the use of PCFs with well-controlled porosity, incorporating MNPs as electrodes materials for supercapacitors, is expected to combine the advantages of both components, resulting in materials with high surface area, suitable pore size distribution, high conductivity, and improved efficiency and stability. Furthermore, due to their combined properties, PCFs and iron oxide (Fe_3O_4) composites represent an excellent multifunctional material that has been used for a wide range of applications, including catalysis [189], oil adsorption [190], microwave absorption [191], and removal of contaminants from groundwater [192], among others (**Figure 6.2**). These magnetic composites present the advantage of being easily removed from solution using a magnet, which is especially useful for dye adsorption applications [193]. More specifically in electrochemical applications, including electrodes materials for supercapacitors [188] and Li-ion batteries [194], the Fe_3O_4 /PCFs composites have shown excellent electrochemical performance. In particular, the use of PtBA-*b*-PAN as carbon precursor containing iron oxide nanoparticles has proven to be an effective method to produce porous carbons with well-defined mesopores and high capacitance values [195].

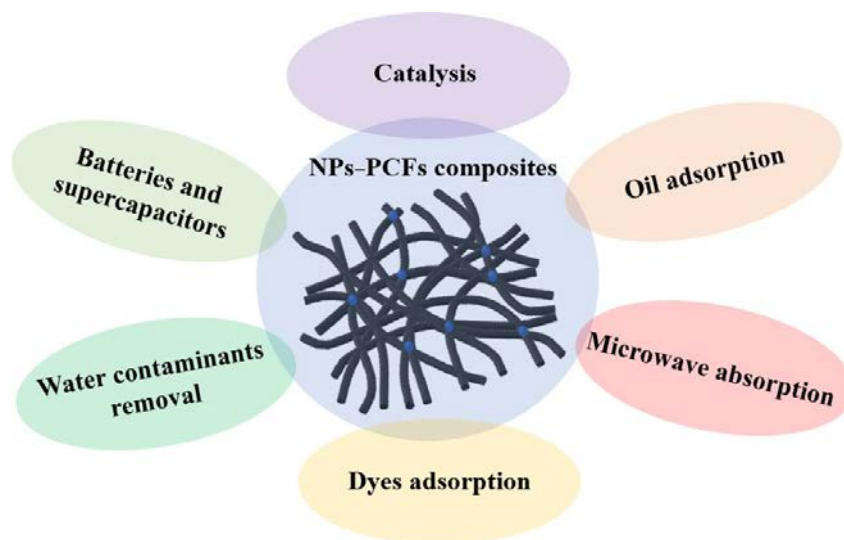


Figure 6.2. Scheme of the different applications of MNPs/PCFs composite multifunctional materials.

6.1. Experimental procedure

6.1.1. Synthesis of magnetic nanoparticles

The magnetite Fe_3O_4 nanoparticles (MNPs) were provided by the research group. MNPs were synthesized by high thermal decomposition of the organic precursors in solution according to previously reported procedure [196]. This method allows to control the morphology, size, and shape of the MNPs. Dibenzyl ether (BE) and 1-octadecene (ODE) were used as solvents, presenting different polarity and, therefore, different affinity with the precursor and the MNPs. Iron (III) acetylacetonate ($\text{Fe}(\text{acac})_3$) was used as iron source, oleic acid (OA), oleylamine (OAm), and 1,2-tetradecanediol (TDD) as surfactants and finally, benzaldehyde (BA) as additive or shape-directing agent. The MNPs obtained were relatively monodispersed, showing a slight variation in shape, varying from quasi-spherical to cubical or hexagonal shapes, with an average size of $\sim 10 \pm 2$ nm (**Figure 6.3**).

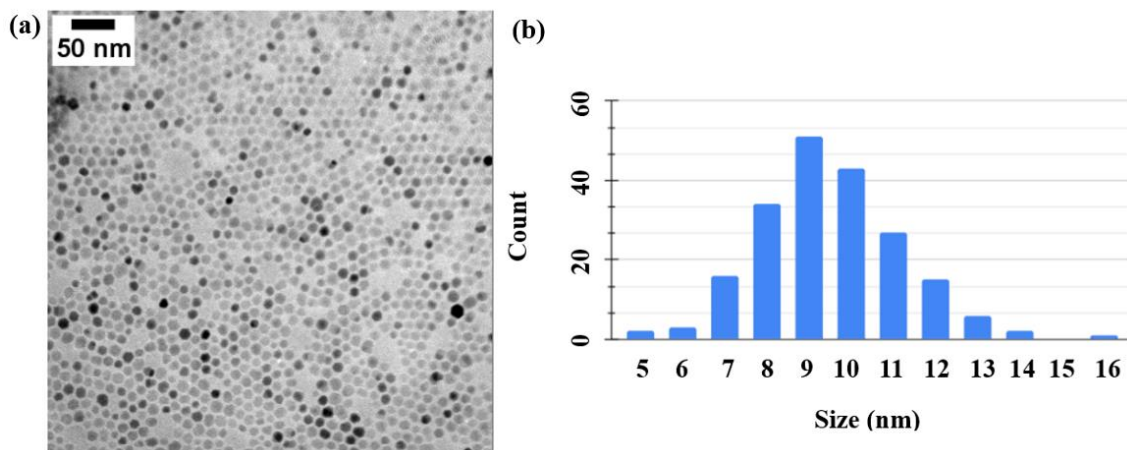


Figure 6.3. (a) TEM image of Fe₃O₄ magnetic nanoparticles and (b) Size distribution.

To obtain a stable dispersion of the MNPs in DMF (polar solvent), an exchange method was used to replace the hydrophobic ligands (oleylamine and oleic acid) to 4-hydroxibenzoic acid, which is a hydrophilic ligand [195]. After ligand exchange, a stable dispersion was prepared by sonication of ~2 wt% MNP in DMF.

6.2. MNPs–PCFs: Morphological and structural characterization

Fibers were obtained by electrospinning, using a mixture of 20 wt% PtBA-*b*-PAN in DMF with ~2 wt% MNPs dispersed in DMF. To ensure a homogenous blend, the mixture was ultrasonically dispersed for 4 h and stirred for 20 h prior to electrospinning. Throughout the mixing process during the transfer from one vial to another, a certain amount of MNPs was lost. Therefore, the effective amount of MNPs used in the electrospinning solution is expected to be lower than the initially intended concentration of 2 wt%. The electrospinning conditions and parameters were the same as those used to obtain nanofibers derived from PtBA-*b*-PAN (see **Table 4.2** in **Section 4.2, Chapter 4**), unlike the feed rate that was reduced to 0.5 mL h⁻¹ to avoid dripping.

The electrospun fiber mat shown in **Figure 6.4** exhibited highly disperse fiber diameters with some large size beads. This morphology suggests that the presence of MNPs could disrupt the jet flow, increasing the surface tension of the solution and causing dripping and electrospray in the process. According to previous work, uniform nanocomposite fibers can be produced from PAN/Fe₃O₄ nanocomposite, prepared from

~1.0 wt% Fe_3O_4 in a 10 wt% PAN DMF solution [197]. However, increased loading (> 5 wt%) resulted in higher viscosity solutions that destabilized the jet and produced non-uniform fibers, highlighting the difficulty of obtaining homogeneous and monodisperse fibers with high MNPs loading.

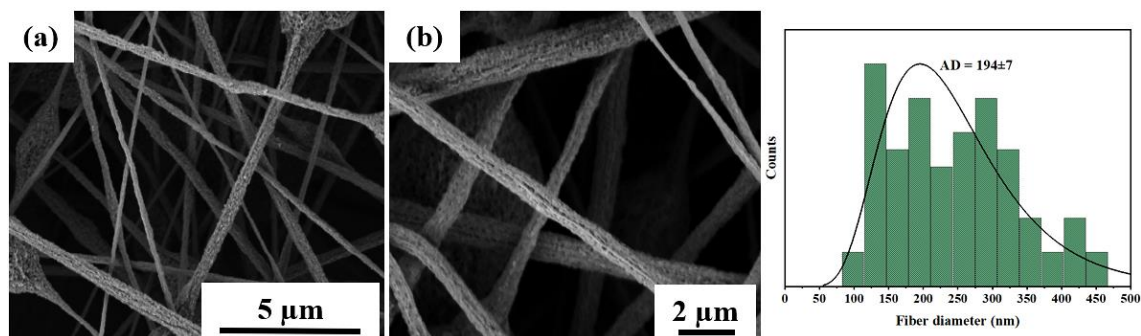


Figure 6.4. (a) and (b) SEM images of the fiber mat derived from PtBA-*b*-PAN containing a dispersion of MNPs, (c) Fiber diameter distribution.

Fibers obtained from PtBA-*b*-PAN showed diameters center around 62 nm (see **Section 4.3.1** in **Chapter 4**) and after adding ~2 wt% MNPs, fiber diameters increased to 194 nm. Depending on the nanoparticle (NP) size, and the interaction with the block copolymer, NPs can be selective towards a certain phase domain [198]. In general terms, small non-selective (no preferential affinity for blocks A or B) nanoparticles dispersed in an A-B block copolymer can be located in the interfacial region between block domains, while larger non-selective nanoparticles are situated mainly in both domains. In contrast, the large nanoparticles aggregates cannot be incorporated into the block copolymer phase separation morphology. Moreover, it was previously studied how the segregation of selective nanoparticles in a specific block can increase the domain volume, and it could be one of the reasons why the fiber diameters increased more than double.

Besides, fibers exhibited a remarkably rough surface, unlike the smoother surface observed in PtBA-*b*-PAN-based nanofibers without MNPs. This increase in roughness is caused by the influence of MNPs on the morphology obtained by microphase separation. Ying Lin et al. [195] reported similar iron oxide nanoparticles ($\text{Fe}_2\text{O}_3\text{-OH}$) surface modified with 4-hydroxylbenzoic acid and embedded in a PtBA-*b*-PAN matrix. The hydrophilic $\text{Fe}_2\text{O}_3\text{-OH}$ NPs selectively interact with PAN domains through hydrogen bonding with nitrile groups ($-\text{C}\equiv\text{N}$). This Van der Waals type of interaction between

hydroxyl and nitrile groups leads to a higher degree of phase segregation, and therefore explained the increase in surface roughness.

PtBA-*b*-PAN/MNPs-derived fiber mat was thermally annealed at 280 °C for 1 h under oxidizing atmosphere and carbonized at 800 °C for 1 h under N₂ flow. Energy dispersive spectrometry (EDS) was performed to qualitatively determine the presence of Fe atoms, which allows to confirm the successful addition of Fe₃O₄. In addition, its distribution throughout the fiber structure was evaluated. Elemental analysis identified the presence of C, N, and O atoms intrinsic to the block copolymer, and Fe atoms. Moreover, iron mapping showed a homogenous distribution along the fiber surface with an apparent concentration of around 0.8 wt% (**Figure 6.5**).

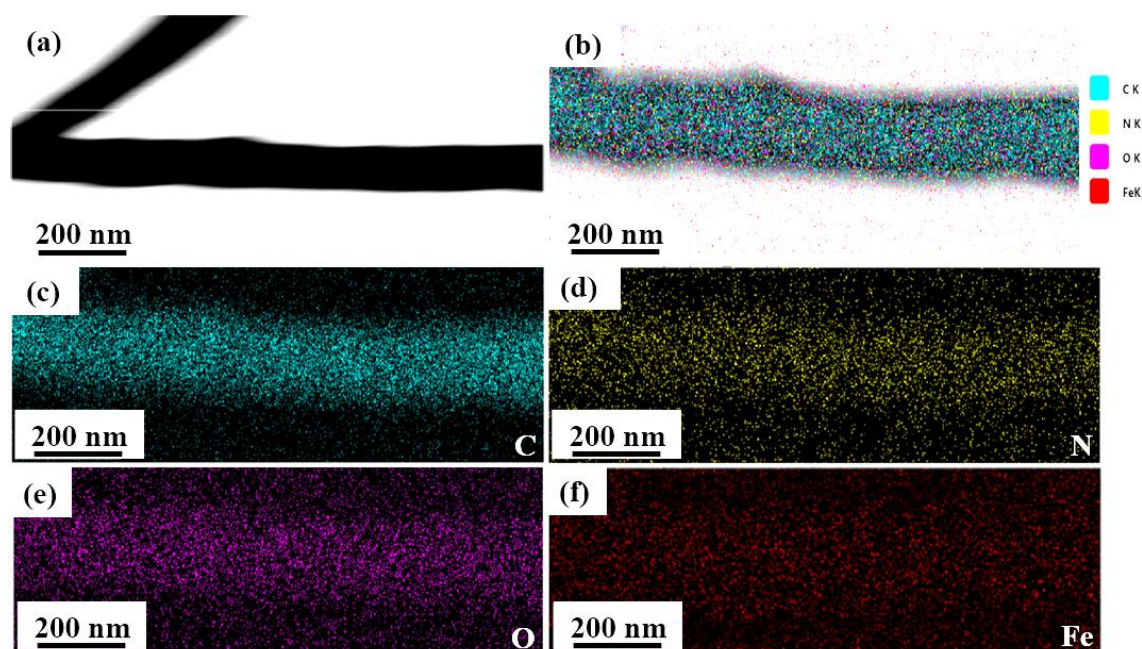


Figure 6.5. EDS images of MNPs-PCFs (a) isolated fiber, (b) overlay mapping of C, N, O and Fe, (c) C, (d) N, (e) O, and (f) Fe mapping.

Furthermore, focusing on the breaking point of the fiber, it is possible to detect some cluster between 50–100 nm (**Figure 6.6**). This MNPs clusters are often local stress concentrations [199], leading to increased fiber breakage after carbonization along these agglomeration points, thus reducing mechanical strength. The clusters formation can be reduced by modifying the protocol for MNPs dispersion.

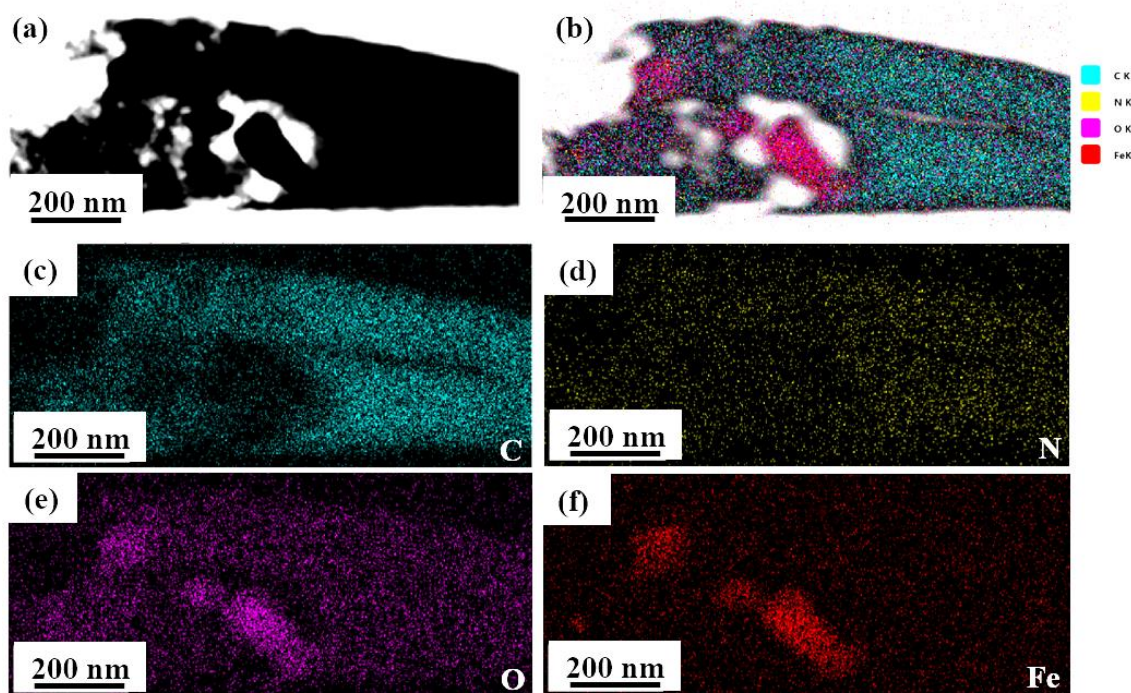


Figure 6.6. EDS images of MNP-PCFs at the breaking point (a) isolated fiber, (b) overlay mapping of C, N, O and Fe, (c) C, (d) N, (e) O, and (f) Fe mapping.

TEM was carried out in order to elucidate the distribution of MNPs along the fiber, as well as the influence on the porosity. As shown in EDS images, large clusters of MNPs can be detected along the breakpoint of the fiber (**Figure 6.7a**). In the surrounding areas of these clusters, large holes, or pores (~30 nm) can be seen. This is attributed to, as previously explained, large nanoparticles agglomerations cannot be incorporated into the block copolymer phase separation morphology. **Figure 6.7b** also showed some small, isolated nanoparticles dispersed into the carbon matrix.

On the other hand, as previously shown for PtBA-*b*-PAN derived PCFs (PtBA-PCFs; see **Figure 4.30** in **Chapter 4**), fibers appeared relatively dense and did not clearly display abundant mesopores. This suggests that MNP-PCFs may preferentially present micropores or small mesopores not detected by TEM with the acquisition conditions used.

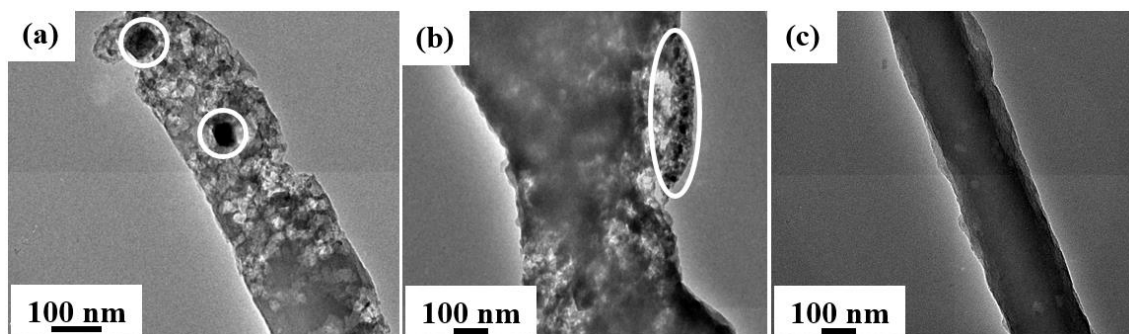


Figure 6.7. TEM images of MNPs-PCFs showing (a) large nanoparticle clusters, (b) small, isolated nanoparticles, and (c) fiber surface.

Raman spectroscopy was evaluated to examine and compare the carbon structure features with and without MNPs (**Figure 6.8a**). Both fibers (MNPs-PCFs and PtBA-PCFs) displayed the distinctive bands related to graphitic (“G band”) between $\sim 1560\text{--}1600\text{ cm}^{-1}$ and disordered features (“D band”) between $\sim 1320\text{--}1350\text{ cm}^{-1}$. The MNPs-PCFs spectra did not reveal the characteristic peak related to the presence of Fe_3O_4 around 680 cm^{-1} [195], due to the low MNPs loading. The intensity ratio between D and G bands (I_D/I_G) presented a value of 0.85 for both fibers, indicating that there were no significant changes in the carbon structure related to order and disorder features after introducing MNPs.

XRD patterns (**Figure 6.8b**) of both MNPs-PCFs and PtBA-PCFs, showed a broad peak around 25° that can be assigned to (002) diffraction, characteristic of pyrolytic or graphitic carbon structures. No additional peaks corresponding to the face center cubic structure of Fe_3O_4 can be observed [72,200], confirming a low MNPs content. As already seen for PtBA-PCFs, the low intensity together with the poor definition of the peak suggest a predominantly amorphous carbon structure for MNPs-PCFs. Furthermore, this peak seems to be shifted to higher angles ($\sim 28.3^\circ$) compared to PtBA-PCFs ($\sim 26.5^\circ$), which according to Braggs’ law, shows a decrease in $d_{(002)}$ interlayer spacing. This modification can be produced by the presence of MNPs, which are assumable located in the PAN domains. Consequently, these domains can increase in volume, which after carbonization can modify the orientation of the resulting layers of graphite. It has been studied for carbon fibers with embedded iron oxide nanoparticles, how these nanoparticles (NPs) induced the formation of a carbon shell of graphitic layers around the NPs surface [200].

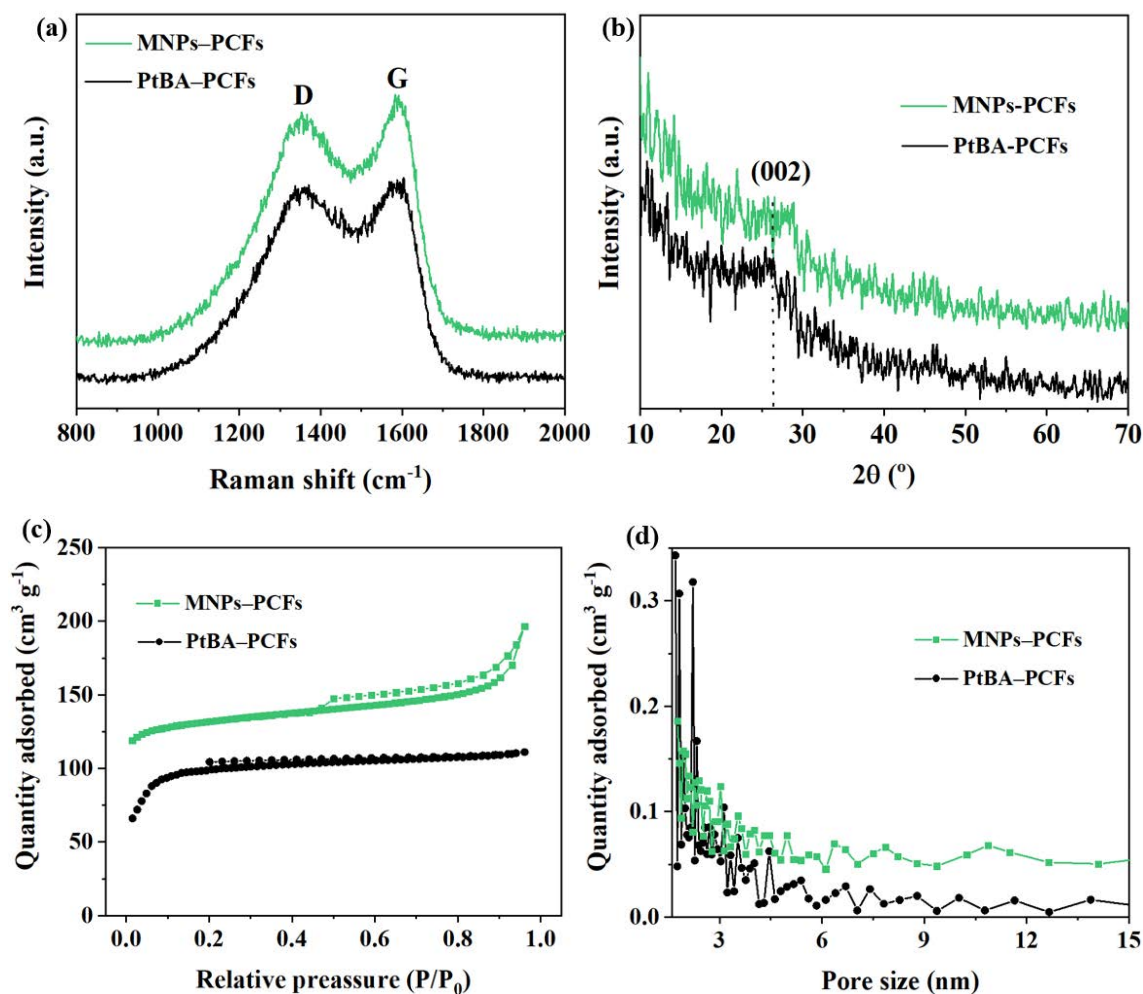


Figure 6.8. (a) Raman spectra, (b) XRD patterns, (c) N_2 adsorption/desorption isotherms, and (d) BJH pore size distribution of MNPs-PCFs and PtBA-PCFs.

To obtain information on the porosity modification after introducing MNPs, N_2 adsorption/desorption analysis was conducted. MNPs-PCFs showed a type IV isotherm (**Figure 6.8c**) related to the presence of mesopores, with a narrow hysteresis loop closed to a H4 type, which according to IUPAC [13] is associated with micropore and is often found in micro-mesoporous carbons. H4 loops are related to slit-shaped pores, which consist of small mesopores stacked between graphitic layers, as shown in **Figure 6.9** [201], unlike PtBA-PCFs that preferentially showed a microporous structure. These changes in the pore shape can be produced by the localization of the MNPs in the PAN domains. After carbonization, it can cause a modified rearrangement of the graphite layers compared to the pore structure observed without the addition of MNP.

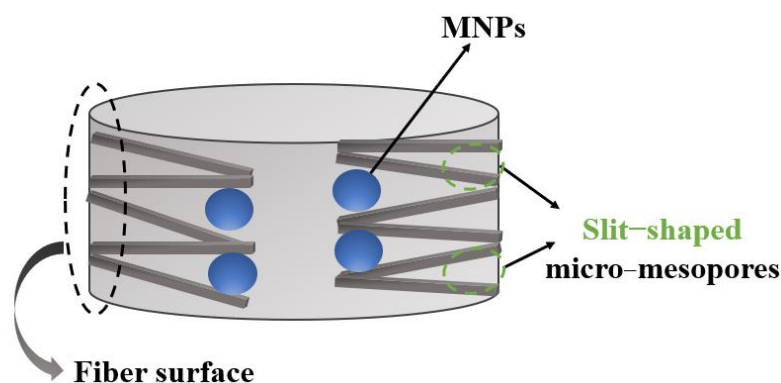


Figure 6.9. Scheme of the proposed type of pore structure for MNPs-PCFs.

The SSA_{BET} reached a value of $416.8 \text{ m}^2 \text{ g}^{-1}$ for MNPs-PCFs, which is considerably higher than that obtained for PtBA-PCFs ($304 \text{ m}^2 \text{ g}^{-1}$). Moreover, MNPs-PCFs showed an increase in the mesopore content as shown in **Table 6.1**. Mesopores as mentioned in previous chapters, enhance ion diffusion, thus improving electrochemical performance. Pore size distribution shown in **Figure 6.8d** exhibited an increase in mesopore adsorption in the range between 3–15 nm.

Table 6.1. MNPs-PCFs and PtBA-PCFs textural properties.

Material	SSA_{BET}^a ($\text{m}^2 \text{ g}^{-1}$)	SSA_{micro}^b ($\text{m}^2 \text{ g}^{-1}$)	V_{tot}^c ($\text{cm}^3 \text{ g}^{-1}$)	V_{micro}^d ($\text{cm}^3 \text{ g}^{-1}$)	SSA_{meso}/SSA_{micro}^e
MNPs-PCFs	416.8	314.5	0.26	0.16	0.33
PtBA-PCFs	304.0	236.75	0.17	0.13	0.28

^a BET surface area calculated from the linear part of the BET plot ($P/P_0=0.05-0.25$), ^b t-plot micropore area, ^c total pore volume, taken from the volume of N_2 adsorbed at $P/P_0=0.90$ and ^d total micropore volume taken from the volume of N_2 adsorbed at $P/P_0=0.015$, ^e mesopore/micropore ratio, where $SSA_{meso} = SSA_{BET} - SSA_{micro}$.

Even though this type of pore structure may introduce some ion diffusion resistance, compared to larger cylindrical type mesopores, narrow micropores have been shown to have a strong CO_2 adsorption potential [202]. Therefore, MNPs-PCFs could be an excellent candidate for CO_2 capture.

X-ray photoelectron spectroscopy (XPS) allows to analyze and determine the surface elemental composition of MNPs-PCFs. The full spectrum showed peaks

corresponding with C 1s, N 1s, O 1s, and slight visible peak around 710 eV corresponding with Fe 2p (**Figure 6.10a**).

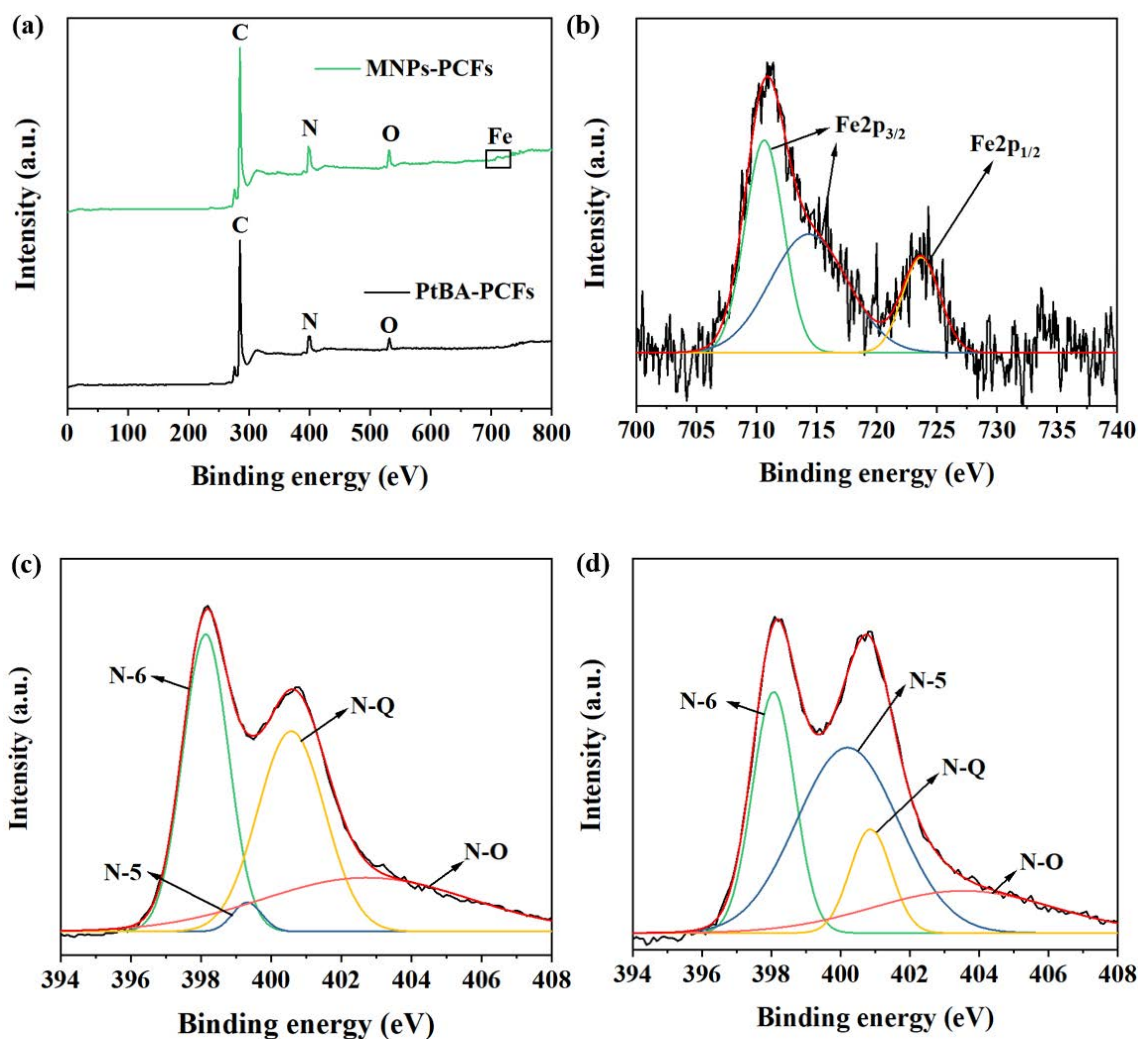


Figure 6.10. (a) Comparative XPS full spectra of MNPs-PCFs and PtBA-PCFs, (b) high-resolution Fe 2p spectrum, and high-resolution N 1s spectra of (c) MNPs-PCFs and (d) PtBA-PCFs.

Deconvolution of the high-resolution C 1s, N 1s, O 1s, and Fe 2p peaks leads to the surface composition compiled in **Table 6.2**. The relative N content increased from 12.6 % in PtBA-PCFs to 14.2 % when MNPs were added. As previously suggested by analyzing XRD patterns, MNPs are presumably positioned in PAN domains. Therefore, after carbonization, this arrangement is expected to lead to the formation of a carbon shell of graphitic layers around the MNPs surface. This causes the N-edge of graphitic layers to be more exposed at the fiber surface as illustrated in **Figure 6.11** and explains the

increase in pyridinic N content. The increase in the volume of PAN domains due to the presence of MNP also produced a significant increase in graphitic N.

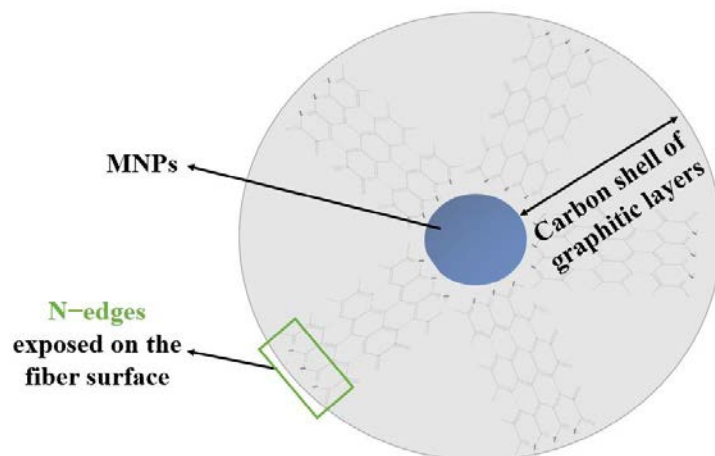


Figure 6.11. Scheme of the proposed carbon graphitic structure surrounding the NPs in the border regions of the fiber.

Likewise, the oxygen content increased after the addition of MNPs, since PAN is the precursor block O-containing functionalities, produced during the stabilization thermal treatment under air atmosphere. Moreover, a slight contribution to the total increase of O content can be due to the iron oxide (Fe_3O_4) nanoparticles.

Finally, the Fe 2p high-resolution presented two main peaks (**Figure 6.10b**), corresponding with $\text{Fe}2p_{3/2}$ at ~ 711.0 eV and $\text{Fe}2p_{1/2}$ at ~ 723.8 eV. $\text{Fe}2p_{1/2}$ peak is attributed to the contribution of Fe (II) and Fe (III) satellites. $\text{Fe}2p_{3/2}$ was deconvoluted into two different peaks: the first one includes the contribution of Fe (II), Fe (III) in octahedral positions, and Fe_2O_3 , the last two are likely to exist in the outermost layer of the MNPs due to the oxidative reactions during the stabilization thermal treatment. The second one includes the contribution of Fe (III) in tetrahedral positions [203,204]. The analysis of the Fe oxidation state is complicated due to the overlapping of the deconvolution of peaks related to Fe (II) and Fe (III) oxidation states. The Fe content along the fiber surface is significantly low (0.4 wt%), considering the initial amount introduced (~ 2 wt%), so part of the MNPs must be embedded in the carbon fiber matrix. Therefore, interior MNPs can only be accessible to the electrolyte ion through mesoporous channels. Looking for a higher contribution of pseudocapacitance, it would be necessary to introduce larger quantities, between 5–40 wt% [203,204].

Table 6.2. Relative atomic composition and surface content of nitrogen, oxygen, and iron species obtained by fitting N 1s, O 1s, and Fe 2p XPS spectra of MNPs–PCFs and PtBA–PCFs.

Material	Heteroatom functional group	Content (%); (binding energy (eV))	N/O/Fe (%)
MNPs–PCFs	N–6	34.8; (398.2)	14.2
	N–5	2.2; (399.3)	
	N–Q	34.4; (400.6)	
	N–O	28.6; (402.7)	
	O–I	5.3; (530.4)	5.2
	O–II	46.2; (532.6)	
	O–III	16.2; (534.1)	
	O–IV	32.3; (535.4)	
	Fe (III) oct	39.1; (710.6)	0.4
	Fe (III) tet	43.8; (714.4)	
	Fe (III) sat	17.0; (723.7)	
PtBA–PCFs	N–6	26.9; (398.1)	12.6
	N–5	44.0; (400.2)	
	N–Q	10.5; (400.9)	
	N–O	18.6; (403.5)	
	O–I	8.4; (530.2)	4.0
	O–II	73.4; (532.1)	
	O–III	18.1; (534.1)	

In summary, according to the structural and textural characterization, the addition of low amounts of MNPs seems to have great influence on the block copolymer phase separation, giving rise to a stronger segregation between blocks. This segregation increase produces several changes in the fiber morphology, including the formation of large size beads, rough surfaces, and larger diameters. After carbonization, MNPs–PCFs exhibited higher specific surface area values and pore shape variations. Moreover, the addition of MNPs modifies the heteroatom surface content, increasing graphitic and pyridinic nitrogen. Improving the MPNs dispersion protocol into the block copolymer matrix, as well as increasing the nanoparticle loading, will be the next steps to continue developing this early stage project.

Chapter 7

*Porous Carbon Fiber material:
electrochemical performance*

Throughout this chapter, the capacitive properties of the different porous carbon fibers (PCFs) produced in this thesis work will be examined. The results will be analyzed based on the morphological and structural characteristics that have been previously outlined. According to the morphology, pore structure and surface chemical composition presented in the different PCFs, it was demonstrated how these physicochemical properties greatly influence their capacitive behaviour, as studied and verified in previous works [38,205,206].

Depending on PCFs mat fragility, electrodes were prepared as a ‘slurry’ or paste composed of an agglutinant, conductive additive and PCFs active material or directly used as self-standing electrodes. An aqueous KOH 6M solution was used as electrolyte for all electrochemical measurements since it allowed a relatively high potential voltage against Ag/AgCl reference electrode (0–0.8 V). Moreover, nickel foam, which was used as current collector, is stable in alkaline electrolytes. Nickel foam was selected due to low cost, low electrode–electrolyte contact resistance [207], and easy processing. As it was explained in **Chapter 2**, most of the electrochemical measurements were performed using a three-electrode cell, even though some PCFs were tested as well in a symmetrical cell. Platinum wire and Ag/AgCl were used as counter and reference electrodes, respectively. To evaluate the PCFs capacitive behavior, cyclic voltammetry (CV), galvanostatic charge–discharge (GCD), and impedance spectroscopy (EIS) were tested. A more detailed experimental procedure can be found in **Chapter 2**.

7.1. PCFs derived from PS-*b*-PAN copolymer

Extensive research has been carried out on the use of PAN-based block copolymers as precursors for the development of porous carbon electrode materials for supercapacitors [208]. Among them, PS-*b*-PAN copolymer has been used as template material to obtain well-defined hierarchical porous carbons in powder or bulk form [60,209]. Polystyrene (PS) effectively serves as sacrificial block or self-templating agent, promoting the formation of mesopores that enhance ion diffusion, ensuring optimal performance.

However, the use of block copolymers (BCPs) as precursors to produce PCFs is a relatively recent approach [64]. These materials exhibit several advantages over porous carbons in powder or bulk form, such as higher specific surface areas and a continuous structure that results in more efficient ion and electron transport [210]. This work examines the capacitive performance of PCFs and carbon powder (bulk) material, produced with the same PS-*b*-PAN precursor, to demonstrate the advantages of PCFs in terms of capacitance values. The bulk material electrode was prepared as follows (previously described in **Chapter 2**): pressing into a clean nickel foam a mixture of active material (~ 1 mg), carbon black, and PTFE 60% dispersion in water with 80:10:10 proportion, respectively. On the other hand, PCFs were directly used as self-standing electrodes, by pressing a piece of PCFs mat in the middle of two nickel foam sheets.

Figure 7.1a shows the CV curves measured at 50 mV s^{-1} for PCF and bulk carbon materials, exhibiting a typical rectangular shape close to an electric double layer capacitor (EDLC) storage mechanism material. None of the curves presented discernible redox peaks, associated with pseudocapacitance. However, they exhibit a slight distortion in reference to the ideal behavior, which reflects a certain polarization resistance, especially in the case of bulk materials [211]. Distortions in the PCFs curve could evidence some intrinsic resistance of the material to electrolyte diffusion. This may be attributed to the ink-bottle pore shape found in PCFs, as ion diffusion may be limited or restricted when crossing the pore neck.

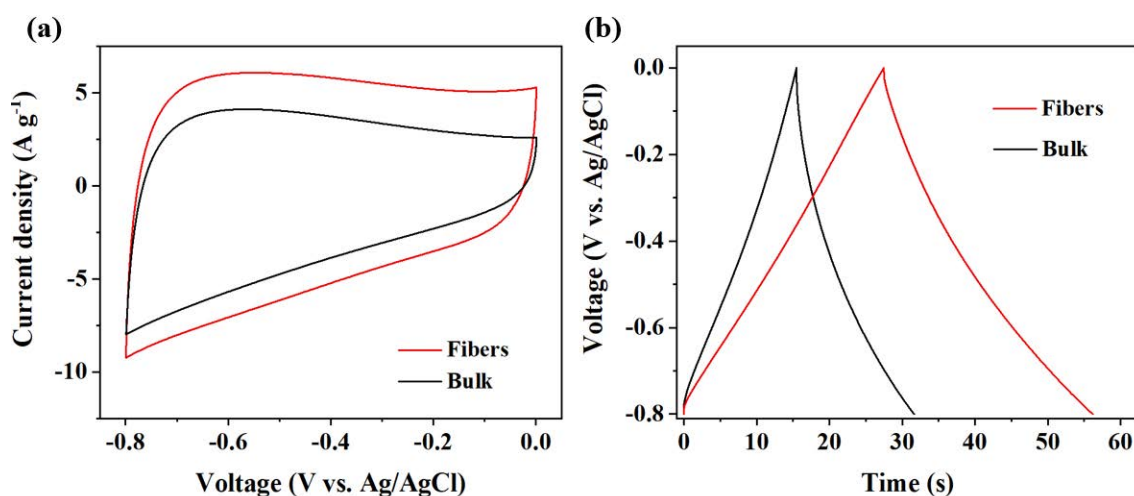


Figure 7.1. (a) CV curves at 50 mV s^{-1} , and (b) GCD curves at 5 A g^{-1} of PCFs and powdered or bulk material.

Consistent with phase separation theories and since pore size and shape have a significant influence on the sacrificial block domains size, increasing the volume fraction of PS suggests that it could gradually evolve from spherical/cylindrical domains to full cylindrical domains. However, as explained in previous chapters, the phase separation and self-assembly of PS-*b*-PAN during electrospinning do not lead to the typical thermodynamic morphologies, but kinetic control operates. Therefore, the generated morphology does not follow the typical block copolymer phase separation diagrams [212]. Although it does not guarantee the formation of well-defined thermodynamic microphases, increasing the volume fraction of polystyrene (PS) can potentially modify the mesopore shape towards a form that offers lower ion-diffusion resistance. Indeed, for PCFs produced from PMMA-*b*-PAN copolymers, it was studied how variations in sacrificial block volume fraction mainly affect the mesopore size and micro-/mesopore ratio. It was reported that only one composition led to a good balance between pore size and capacitance values [58].

In addition, deviation from ideal behavior can be influenced as well by certain contribution from the pseudocapacitive storage mechanism involving fast and reversible redox reactions due to N and O surface functionalities [213].

Galvanostatic charge-discharge (GCD) curves measured at 5 A g^{-1} are shown in **Figure 7.1b**. Both curves displayed similar charge-discharge rates, close to a triangular shape without an appreciable ohmic drop. Consistent with CV data, some deviation from the ideal behavior can be found for both, PCFs and bulk material, due to some ionic or electronic resistance contribution. Capacitance values were calculated from the discharge curve at 1 A g^{-1} , reaching 254 F g^{-1} for PCFs. This value is much higher than 145 F g^{-1} found for the bulk material. The high capacitance value obtained for PCFs is due to the synergistic effect of relatively high SSA_{BET} ($495.7 \text{ m}^2 \text{ g}^{-1}$), hierarchical porosity rich in micro- and mesopores, as well as moderately high content of N/O surface functionalities (7.8 and 4.5 %, respectively). These results demonstrate the improved electrochemical performance by producing fibers instead of powdered carbons from block copolymer templating.

PCFs capacitance value can be found in **Table 7.1**, as well as capacitance values obtained for previously reported fiber and powder carbon materials derived from

PAN-based block copolymers or blends. Our fibers show competitive values without requiring additional activation process to increase porosity.

Table 7.1. Specific capacitance (C_s) values measured at different current densities ($A\ g^{-1}$) of various porous carbon electrode materials.

Material	Precursor	SSA _{BET} ($m^2\ g^{-1}$)	C_s ($F\ g^{-1}$)	Electrolyte	Ref
Powdered carbons					
S/N-doped porous carbons	PBA- <i>b</i> -PAN	478	236 ($0.1\ A\ g^{-1}$)	KOH 6M	[208]
Open-ended hollow carbon spheres	PAN- <i>b</i> -PS- <i>b</i> -PAN	954	185 ($0.625\ A\ g^{-1}$)	KOH 2M	[60]
N-doped hierarchical porous carbons	PS- <i>b</i> -PAN/ KOH activation	2105	230 ($1\ A\ g^{-1}$)	KOH 6M	[209]
Mesoporous carbons	PS- <i>b</i> -P4VP/ KOH activation	1583	249 ($0.5\ A\ g^{-1}$)	KOH 6M	[214]
Fibers					
Linear-tube carbon nanofibers	PAN/PS	212	188 ($0.5\ A\ g^{-1}$)	LiOH 3M	[133]
Multichannel PCFs	PAN/PS	750	250 ($1\ A\ g^{-1}$)	KOH 6M	[215]
N-doped multi-nano-channel PCFs	PAN/PS	840	461 ($0.25\ A\ g^{-1}$)	H ₂ SO ₄ 1M	[216]
Mesoporous carbon nanofibers	PAN/ PAA- <i>b</i> -PAN- <i>b</i> - PAA	250	256 ($0.5\ A\ g^{-1}$)	KOH 4M	[217]
PCFs	PAN/PMMA	683	140 ($0.5\ A\ g^{-1}$)	KOH 6M	[218]
Interconnected PCFs	PMMA- <i>b</i> -PAN	503	360 ($1\ A\ g^{-1}$)	KOH 6M	[64]
Hierarchical PCFs	PS- <i>b</i> -PAN	496	254 ($1\ A\ g^{-1}$)	KOH 6M	This work

To further evaluate the behavior of PCFs, electrodes were tested in a symmetrical Swagelok type cell (**Figure 7.2**). **Figure 7.2a** shows CV curves measured at different sweep rates. The curves presented a rectangular shape, which is maintain at higher sweep

rates. CV deviations observed in three-electrode cell measurements were not visible in the symmetrical setup, which suggests that deviations from ideal behavior can be produced by intrinsic resistance derived from the electrochemical setup as well. GCD curves (Figure 7.2b), exhibited an almost triangular shape with a specific capacitance value of 234 F g^{-1} measured at a current density of 1 A g^{-1} .

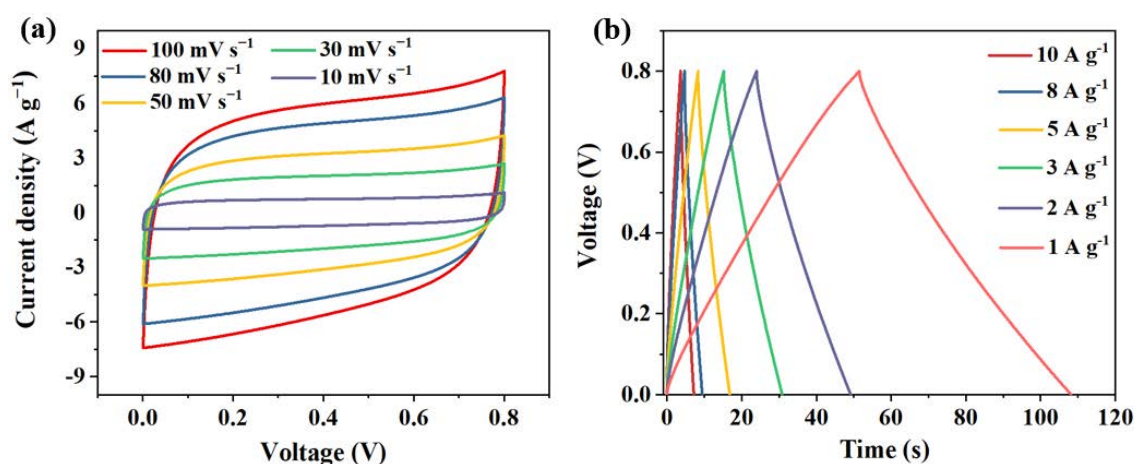


Figure 7.2. PCFs symmetrical cell measurements; (a) CV curves at different sweep rates, and (b) GCD curves at different current densities.

Electrochemical Impedance Spectroscopy (EIS) data had been represented as a Nyquist diagram in Figure 7.3a, which exhibited three main regions. At high frequencies, displayed a semicircle shape. From the intersection of semicircle region of Nyquist plot with real part (Z' axis) at higher frequencies, series resistance (R_s) value can be obtained. By using a combination of resistive and capacitive elements, the equivalent circuit shown in Chapter 2 (Figure 2.6) was defined to describe the impedance behavior of these porous materials. From the fit with the equivalent circuit, R_s gives a value of 0.25Ω . This element is responsible for the dissipation of the stored energy, and its magnitude limits the overall power performance of the electrochemical cell. Therefore, a low value implies higher efficiency. Furthermore, R_s can be related to the electrode internal resistance, a low value suggests a relatively high electronic conductivity.

The clear semicircle shape at lower frequencies represents the impedance response associated with charge transfer processes occurring at the electrode–electrolyte interface. The charge–transfer resistance (R_{CT}) value can be obtained from the semicircle diameters. R_{CT} is mainly governed by Faradaic process involving redox reactions with

heteroatom-containing functionalities at the electrode surface. In PAN-derived porous carbon material, a contribution to the charge-transfer resistance is expected due to the inherent N and O functionalities. Moreover, this resistance can be associated to the contribution of interfacial impedance occurring at the current collector/active material interface [219,220]. PCF exhibited a relatively low R_{CT} value of $0.5\ \Omega$, reflecting some pseudocapacitance phenomena through additional Faradaic redox reactions, coming from the N/O-containing surface functionalities. The R_{CT} value also is affected by the pore structure. In this regard, hierarchical porosity facilitates the ion-diffusion through the material, resulting in low R_{CT} values. Microporous structures with small pores ($< 0.7\text{ nm}$) tend to exhibit higher values, due to the hindered ion-diffusion. The presence of mesopores, not only increase the accessible-surface area, but also provide pathways that increase ion-diffusion. The structural and textural characterization evidence that PCFs exhibited a relatively high meso-and micropore ratio that contribute to decrease the R_{CT} value.

As shown in **Figure 7.3.a** the semicircle shape is followed by a transition zone in the high and mid-high frequencies region, which represents the Warburg impedance region/line (B–C region in **Figure 2.6**). This resistance is mainly associated with the ion diffusion. At the lower frequencies, an ideally polarizable capacitance would give rise to a straight line parallel to the imaginary axis [221]. However, the low-frequency segment clearly showed a slope inclination, which suggests that PCFs presents certain degree of ion resistance, probably due to ink-bottle type of pores, as ion diffusion may be limited or restricted when crossing the pore neck.

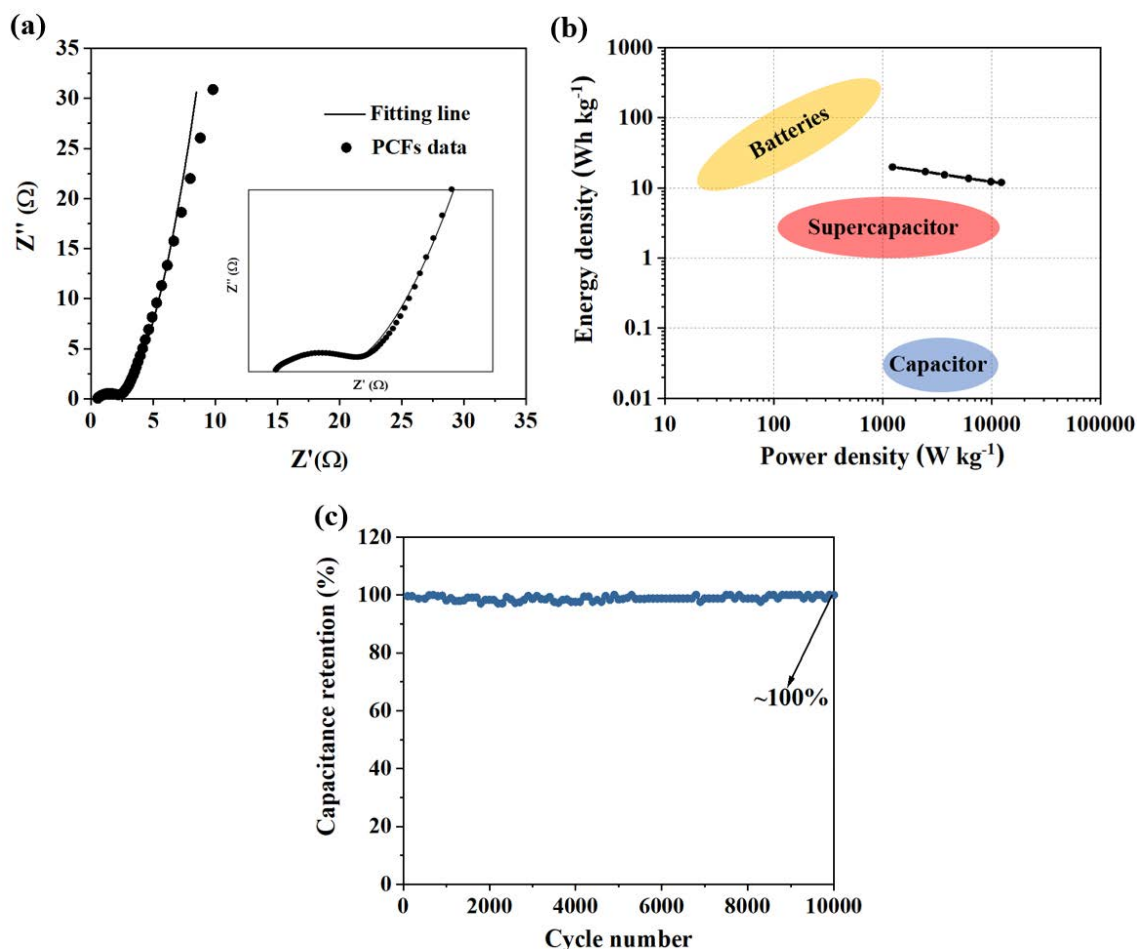


Figure 7.3. PCFs symmetrical cell measurements; (a) EIS diagram, (b) Ragone plot and (c) cycle stability.

Ragone plot of the fibers (**Figure 7.3b**) displayed a high energy density and power density of 20 W h/Kg and 12,300 W/Kg, respectively. Electrode stability was further evaluated (**Figure 7.3c**). Capacitance remained stable without noticeable degradation along 10,000 cycles measured at 100 A g⁻¹, showing a capacitance retention of 99.9% and significant electrode stability.

7.2. Sacrificial block and degree of polymerization influence

Throughout **Chapter 4**, the influence on the BCP precursor phase-separation of the sacrificial block nature and molecular weight has been examined, as well as their effect on the PCFs pore structure and physicochemical properties. In this section, the capacitive behavior of PCFs derived from BCPs presenting different sacrificial block and

total degree of polymerization (N) has been studied. In this regard, the electrochemical performance of PS-*b*-PAN-derived PCFs (PS-PCFs) and PtBA-*b*-PAN-derived PCFs (PtBA-PCFs) has been compared. The capacitive behavior of PCF obtained from high molecular weight PS-*b*-PAN (HN_PS-PCFs) has been analyzed.

The PCFs electrodes were tested in a three-electrode electrochemical cell. PtBA-PCFs exhibited narrow fiber diameters (~ 62 nm) and HN_PS-PCFs showed some beads during the fiber production process, leading in both cases to poor mechanical strength of the fiber mat and consequently, they cannot be used as self-standing electrodes. The electrodes were prepared as follows: pressing into a clean nickel foam a mixture of active material (around ~ 1 mg), carbon black, and PTFE 60% dispersion in water with 80:10:10 proportion, respectively. Contrary, PS-PCFs exhibited sufficient mechanical consistency to be used as self-standing electrodes.

Cyclic voltammetry (CV) curves measured at 50 mV s^{-1} are shown in **Figure 7.4a**. PS-PCFs, PtBA-PCF and HN_PS-PCFs curves follow a characteristic rectangular-shaped, without visible faradaic peaks. However, some inclination or distortion was observed for both, PtBA-PCFs and HN_PS-PCFs, due to an increased resistivity or ion resistance. Furthermore, the area under the CV curve also decreased for both materials, indicating lower capacitance values, compared to PS-PCFs curve. Galvanostatic charge-discharge (GCD) curves measured at 5 A g^{-1} (shown in **Figure 7.4b**) presented some deviation as well from the ideal capacitive behavior, although the obtained curves are close to triangular-type shapes without appreciable IR drop. The specific or gravimetric capacitance (C_s) values was calculated from the discharge curve at 1 A g^{-1} , reaching 203 and 171 F g^{-1} for PtBA-PCFs and HN_PS-PCFs, respectively. Those values are significantly lower compared to 254 F g^{-1} obtained for PS-PCFs.

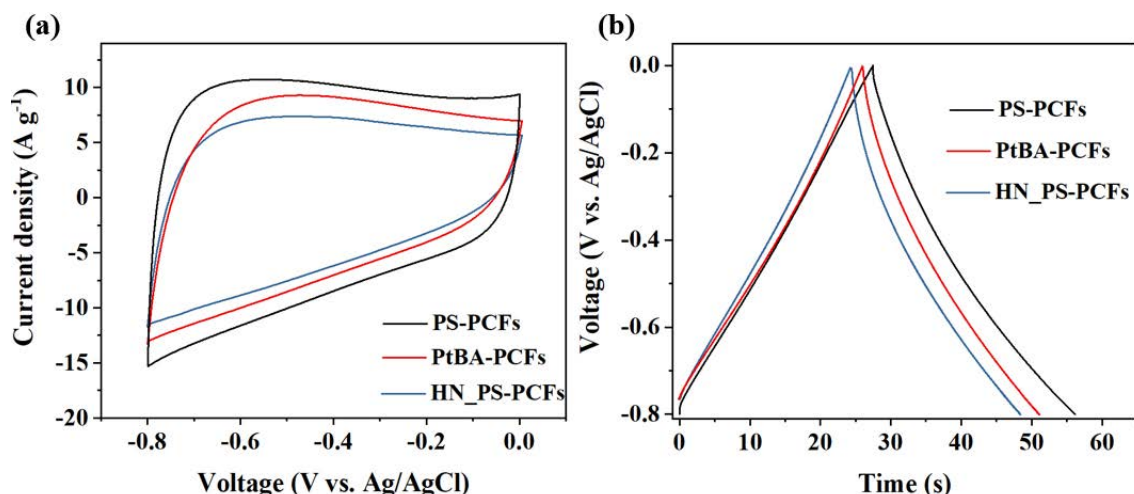


Figure 7.4. (a) CV curves at 50 mV s^{-1} and (b) GCD curves at 5 A g^{-1} of PS-PCFs, PtBA-PCFs and HN_PS-PCFs.

Capacitance seems to be greatly influenced by the surface area, since a decrease in SSA_{BET} values results in lower capacitance values. The bar graph in **Figure 7.5a** shows the correlation between SSA_{BET} and capacitance values calculated for the PCFs under study. Since the electrical conductivity in PtBA-PCFs is expected to be higher than that in PS-PCFs due to the higher graphitization degree and higher content of graphitic nitrogen, lower capacitance values and larger CV and GCD distortion may be produced by an increase of ion resistance rather than electrical resistance. Therefore, for PtBA-PCFs, it is suggested that the decrease in capacitance is due to the lower mesopore content. The presence of mesopores serves as ion-reservoirs and ion transport pathways reducing distances from the bulk electrolyte to micropores active sites. In a predominantly microporous structure, such as that obtained for PtBA-PCFs, the electrolyte ions usually exhibit higher diffusion resistance through the carbon material. These results are in agreement with other mesopore-dominated carbon materials, that showed a significant increase in the capacitance values compared to micropore-dominated materials [222]. Besides, HN_PS-PCFs, characterized by a low pore density structure, exhibited an insufficient SSA_{BET} value and micropore content, resulting in a poor capacitive behavior.

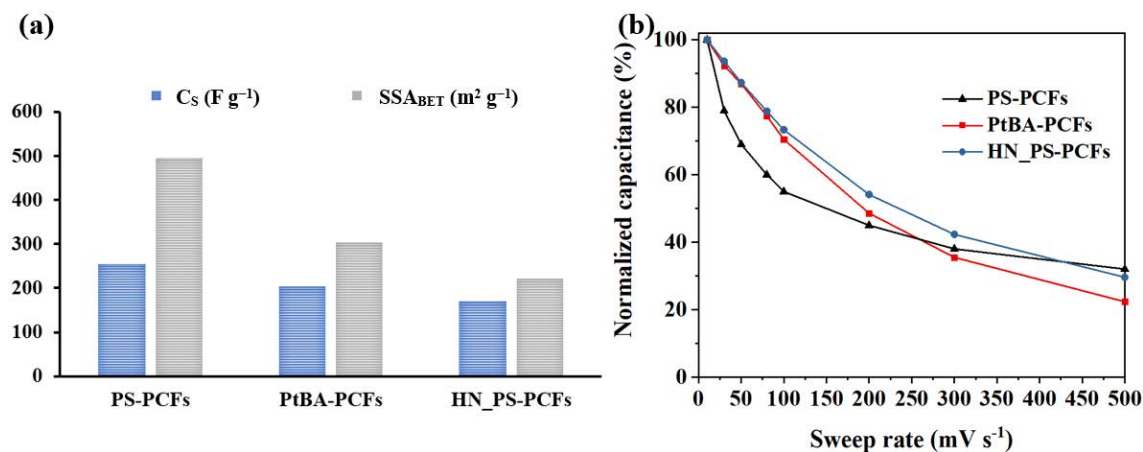


Figure 7.5. (a) Specific capacitance (C_s) and specific surface area (SSA) values, and (b) capacitance retention at different sweep rates for PS-PCFs, PtBA-PCFs and HN_PS-PCFs.

From the CV curves measured at different sweep rates, capacitance retention has been determined. Contrary to expectations, capacitance retention up to $300 mV s^{-1}$ is higher for both PtBA-PCFs and HN_PS-PCFs than for PS-PCFs. This may be attributed to an increase in the surface N content, since PtBA-PCFs and HN_PS-PCFs presented 12.4 and 16.1 %, respectively, compared to 7.8 % found in PS-PCFs. It has been previously demonstrated for carbon porous materials how increasing heteroatom surface content leads to an improvement in rate capability [223,224]. Moreover, capacitance retention reached for the PCFs materials under study does not exceed 35 %, showing a 32.8% for PS-PCFs, which is a value that could be improved. As previously discussed, some mesopores present an ink-bottle shape and at higher sweep ion-access through the bottleneck may be further hindered.

In summary, it has been shown how larger specific surface area with suitable pore size distribution, including a high content of micro- and mesopores, is crucial to achieve higher capacitance values. However, introducing N-containing surface functional groups, seems to improve rate capability due to fast redox reaction at the electrode surface that enhance electrolyte ion adsorption. Although, it has been studied how N surface functional groups increases the basicity of the surface material and benefit the proton adsorption of acidic electrolytes compared to basic ones [225]. Therefore, the testing of PCFs materials in H_2SO_4 aqueous electrolyte will be further needed in future research to possibly improve the electrochemical performance.

7.3. N and N/S co-doped PCFs

An activation process of PCFs derived from PS-*b*-PAN copolymer was carried out using urea and thiourea heteroatom precursors to obtain N-rich and N/S-rich PCFs, respectively. The resulting N-doped (NPCFs) and N/S co-doped (SPCFs) PCFs showed different relative N and O concentration (12.2% and 3.3% for NPCFs, and 14.2% and 3.5% for SPCFs) along the fiber surface without compromising specific surface area. Moreover, SPCFs showed a relative low concentration of 0.4 % of S-containing surface functionalities. However, slight variations were found with respect to pore structure and pore size distribution (see **Chapter 5**). In this section, the influence of the N and S doping process on the electrochemical performance have been examined. Since NPCFs and SPCFs exhibited certain fragility after the activation process involving some fiber break, the mechanical resistance of the fiber mat seems to decrease compared to PCFs before activation. For this reason, NPCFs and SPCFs electrodes were prepared as a ‘slurry’ pressed into Ni foam.

Electrodes of PCFs, NPCFs, and SPCFs were tested by cyclic voltammetry (CV) at different sweep rates. The **Figure 7.6a** shows CV curves measured at 50 mV s⁻¹. The three fiber materials showed a rectangular shape voltammogram, close to an ideal electric double-layer capacitor (EDLC) with small deviations. As previously explained, this behavior can be attributed to the high content of surface functional groups containing N and O heteroatom, and S for SPCFs, leading to a slight pseudocapacitive contribution [159]. Both NPCFs and SPCFs activated fibers exhibited larger areas under the CV curve, suggesting an increase in capacitance compared to the starting PCFs material.

This suggestion is confirmed by testing the materials to galvanostatic charge-discharge (GCD) at different current densities (**Figure 7.6b**). All charge-discharge curves (PCFs, NPCFs and SPCFs) measured at 5 A g⁻¹ presented symmetrical triangular shape, without appreciable ohmic drops, demonstrating excellent –cat a 1 A g⁻¹ current density and are displayed in **Table 7.2**. NPCFs shown the highest value of 341 F g⁻¹, followed by SPCFs with 280 F g⁻¹ and PCFs showing a capacitance value of 254 A g⁻¹. This improvement is due to the synergetic effect of increasing mesopore/micropore ratio (0.58 and 0.44 for NPCFs and SPCFs, respectively, compared to 0.35 for PCFs) and increasing the relative heteroatom content after the doping process.

As mentioned before, mesopores increase the accessible-surface area potentially enhancing the electrochemical performance. Besides, introducing N-containing functional groups can produce additional active sites and changes in the surface energy (or hydrophilicity), which increase wettability, increasing interactions between the carbon surface and the electrolyte.

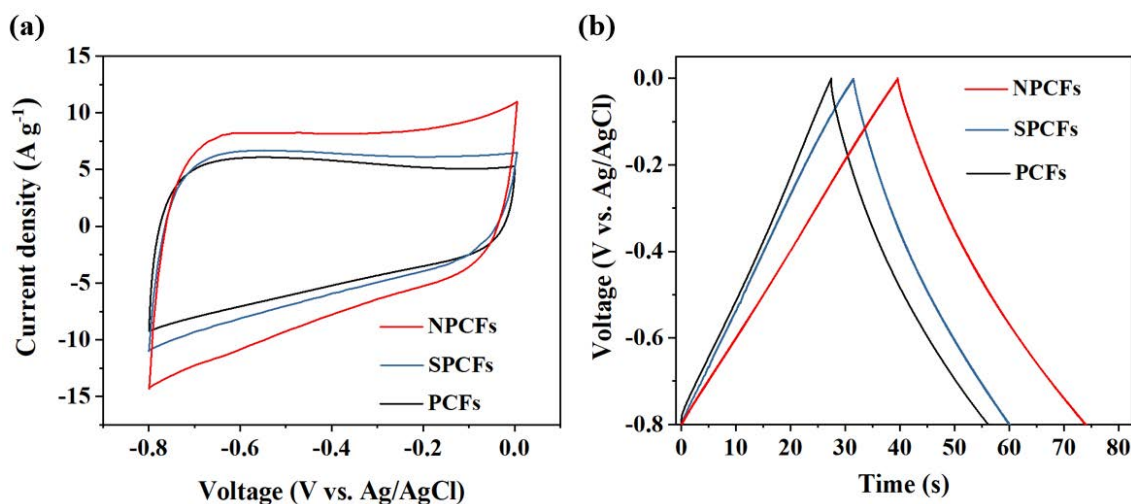


Figure 7.6. (a) CV curves measured at 50 mV s^{-1} and (b) GCD curves at 5 measured at 5 A g^{-1} of NPCFs, SPCFs, and PCFs.

The differences found between NPCFs and SPCFs can be explained by the most suitable pore structure with a higher mesopore content for NPCFs, but also by the type and concentration of the different N-containing functional groups. In **Figure 7.7a**, it is represented the content of the different N surface functionalities for each PCF under study, corresponding to pyridinic nitrogen (N-6), pyrrolic nitrogen (N-5), quaternary nitrogen (N-Q) and oxidized pyridinic nitrogen (N-O). Concentration of pyrrolic and pyridinic N increases for NPCFs compared to SPCFs. These nitrogen species have demonstrated to be the most electrochemically active. Therefore, their increase is directly related to the increase in capacitance values. **Table 7.2** compiles capacitance values, heteroatom content, and specific surface areas of other carbon and fiber materials doped or activated with N and S heteroatoms. Data for NPCFs and SPCFs are also included, showing highly competitive capacitance values, especially for NPCFs.

Table 7.2. Comparison of N and S content, SSA_{BET} , and capacitance values of different carbon materials measured in a three-electrode electrochemical cell.

Material	N (%)	S (%)	SSA_{BET} ($m^2 g^{-1}$)	C_s ($F g^{-1}$)	Electrolyte	Ref
N-doped carbon nanospheres	21.81	-	145.0	191.9 (0.1 A g^{-1})	H ₂ SO ₄ 1M	[226]
N/S-doped carbons	1.40	1.83	1199.0	241.0 (1 A g^{-1})	KOH 6M	[227]
N/S-doped carbon nanosheets	3.13	1.84	1552.0	363.1 (0.5 A g^{-1})	KOH 6M	[228]
N/S co-doped carbon nanospheres	4.29	3.38	1830.8	416.0 (0.2 A g^{-1})	KOH 6M	[229]
N/S co-doped carbons	2.40	0.50	2711.7	322.0 (1 A g^{-1})	KOH 6M	[230]
N/S co-doped carbons	3.65	0.97	894.2	206.0 (1 A g^{-1})	KOH 6M	[231]
N/S co-doped carbons	0.94	0.21	1838.0	350.0 (1 A g^{-1})	KOH 6M	[205]
N/S-doped PCtextiles	3.20	1.10	932.0	268.0 (1 mV s^{-1})	KOH 6M	[181]
N/S co-doped PCFs	14.00	0.90	207.4	307.8 (2 mV s^{-1})	KOH 6M	[70]
N-doped PCFs	12.20	-	427.9	341.0 (1 A g^{-1})	KOH 6M	This work
N/S-doped PCFs	14.20	0.50	440.8	280.0 (1 A g^{-1})	KOH 6M	This work

In order to examine the capacitance retention of these materials, CV was conducted between 5 and 500 mV s^{-1} scan rate. For all PCFs, capacitance values decrease as sweep rate increase, since at higher rates the penetration of ions into the core material is hindered and therefore the area accessible to the electrolyte ions is reduced.

Activated fibers (NPCFs and SPCFs) exhibited enhanced capacitance retention at high rates compared to non-activated fibers (starting PCFs). This improved performance has been attributed to several factors related to the increased meso-/micropore ratio, and the presence of N-containing surface functional group [232], which reduce ion-diffusion resistance and electrode-electrolyte interfacial resistance. Similar capacitance retention was found in NPCFs and SPCFs, due to the high graphitic-N concentration in SPCFs which improves charge transfer at higher sweep rates.

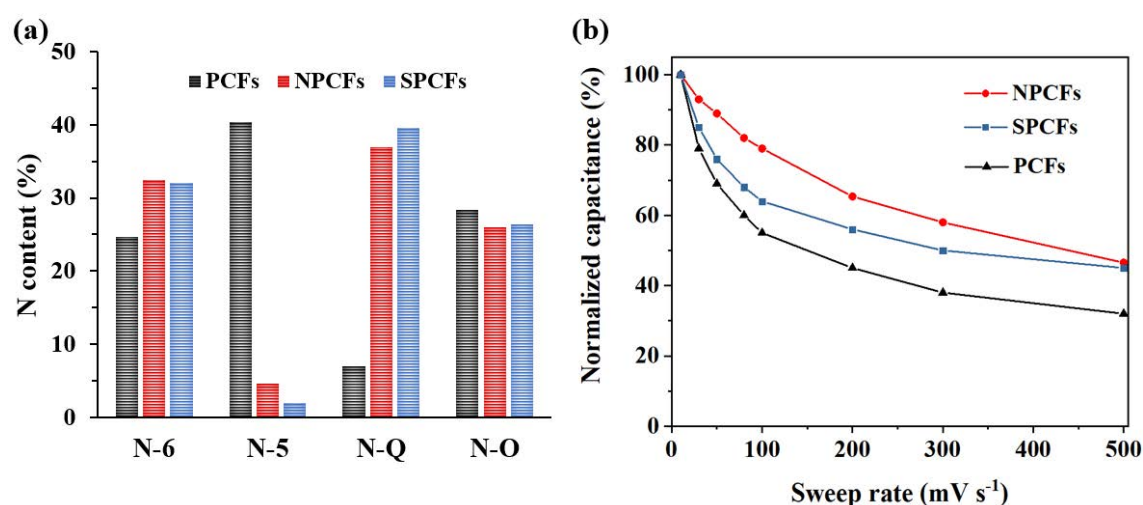


Figure 7.7. (a) Content of the different N species found in PCFs, NPCFs and SPCFs, and (b) normalized capacitance retention measured from 5 to 500 mV s⁻¹ of the porous carbon fibers.

Electrochemical impedance spectroscopy (EIS) was measured to determine the capacitive behavior and diffusion kinetics of PCFs before and after activation under AC conditions. Moreover, EIS was carried out to differentiate the resistance contributions related to different process. The Nyquist diagrams shown in **Figure 7.8a** were fitted to the equivalence circuit shown in **Chapter 2**. For the three materials, three main regions can be detected. At high frequencies, all samples displayed a semicircle shape. From the intersection of the Nyquist plot with the real part axis (Z') series resistance (R_s) values can be obtained.

R_s is related to the electrode internal resistance, although the three materials presented low resistance values ($< 1 \Omega$), NPCFs and SPCFs showed lower R_s values (0.53 Ω and 0.61 Ω respectively), compared to 0.81 Ω of the starting PCFs material. This was attributed to higher graphitization degree observed in Raman spectra and higher N

content, which potentially increases the electronic conductivity. Since R_s is also related to the electrode–electrolyte resistance, the higher R_s value for SPCFs can be due to the increased N-containing functional groups at the surface, which increased the basicity of the surface, and therefore, decreased interaction with OH^- electrolyte ions. Based on these results, a higher graphitization degree and a higher nitrogen content can individually contribute to an increase in overall electrochemical performance of activated fibers.

The charge–transfer resistance (R_{CT}) values decrease notably for both doped PCFs with values of 0.91 Ω , and 1.20 Ω for SPCFs and NPCFs respectively, compared with starting PCFs (1.9 Ω). This charge transfer improvement is attributed to their higher heteroatom content after the activation. This increased heteroatom content particularly higher nitrogen and sulfur content in SPCFs was stated to be superior to that of NPCFs.

R_{CT} (charge–transfer resistance) value can be obtain from semicircle diameters and as mentioned before, is mainly governed by faradaic process involving faradaic reactions with heteroatoms. R_{CT} values decrease notably for both activated fibers with values of 0.91 Ω , 1.20 Ω for SPCFs, NPCFs respectively, compared with starting PCFs (1.9 Ω). This charge transfer improvement is due to the higher heteroatom content after the activation, which is improved for SPCFs due to the higher total N content and some S as well compared to NPCFs. This improvement is also attributed to a more suitable pore structure rich in mesopores after both activation process.

Warburg diffusion coefficient (W_0) can be found between high and mid–high frequencies. It is mainly associated with the ion diffusion into the pores of the electrode surface and the formation of the diffusion layer on the electrode surface. Ideal capacitive behavior would present a vertical line in that frequency range [221]. The Nyquist plot shows that the slope gradually inclines from NPCFs to SPCFs and PCFs in that region. NPCFs have a lower resistance due to their higher mesopore content compared to other carbon fibers. This facilitates ion transportation and suggests ion diffusion occurs not only on the surface. To quantify the ion diffusion resistance values, the real part Z was plotted against the angular frequency raised to 0.5 ($\omega^{-0.5}$) for a frequency range between 1 to 20 Hz (**Figure 7.8b**). Ion diffusion resistance can be obtained from the slope, showing the lower value of 0.95 $\Omega \text{ s}^{-0.5}$, 1.02 $\Omega \text{ s}^{-0.5}$, and 3.0 $\Omega \text{ s}^{-0.5}$ for NPCFs, SPCFs and PCFs respectively. The results obtained show that NPCFs possess an improved pore structure

with surface functionalities rich in pyridinic and pyrrolic nitrogen, which make them well-suited for improving the electrochemical performance of starting PCFs.

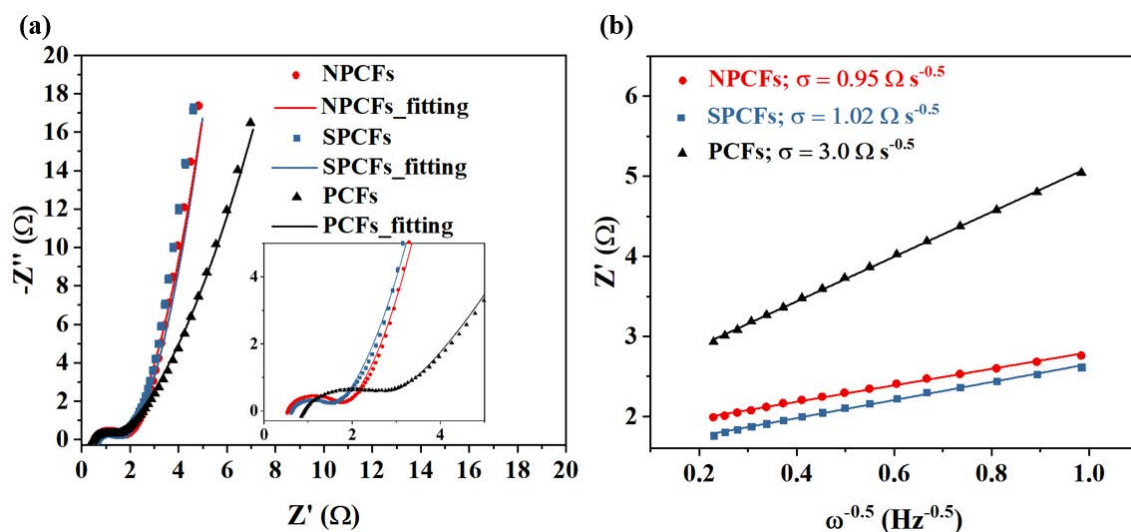


Figure 7.8. (a) EIS of porous carbon fibers fitted to the equivalent circuit and, (b) ion diffusion resistances of PCFs, NPCFs and SPCFs.

In conclusion, regarding SPCFs, the higher total N content and some S content are believed to contribute to improved charge transfer performance compared to NPCFs and starting SPCFs. However, although surface heteroatom content is an important factor, it is not the only determinant of electrochemical performance. The pore structure and pore size distribution of the material also play a crucial role in achieving higher capacitance values and retention capability. However, the activation process can also lead to increased fragility of the fiber mat. This is primarily due to the second thermal treatment causes the volatilization of non-carbon-based gases that produce fiber breakage, which compromises their use as self-standing electrodes.

7.4. PCFs containing magnetite nanoparticles

In **Chapter 6**, the influence of adding a low content of magnetite nanoparticles (MNPs) on the PtBA-*b*-PAN copolymer phase separation was analysed. This phase separation changes induced modifications on the pore structure of the resulting PCFs. Although the size and concentration of MNPs, as well as their specific interactions with the polymer chains need to be carefully considered to achieve the desired phase behavior

and control over the self-assembly process, this preliminary research demonstrate an improvement of SSA values and mesopore content after the addition of MNPs.

To study the influence of the addition of MNPs on the electrochemical performance and potential pseudocapacitance behaviour, a preliminary electrochemical examination was conducted using a three-electrode cell. Electrodes of starting PCFs (named as PtBA-PCFs) and PCFs derived from a dispersion of MNPs into PtBA-*b*-PAN matrix (MNPs-PCFs) were prepared as a 'slurry' pressed into Ni foam.

CV was measured at different sweep rates for both materials (PtBA-PCFs and MNPs-PCFs). **Figure 7.9a** shows CV curves measured at 50 mV s⁻¹. MNPs-PCFs exhibited larger area under the CV curve confirming an increase capacitance with respect to PtBA-PCFs. No visible redox peaks produced by redox reaction between Fe₃O₄ and OH⁻ electrolyte ions were detected. Although some slightly visible distortions could be observed compared to PtBA-PCFs curve. Consistent with CV data, GCD curve measured at 4 A g⁻¹ (**Figure 7.9b**) did not show any visible deviation due to Faradaic reactions. Capacitance value obtained from the discharge curve at 1 A g⁻¹ reached 248 F g⁻¹, which is notably higher than the one obtained for PtBA-PCFs (204 F g⁻¹). This improvement is likely attributed to increased specific surface area and mesopore concentration, resulting from the interaction between the MNP and block polymer chains. The MNPs modified with phenolic acid have a strong affinity for the PAN domain phase, which leads to a higher degree of segregation and, consequently, increasing pore size without compromising specific surface area (see **Chapter 6**). These factors mainly contribute to enhance the capacitance. To enhance the pseudocapacitance contribution, it will be explored different loading of MNPs on the PCFs.

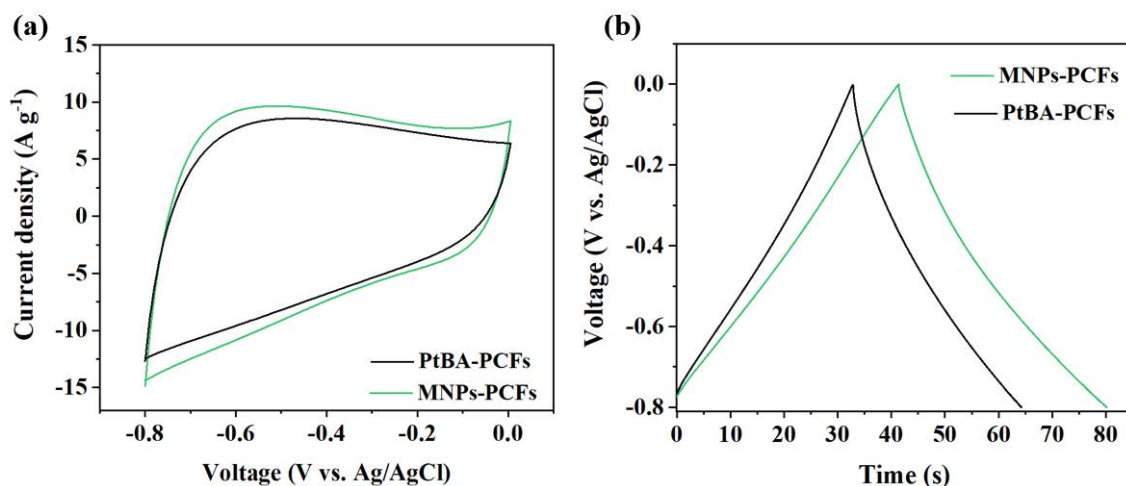


Figure 7.9. (a) CV curves at 50 mV s^{-1} and (b) GCD curves at 4 A g^{-1} of PtBA-PCFs and MNPs-PCFs.

In summary, the introduction of MNPs has been found to induce morphological changes that impact the overall porosity and electrochemical capacitance of the PCF, even at low loading concentrations. The presence of MNPs alters the arrangement and distribution of the block copolymer domains, which leads to changes in the pore structure and probably to connectivity within the fibers.

Chapter 8

Conclusions and future prospects

In this thesis work various PAN-based block copolymers (BCPs) have been used as precursors to produce porous carbon fibers (PCFs) with a well-defined and hierarchical pore structure. Fibers were successfully obtained by electrospinning of BCP precursors with different sacrificial blocks, compositions, and molecular weights. The fiber mats were subsequently carbonized to produce PCFs with various well-defined pore structures and surface chemical compositions, as demonstrated through morphological and structural characterization. Additionally, it has been determined how the different structural and chemical characteristics of the PCFs produced in this thesis, directly influence their electrochemical behavior as electrode materials for supercapacitors. Herein, a summary of the main conclusions and future prospects is presented.

8.1. Conclusions

- *Synthesis and characterization of block copolymers*

Novel synthetic routes have been presented using Reversible Addition-Fragmentation Chain Transfer (RAFT) polymerization to successfully synthesized various PAN-based block copolymer with polystyrene, and poly(tert-butyl acrylate) as sacrificial blocks. Polymerizations were optimized to produce well-controlled block copolymers with low sacrificial block (SB) volume fractions ($f_{SB} \sim 0.11-0.16$), resulting in high carbon yields after carbonization. Different high and controlled BCPs molecular weights were also obtained, allowing, and facilitating their use as fiber precursors by electrospinning.

- *Fabrication of porous carbon fibers*

The phase-separation behavior and the ability of PAN-based block copolymers to maintain its disordered morphologies after carbonization were analyzed. The block copolymers were used as precursors for producing fibers by electrospinning after parameter optimization to obtain a suitable homogenous fiber mat. Some parameters such as monomer, composition, and molecular weight were modified to study their influence on morphology and porous structure. Fibers mats derived from PtBA-*b*-PAN and high molecular weight PS-*b*-PAN presented a beaded-fiber structure. This is mainly attributed to processing conditions, confirming how small variation in the electrospinning precursor solution affects the morphology and properties of the resulting electrospun

fibers. PCFs with varied and well-controlled pore structures have been obtained through stabilization and subsequent carbonization of the electrospun fiber mats derived from all the different synthesized block copolymers (PS-PCFs, PtBA-PCFs, and HN_PS-PCFs).

- *PCFs morphological and structural characterization*

Detailed morphological and structural characterization was assessed to determine fiber morphology, carbon and pore structure, and surface chemical composition. Variations in sacrificial block and molecular weight have been shown to modulate textural properties such as specific surface areas, pore sizes and shapes, and surface chemical composition. Among all the PCFs under study, PCFs derived from PS-*b*-PAN (PS-PCFs) presented the highest surface area ($SSA_{BET} = 495 \text{ m}^2 \text{ g}^{-1}$) with the most suited meso-/micropore ratio and a relatively high content of N and O (7.8 and 4.5 %, respectively). Although, according to the information revealed by the N_2 adsorption/desorption isotherm, some pores presented an ink-bottle shape that can contribute to increase ion-diffusion resistance. Therefore, further research will be required, such as varying the sacrificial block volume fraction to produce pores shapes with reduced ion-diffusion resistance without compromising the surface area values.

- *PCFs capacitive properties*

All PCFs produced in this thesis work (PS-PCFs, PtBA-PCFs and HN_PS-PCFs) were tested as electrode materials for supercapacitors in a three-electrode cell. Among the PCFs under study, PS-PCFs exhibited the highest capacitance value (254 F g^{-1} measured at 1 A g^{-1}) due to the synergetic effect of higher surface area and hierarchical porosity, rich in micro- and mesopores; since capacitance values are gradually reduced with decreasing SSA_{BET} values. In contrast, both PtBA-PCFs and HN_PS-PCFs exhibited lower capacitance values compared to PS-PCFs. However, capacitance retention increased for both, up to 300 mV s^{-1} . This enhancement can be attributed to higher nitrogen surface concentration. These results demonstrate the importance of both, the concentration of surface heteroatom functionalities and the textural characteristics, such as surface area, pore size and pore volume. Finally, PS-PCFs also presented satisfactorily capacitive behavior in a symmetrical cell, including, low series resistance (R_s) and charge-transfer resistance and (R_{CT}), indicating considerable electrical conductivity, and remarkable cycle stability.

- *PCFs optimization through material modifications*

Based on previous results, PCFs derived from PS-*b*-PAN were successfully doped with N and N/S heteroatoms through an activation process with urea and thiourea, respectively. NPCFs (N-doped PCFs) and SPCFs (N/S co-doped PCFs) exhibited improved electrochemical performance, with higher capacitance values and capacitance retention, and lower ion-diffusion resistance (σ) and charge-transfer resistance (R_{CT}), indicating enhanced electrical conductivity. These improvements are assigned to the higher content of heteroatom surface functionalities and enhanced meso-/micropore ratio without compromising the surface areas, which contribute to pseudocapacitance. As already mentioned above, obtaining advanced and flexible electrode materials for supercapacitors required a self-standing nature. Due to the second thermal treatment of the activation process, fibers decreased in diameter and fiber breakage increased. As a result, NPCFs and SPCFs present some fragility. Therefore, further research will be required to overcome these limitations, including immersing the electrospun fiber mat in saturated solutions of urea and thiourea before carbonization. This approach may avoid fiber diameter decrease and breakage through the second carbonization.

Moreover, magnetite nanoparticles were included in the PCFs carbon framework. This addition produced changes in the phase-separation morphologies that increased the SSA_{BET} values, as well as the meso-/micropore ratio, which translated into higher capacitance values. Although, due to the insufficient concentration of nanoparticles embedded in the PCFs, no redox peaks were observed, indicating a low pseudocapacitance contribution. This suggests that pseudocapacitance could be increased by expanding the nanoparticle loading to higher concentrations.

8.2. Future prospects

Porous carbon fibers (PCFs) with well-controlled and defined pore structures are considered advanced multifunctional materials for different applications. Ongoing efforts are focused on improving the scalability, efficiency, and sustainability of manufacturing processes, as well as developing novel methods to tailor the PCFs properties to specific requirements. These fibers are expected to play a vital role in addressing various challenges, especially in energy storage, environmental remediation, and other fields requiring high-performance materials.

This work demonstrates that obtaining PCFs from PAN-block copolymers is a promising potential strategy. However, further investigations are required to optimize the pore structure and morphology. Future research is focused on exploring novel monomers and polymers, optimizing block copolymer compositions and electrospinning parameters. These efforts aim to produce PCFs with various desirable properties, including high mechanical strength that allows them to be used as self-standing materials. A summary of some future perspectives is presented hereinafter.

- *PCFs derived from poly ionic liquids (PIL)*

A preliminary study to produce PCFs derived from poly(ionic liquids) (PILs) and block copolymer (BCPs) blends as precursors was developed in collaboration with professor Jiayin Yuan of the Functional Polymers and Carbons research group at Stockholm University (SU).

Poly(ionic liquid)s (PILs) are polymers derived from ionic liquid monomers. PILs hold great promise in producing carbon with enhanced electrical conductivity, which is attributed to their inherent ionic nature. In addition to their inherent high conductivity, the idea of using poly(ionic liquids) (PILs) as PCFs precursors arose due to their high content of nitrogenous functional groups, which upon carbonization will produce a high relative nitrogen content PCFs, without requiring an additional doping process. The poly(ionic liquid) used in this preliminary project was provided by the research group. Poly(1-cyanomethyl-3-vinylimidazolium bis(trifluoromethane sulfonyl)imide) was synthesized according to previously published procedure [233] and exhibited a low

molecular weight $\sim 20.000 \text{ g mol}^{-1}$. This PIL polymer has been used to prepared highly porous membranes. The mixture of this polymer with certain amounts of poly (acrylic acid) (PAA) in NH_3 media causes the following process:

- i) Deprotonation of the $-\text{COOH}$ group of PAA to form $-\text{COO}^-\text{NH}_4^+$.
- ii) Driven by entropy, PAA deprotonated groups ($-\text{COO}^-$) will ionically crosslink PIL functional groups to form an inter-polyelectrolyte complex.
- iii) The diffusion of water into the crosslinked PIL-complex will cause phase separation producing pores.

The BCP selected for this experiment was PMMA-*b*-PAN, in which the sacrificial block is poly methyl methacrylate. This BCP was synthesized according to previously reported procedure [58]. It was selected due to the higher volume fraction of PMMA ($f = 0.53$) compared to the BCPs presented in this thesis work ($f_{\text{SB}} \sim 0.11\text{--}0.16$). Since the concentration used for the electrospinning solution was only 5 wt%, it was assumed that a higher sacrificial block content guaranteed a higher porosity after carbonization.

The experimental procedure illustrated in **Figure 8.1**, first included the preparation of fibers by electrospinning using a mixture containing 20 wt% of PIL, 3.8 wt % of PAA and 5 wt% of BCP. Electrospinning parameters were set at 18 kV, 10 cm distance from tip to collector and a feed rate of 0.5 mL h^{-1} . The resulting fibers were then immersed in a saturated NH_3 solution for 24 h for crosslinking process. Immediately after, the fiber mat was washed with distilled water and carbonized through a two-step thermal treatment, first at $280 \text{ }^\circ\text{C}$ under air for 1h followed by carbonization at $800 \text{ }^\circ\text{C}$ under N_2 for 1h.

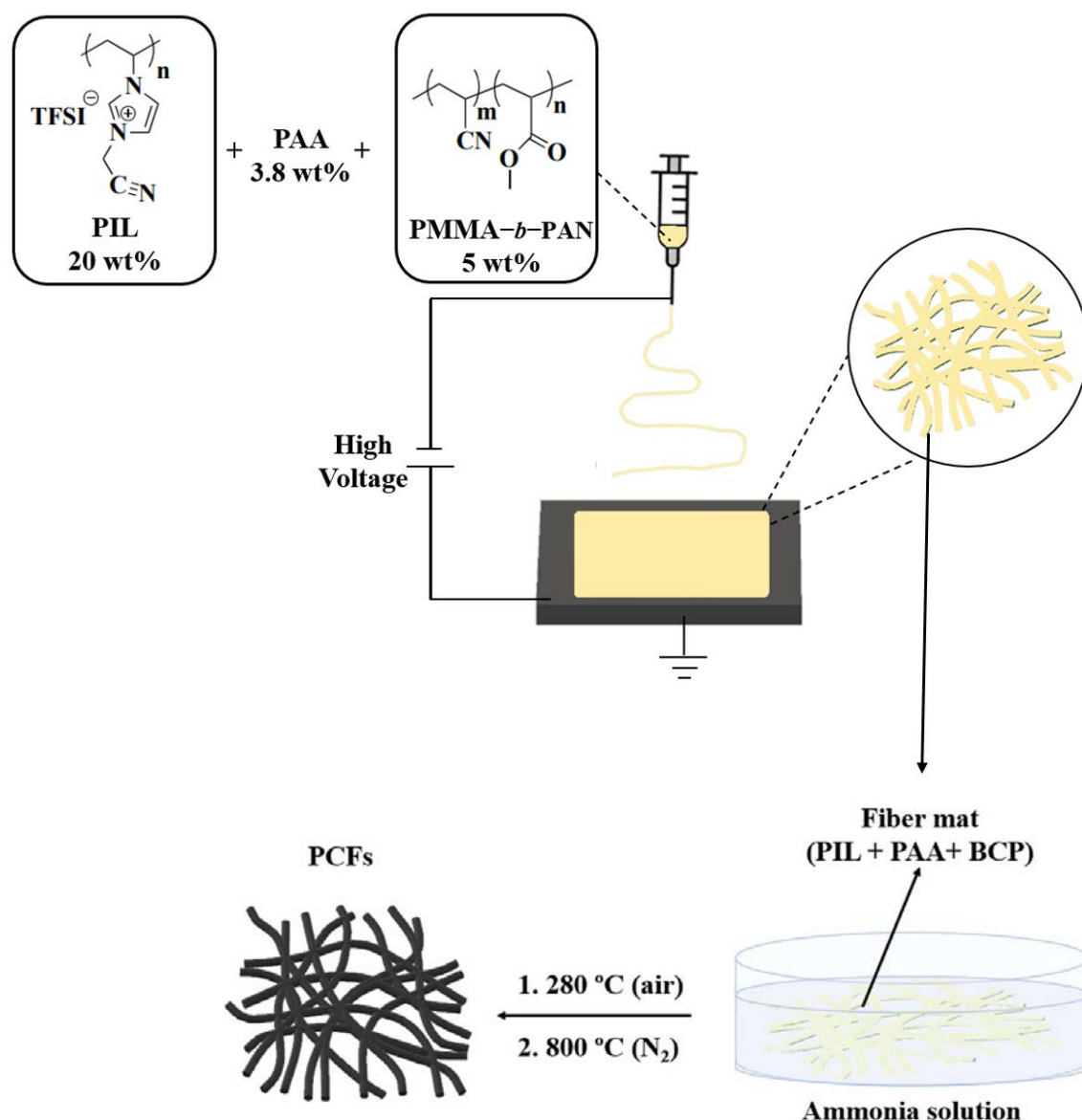


Figure 8.1. Scheme representing the process to produced PCFs from PIL, PAA and BCP.

Fibers were characterized by SEM (shown in **Figure 8.2**), exhibiting a homogeneous diameter distribution. After crosslinking, some anchored points can be observed between fibers. After stabilization and carbonization, the fibers maintain their integrity, although some agglomerations can be detected. The measured SSA_{BET} value reached $498 \text{ m}^2 \text{ g}^{-1}$. The PCFs mat showed certain degree of flexibility and sufficient mechanical strength to be used as self-standing electrode material. The capacitance measured in a symmetrical cell reached a value of 200 F g^{-1} at 1 A g^{-1} .

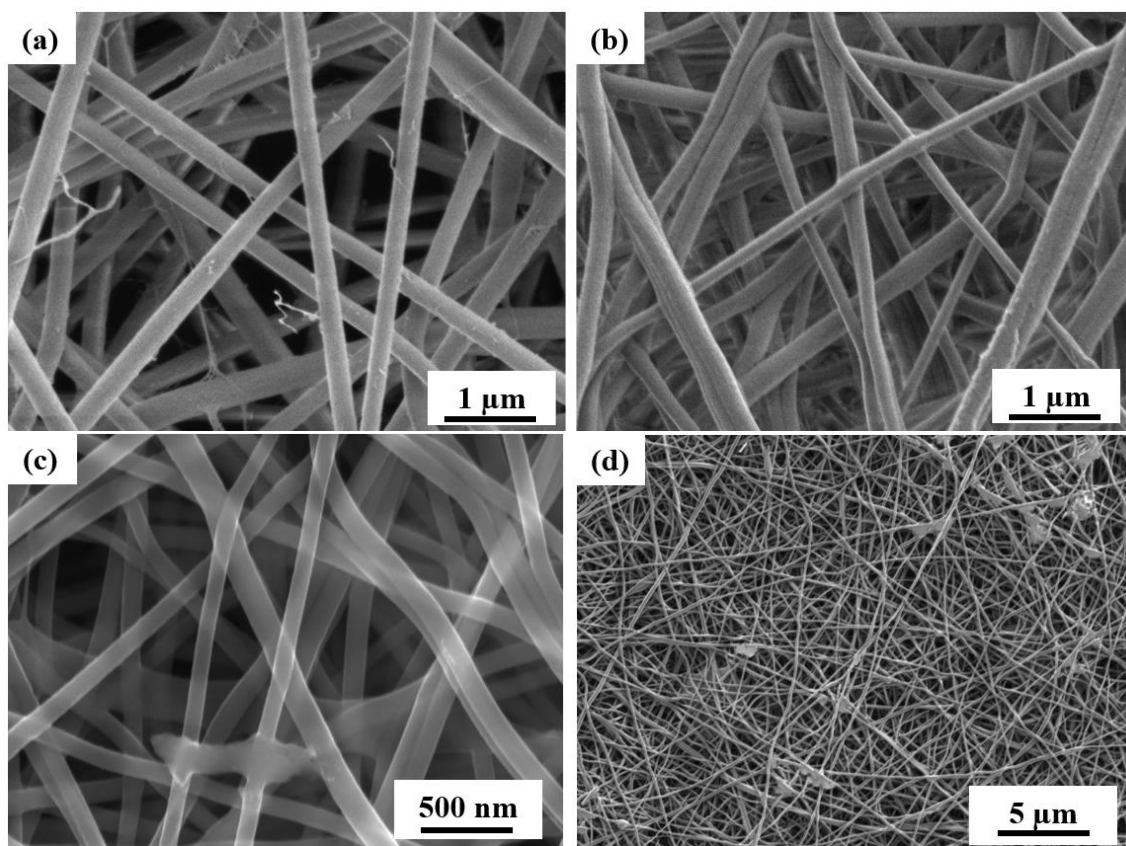


Figure 8.2. SEM images of PCFs derived from PIL/PAA/BCP blend (a) electrospun fiber mat, (b) after crosslinking, (c) after stabilization and (d) after carbonization.

This project has shown how fibers can be produced from highly concentrated PIL solutions. The PIL-derived PCFs exhibited homogenous diameters and, after carbonization, morphology and structure are preserved without visible fiber breaks, allowing them to be used as self-standing electrodes for supercapacitors. Due to the low concentration of BCP (PMMA-*b*-PAN), a low mesopore content is expected, which translates into an improvable capacitive performance.

This work opens a new research line, which requires optimizing the concentrations of PIL and BCP to reach the highest specific surface area with the most suitable pore size distribution, in order to improve the electrochemical performance.

- *PCFs derived from Polyimides*

Polyacrylonitrile (PAN) was selected in this thesis work as the carbon precursor block for all the different block copolymers produced. Nevertheless, other carbon precursors have attracted significant interest, such as polyimides. This polymer is

composed of aromatic rings coupled by imide linkages, with a high content of electron-rich nitrogen and oxygen heteroatoms. This feature is especially interesting for their application as electrode materials for supercapacitors, since heteroatom functionalities on the electrode surface increase capacitance through pseudocapacitive contribution. Furthermore, oxygen and nitrogen exhibit a good affinity towards carbon dioxide, so polyimide-derived fibers were also considered excellent materials for CO₂ capture [26]. In addition, due to the heteroaromatic skeleton and firmly structure, the polyimides showed high carbon yield after carbonization. Therefore, polyimides emerge as promising carbon precursors to produce well-defined porous carbon fibers for various applications through activation process [234,235]. However, since polyimides can be coupled with sacrificial blocks, among other approaches, through condensation reactions [236], polyimide-derived copolymers will be precursor materials of notable attention for producing advanced PCFs.

- *PCFs for CO₂ capture and dye adsorption*

As explained in the introduction, porous carbon materials with hierarchical porosity can improve the adsorption of different organic dyes, such as methyl orange and methylene blue. In addition, the surface functionalities play an important role in increasing the affinity towards the adsorbate. In this context, porous carbon materials containing Fe₃O₄ magnetic nanoparticles have shown to introduce more adsorption actives sites, leading to high adsorption and regeneration capacity [237]. Considering these promising results, the PCFs containing Fe₃O₄ nanoparticles produced in this thesis work can potentially be used for dye adsorption applications. This will open up new lines of research that will require optimization of nanoparticle loading and dispersion protocols to produce a homogenous fiber mat with uniformly dispersed nanoparticles.

Porous carbon materials with hierarchical pore structures can also enhance CO₂ capture, which allows easy access of CO₂ molecules to micropore actives sites. Furthermore, as mentioned above, heteroatom-rich surface functionalities offer improved affinity towards carbon dioxide [238]. Therefore, the PCFs presented in this thesis work, with well-controlled pore size distribution and high relative N/O surface concentrations, stand out as promising adsorbent materials. For this reason, future CO₂ physisorption experiments will be expected to show high CO₂ intakes.

- *PCFs with conductive additives*

Composite materials comprising porous carbons with pseudocapacitive materials, combines the advantages of high stability with high capacitance. In this regard, MXenes has emerged in the last decade as a novel 2D material with high metallic conductivity and high hydrophilicity. The general formula of MXenes is $M_{n+1}X_nT_x$, where M is a transition metal, and X correspond with C and/or N. Furthermore, MXenes sheets are often coated with hydrophilic surface parts (T_x), such as OH [239]. Due to advantages including metal conductivity and high hydrophilicity, MXenes has been used as electrode materials for supercapacitors showing an excellent electrochemical performance.

Producing composite materials comprising the PCFs produced in this thesis work and Mxenes sheets, could be a promising approach to improve the electrochemical performance. Impregnating of Mxenes onto the PCFs membrane, has been proven to promote rapid ion-diffusion and increase electron conductivity [240]. A different approach involves the introduction of Mxenes sheets embedded in the carbon fiber structure [241], which could prevent the sheets from twisting or bending, resulting in decreased conductivity. Therefore, using block copolymers and Mxenes blends to produce porous carbon fibers by electrospinning will be an interesting method to increase electronic and ionic conductivity.

- *PCFs produced by wet-spinning*

Fibers produced along this thesis work has been obtained by electrospinning. This technique allows to obtain nanosized fiber diameters that enables to reach high specific surface areas. However, a different method to produce wider fiber diameters will be through the use of wet-spinning. This method is based on the extrusion of a polymeric solution directly into a coagulation bath containing a non-solvent, therefore, it allows the use of multiple precursors. This process leads to polymer filaments that solidify as continuous polymeric fibers, presenting diameters in the range of μm [242]. Porous carbon fibers produced by wet-spinning have been shown to achieve relatively high surface areas and high electrochemical performance while offering high mechanical strength [243–245].

Bibliography

1. Omer, A.M. Energy , Environment and Sustainable Development. **2008**, *12*, 2265–2300, doi:10.1016/j.rser.2007.05.001.
2. Liu, H.; Li, M.; Kaner, R.B.; Chen, S.; Pei, Q. Monolithically Integrated Self-Charging Power Pack Consisting of a Silicon Nanowire Array/Conductive Polymer Hybrid Solar Cell and a Laser-Scribed Graphene Supercapacitor. *ACS Appl. Mater. Interfaces* **2018**, *10*, 15609–15615, doi:10.1021/acsami.8b00014.
3. Shi, M.; Yang, C.; Song, X.; Zhao, L.; Liu, J.; Zhang, P.; Gao, L. Integrated Sustainable Wind Power Harvesting and Ultrahigh Energy Density Wire-Shaped Supercapacitors Based on Vertically Oriented Nanosheet-Array-Coated Carbon Fibers. *Adv. Sustain. Syst.* **2017**, *1*, 1–9, doi:10.1002/adsu.201700044.
4. Pandolfo, A.G.; Hollenkamp, A.F. Carbon Properties and Their Role in Supercapacitors. *J. Power Sources* **2006**, *157*, 11–27, doi:10.1016/j.jpowsour.2006.02.065.
5. Ko, R.; Carlen, M. Principles and Applications of Electrochemical Capacitors. **2000**, *45*, 2483–2498.
6. Fleischmann, S.; Mitchell, J.B.; Wang, R.; Zhan, C.; Jiang, D.E.; Presser, V.; Augustyn, V. Pseudocapacitance: From Fundamental Understanding to High Power Energy Storage Materials. *Chem. Rev.* **2020**, *120*, 6738–6782, doi:10.1021/acs.chemrev.0c00170.
7. Yan, L.; Liu, A.; Ma, R.; Guo, C.; Ding, X.; Feng, P.; Jia, D. Regulating the Specific Surface Area and Porous Structure of Carbon for High Performance Supercapacitors. *Appl. Surf. Sci.* **2023**, *615*, 156267, doi:10.1016/j.apsusc.2022.156267.
8. Wang, F. Superior Pseudocapacitive Performance and Mechanism of Self-Assembled MnO₂/MXene Films as Positive Electrodes for Flexible Supercapacitors. *J. Alloys Compd.* **2022**, *899*, 163241, doi:10.1016/j.jallcom.2021.163241.

9. Zhu, L.; Wang, Y.; Wang, M.; Huang, M.; Huang, Y.; Zhang, Z.; Yu, J.; Qu, Y.; Li, C.; Yang, Z. High Edge-Nitrogen-Doped Porous Carbon Nanosheets with Rapid Pseudocapacitive Mechanism for Boosted Potassium-Ion Storage. *Carbon N. Y.* **2022**, *187*, 302–309, doi:10.1016/j.carbon.2021.11.021.
10. Lv, H.; Xiao, Z.; Zhai, S.; Hao, J.; Tong, Y.; Wang, G.; An, Q. Construction of Nickel Ferrite Nanoparticle-Loaded on Carboxymethyl Cellulose-Derived Porous Carbon for Efficient Pseudocapacitive Energy Storage. *J. Colloid Interface Sci.* **2022**, *622*, 327–335, doi:10.1016/j.jcis.2022.04.133.
11. González, A.; Goikolea, E.; Barrena, J.A.; Mysyk, R. Review on Supercapacitors: Technologies and Materials. *Renew. Sustain. Energy Rev.* **2016**, *58*, 1189–1206, doi:10.1016/j.rser.2015.12.249.
12. Brochardt, L.; Oschatz, M.; Kaskel, S. Tailoring Porosity in Carbon Materials for Supercapacitor Applications. *Mater. Horizons* **2014**, *1*, 157–168, doi:10.1039/c3mh00112a.
13. Thommes, M.; Kaneko, K.; Neimark, A. V.; Olivier, J.P.; Rodriguez-Reinoso, F.; Rouquerol, J.; Sing, K.S.W. Physisorption of Gases, with Special Reference to the Evaluation of Surface Area and Pore Size Distribution (IUPAC Technical Report). *Pure Appl. Chem.* **2015**, *87*, 1051–1069, doi:10.1515/pac-2014-1117.
14. Li, B. Nitrogen-Doped Activated Carbon for High Energy Hybrid Supercapacitor. *Energy Environ. Sci.* **2015**, *9*, 102–106, doi:10.1039/C5EE03149D.
15. Conway, B.E.; Pell, W.G. Power Limitations of Supercapacitor Operation Associated with Resistance and Capacitance Distribution in Porous Electrode Devices. **2002**, *105*, 169–181.
16. Sun, N.; Li, Z.; Zhang, X.; Qin, W.; Zhao, C.; Zhang, H.; Ng, D.H.L.; Kang, S.; Zhao, H.; Wang, G. Hierarchical Porous Carbon Materials Derived from Kelp for Superior Capacitive Applications. *ACS Sustain. Chem. Eng.* **2019**, *7*, 8735–8743, doi:10.1021/acssuschemeng.9b00635.
17. Yang, W.; Wang, P.; Tu, Z.; Hou, L.; Yan, L.; Jiang, B.; Zhang, C.; Huang, G.; Yang, F.; Li, Y. Heteroatoms-Doped Hierarchical Porous Carbon with Multi-Scale

Structure Derived from Petroleum Asphalt for High-Performance Supercapacitors. *Carbon N. Y.* **2022**, *187*, 338–348, doi:10.1016/j.carbon.2021.11.008.

18. Kierzek, K.; Frackowiak, E.; Lota, G.; Gryglewicz, G.; Machnikowski, J. Electrochemical Capacitors Based on Highly Porous Carbons Prepared by KOH Activation. *Electrochim. Acta* **2004**, *49*, 515–523, doi:10.1016/j.electacta.2003.08.026.
19. He, X.; Ling, P.; Yu, M.; Wang, X.; Zhang, X.; Zheng, M. Rice Husk-Derived Porous Carbons with High Capacitance by ZnCl₂ Activation for Supercapacitors. *Electrochim. Acta* **2013**, *105*, 635–641, doi:10.1016/j.electacta.2013.05.050.
20. Daraghmeh, A.; Hussain, S.; Saadeddin, I.; Servera, L.; Xuriguera, E.; Cornet, A.; Cirera, A. A Study of Carbon Nanofibers and Active Carbon as Symmetric Supercapacitor in Aqueous Electrolyte: A Comparative Study. *Nanoscale Res. Lett.* **2017**, *12*, 639, doi:10.1186/s11671-017-2415-z.
21. Nie, G.; Zhao, X.; Luan, Y.; Jiang, J.; Kou, Z.; Wang, J. Key Issues Facing Electrospun Carbon Nanofibers in Energy Applications: On-Going Approaches and Challenges. *Nanoscale* **2020**, *12*, 13225–13248, doi:10.1039/d0nr03425h.
22. Chen, L.; Wen, Z.; Chen, L.; Wang, W.; Ai, Q.; Hou, G.; Li, Y.; Lou, J.; Ci, L. Nitrogen and Sulfur Co-Doped Porous Carbon Fibers Film for Flexible Symmetric All-Solid-State Supercapacitors. *Carbon N. Y.* **2020**, *158*, 456–464, doi:10.1016/j.carbon.2019.11.012.
23. Chen, Y.; Xu, P.; Liu, Q.; Yuan, D.; Long, X.; Zhu, S. Cobalt Embedded in Porous Carbon Fiber Membranes for High- Performance Lithium-Sulfur Batteries. *Carbon N. Y.* **2022**, *187*, 187–195, doi:10.1016/j.carbon.2021.11.015.
24. https://Gml.Noaa.Gov/Ccgg/Trends/Gl_trend.Html.
25. Ma, C.; Bai, J.; Demir, M.; Yu, Q.; Hu, X.; Jiang, W.; Wang, L. Polyacrylonitrile-Derived Nitrogen Enriched Porous Carbon Fiber with High CO₂ Capture Performance. *Sep. Purif. Technol.* **2022**, *303*, 122299, doi:10.1016/j.seppur.2022.122299.

26. Wang, X.; Xiong, L.; Zhong, J.; Jin, L.; Yan, J.; Mu, B.; Zhang, Y.; Song, S. Nitrogen-Containing Porous Carbon Fibers Prepared from Polyimide Fibers for CO₂ Capture. *Ind. Eng. Chem. Res.* **2020**, *59*, 18106–18114, doi:10.1021/acs.iecr.0c03318.
27. Lu, K.; Zhang, X.; Zhao, Y.; Wu, Z. Removal of Color from Textile Dyeing Wastewater by Foam Separation. *J. Hazard. Mater.* **2010**, *182*, 928–932, doi:10.1016/j.jhazmat.2010.06.024.
28. Nohynek, G.J.; Fautz, R.; Benech-kieffer, F.; Toutain, H. Toxicity and Human Health Risk of Hair Dyes. *Food Chem. Toxicol.* **2004**, *42*, 517–543, doi:10.1016/j.fct.2003.11.003.
29. Lei, S.; Miyamoto, J.; Kanoh, H. Enhancement of the Methylene Blue Adsorption Rate for Ultramicroporous Carbon Fiber by Addition of Mesopores. *Carbon N. Y.* **2006**, *44*, 1884–1890, doi:10.1016/j.carbon.2006.02.028.
30. Dong, Y.; Lin, H.; Jin, Q.; Li, L.; Wang, D.; Zhou, D.; Qu, F. Synthesis of Mesoporous Carbon Fibers with a High Adsorption Capacity for Bulky Dye Molecules. *J. Mater. Chem. A* **2013**, *1*, 7391–7398, doi:10.1039/c3ta10787f.
31. Serrano, J.M.; Khan, A.U.; Liu, T.; Xu, Z.; Esker, A.R.; Liu, G. Capacitive Organic Dye Removal by Block Copolymer Based Porous Carbon Fibers. **2020**, *2000507*, 1–9, doi:10.1002/admi.202000507.
32. Endo, M.; Kim, Y.A.; Hayashi, T.; Nishimura, K.; Matusita, T.; Miyashita, K. Vapor-Grown Carbon Fibers (VGCFs) Basic Properties and Their Battery Applications. *Carbon N. Y.* **2001**, *39*, 1287–1297.
33. Huang, Z.; Zhang, Y.; Kotaki, M.; Ramakrishna, S. A Review on Polymer Nanofibers by Electrospinning and Their Applications in Nanocomposites. *Compos. Sci. Technol.* **2003**, *63*, 2223–2253, doi:10.1016/S0266-3538(03)00178-7.
34. Wen, Y.; Kok, M.D.R.; Tafoya, J.P.V.; Sobrido, A.B.J.; Bell, E.; Gostick, J.T.; Herou, S.; Schlee, P.; Titirici, M.M.; Brett, D.J.L.; et al. Electrospinning as a Route to Advanced Carbon Fibre Materials for Selected Low-Temperature

- Electrochemical Devices: A Review. *J. Energy Chem.* **2021**, *59*, 492–529, doi:10.1016/j.jechem.2020.11.014.
35. García-mateos, F.J.; Ruiz-rosas, R.; María, J.; Morallón, E. Activation of Electrospun Lignin-Based Carbon Fibers and Their Performance as Self-Standing Supercapacitor Electrodes. *Sep. Purif. Technol.* **2020**, *241*, 116724, doi:10.1016/j.seppur.2020.116724.
 36. Yang, Y.; Centrone, A.; Chen, L.; Simeon, F.; Alan Hatton, T.; Rutledge, G.C. Highly Porous Electrospun Polyvinylidene Fluoride (PVDF)-Based Carbon Fiber. *Carbon N. Y.* **2011**, *49*, 3395–3403, doi:10.1016/j.carbon.2011.04.015.
 37. Newcomb, B.A. Processing, Structure, and Properties of Carbon Fibers. *Compos. Part A Appl. Sci. Manuf.* **2016**, *91*, 262–282, doi:10.1016/j.compositesa.2016.10.018.
 38. Heo, Y.J.; Lee, H.I.; Lee, J.W.; Park, M.; Rhee, K.Y.; Park, S.J. Optimization of the Pore Structure of PAN-Based Carbon Fibers for Enhanced Supercapacitor Performances via Electrospinning. *Compos. Part B Eng.* **2019**, *161*, 10–17, doi:10.1016/j.compositesb.2018.10.026.
 39. Zhou, T.; Jiang, Q.; Wang, L.; Qiu, Z.; Liu, Y.; Zhou, J.; Liu, B. Facile Preparation of Nitrogen-Enriched Hierarchical Porous Carbon Nano Fibers by Mg (OAc)₂-Assisted Electrospinning for Flexible Supercapacitors. *Appl. Surf. Sci.* **2018**, *456*, 827–834, doi:10.1016/j.apsusc.2018.06.214.
 40. Yin, J.; Zhang, W.; Alhebshi, N.A.; Salah, N.; Alshareef, H.N. Synthesis Strategies of Porous Carbon for Supercapacitor Applications. *Small Methods* **2020**, *4*, 1–31, doi:10.1002/smtd.201900853.
 41. Liang, H.; Wei, W.; Wu, Z.; Feng, X. Mesoporous Metal–Nitrogen-Doped Carbon Electrocatalysts for Highly Efficient Oxygen Reduction Reaction. *J. Am. Chem. Soc.* **2013**, *135*, 16002–16005.
 42. Fang, Y.; Lv, Y.; Che, R.; Wu, H.; Zhang, X.; Gu, D.; Zheng, G.; Zhao, D. Two-Dimensional Mesoporous Carbon Nanosheets and Their Derived Graphene Nanosheets: Synthesis and Efficient Lithium Ion Storage. *J. Am. Chem. Soc.*

2013, 135, 1524–1530.

43. Lee, D.; Jung, J.; Jung, M.; Lee, Y. Hierarchical Porous Carbon Fibers Prepared Using a SiO₂ Template for High-Performance EDLCs. *Chem. Eng. J.* **2015**, 263, 62–70, doi:10.1016/j.cej.2014.10.070.
44. Liu, Q.; Tang, Z.; Ou, B.; Liu, L.; Zhou, Z.; Shen, S.; Duan, Y. Design, Preparation, and Application of Ordered Porous Polymer Materials. *Mater. Chem. Phys.* **2014**, 144, 213–225, doi:10.1016/j.matchemphys.2014.01.013.
45. Boyer, C.; H. Stenzel, M.; P. Davis, T. Building Nanostructures Using RAFT Polymerization. *J. Polym. Sci. Part A Polym. Chem.* **2011**, 49, 551–819, doi:10.1002/pola.
46. Matyjaszewski, K. Atom Transfer Radical Polymerization (ATRP): Current Status and Future Perspectives. *Macromolecules* **2012**, 45, 4015–4039, doi:10.1021/ma3001719.
47. Hulicova, D.; Oya, A. The Polymer Blend Technique as a Method for Designing Fine Carbon Materials. *Carbon N. Y.* **2003**, 41, 1443–1450.
48. Patel, N.; Okabe, K.; Oya, A. Designing Carbon Materials with Unique Shapes Using Polymer Blending and Coating Techniques. **2002**, 40, 315–320.
49. Kopeć, M.; Lamson, M.; Yuan, R.; Tang, C.; Kruk, M.; Zhong, M.; Matyjaszewski, K.; Kowalewski, T. Polyacrylonitrile-Derived Nanostructured Carbon Materials. *Prog. Polym. Sci.* **2019**, 92, 89–134, doi:10.1016/j.progpolymsci.2019.02.003.
50. Jo, E.; Yeo, J.G.; Kim, D.K.; Oh, J.S.; Hong, C.K. Preparation of Well-Controlled Porous Carbon Nanofiber Materials by Varying the Compatibility of Polymer Blends. *Polym. Int.* **2014**, 63, 1471–1477, doi:10.1002/pi.4645.
51. Ishita, I.; Singhal, R. Porous Multi-Channel Carbon Nanofiber Electrodes Using Discarded Polystyrene Foam as Sacrificial Material for High-Performance Supercapacitors. *J. Appl. Electrochem.* **2020**, 50, 809–820, doi:10.1007/s10800-020-01433-0.

52. He, T.; Fu, Y.; Meng, X.; Yu, X.; Wang, X. A Novel Strategy for the High Performance Supercapacitor Based on Polyacrylonitrile-Derived Porous Nanofibers as Electrode and Separator in Ionic Liquid Electrolyte. *Electrochim. Acta* **2018**, *282*, 97–104, doi:10.1016/j.electacta.2018.06.029.
53. Wang, H.; Shao, Y.; Mei, S.; Lu, Y.; Zhang, M.; Sun, J.K.; Matyjaszewski, K.; Antonietti, M.; Yuan, J. Polymer-Derived Heteroatom-Doped Porous Carbon Materials. *Chem. Rev.* **2020**, *120*, 9363–9419, doi:10.1021/acs.chemrev.0c00080.
54. Li, C.; Li, Q.; Kaneti, Y.V.; Hou, D.; Yamauchi, Y.; Mai, Y. Self-Assembly of Block Copolymers towards Mesoporous Materials for Energy Storage and Conversion Systems. *Chem. Soc. Rev.* **2020**, *49*, 4681–4736, doi:10.1039/d0cs00021c.
55. Mai, Y.; Eisenberg, A. Self-Assembly of Block Copolymers. *Chem. Soc. Rev.* **2012**, *41*, 5969–5985, doi:10.1039/c2cs35115c.
56. Liu, T.; Liu, G. Block Copolymers for Supercapacitors, Dielectric Capacitors and Batteries. *J. Phys. Condens. Matter* **2019**, *31*, doi:10.1088/1361-648X/ab0d77.
57. Kopeć, M.; Yuan, R.; Gottlieb, E.; Abreu, C.M.R.; Song, Y.; Wang, Z.; Coelho, J.F.J.; Matyjaszewski, K.; Kowalewski, T. Polyacrylonitrile-b-Poly(Butyl Acrylate) Block Copolymers as Precursors to Mesoporous Nitrogen-Doped Carbons: Synthesis and Nanostructure. *Macromolecules* **2017**, *50*, 2759–2767, doi:10.1021/acs.macromol.6b02678.
58. Serrano, J.M.; Liu, T.; Khan, A.U.; Botset, B.; Stovall, B.J.; Xu, Z.; Guo, D.; Cao, K.; Hao, X.; Cheng, S.; et al. Composition Design of Block Copolymers for Porous Carbon Fibers. *Chem. Mater.* **2019**, doi:10.1021/acs.chemmater.9b02918.
59. Nothling, M.D.; Fu, Q.; Reyhani, A.; Allison-Logan, S.; Jung, K.; Zhu, J.; Kamigaito, M.; Boyer, C.; Qiao, G.G. Progress and Perspectives Beyond Traditional RAFT Polymerization. *Adv. Sci.* **2020**, *7*, 1–12, doi:10.1002/advs.202001656.
60. Wang, Y.; Kong, L. Bin; Li, X.M.; Ran, F.; Luo, Y.C.; Kang, L. Mesoporous Carbons for Supercapacitors Obtained by the Pyrolysis of Block Copolymers.

Xinxing Tan Cailiao/New Carbon Mater. **2015**, *30*, 302–309, doi:10.1016/s1872-5805(15)60191-3.

61. Kruk, M.; Dufour, B.; Celer, E.B.; Kowalewski, T.; Jaroniec, M.; Matyjaszewski, K. Well-Defined Poly(Ethylene Oxide)-Polyacrylonitrile Diblock Copolymers as Templates for Mesoporous Silicas and Precursors for Mesoporous Carbons. *Chem. Mater.* **2006**, *18*, 1417–1424, doi:10.1021/cm0516154.
62. Aqil, A.; Detrembleur, C.; Gilbert, B.; Jérôme, R.; Jérôme, C. Controlled RAFT Synthesis of Polyacrylonitrile-*b*-Poly(Acrylic Acid) Diblocks as Precursors of Carbon Nanocapsules with Assistance of Gold Nanoparticles. *Chem. Mater.* **2007**, *19*, 2150–2154, doi:10.1021/cm062152k.
63. Nguyen, C.T.; Kim, D.P. Direct Preparation of Mesoporous Carbon by Pyrolysis of Poly(Acrylonitrile-*b*-Methylmethacrylate) Diblock Copolymer. *J. Mater. Chem.* **2011**, *21*, 14226–14230, doi:10.1039/c1jm10920k.
64. Zhou, Z.; Liu, T.; Khan, A.U.; Liu, G. Block Copolymer–Based Porous Carbon Fibers. *Sci. Adv.* **2019**, *5*, 1–10, doi:10.1126/sciadv.aau6852.
65. Dong, W.; Wang, Z.; Zhang, Q.; Ravi, M.; Yu, M.; Tan, Y.; Liu, Y.; Kong, L.; Kang, L.; Ran, F. Polymer/Block Copolymer Blending System as the Compatible Precursor System for Fabrication of Mesoporous Carbon Nanofibers for Supercapacitors. *J. Power Sources* **2019**, *419*, 137–147, doi:10.1016/j.jpowsour.2019.02.070.
66. Zhang, Y.; Sun, Q.; Xia, K.; Han, B.; Zhou, C.; Gao, Q.; Wang, H.; Pu, S.; Wu, J. Facile Synthesis of Hierarchically Porous N/P Codoped Carbon with Simultaneously High-Level Heteroatom-Doping and Moderate Porosity for High-Performance Supercapacitor Electrodes. *ACS Sustain. Chem. Eng.* **2019**, *7*, 5717–5726, doi:10.1021/acssuschemeng.8b05024.
67. Zhao, G.; Li, Y.; Zhu, G.; Shi, J.; Lu, T.; Pan, L. Biomass-Based N, P, and S Self-Doped Porous Carbon for High-Performance Supercapacitors. *ACS Sustain. Chem. Eng.* **2019**, *7*, 12052–12060, doi:10.1021/acssuschemeng.9b00725.
68. Gunasekaran Govindarasu, K.; Venkatesan, R.; Eswaran, M.; Arumugam, P.

- Simple and Efficient CVD Synthesis of Graphitic P-Doped 3D Cubic Ordered Mesoporous Carbon at Low Temperature with Excellent Supercapacitor Performance. *Adv. Powder Technol.* **2022**, *33*, 103439, doi:10.1016/j.appt.2022.103439.
69. Yang, X.; Zheng, Y.; He, C.; Qiu, Y.; Hou, W.; Lu, B.; Chen, Y.; Huang, B.; Lv, J.; Lin, G. Preparation of Biomass-Based N, P, and S Co-Doped Porous Carbon with High Mesoporosity Based on the Synergistic Effect of NaOH/Thiourea and Melamine Phosphate and Its Application in High Performance Supercapacitors. *J. Anal. Appl. Pyrolysis* **2023**, *169*, 105822, doi:10.1016/j.jaap.2022.105822.
 70. Chen, L.; Wen, Z.; Chen, L.; Wang, W.; Ai, Q.; Hou, G.; Li, Y.; Lou, J.; Ci, L. Nitrogen and Sulfur Co-Doped Porous Carbon Fibers Film for Flexible Symmetric All-Solid-State Supercapacitors. *Carbon N. Y.* **2020**, *158*, 456–464, doi:10.1016/j.carbon.2019.11.012.
 71. Ko, W.Y.; Liu, Y.C.; Lai, J.Y.; Chung, C.C.; Lin, K.J. Vertically Standing MnO₂ Nanowalls Grown on AgCNT-Modified Carbon Fibers for High-Performance Supercapacitors. *ACS Sustain. Chem. Eng.* **2019**, *7*, 669–678, doi:10.1021/acssuschemeng.8b04176.
 72. Lv, X.; Li, G.; Zhou, H.; Li, D.; Zhang, J.; Pang, Z.; Lv, P.; Cai, Y.; Huang, F.; Wei, Q. Novel Freestanding N-Doped Carbon Coated Fe₃O₄ Nanocomposites with 3D Carbon Fibers Network Derived from Bacterial Cellulose for Supercapacitor Application. *J. Electroanal. Chem.* **2018**, *810*, 18–26, doi:10.1016/j.jelechem.2017.12.082.
 73. Feng, Y.; Zhang, H.; Zhang, Y.; Bai, Y.; Wang, Y. Novel Peapod NiO Nanoparticles Encapsulated in Carbon Fibers for High-Efficiency Supercapacitors and Lithium-Ion Batteries. *J. Mater. Chem. A* **2016**, *4*, 3267–3277, doi:10.1039/c5ta09699e.
 74. Yang, S.; Han, Z.; Zheng, F.; Sun, J.; Qiao, Z.; Yang, X.; Li, L.; Li, C.; Song, X.; Cao, B. ZnFe₂O₄ Nanoparticles-Cotton Derived Hierarchical Porous Active Carbon Fibers for High Rate-Capability Supercapacitor Electrodes. *Carbon N. Y.* **2018**, *134*, 15–21, doi:10.1016/j.carbon.2018.03.071.

75. Deng, J.; Zhang, J.; Chen, J.; Luo, Y.; Chen, Y.; Xue, Y.; Wang, G.; Wang, R. Fabrication of Layered Porous TiO₂/Carbon Fiber Paper Decorated by Pt Nanoparticles Using Atomic Layer Deposition for Efficient Methanol Electro-Oxidation. *J. Electroanal. Chem.* **2020**, *874*, 114468, doi:10.1016/j.jelechem.2020.114468.
76. Wu, D.; Xie, X.; Zhang, J.; Ma, Y.; Hou, C.; Sun, X.; Yang, X.; Zhang, Y.; Kimura, H.; Du, W. Embedding NiS Nanoflakes in Electrospun Carbon Fibers Containing NiS Nanoparticles for Hybrid Supercapacitors. *Chem. Eng. J.* **2022**, *446*, 137262, doi:10.1016/j.cej.2022.137262.
77. Liu, C.; Li, Q.; Kang, W.; Lei, W.; Wang, X.; Lu, C.; Naebe, M. Structural Design and Mechanism Analysis of Hierarchical Porous Carbon Fibers for Advanced Energy and Environmental Applications. *J. Mater. Chem. A* **2022**, *10*, 10–49, doi:10.1039/d1ta08646d.
78. Wang, R.; Li, X.; Nie, Z.; Jing, Q.; Zhao, Y.; Song, H.; Wang, H. Ag Nanoparticles-Decorated Hierarchical Porous Carbon from Cornstalk for High-Performance Supercapacitor. *J. Energy Storage* **2022**, *51*, 104364, doi:10.1016/j.est.2022.104364.
79. Zhu, R.; Yu, X.; Li, W.; Li, M.; Bo, X.; Gan, G. Cobalt Nanoparticles-Embedded Porous Carbon Nanocages Uniformly Dispersed Hollow Carbon Fibers as the Accelerated Electrocatalysts toward Water Splitting. *J. Alloys Compd.* **2023**, *947*, 169488, doi:10.1016/j.jallcom.2023.169488.
80. Zhang, Y.; Xia, X.; Cao, X.; Zhang, B.; Tiep, N.H.; He, H.; Chen, S.; Huang, Y.; Fan, H.J. Ultrafine Metal Nanoparticles/N-Doped Porous Carbon Hybrids Coated on Carbon Fibers as Flexible and Binder-Free Water Splitting Catalysts. *Adv. Energy Mater.* **2017**, *7*, 1–8, doi:10.1002/aenm.201700220.
81. Shrivastava, A. Introduction to Plastics Engineering. *Introd. to Plast. Eng.* **2018**, 1–16, doi:10.1016/b978-0-323-39500-7.00001-0.
82. Fu, Z.; Gui, Y.; Liu, S.; Wang, Z.; Liu, B.; Cao, C.; Zhang, H. Effects of an Itaconic Acid Comonomer on the Structural Evolution and Thermal Behaviors of Polyacrylonitrile Used for Polyacrylonitrile-Based Carbon Fibers. *J. Appl. Polym.*

- Sci.* **2014**, *131*, 1–8, doi:10.1002/app.40834.
83. Shao, H.; Fang, J.; Wang, H.; Lin, T. Effect of Electrospinning Parameters and Polymer Concentrations on Mechanical-to-Electrical Energy Conversion of Randomly-Oriented Electrospun Poly(Vinylidene Fluoride) Nanofiber Mats. *RSC Adv.* **2015**, *5*, 14345–14350, doi:10.1039/c4ra16360e.
 84. Jacobs, V.; D. Anandjiwala, R.; Maaza, M. The Influence of Electrospinning Parameters on the Structural Morphology and Diameter of Electrospun Nanofibers. *J. Appl. Polym. Sci.* **2010**, *115*, 3130–3136, doi:10.1002/app.
 85. Beachley, V.; Wen, X. Effect of Electrospinning Parameters on the Nanofiber Diameter and Length. *Mater. Sci. Eng. C* **2009**, *29*, 663–668, doi:10.1016/j.msec.2008.10.037.
 86. Ren, L.F.; Xia, F.; Shao, J.; Zhang, X.; Li, J. Experimental Investigation of the Effect of Electrospinning Parameters on Properties of Superhydrophobic PDMS/PMMA Membrane and Its Application in Membrane Distillation. *Desalination* **2017**, *404*, 155–166, doi:10.1016/j.desal.2016.11.023.
 87. Russell, P.; Batchelor, D.; Facility, A.I.; Russell, P.E. SEM and AFM: Complementary Techniques for Surface Investigations. *Microsc. Anal.* **2001**, 9–12.
 88. Adelajda Polkowska¹, Małgorzata Warmuzek¹, Julia Kalarus², Wojciech Polkowski¹, N.S. A Comparison of Various Imaging Modes in Scanning Electron Microscopy during Evaluation of Selected Si/Refractory Sessile Drop Couples after Wettability Tests at Ultra-High Temperature. *Pr. Inst. Odlew.* **2017**, *57*, 337–344, doi:10.7356/iod.2017.35.
 89. Shimodaira, N.; Masui, A. Raman Spectroscopic Investigations of Activated Carbon Materials. *J. Appl. Phys.* **2002**, *92*, 902–909, doi:10.1063/1.1487434.
 90. Li, Z.; Deng, L.; Kinloch, I.A.; Young, R.J. Raman Spectroscopy of Carbon Materials and Their Composites: Graphene, Nanotubes and Fibres. *Prog. Mater. Sci.* **2023**, *135*, 101089, doi:10.1016/j.pmatsci.2023.101089.

91. Zhou, Z.; Liu, G. Controlling the Pore Size of Mesoporous Carbon Thin Films through Thermal and Solvent Annealing. *Small* **2017**, *13*, 19–21, doi:10.1002/sml.201603107.
92. Tzeng, S. Catalytic Graphitization of Electroless Ni – P Coated PAN-Based Carbon Fibers. **2006**, *44*, 1986–1993, doi:10.1016/j.carbon.2006.01.024.
93. Zhong, M.; Kim, E.K.; McGann, J.P.; Chun, S.; Whitacre, J.F.; Jaroniec, M.; Matyjaszewski, K.; Kowalewski, T. Electrochemically Active Nitrogen-Enriched Nanocarbons with Well-Defined Morphology Synthesized by Pyrolysis of Self-Assembled Block Copolymer. **2012**.
94. Bardestani, R.; Patience, G.S. Experimental Methods in Chemical Engineering : Specific Surface Area and Pore Size Distribution Measurements — BET ,. **2019**, 2781–2791, doi:10.1002/cjce.23632.
95. Huang, B.; Bartholomew, C.H.; Woodfield, B.F. Microporous and Mesoporous Materials Improved Calculations of Pore Size Distribution for Relatively Large , Irregular Slit-Shaped Mesopore Structure. *Microporous Mesoporous Mater.* **2014**, *184*, 112–121, doi:10.1016/j.micromeso.2013.10.008.
96. Castro-Gutiérrez, J.; Celzard, A.; Fierro, V. Energy Storage in Supercapacitors: Focus on Tannin-Derived Carbon Electrodes. *Front. Mater.* **2020**, *7*, 1–25, doi:10.3389/fmats.2020.00217.
97. Mei, B.A.; Munteshari, O.; Lau, J.; Dunn, B.; Pilon, L. Physical Interpretations of Nyquist Plots for EDLC Electrodes and Devices. *J. Phys. Chem. C* **2018**, *122*, 194–206, doi:10.1021/acs.jpcc.7b10582.
98. Mei, B.; Munteshari, O.; Lau, J.; Dunn, B.; Pilon, L. Physical Interpretations of Nyquist Plots for EDLC Electrodes and Devices. **2018**, doi:10.1021/acs.jpcc.7b10582.
99. Ponnusamy, K.; Babu, R.P.; Dhamodharan, R. Synthesis of Block and Graft Copolymers of Styrene by Raft Polymerization, Using Dodecyl-Based Trithiocarbonates as Initiators and Chain Transfer Agents. *J. Polym. Sci. Part A Polym. Chem.* **2013**, *51*, 1066–1078, doi:10.1002/pola.26466.

100. Germack, D.S.; Wooley, K.L. RAFT-Based Synthesis and Characterization of ABC versus ACB Triblock Copolymers Containing Tert-Butyl Acrylate, Isoprene, and Styrene Blocks. *Macromol. Chem. Phys.* **2007**, *208*, 2481–2491, doi:10.1002/macp.200700433.
101. Moskowitz, J.D.; Abel, B.A.; McCormick, C.L.; Wiggins, J.S. High Molecular Weight and Low Dispersity Polyacrylonitrile by Low Temperature RAFT Polymerization. *J. Polym. Sci. Part A Polym. Chem.* **2016**, *54*, 553–562, doi:10.1002/pola.27806.
102. Jenkins, A.D.; Jones, R.G.; Moad, G. Terminology for Reversible-Deactivation Radical Polymerization Previously Called “Controlled” Radical or “Living” Radical Polymerization (IUPAC Recommendations 2010). *Pure Appl. Chem.* **2010**, *82*, 483–491, doi:10.1351/PAC-REP-08-04-03.
103. Barner-Kowollik, C.; Buback, M.; Charleux, B.; L. Coote, M.; Drache, M.; Fukuda, T.; Goto, A.; Klumperman, B.; B. Lowe, A.; B. Mcleary, J.; et al. Mechanism and Kinetics of Dithiobenzoate-Mediated RAFT Polymerization. I. The Current Situation. *J. Polym. Sci. Part A Polym. Chem.* **2006**, *44*, 5809–6146, doi:10.1002/pola.
104. Opiyo, G.; Jin, J. Recent Progress in Switchable RAFT Agents: Design, Synthesis and Application. *Eur. Polym. J.* **2021**, *159*, 110713, doi:10.1016/j.eurpolymj.2021.110713.
105. Álvarez-Gómez, A.; Yuan, J.; Fernández-Blázquez, J.P.; San-Miguel, V.; Serrano, M.B. Polyacrylonitrile-b-Polystyrene Block Copolymer-Derived Hierarchical Porous Carbon Materials for Supercapacitor. *Polymers (Basel)*. **2022**, *14*, doi:10.3390/polym14235109.
106. Liu, Y.; Cavicchi, K.A. Reversible Addition Fragmentation Chain Transfer (RAFT) Polymerization with a Polymeric RAFT Agent Containing Multiple Trithiocarbonate Groups. *Macromol. Chem. Phys.* **2009**, *210*, 1647–1653, doi:10.1002/macp.200900201.
107. Perrier, S. 50th Anniversary Perspective: RAFT Polymerization - A User Guide. *Macromolecules* **2017**, *50*, 7433–7447, doi:10.1021/acs.macromol.7b00767.

108. Johnston-Hall, G.; Monteiro, M.J. Kinetic Modeling of “Living” and Conventional Free Radical Polymerizations of Methyl Methacrylate in Dilute and Gel Regimes. *Macromolecules* **2007**, *40*, 7171–7179, doi:10.1021/ma070984d.
109. Valdebenito, A.; Encinas, M.V. Effect of Solvent on the Free Radical Polymerization of N,N-Dimethylacrylamide. *Polym. Int.* **2010**, *59*, 1246–1251, doi:10.1002/pi.2856.
110. Wypych, G. Introduction. *Handb. Polym.* **2012**, 1–2, doi:10.1016/b978-1-895198-47-8.50003-5.
111. Gupta, A.K.; Paliwal, D.K.; Bajaj, P. Melting Behavior of Acrylonitrile Polymers. *J. Appl. Polym. Sci.* **1998**, *70*, 2703–2709, doi:10.1002/(sici)1097-4628(19981226)70:13<2703::aid-app15>3.0.co;2-2.
112. Wang, Y.-X.; Wang, C.-G.; Wu, J.-W.; Jing, M. High-Temperature DSC Study of Polyacrylonitrile Precursors during Their Conversion to Carbon Fibers. *J. Appl. Polym. Sci.* **2007**, *106*, 1787–1792, doi:10.1002/app.
113. Fernández-García, M.; De la Fuente, J.L.; Cerrada, M.L.; Madruga, E.L. Preparation of Poly(Tert-Butyl Acrylate-g-Styrene) as Precursors of Amphiphilic Graft Copolymers. 1. Kinetic Study and Thermal Properties. *Polymer (Guildf)*. **2002**, *43*, 3173–3179, doi:10.1016/S0032-3861(02)00140-4.
114. Kowalewski, T.; Tsarevsky, N. V.; Matyjaszewski, K. Nanostructured Carbon Arrays from Block Copolymers of Polyacrylonitrile. *J. Am. Chem. Soc.* **2002**, *124*, 10632–10633, doi:10.1021/ja0178970.
115. Kowalewski, T.; McCullough, R.D.; Matyjaszewski, K. Complex Nanostructured Materials from Segmented Copolymers Prepared by ATRP. *Eur. Phys. J. E* **2003**, *10*, 5–16, doi:10.1140/epje/e2003-00009-x.
116. John, M.G.C.; Lath, D. MISCIBILITY MAPPING IN SOME BLENDS INVOLVING POLY(STYRENE-Co- ACRYLONITRILE). *Makromol. Chem., Macromol. Symp.* **1988**, *16*, 103–112.
117. Tang, C.; Jia, S.; Matyjaszewski, K.; Kowalewski, T. Morphology and Thermal

Behavior of Well-Defined Polyacrylonitrile-b-Poly (n-Butyl Acrylate) Block Copolymer Precursors for Nanostructured Carbons. **2004**, 1–8.

118. Sundararajan, P.R. *Physical Aspects of Polymer Self-Assembly*; Jonh Wiley & Sons., 2016;
119. Seo, M.; Hillmyer, M.A. Reticulated Nanoporous Polymers by Controlled Polymerization-Induced Microphase Separation. *Science (80-.).* **2012**, 336, 1422–1425, doi:10.1126/science.1221383.
120. Ran, F.; Shen, K.; Tan, Y.; Peng, B.; Chen, S.; Zhang, W.; Niu, X.; Kong, L.; Kang, L. Activated Hierarchical Porous Carbon as Electrode Membrane Accommodated with Triblock Copolymer for Supercapacitors. *J. Memb. Sci.* **2016**, 514, 366–375, doi:10.1016/j.memsci.2016.05.011.
121. Sun, Y.; Cheng, S.; Lu, W.; Wang, Y.; Zhang, P.; Yao, Q. Electrospun Fibers and Their Application in Drug Controlled Release, Biological Dressings, Tissue Repair, and Enzyme Immobilization. *RSC Adv.* **2019**, 9, 25712–25729, doi:10.1039/c9ra05012d.
122. Wang, X.X.; Yu, G.F.; Zhang, J.; Yu, M.; Ramakrishna, S.; Long, Y.Z. Conductive Polymer Ultrafine Fibers via Electrospinning: Preparation, Physical Properties and Applications. *Prog. Mater. Sci.* **2021**, 115, 100704, doi:10.1016/j.pmatsci.2020.100704.
123. Ryšánek, P.; Benada, O.; Tokarský, J.; Syrový, M.; Čapková, P.; Pavlík, J. Specific Structure, Morphology, and Properties of Polyacrylonitrile (PAN) Membranes Prepared by Needleless Electrospinning; Forming Hollow Fibers. *Mater. Sci. Eng. C* **2019**, 105, doi:10.1016/j.msec.2019.110151.
124. Lu, C.; Chiang, S.W.; Du, H.; Li, J.; Gan, L.; Zhang, X.; Chu, X.; Yao, Y.; Li, B.; Kang, F. Thermal Conductivity of Electrospinning Chain-Aligned Polyethylene Oxide (PEO). *Polymer (Guildf).* **2017**, 115, 52–59, doi:10.1016/j.polymer.2017.02.024.
125. Pervez, M.N.; Talukder, M.E.; Mishu, M.R.; Buonerba, A.; del Gaudio, P.; Stylios, G.K.; Hasan, S.W.; Zhao, Y.; Cai, Y.; Figoli, A.; et al. Fabrication of

- Polyethersulfone/Polyacrylonitrile Electrospun Nanofiber Membrane for Food Industry Wastewater Treatment. *J. Water Process Eng.* **2022**, *47*, 102838, doi:10.1016/j.jwpe.2022.102838.
126. Zhang, X.; Qi, Y.; Yang, J.; Dong, S.; Liu, J.; Li, J.; Shi, K. Insight into Stabilization Behaviors of Lignin/PAN-Derived Electrospun Precursor Fibers. *Polym. Degrad. Stab.* **2021**, *191*, 109680, doi:10.1016/j.polymdegradstab.2021.109680.
 127. Kim, J.K.; Yang, S.Y.; Lee, Y.; Kim, Y. Functional Nanomaterials Based on Block Copolymer Self-Assembly. *Prog. Polym. Sci.* **2010**, *35*, 1325–1349, doi:10.1016/j.progpolymsci.2010.06.002.
 128. Elkasaby, M.; Hegab, H.A.; Mohany, A.; Rizvi, G.M. Modeling and Optimization of Electrospinning of Polyvinyl Alcohol (PVA). *Adv. Polym. Technol.* **2018**, *37*, 2114–2122, doi:10.1002/adv.21869.
 129. Li, P.; Qiao, Y.; Zhao, L.; Yao, D.; Sun, H.; Hou, Y.; Li, S.; Li, Q. Electrospun PS/PAN Fibers with Improved Mechanical Property for Removal of Oil from Water. *Mar. Pollut. Bull.* **2015**, *93*, 75–80, doi:10.1016/j.marpolbul.2015.02.012.
 130. Wei, P.; Qi, Z.; Yan, C. Preparation of Polyacrylonitrile and Polystyrene Blend Fibers through Electrospinning. *Adv. Mater. Res.* **2011**, *332–334*, 235–238, doi:10.4028/www.scientific.net/AMR.332-334.235.
 131. Yi, Y.; Tu, H.; Zhou, X.; Liu, R.; Wu, Y.; Li, D.; Wang, Q.; Shi, X.; Deng, H. Acrylic Acid-Grafted Pre-Plasma Nanofibers for Efficient Removal of Oil Pollution from Aquatic Environment. *J. Hazard. Mater.* **2019**, *371*, 165–174, doi:10.1016/j.jhazmat.2019.02.085.
 132. Liu, J.; Xiong, Z.; Wang, S.; Cai, W.; Yang, J.; Zhang, H. Structure and Electrochemistry Comparison of Electrospun Porous Carbon Nanofibers for Capacitive Deionization. *Electrochim. Acta* **2016**, *210*, 171–180, doi:10.1016/j.electacta.2016.05.133.
 133. Bhoyate, S.; Kahol, P.K.; Sapkota, B.; Mishra, S.R.; Perez, F.; Gupta, R.K. Polystyrene Activated Linear Tube Carbon Nanofiber for Durable and High-

- Performance Supercapacitors. *Surf. Coatings Technol.* **2018**, *345*, 113–122, doi:10.1016/j.surfcoat.2018.04.026.
134. Munir, M.M.; Suryamas, A.B.; Iskandar, F.; Okuyama, K. Scaling Law on Particle-to-Fiber Formation during Electrospinning. *Polymer (Guildf)*. **2009**, *50*, 4935–4943, doi:10.1016/j.polymer.2009.08.011.
 135. Gupta, P.; Elkins, C.; Long, T.E.; Wilkes, G.L. Electrospinning of Linear Homopolymers of Poly(Methyl Methacrylate): Exploring Relationships between Fiber Formation, Viscosity, Molecular Weight and Concentration in a Good Solvent. *Polymer (Guildf)*. **2005**, *46*, 4799–4810, doi:10.1016/j.polymer.2005.04.021.
 136. Zhang, C.; Yuan, X.; Wu, L.; Han, Y.; Sheng, J. Study on Morphology of Electrospun Poly(Vinyl Alcohol) Mats. *Eur. Polym. J.* **2005**, *41*, 423–432, doi:10.1016/j.eurpolymj.2004.10.027.
 137. Ferrari, A.C.; Rodil, S.E.; Robertson, J.; Rodil, S.E.; Robertson, J. Interpretation of Infrared and Raman Spectra of Amorphous Carbon Nitrides. *Phys. Rev. B - Condens. Matter Mater. Phys.* **2003**, *67*, 1–20, doi:10.1103/PhysRevB.67.155306.
 138. Lee, H.; Kang, H.; An, K.; Kim, H.; Kim, B. Comparative Studies of Porous Carbon Nanofibers by Various Activation Methods. *Carbon Lett.* **2013**, *14*, 180–185, doi:10.5714/CL.2013.14.3.180.
 139. Zhou, Z.; Liu, T.; Khan, A.U.; Liu, G. Controlling the Physical and Electrochemical Properties of Block Copolymer-Based Porous Carbon Fibers by Pyrolysis Temperature. *Mol. Syst. Des. Eng.* **2019**, *5*, 153–165, doi:10.1039/C9ME00066F.
 140. Thommes, M. Physical Adsorption Characterization of Nanoporous Materials. *Chemie Ing. Tech.* **2010**, *82*, 951–1122, doi:10.1002/cite.201000064.
 141. Thommes, M.; Smarsly, B.; Groenewolt, M.; Ravikovitch, P.I.; Neimark, A. V Adsorption Hysteresis of Nitrogen and Argon in Pore Networks and Characterization of Novel Micro- and Mesoporous Silicas. **2006**, 756–764.

142. Álvarez, M.; Baselga, J.; Pozuelo, J. Tuning the Electromagnetic Shielding Mechanism with Nitrogen-Doped Graphene Aerogels. *ChemNanoMat* **2023**, *9*, 1–10, doi:10.1002/cnma.202200451.
143. Lin, Y.; Chen, Z.; Yu, C.; Zhong, W. Facile Synthesis of High Nitrogen-Doped Content, Mesopore-Dominated Biomass-Derived Hierarchical Porous Graphitic Carbon for High Performance Supercapacitors. *Electrochim. Acta* **2020**, *334*, 135615, doi:10.1016/j.electacta.2020.135615.
144. Hulicova-Jurcakova, D.; Seredych, M.; Lu, G.Q.; Bandosz, T.J. Combined Effect of Nitrogen- and Oxygen-Containing Functional Groups of Microporous Activated Carbon on Its Electrochemical Performance in Supercapacitors. *Adv. Funct. Mater.* **2009**, *19*, 438–447, doi:10.1002/adfm.200801236.
145. Gao, Y.; Qing, W.; Guozhao, J.; Aimin, L.; Jiamin, N. Doping Strategy, Properties and Application of Heteroatom-Doped Ordered Mesoporous Carbon. *RSC Adv.* **2021**, *11*, 5361–5383, doi:10.1039/d0ra08993a.
146. Chen, T.; Luo, L.; Luo, L.; Deng, J.; Wu, X.; Fan, M.; Du, G.; Zhao, W. High Energy Density Supercapacitors with Hierarchical Nitrogen-Doped Porous Carbon as Active Material Obtained from Bio-Waste. **2021**, *175*, doi:10.1016/j.renene.2021.05.006.
147. Oda, H.; Yamashita, A.; Minoura, S.; Okamoto, M.; Morimoto, T. Modification of the Oxygen-Containing Functional Group on Activated Carbon Fiber in Electrodes of an Electric Double-Layer Capacitor. *J. Power Sources* **2006**, *158*, 1510–1516, doi:10.1016/j.jpowsour.2005.10.061.
148. Koski, A.; Yim, K.; Shivkumar, S. Effect of Molecular Weight on Fibrous PVA Produced by Electrospinning. *Mater. Lett.* **2004**, *58*, 493–497, doi:10.1016/S0167-577X(03)00532-9.
149. Ji, S.; Wan, L.; Liu, C.C.; Nealey, P.F. Directed Self-Assembly of Block Copolymers on Chemical Patterns: A Platform for Nanofabrication. *Prog. Polym. Sci.* **2016**, *54–55*, 76–127, doi:10.1016/j.progpolymsci.2015.10.006.
150. De La Olvera Cruz, M. Theory of Microphase Separation in Block Copolymer

Solutions. *J. Chem. Phys.* **1989**, *90*, 1995–2002, doi:10.1063/1.456042.

151. Tao, J.; Shivkumar, S. Molecular Weight Dependent Structural Regimes during the Electrospinning of PVA. *Mater. Lett.* **2007**, *61*, 2325–2328, doi:10.1016/j.matlet.2006.09.004.
152. Park, G.S.; Lee, J.; Kim, S.T.; Park, S.; Cho, J. Porous Nitrogen Doped Carbon Fiber with Churros Morphology Derived from Electrospun Bicomponent Polymer as Highly Efficient Electrocatalyst for Zn e Air Batteries. *J. Power Sources* **2013**, *243*, 267–273, doi:10.1016/j.jpowsour.2013.06.025.
153. Ramachandran, J.; Lu, M.; Arias-Monje, P.J.; Kirmani, M.H.; Shirolkar, N.; Kumar, S. Towards Designing Strong Porous Carbon Fibers through Gel Spinning of Polymer Blends. *Carbon N. Y.* **2021**, *173*, 724–735, doi:10.1016/j.carbon.2020.10.029.
154. Aydin, S.; Erdogan, T.; Sakar, D.; Hizal, G.; Cankurtaran, O.; Tunca, U.; Karaman, F. Detection of Microphase Separation in Poly(Tert-Butyl Acrylate-b-Methyl Methacrylate) Synthesized via Atom Transfer Radical Polymerization by Inverse Gas Chromatography. *Eur. Polym. J.* **2008**, *44*, 2115–2122, doi:10.1016/j.eurpolymj.2008.04.010.
155. Lessard, B.; Tervo, C.; Marić, M. High-Molecular-Weight Poly(Tert-Butyl Acrylate) by Nitroxide-Mediated Polymerization: Effect of Chain Transfer to Solvent. *Macromol. React. Eng.* **2009**, *3*, 245–256, doi:10.1002/mren.200900014.
156. Miao, L.; Zhu, D.; Zhao, Y.; Liu, M.; Duan, H.; Xiong, W.; Zhu, Q.; Li, L.; Lv, Y.; Gan, L. Design of Carbon Materials with Ultramicro-, Supermicro- and Mesopores Using Solvent- and Self-Template Strategy for Supercapacitors. *Microporous Mesoporous Mater.* **2017**, *253*, 1–9, doi:10.1016/j.micromeso.2017.06.032.
157. Fuertes, A.B.; Lota, G.; Centeno, T.A.; Frackowiak, E. Templated Mesoporous Carbons for Supercapacitor Application. *Electrochim. Acta* **2005**, *50*, 2799–2805, doi:10.1016/j.electacta.2004.11.027.
158. Zhang, Z.; Song, L.; Cheng, L.; Tan, J.; Yang, W. Accelerated Graphitization of

- PAN-Based Carbon Fibers: K⁺-Effected Graphitization via Laser Irradiation. *ACS Sustain. Chem. Eng.* **2022**, *10*, 8086–8093, doi:10.1021/acssuschemeng.2c02417.
159. McGann, J.P.; Zhong, M.; Kim, E.K.; Natesakhawat, S.; Jaroniec, M.; Whitacre, J.F.; Matyjaszewski, K.; Kowalewski, T. Block Copolymer Templating as a Path to Porous Nanostructured Carbons with Highly Accessible Nitrogens for Enhanced (Electro)Chemical Performance. *Macromol. Chem. Phys.* **2012**, *213*, 1078–1090, doi:10.1002/macp.201100691.
 160. Song, M.; Zhou, Y.; Ren, X.; Wan, J.; Du, Y.; Wu, G.; Ma, F. Biowaste-Based Porous Carbon for Supercapacitor: The Influence of Preparation Processes on Structure and Performance. *J. Colloid Interface Sci.* **2019**, *535*, 276–286, doi:10.1016/j.jcis.2018.09.055.
 161. Gang, B.; Zhang, F.; Li, X.; Zhai, B.; Wang, X.; Song, Y. A Ulva Lactuca-Derived Porous Carbon for High-Performance Electrode Materials in Supercapacitor: Synergistic Effect of Porous Structure and Graphitization Degree. *J. Energy Storage* **2021**, *33*, 102132, doi:10.1016/j.est.2020.102132.
 162. Liu, Y.; Dai, H.; Wu, L.; Zhou, W.; He, L.; Wang, W.; Yan, W.; Huang, Q.; Fu, L.; Wu, Y. A Large Scalable and Low-Cost Sulfur/Nitrogen Dual-Doped Hard Carbon as the Negative Electrode Material for High-Performance Potassium-Ion Batteries. *Adv. Energy Mater.* **2019**, *9*, 1–9, doi:10.1002/aenm.201901379.
 163. Lv, H.; Xiao, Z.; Zhai, S.; Hao, J.; Tong, Y.; Wang, G.; An, Q. Construction of Nickel Ferrite Nanoparticle-Loaded on Carboxymethyl Cellulose-Derived Porous Carbon for Efficient Pseudocapacitive Energy Storage. *J. Colloid Interface Sci.* **2022**, *622*, 327–335, doi:10.1016/j.jcis.2022.04.133.
 164. Hu, X.; Luo, Y.; Wu, X.; Niu, J.; Tan, M.; Sun, Z.; Liu, W. Heteroatom-Doped Microporous Carbon Nanosheets Derived from Pentaerythritol-Melamine for Supercapacitors and CO₂ Capture. *Mater. Today Energy* **2022**, *27*, 101010, doi:10.1016/j.mtener.2022.101010.
 165. Yu, X.; Kang, Y.; Park, H.S. Sulfur and Phosphorus Co-Doping of Hierarchically Porous Graphene Aerogels for Enhancing Supercapacitor Performance. *Carbon N. Y.* **2016**, *101*, 49–56, doi:10.1016/j.carbon.2016.01.073.

166. Yusof, N.; Ismail, A.F. Post Spinning and Pyrolysis Processes of Polyacrylonitrile (PAN)-Based Carbon Fiber and Activated Carbon Fiber: A Review. *J. Anal. Appl. Pyrolysis* **2012**, *93*, 1–13, doi:10.1016/j.jaap.2011.10.001.
167. Qin, X.; Lu, Y.; Xiao, H.; Wen, Y.; Yu, T. A Comparison of the Effect of Graphitization on Microstructures and Properties of Polyacrylonitrile and Mesophase Pitch-Based Carbon Fibers. *Carbon N. Y.* **2012**, *50*, 4459–4469, doi:10.1016/j.carbon.2012.05.024.
168. Tavanai, H.; Jalili, R.; Morshed, M. Effects of Fiber Diameter and CO₂ Activation Temperature on the Pore Characteristics of Polyacrylonitrile Based Activated Carbon Nanofibers. *Surf. Interface Anal.* **2009**, *41*, 814–819, doi:10.1002/sia.3104.
169. Ma, G.; Ning, G.; Wei, Q. S-Doped Carbon Materials: Synthesis, Properties and Applications. *Carbon N. Y.* **2022**, *195*, 328–340, doi:10.1016/j.carbon.2022.03.043.
170. Wabo, S.G.; Klepel, O. Nitrogen Release and Pore Formation through KOH Activation of Nitrogen-Doped Carbon Materials: An Evaluation of the Literature. *Carbon Lett.* **2021**, *31*, 581–592, doi:10.1007/s42823-021-00252-3.
171. Zhou, J.; Wang, M.; Li, X. Facile Preparation of Nitrogen-Doped High-Surface-Area Porous Carbon Derived from Sucrose for High Performance Supercapacitors. *Appl. Surf. Sci.* **2018**, *462*, 444–452, doi:10.1016/j.apsusc.2018.08.158.
172. Kelemen, S.R.; Afeworki, M.; Gorbaty, M.L.; Kwiatek, P.J.; Sansone, M.; Walters, C.C.; Cohen, A.D. Thermal Transformations of Nitrogen and Sulfur Forms in Peat Related to Coalification. *Energy and Fuels* **2006**, *20*, 635–652, doi:10.1021/ef050307p.
173. Kelemen, S.R.; Gorbaty, M.L.; Kwiatek, P.J.; Fletcher, T.H.; Watt, M.; Solum, M.S.; Pugmire, R.J. Nitrogen Transformations in Coal during Pyrolysis. *Energy and Fuels* **1998**, *12*, 159–173, doi:10.1021/ef9701246.
174. Zhang, H.; Ling, Y.; Peng, Y.; Zhang, J.; Guan, S. Nitrogen-Doped Porous Carbon Materials Derived from Ionic Liquids as Electrode for Supercapacitor. *Inorg. Chem. Commun.* **2020**, *115*, 107856, doi:10.1016/j.inoche.2020.107856.

175. Sun, Y.; Xiao, H.; Li, H.; He, Y.; Zhang, Y.; Hu, Y.; Ju, Z.; Zhuang, Q.; Cui, Y. Nitrogen/Oxygen Co-Doped Hierarchically Porous Carbon for High-Performance Potassium Storage. *Chem. - A Eur. J.* **2019**, *25*, 7359–7365, doi:10.1002/chem.201900448.
176. Figueiredo, J.L.; Pereira, M.F.R.; Freitas, M.M.A.; Órfão, J.J.M. Modification of the Surface Chemistry of Activated Carbons. *Carbon N. Y.* **1999**, *37*, 1379–1389, doi:10.1016/S0008-6223(98)00333-9.
177. Li, J.; Liu, W.; Xiao, D.; Wang, X. Oxygen-Rich Hierarchical Porous Carbon Made from Pomelo Peel Fiber as Electrode Material for Supercapacitor. *Appl. Surf. Sci.* **2017**, *416*, 918–924, doi:10.1016/j.apsusc.2017.04.162.
178. Zhang, J.; Zhou, J.; Wang, D.; Hou, L.; Gao, F. Nitrogen and Sulfur Codoped Porous Carbon Microsphere: A High Performance Electrode in Supercapacitor. *Electrochim. Acta* **2016**, *191*, 933–939, doi:10.1016/j.electacta.2016.01.150.
179. Lei, W.; Guo, J.; Wu, Z.; Xuan, C.; Xiao, W.; Wang, D. Highly Nitrogen and Sulfur Dual-Doped Carbon Microspheres for Supercapacitors. *Sci. Bull.* **2017**, *62*, 1011–1017, doi:10.1016/j.scib.2017.06.001.
180. Mou, Z.; Chen, X.; Du, Y.; Wang, X.; Yang, P.; Wang, S. Forming Mechanism of Nitrogen Doped Graphene Prepared by Thermal Solid-State Reaction of Graphite Oxide and Urea. *Appl. Surf. Sci.* **2011**, *258*, 1704–1710, doi:10.1016/j.apsusc.2011.10.019.
181. Barczak, M.; Bandosz, T.J. Evaluation of Nitrogen- and Sulfur-Doped Porous Carbon Textiles as Electrode Materials for Flexible Supercapacitors. *Electrochim. Acta* **2019**, *305*, 125–136, doi:10.1016/j.electacta.2019.03.014.
182. Wang, Y.; Fu, A.; Liu, X.; Wang, Y.; Li, Y.; Guo, P.; Li, H.; Zhao, X.S. Porous Carbon Directed Growth of Carbon Modified MnO₂ Porous Spheres for Pseudocapacitor Applications. *J. Alloys Compd.* **2017**, *717*, 341–349, doi:10.1016/j.jallcom.2017.05.035.
183. Zhang, X.; Shi, W.; Zhu, J.; Kharistal, D.J.; Zhao, W.; Lalia, B.S.; Hng, H.H.; Yan, Q. High-Power and High-Energy-Density Flexible Pseudocapacitor Electrodes

Made from Porous CuO Nanobelts and Single-Walled Carbon Nanotubes. *ACS Nano* **2011**, 5, 2013–2019, doi:10.1021/nn1030719.

184. Guo, D.; Zhao, W.; Pan, F.; Liu, G. Block Copolymer-Derived Porous Carbon Fibers Enable High MnO₂ Loading and Fast Charging in Aqueous Zinc-Ion Battery. *Batter. Supercaps* **2022**, 5, doi:10.1002/batt.202100380.
185. Thomas, S.; Amiradegh, R.N. *Handbook of Magnetic Hybrid Nanoalloys and Their Nanocomposites*; Springer Nature, 2022;
186. Li, R.; Wang, Y.; Zhou, C.; Wang, C.; Ba, X.; Li, Y.; Huang, X.; Liu, J. Carbon-Stabilized High-Capacity Ferroferric Oxide Nanorod Array for Flexible Solid-State Alkaline Battery-Supercapacitor Hybrid Device with High Environmental Suitability. *Adv. Funct. Mater.* **2015**, 25, 5384–5394, doi:10.1002/adfm.201502265.
187. Jabbar, A.; Khan, A.; Sufyan, M.; Arshad, M.; Asim, S.; Khalid, M.; Hussain, S.; Hussain, S.; Hanif, M.; Liu, Z. Surface Assembly of Fe₃O₄ Nanodiscs Embedded in Reduced Graphene Oxide as a High-Performance Negative Electrode for Supercapacitors. *Ceram. Int.* **2020**, 46, 19499–19505, doi:10.1016/j.ceramint.2020.04.303.
188. Kwon, T.; Park, H.; Jo, O.H.; Chun, J.; Kang, B. Facile Preparation of Magnetite-Incorporated Polyacrylonitrile-Derived Carbons for Li-Ion Battery Anodes. *ACS Appl. Energy Mater.* **2022**, 5, 1262–1270, doi:10.1021/acsaem.1c03679.
189. Lv, J.; Liu, Z.; Dong, Z. Iron Oxide Modified N-Doped Porous Carbon Derived from Porous Organic Polymers as a Highly-Efficient Catalyst for Reduction of Nitroarenes. *Mol. Catal.* **2020**, 498, 111249, doi:10.1016/j.mcat.2020.111249.
190. Qiao, K.; Tian, W.; Bai, J.; Wang, L.; Zhao, J.; Du, Z. Application of Magnetic Adsorbents Based on Iron Oxide Nanoparticles for Oil Spill Remediation: A Review. *J. Taiwan Inst. Chem. Eng.* **2019**, 97, 227–236, doi:10.1016/j.jtice.2019.01.029.
191. Chen, J.; Zheng, J.; Wang, F.; Huang, Q.; Ji, G. Carbon Fibers Embedded with FeIII-MOF-5-Derived Composites for Enhanced Microwave Absorption. *Carbon*

N. Y. **2021**, *174*, 509–517, doi:10.1016/j.carbon.2020.12.077.

192. Wei, Y.; Wei, S.; Liu, C.; Chen, T.; Tang, Y.; Ma, J.; Yin, K.; Luo, S. Efficient Removal of Arsenic from Groundwater Using Iron Oxide Nanoneedle Array-Decorated Biochar Fibers with High Fe Utilization and Fast Adsorption Kinetics. *Water Res.* **2019**, *167*, 115107, doi:10.1016/j.watres.2019.115107.
193. Juang, R.S.; Yei, Y.C.; Liao, C.S.; Lin, K.S.; Lu, H.C.; Wang, S.F.; Sun, A.C. Synthesis of Magnetic Fe₃O₄/Activated Carbon Nanocomposites with High Surface Area as Recoverable Adsorbents. *J. Taiwan Inst. Chem. Eng.* **2018**, *90*, 51–60, doi:10.1016/j.jtice.2017.12.005.
194. Meng, X.; Huang, J.; Bian, Y.; Du, H.; Xu, Y.; Zhu, S.; Li, Q.; Chen, M.; Lin, M. Flexible Fe₃O₄/PCNFs Membrane Prepared by an Innovative Method as High-Performance Anode for Lithium-Ion Battery. *J. Solid State Chem.* **2021**, *303*, 122456, doi:10.1016/j.jssc.2021.122456.
195. Lin, Y.; Wang, X.; Qian, G.; Watkins, J.J. Additive-Driven Self-Assembly of Well-Ordered Mesoporous Carbon/Iron Oxide Nanoparticle Composites for Supercapacitors. *Chem. Mater.* **2014**, *26*, 2128–2137, doi:10.1021/cm404199z.
196. Qiao, L.; Fu, Z.; Li, J.; Ghosen, J.; Zeng, M.; Stebbins, J.; Prasad, P.N.; Swihart, M.T. Standardizing Size- and Shape-Controlled Synthesis of Monodisperse Magnetite (Fe₃O₄) Nanocrystals by Identifying and Exploiting Effects of Organic Impurities. *ACS Nano* **2017**, *11*, 6370–6381, doi:10.1021/acsnano.7b02752.
197. Zhang, D.; Karki, A.B.; Rutman, D.; Young, D.P.; Wang, A.; Cocke, D.; Ho, T.H.; Guo, Z. Electrospun Polyacrylonitrile Nanocomposite Fibers Reinforced with Fe₃O₄ Nanoparticles : Fabrication and Property Analysis. *Polymer (Guildf)*. **2009**, *50*, 4189–4198, doi:10.1016/j.polymer.2009.06.062.
198. Sarkar, B.; Alexandridis, P. Block Copolymer-Nanoparticle Composites: Structure, Functional Properties, and Processing. *Prog. Polym. Sci.* **2015**, *40*, 33–62, doi:10.1016/j.progpolymsci.2014.10.009.
199. Gang, Q.; Niaz Akhtar, M.; Boudaghi, R. Development of High-Efficient Double Layer Microwave Absorber Based on Fe₃O₄/Carbon Fiber and Fe₃O₄/RGO. *J.*

- Magn. Magn. Mater.* **2021**, 537, 168181, doi:10.1016/j.jmmm.2021.168181.
200. Pang, X.; Zhou, T.; Jiang, Q.; Kumar, P.; Geng, S.; Jia, M.; Zhou, J.; Liu, B.; Qin, H. Porous Graphitic Carbon Fibers for Fast-Charging Supercapacitor Applications. *Energy Technol.* **2020**, 8, 1–9, doi:10.1002/ente.202000050.
 201. Hsieh, W.; Horng, T.L.A.; Huang, H.C.; Teng, H. Facile Simulation of Carbon with Wide Pore Size Distribution for Electric Double-Layer Capacitance Based on Helmholtz Models. *J. Mater. Chem. A* **2015**, 3, 16535–16543, doi:10.1039/c5ta04125b.
 202. Atrei, A.; Lesiak-Orlowska, B.; Tóth, J. Magnetite Nanoparticles Functionalized with Citrate: A Surface Science Study by XPS and ToF-SIMS. *Appl. Surf. Sci.* **2022**, 602, doi:10.1016/j.apsusc.2022.154366.
 203. Zhang, R.; Bao, S.; Tan, Q.; Li, B.; Wang, C.; Shan, L.; Wang, C.; Xu, B. Facile Synthesis of a Rod-like Porous Carbon Framework Confined Magnetite Nanoparticle Composite for Superior Lithium-Ion Storage. *J. Colloid Interface Sci.* **2021**, 600, 602–612, doi:10.1016/j.jcis.2021.05.065.
 204. Butnoi, P.; Pangoon, A.; Berger, R.; Butt, H.J.; Intasanta, V. Electrospun Nanocomposite Fibers from Lignin and Iron Oxide as Supercapacitor Material. *J. Mater. Res. Technol.* **2021**, 12, 2153–2167, doi:10.1016/j.jmrt.2021.04.017.
 205. Zhou, Y.; Ren, X.; Du, Y.; Jiang, Y.; Wan, J.; Ma, F. In-Situ Template Cooperated with Urea to Construct Pectin-Derived Hierarchical Porous Carbon with Optimized Pore Structure for Supercapacitor. *Electrochim. Acta* **2020**, 355, doi:10.1016/j.electacta.2020.136801.
 206. Xie, L.; Su, F.; Xie, L.; Guo, X.; Wang, Z.; Kong, Q.; Sun, G.; Ahmad, A.; Li, X.; Yi, Z.; et al. Effect of Pore Structure and Doping Species on Charge Storage Mechanisms in Porous Carbon-Based Supercapacitors. *Mater. Chem. Front.* **2020**, 4, 2610–2634, doi:10.1039/d0qm00180e.
 207. Banerjee, S.; De, B.; Sinha, P.; Cherusseri, J.; Kar, K.K. *Handbook of Nanocomposite Supercapacitor Materials I: Characteristics*; 2020; Vol. 300; ISBN 9783030430085.

208. Yuan, R.; Wang, H.; Sun, M.; Damodaran, K.; Gottlieb, E.; Kopeć, M.; Eckhart, K.; Li, S.; Whitacre, J.; Matyjaszewski, K.; et al. Well-Defined N/S Co-Doped Nanocarbons from Sulfurized PAN- b-PBA Block Copolymers: Structure and Supercapacitor Performance. *ACS Appl. Nano Mater.* **2019**, *2*, 2467–2474, doi:10.1021/acsanm.9b00340.
209. Tong, Y.X.; Li, X.M.; Xie, L.J.; Su, F.Y.; Li, J.P.; Sun, G.H.; Gao, Y.D.; Zhang, N.; Wei, Q.; Chen, C.M. Nitrogen-Doped Hierarchical Porous Carbon Derived from Block Copolymer for Supercapacitor. *Energy Storage Mater.* **2016**, *3*, 140–148, doi:10.1016/j.ensm.2016.02.005.
210. Josef, E.; Yan, R.; Guterman, R.; Oschatz, M. Electrospun Carbon Fibers Replace Metals as a Current Collector in Supercapacitors. *ACS Appl. Energy Mater.* **2019**, *2*, 5724–5733, doi:10.1021/acsaem.9b00854.
211. Eftekhari, A. Surface Diffusion and Adsorption in Supercapacitors. *ACS Sustain. Chem. Eng.* **2019**, *7*, 3692–3701, doi:10.1021/acssuschemeng.8b01075.
212. Thomas, E.L.; Lescanec, R.L.; Frank, F.C.; Higgins, J.S.; Klug, A. Phase Morphology in Block Copolymer Systems. *Philos. Trans. R. Soc. London. Ser. A Phys. Eng. Sci.* **1994**, *348*, 149–166, doi:10.1098/rsta.1994.0086.
213. Zhang, J.; Chen, H.; Bai, J.; Xu, M.; Luo, C.; Yang, L.; Bai, L.; Wei, D.; Wang, W.; Yang, H. N-Doped Hierarchically Porous Carbon Derived from Grape Marcs for High-Performance Supercapacitors. *J. Alloys Compd.* **2021**, *854*, 157207, doi:10.1016/j.jallcom.2020.157207.
214. Cao, S.; Qu, T.; Zhang, A.; Zhao, Y.; Chen, A. N-Doped Hierarchical Porous Carbon with Open-Ended Structure for High-Performance Supercapacitors. *ChemElectroChem* **2019**, *6*, 1696–1703, doi:10.1002/celec.201801813.
215. Zhang, L.; Han, L.; Liu, S.; Zhang, C.; Liu, S. High-Performance Supercapacitors Based on Electrospun Multichannel Carbon Nanofibers. *RSC Adv.* **2015**, *5*, 107313–107317, doi:10.1039/c5ra23338k.
216. Ramakrishnan, P.; Shanmugam, S. Nitrogen-Doped Porous Multi-Nano-Channel Nanocarbons for Use in High-Performance Supercapacitor Applications. *ACS*

- Sustain. Chem. Eng.* **2016**, *4*, 2439–2448, doi:10.1021/acssuschemeng.6b00289.
217. Dong, W.; Wang, Z.; Zhang, Q.; Ravi, M.; Yu, M.; Tan, Y.; Liu, Y.; Kong, L.; Kang, L.; Ran, F. Polymer/Block Copolymer Blending System as the Compatible Precursor System for Fabrication of Mesoporous Carbon Nanofibers for Supercapacitors. *J. Power Sources* **2019**, *419*, 137–147, doi:10.1016/j.jpowsour.2019.02.070.
 218. He, G.; Song, Y.; Chen, S.; Wang, L. Porous Carbon Nanofiber Mats from Electrospun Polyacrylonitrile/Polymethylmethacrylate Composite Nanofibers for Supercapacitor Electrode Materials. *J. Mater. Sci.* **2018**, *53*, 9721–9730, doi:10.1007/s10853-018-2277-5.
 219. Portet, C.; Taberna, P.L.; Simon, P.; Laberty-Robert, C. Modification of Al Current Collector Surface by Sol-Gel Deposit for Carbon-Carbon Supercapacitor Applications. *Electrochim. Acta* **2004**, *49*, 905–912, doi:10.1016/j.electacta.2003.09.043.
 220. Mathis, T.S.; Kurra, N.; Wang, X.; Pinto, D.; Simon, P.; Gogotsi, Y. Energy Storage Data Reporting in Perspective—Guidelines for Interpreting the Performance of Electrochemical Energy Storage Systems. *Adv. Energy Mater.* **2019**, *9*, 1–13, doi:10.1002/aenm.201902007.
 221. Masarapu, C.; Zeng, H.F.; Hung, K.H.; Wei, B. Effect of Temperature on the Capacitance of Carbon Nanotube Supercapacitors. *ACS Nano* **2009**, *3*, 2199–2206, doi:10.1021/nn900500n.
 222. Lu, Y.; Zhang, S.; Yin, J.; Bai, C.; Zhang, J.; Li, Y.; Yang, Y.; Ge, Z.; Zhang, M.; Wei, L.; et al. Mesoporous Activated Carbon Materials with Ultrahigh Mesopore Volume and Effective Specific Surface Area for High Performance Supercapacitors. *Carbon N. Y.* **2017**, *124*, 64–71, doi:10.1016/j.carbon.2017.08.044.
 223. Niu, L.; Shen, C.; Yan, L.; Zhang, J.; Lin, Y.; Gong, Y.; Li, C.; Sun, C.Q.; Xu, S. Waste Bones Derived Nitrogen-Doped Carbon with High Micropore Ratio towards Supercapacitor Applications. *J. Colloid Interface Sci.* **2019**, *547*, 92–101, doi:10.1016/j.jcis.2019.03.097.

224. Mofokeng, T.P.; Tetana, Z.N.; Ozoemena, K.I. Defective 3D Nitrogen-Doped Carbon Nanotube-Carbon Fibre Networks for High-Performance Supercapacitor: Transformative Role of Nitrogen-Doping from Surface-Confined to Diffusive Kinetics. *Carbon N. Y.* **2020**, *169*, 312–326, doi:10.1016/j.carbon.2020.07.049.
225. Lee, Y.H.; Chang, K.H.; Hu, C.C. Differentiate the Pseudocapacitance and Double-Layer Capacitance Contributions for Nitrogen-Doped Reduced Graphene Oxide in Acidic and Alkaline Electrolytes. *J. Power Sources* **2013**, *227*, 300–308, doi:10.1016/j.jpowsour.2012.11.026.
226. Lee, W.H.; Moon, J.H. Monodispersed N-Doped Carbon Nanospheres for Supercapacitor Application. *ACS Appl. Mater. Interfaces* **2014**, *6*, 13968–13976, doi:10.1021/am5033378.
227. Yin, W.M.; Tian, L.F.; Pang, B.; Guo, Y.R.; Li, S.J.; Pan, Q.J. Fabrication of Dually N/S-Doped Carbon from Biomass Lignin: Porous Architecture and High-Rate Performance as Supercapacitor. *Int. J. Biol. Macromol.* **2020**, *156*, 988–996, doi:10.1016/j.ijbiomac.2020.04.102.
228. Guo, Y.; Wang, T.; Wu, D.; Tan, Y. One-Step Synthesis of in-Situ N, S Self-Doped Carbon Nanosheets with Hierarchical Porous Structure for High Performance Supercapacitor and Oxygen Reduction Reaction Electrocatalyst. *Electrochim. Acta* **2021**, *366*, doi:10.1016/j.electacta.2020.137404.
229. Xin, G.; Wang, M.M.; Zhang, W.; Song, J.; Zhang, B. Preparation of High-Capacitance N,S Co-Doped Carbon Nanospheres with Hierarchical Pores as Supercapacitors. *Electrochim. Acta* **2018**, *291*, 168–176, doi:10.1016/j.electacta.2018.08.137.
230. Liu, M.; Huo, S.; Xu, M.; Wu, L.; Liu, M.; Xue, Y.; Yan, Y.M. Structural Engineering of N/S Co-Doped Carbon Material as High-Performance Electrode for Supercapacitors. *Electrochim. Acta* **2018**, *274*, 389–399, doi:10.1016/j.electacta.2018.04.084.
231. Lei, J.; Guo, Q.; Yin, D.; Cui, X.; He, R.; Duan, T.; Zhu, W. Bioconcentration and Bioassembly of N/S Co-Doped Carbon with Excellent Stability for Supercapacitors. *Appl. Surf. Sci.* **2019**, *488*, 316–325,

doi:10.1016/j.apsusc.2019.05.136.

232. Wang, T.; Wang, L.X.; Wu, D.L.; Xia, W.; Jia, D.Z. Interaction between Nitrogen and Sulfur in Co-Doped Graphene and Synergetic Effect in Supercapacitor. *Sci. Rep.* **2015**, *5*, 1–9, doi:10.1038/srep09591.
233. Shao, Y.; Wang, Y.; Li, X.; Kheirabad, A.K.; Zhao, Q.; Yuan, J.; Wang, H. Crosslinking of a Single Poly(Ionic Liquid) by Water into Porous Supramolecular Membranes. *Angew. Chemie* **2020**, *132*, 17340–17344, doi:10.1002/ange.202002679.
234. Yan, S.; Li, R.; Fu, X.; Yuan, W.; Jin, L.; Li, Y.; Wang, X.; Zhang, Y. Porous Polyimide-Based Activated Carbon Fibers for CO₂ Capture and Supercapacitor. *Energy and Fuels* **2022**, *36*, 11012–11024, doi:10.1021/acs.energyfuels.2c01513.
235. Liu, Z.; Lv, Y.; Fang, J.; Zuo, X.; Zhang, C.; Yue, X. A New Method for an Efficient Porous Carbon/Fe₃O₄ Composite Based Electromagnetic Wave Absorber Derived from a Specially Designed Polyimide. *Compos. Part B Eng.* **2018**, *155*, 148–155, doi:10.1016/j.compositesb.2018.08.038.
236. Hernández, G.; Casado, N.; Coste, R.; Shanmukaraj, D.; Rubatat, L.; Armand, M.; Mecerreyes, D. Redox-Active Polyimide-Polyether Block Copolymers as Electrode Materials for Lithium Batteries. *RSC Adv.* **2015**, *5*, 17096–17103, doi:10.1039/c4ra15976d.
237. Azam, K.; Raza, R.; Shezad, N.; Shabir, M.; Yang, W.; Ahmad, N.; Shafiq, I.; Akhter, P.; Razzaq, A.; Hussain, M. Development of Recoverable Magnetic Mesoporous Carbon Adsorbent for Removal of Methyl Blue and Methyl Orange from Wastewater. *J. Environ. Chem. Eng.* **2020**, *8*, 104220, doi:10.1016/j.jece.2020.104220.
238. Ma, C.; Bai, J.; Demir, M.; Yu, Q.; Hu, X.; Jiang, W.; Wang, L. Polyacrylonitrile-Derived Nitrogen Enriched Porous Carbon Fiber with High CO₂ Capture Performance. *Sep. Purif. Technol.* **2022**, *303*, 122299, doi:10.1016/j.seppur.2022.122299.
239. Hu, M.; Li, Z.; Li, G.; Hu, T.; Zhang, C.; Wang, X. All-Solid-State Flexible Fiber-

- Based MXene Supercapacitors. *Adv. Mater. Technol.* **2017**, *2*, 1–6, doi:10.1002/admt.201700143.
240. Sun, L.; Fu, Q.; Pan, C. Hierarchical Porous “Skin/Skeleton”-like MXene/Biomass Derived Carbon Fibers Heterostructure for Self-Supporting, Flexible All Solid-State Supercapacitors. *J. Hazard. Mater.* **2021**, *410*, 124565, doi:10.1016/j.jhazmat.2020.124565.
 241. Levitt, A.S.; Alhabeb, M.; Hatter, C.B.; Sarycheva, A.; Dion, G.; Gogotsi, Y. Electrospun MXene/Carbon Nanofibers as Supercapacitor Electrodes. *J. Mater. Chem. A* **2019**, *7*, 269–277, doi:10.1039/c8ta09810g.
 242. Puppi, D.; Chiellini, F. Wet-Spinning of Biomedical Polymers: From Single-Fibre Production to Additive Manufacturing of Three-Dimensional Scaffolds. *Polym. Int.* **2017**, *66*, 1690–1696, doi:10.1002/pi.5332.
 243. Hu, W.; Xiang, R.; Zhang, K.; Xu, Q.; Liu, Y.; Jing, Y.; Zhang, J.; Hu, X.; Zheng, Y.; Jin, Y.; et al. Electrochemical Performance of Coaxially Wet-Spun Hierarchically Porous Lignin-Based Carbon/Graphene Fiber Electrodes for Flexible Supercapacitors. *ACS Appl. Energy Mater.* **2021**, *4*, 9077–9089, doi:10.1021/acsaem.1c01379.
 244. Khumujam, D.D.; Kshetri, T.; Singh, T.I.; Kim, N.H.; Lee, J.H. Fibrous Asymmetric Supercapacitor Based on Wet Spun MXene/PAN Fiber-Derived Multichannel Porous MXene/CF Negatrode and NiCo₂S₄ Electrodeposited MXene/CF Positrode. *Chem. Eng. J.* **2022**, *449*, 137732, doi:10.1016/j.cej.2022.137732.
 245. Ma, W.; Chen, S.; Yang, S.; Zhu, M. Hierarchically Porous Carbon Black/Graphene Hybrid Fibers for High Performance Flexible Supercapacitors. *RSC Adv.* **2016**, *6*, 50112–50118, doi:10.1039/c6ra08799j.